

UNIVERSITY OF NAPLES “FEDERICO II”



“SCUOLA POLITECNICA E DELLE SCIENZE DI BASE”

DEPARTMENT OF INDUSTRIAL ENGINEERING

(Mechanic and Energetic Section)

DOCTOR OF PHYLOSOPHY IN MECHANICAL SYSTEMS ENGINEERING

(XXVIII Cycle)

DOCTORAL THESIS

**MODELING OF TURBULENCE, COMBUSTION AND KNOCK FOR
PERFORMANCE PREDICTION, CALIBRATION AND DESIGN OF A
TURBOCHARGED SPARK IGNITION ENGINE**

COORDINATOR OF DOCTORAL SCHOOL:

Prof. Fabio Bozza

Tutors:

Candidate:

Prof. Fabio Bozza

Eng. Luigi Teodosio

Eng. Vincenzo De Bellis

Acknowledgments

At the end of the Doctoral course there are many people I would like to thank.

First and foremost, I would like to express my sincere gratitude to **Prof. Fabio Bozza**, my supervisor of this thesis work, who always gave me his full availability and support during the course of this project, not only by a professional point of view but also on a personal level. The realization of this thesis work would have not been possible without him.

I want to thank Eng. **Vincenzo De Bellis** and Prof. **Alfredo Gimelli** for their availability, competence and also personal support, which contributed to the resolution of many of the problems faced during the course of this work.

I want to give special thanks and my endless gratitude to my father, my mother and my brothers, who were always there for me in any moment: without their unconditional support nothing could have been possible.

Last but not least, thanks to all the friends who spent with me these years at University of Naples: the path was hard but it surely would have been harder without your friendship.

Contents

Abstract	15
Introduction	17
1. Description of characteristics and operation of modern Spark Ignition Engines	21
1.1 Description of Spark Ignition internal combustion engine	21
1.2 Modern technologies for gasoline engine	25
1.2.1 Downsizing by Turbocharging	25
1.2.2 Variable Valve Actuation Systems and strategies	26
1.2.3 Cylinder deactivation	32
1.2.4 Compression ratio adjustment	32
1.2.5 Stratified charge by direct injection	33
1.2.6 Homogeneous Charge Compression Ignition (HCCI)	34
1.2.7 EGR systems and water injection technology	35
1.2.8 Engine friction reduction	36
1.3 Turbulent Combustion in Spark Ignition Engine	36
1.3.1 Turbulence phenomenon	40
1.3.2 Turbulent premixed flames	43
1.3.3 Flame propagation within the combustion chamber	46
1.4 Cycle by cycle variation	48
1.5 Knock phenomenon	54
1.6 Engine system description	58
1.6.1 Experimental activities	60
1.6.2 Engine calibration issues	63
1.7 Structure of this work	65
2. Modeling of Internal Combustion engines and in-cylinder processes	67
2.1 Modeling Approaches	67
2.1.1 Zero-dimensional Approach	68
2.1.2 One-dimensional Approach	71
2.1.3 Three-dimensional Approach	77
2.2 Integration of Modeling Approaches: 1D/3D methodology	80

2.3 0D Combustion Modeling: “Fractal Combustion Model”	82
2.4 Turbulence Modeling in 3D codes: RANS technique and “k-ε model”	85
2.4.1 0D/3D hierarchical approach for turbulence modeling	89
2.5 0D Turbulence Modeling: K-k model	89
3. Engine Model Validation	93
3.1 0D-1D Models Description	93
3.1.1 Air Intake System	93
3.1.2 Compressor	94
3.1.3 Intercooler	95
3.1.4 Intake Manifold and Runners	95
3.1.5 Intake Pipes and Fuel Injectors	96
3.1.6 Engine Cylinders and Intake/Exhaust valves	97
3.1.7 Exhaust System and Turbine Object	98
3.1.8 Model Subroutines	99
3.2 0D Turbulence model validation	100
3.3 Engine Model Tuning at Full Load Operation	104
3.4 Engine Model Tuning at Part Load Operation	107
4. Experimental Knock Detection and Modeling	110
4.1 Overview of knock detection	110
4.2 Experimental Approaches for knock detection	114
4.2.1 Maximum Amplitude of Pressure Oscillation (MAPO) Analysis	114
4.2.2 ARMA Technique	115
4.3 Cyclic dispersion through random perturbation of combustion parameters	119
4.4 Cycle by cycle variation model and validation	121
4.5 Knock model description and validation	125
5. EGR System Employment to reduce the fuel consumption and the knock occurrence	128
5.1 Adoption of EGR Systems for SI Engine	128
5.2 Numerical analyses description	131
5.3 Results of Cooled EGR Analyses	134

6. Port Water Injection to improve fuel economy and reduce knock occurrence	140
6.1 Employment of water injection technique for Spark Ignition engine	140
6.2 Numerical set-up for water injection investigation	142
6.3 Results discussion	145
6.4 Comparison between cooled EGR and water injection techniques	150
7. Gas-dynamic noise prediction and re-design of the air-filter box to improve the acoustic performance	155
7.1 Introduction	155
7.2 Air Box device: 1D/3D Models Description	158
7.2.1 1D Model	158
7.2.2 3D Model	158
7.3 Refined Turbocharger Modeling	160
7.4 Gas-dynamic noise: Validation at Full Load	161
7.5 Air-box redesign	166
7.6 Transmission Loss: 3D FEM Model and Results	170
7.7 Gas-dynamic noise: 3D CFD results at Full and part Load Operation	172
8. Virtual Engine Calibration through optimization code	176
8.1 Introduction and formulation of Multi-objectives Optimization	176
8.1.1 Description of Genetic Algorithms for Multi-objectives Optimization	177
8.2 Engine Model Validation for <i>Full Lift</i> and <i>EIVC</i> Strategies	181
8.3 Optimization Procedure Description at Full Load	184
8.4 Results Discussion at Full Load	185
8.5 Optimization Procedure Description at Part Load	191
8.6 Results Discussion at Part Load	192
Conclusions	196
List of papers during doctoral studies	199
References	200

Nomenclature

Abbreviations

0D	Zero dimensional
1D	One dimensional
3D	Three dimensional
A/F	Air to fuel ratio
AFTDC	After Top dead centre
AIC	Akaike information criterion
A/R	Auto Regressive
ARMA	Auto Regressive Moving Average
BC	Boundary condition
BDC	Bottom dead centre
BMEP	Brake mean effective pressure
BSFC	Brake specific fuel consumption
CAD	Computer Aided Design
CCV	Cycle by cycle variation
CD	Cylinder deactivation
CFD	Computational fluid dynamic
CI	Compression Ignition
CoV	Coefficient of variation
DFT	Discrete Fourier Transform
DI	Direct Injection
DISC	Direct injection stratified charge
DMOEA	Dynamic Multi-objective evolutionary algorithm
DNA	Deoxyribonucleic acid

DNS	Direct Numerical Simulation
ECU	Electronic control unit
EGR	Exhaust gas recirculation
EIVC	Early intake valve closure
ETBE	Ethyl tertiary butyl ether
EVM	Eddy viscosity models
EVO	Exhaust valve opening
FEM	Finite element method
FL	Full Lift
FTDC	Firing Top dead centre
GA	Genetic algorithm
HCCI	Homogeneous charge compression ignition
HP-EGR	High pressure exhaust gas recirculation
HVA	Hydraulic valve lash adjustment
ICEs	Internal combustion engines
IMEP	Indicated mean effective pressure
IMPO	Integral of Modulus of pressure oscillations
ISFC	Indicated specific fuel consumption
IVC	Intake valve closure
IVO	Intake valve opening
KLSA	Knock limited spark advance
LES	Large eddy simulation
LHV	Lower heating value
LIVO	Late intake valve opening
LP	Low pressure
LP-EGR	Low pressure exhaust gas recirculation
MAPO	Maximum Amplitude of pressure oscillation
MBT	Maximum Brake Torque

MEA	Multi-objective Evolutionary Algorithm
MFB	Mass fraction burned
MKE	Mean flow kinetic energy
ML	Multi lift
MOGA	Multi-objective Genetic Algorithm
MTBE	Methyl tertiary butyl ether
NA	Naturally aspirated
NEDC	New European driving cycle
NPGA	Niched Pareto Genetic Algorithm
NSGA	Nondominated Sorting Genetic Algorithm
NV	Noise Variance
OEM	Original equipment manufacturer
ORC	Organic Rankine cycle
PAES	Pareto-Archived Evolution Strategy
PESA	Pareto Envelope-based Selection Algorithm
PFI	Port Fuel injection
PID	Proportional Integral Derivative
PMEP	Pumping mean effective pressure
RANS	Reynolds averaged Navier Stokes
RDGA	Rank-Density Based Genetic Algorithm
RWGA	Random Weighted Genetic Algorithm
SA	Spark Advance
SI	Spark Ignition
SMC	Second Moment Closure
SPEA	Strength Pareto Evolutionary Algorithm
SPL	Sound pressure level
TDC	Top dead centre
TIT	Turbine inlet temperature

TKE	Turbulent kinetic energy
TL	Transmission loss
VCR	Variable compression ratio
VEGA	Vector evaluated Genetic Algorithm
VVA	Variable valve actuation
VVL	Variable valve lift
VVT	Variable valve timing
WBGA	Weight-based Genetic Algorithm
W/F	Water fuel ratio
WG	Wastegate valve
WI	Water injection
WOT	Wide open throttle

Latin Letters

a	Speed of sound
A	Area of surface S
A_L	Laminar flame surface
A_T	Turbulent flame surface
c	Perimeter of the single pipe
c_i	CoV _{IMEP} correlation parameters
c_k	Concentration of k-th chemical species
c_p	Specific heat at constant pressure
c_v	Specific heat at constant volume
d_i	CoV _{pmax} correlation parameters
D	Molecular diffusivity
D₃	Fractal dimension

Da	Damköhler number
D_r	Rate of dissipation of turbulent kinetic energy
e	Specific energy
E	Total energy
f_a	Friction coefficient
F	Vector of flows
g_i	Gravity acceleration
G	Production/destruction of turbulent kinetic energy k due to mass forces
h_i	Specific enthalpy
h_{max}	Maximum valve lift
H	Total enthalpy
k	Turbulent kinetic energy
K	Mean kinetic energy
Ka	Karlovitz number
L	Energy in terms of mechanical work
L_T	Integral length scale
L_{max}	Maximum flame wrinkling scale
L_{min}	Minimum flame wrinkling scale
m	Mass
P	Production of turbulent kinetic energy
p	Pressure
Q̇	Thermal power
q̇	Heat exchange through the wall per unit time and fluid mass
R	Constant of gas
Re	Reynolds number
S	Vector of source term
S_L	Laminar flame speed
S_{ij}	Mean rate of strain

t	Time
T	Temperature
u	Velocity
U	Vector of conservative variables
V	Volume
x	Mass fraction
x_b	Burnt mass fraction
x_i	Axis coordinate

Greek Letters

α	Air to fuel ratio
α_A	Geometrical parameter in 1D continuity equation
β	Throttle opening angle
γ	Ratio between c_p and c_v
δ	Flame thickness
ε	Dissipation rate of kinetic energy
η	Kinematic viscosity
η_T	Kolmogorov length scale
θ	Crank angle
Θ	Fluctuation part of Temperature for turbulent flows
λ	Thermal conductivity
μ	Dynamic viscosity
ν	Kinematic viscosity
ρ	Density
τ	Time
τ_{ij}	Stress tensor

φ	Intake valve angle
χ	Spark ignition timing
ω	Fluctuation part of single parameter for turbulent flows
Ω	Mean part of single parameter for turbulent flow

Subscripts

air	Referred to air flow
avg	Referred to average pressure cycle
b	Burned gas
c	Referred to chamber of Helmholtz resonator
ch	Referred to Chemical time scale
cyl	cylinder
EGR	Referred to the exhaust gas recirculation
fu	Fuel
f	Flame
h	Referred to high pressure cycle
IMEP	Referred to the indicated mean effective pressure
k	Referred to the Kolmogorov length scale
knock	Referred to the knock phenomenon
L	Referred to the Laminar flows
max	maximum value
MBT	Referred to the Maximum brake torque condition
min	minimum value
n	Referred to the neck of the Helmholtz resonator
pist	Referred to the engine piston
pmax	maximum pressure

r	Referred to the residual gas
T	Referred to the turbulent flows
trans	Referred to the transition from laminar to turbulent flame
tumb	Referred to the tumble motion
u	unburned gas
valve	Referred to the engine valve
w	Referred to the water
wall	Referred to the wall
wc	Referred to the wall combustion
wr	Referred to the wrinkling of the flame front

Abstract

In this thesis work, a downsized VVA Spark Ignition engine is numerically and experimentally studied. In particular, the following topics are considered:

- In-cylinder turbulence and combustion processes;
- Knock and cycle by cycle variation (CCV) phenomena;
- Techniques aiming to mitigate knock occurrence and improve fuel economy such as EGR and water injection methods;
- Intake system redesign to reduce the emitted gas-dynamic noise;
- Engine calibration.

A deep experimental campaign is carried out to characterize the engine behaviour. Indeed, engine system is investigated both in terms of the overall performance (torque, power, fuel consumption, air flow rate, boost pressure etc.) and of the intake gas-dynamic noise at full load operation. In addition, proper experimental analyses are performed on the engine to characterize the CCV phenomenon and the knock occurrence. Measured data are post-processed to derive experimental parameters which synthesize CCV and knock levels, according to the engine operating conditions. A 1D CFD model of the whole engine is realized in GT-PowerTM environment. Refined “in-house developed” sub-models capable to reproduce turbulence, combustion, CCVs and knock processes are introduced into 1D code through user routines. First of all, the whole engine model is validated against the experimental data both in terms of overall performance parameters and *ensemble averaged* pressure cycles and intake gas-dynamic noise at part and full load operation. Cycle by cycle variation is reproduced through a proper correlation and consequently a representative *faster than average* in-cylinder pressure cycle is obtained. Then, the knock model, with reference to the latter pressure cycle, allows to evaluate a proper knock index and to identify the knock limited spark advance (KLSA), basing on the same threshold level adopted in experimental knock analysis. In this way, the knock model taking into account the CCV is validated at full load operation. Once validated, the original engine architecture is modified by virtually installing a “Low pressure” EGR system. 1D simulations accounting for various EGR rates and mixture leaning are performed at full load points, showing improvements in the fuel economy with the same knock intensity of the base engine configuration. Water injection technique is also investigated by virtually mounting a water injector in the intake runners for each engine cylinder. In a similar way, 1D analyses are carried out

for various water/fuel and air-to-fuel ratios, highlighting BSFC improvements at full load operation. Since the engine under study is characterized by higher intake gas-dynamic noise levels, a partial redesign of the intake system is properly identified and subsequently tested with 1D and 3D CFD simulations to numerically quantify the gains in terms of reduction in the gas-dynamic noise emitted at the intake mouth. Finally, a numerical methodology aiming to calibrate the considered engine at high load knock-limited and at part load operations is developed. First, it shows the capability to identify with satisfactory accuracy the experimentally advised engine calibration. In addition, it allows the comparison of different intake valve strategies, underlining, in certain engine operating conditions, the fuel consumption benefits of an early intake valve closure (*EIVC*) strategy with respect to a *Full Lift* one, due to a better combustion phasing and a reduced mixture over-fuelling. The developed automatic procedure presents the capability to realize a “virtual” engine calibration on completely theoretical basis and proves to be very helpful in reducing time and costs related to experimental activities at the test bench.

Introduction

Nowadays the growing demand for sustainable worldwide transportation poses as the main challenge for internal combustion engines, as well as for thermal machines, the reduction of the pollutant emissions and the improvement in the specific fuel consumption. The spark ignition (SI) engines show a relevant contribution to the problem of the air pollution, since this type of engine is widely employed as propulsion system for vehicles within the transport sector [1]. The worldwide growing of the total number of vehicles, needed to meet the increased demand of transportation, has led to a consequently increase in the global fuel consumption and CO₂ emissions. As an example, Figure I shows the trend of the world car production over 30 years and it can be noted that more than 56 millions of cars have been produced till the 2013 [2].

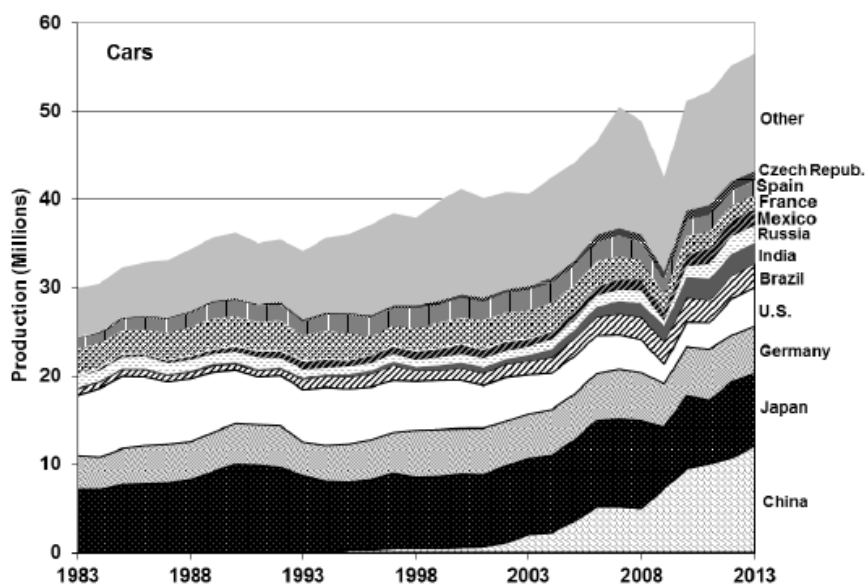


Figure I – World production of cars as function of years and countries [2]

In the future, the people of emerging countries (such as China, India, South Korea, etc.) will contribute to the worsening of the global fuel consumption through the increased sales of vehicles. Table A reports the average numbers of vehicles per 1000 people in different regions of the world. As expected, the above table confirms that the presence of vehicle is high for very rich countries like USA, Canada, Western Europe while vehicle ownership is low in developing countries (like Africa and Indonesia).

Country/Region	Vehicles per 1,000 people	
	2003	2013
Africa	22.6	34.6
Asia, Far East	45.0	81.9
Asia, Middle East	85.5	129.5
Brazil	114.8	197.5
Canada	580.0	646.1
Central & South America	114.2	184.6
China	18.7	88.6
Europe, East	224.5	332.4
Europe, West	565.7	589.6
India	10.1	26.6
Indonesia	28.1	77.2
Pacific	515.3	576.2
United States	816.1	808.6

Table A – Number of vehicles per 1000 inhabitants in various regions (Years 2003 and 2013) [2].

It is the case to highlight that the developing countries are characterized by a continuous growing population and for this reason the number of vehicles will increase even more than expected prevision. This involves additional problems for the reduction of the global fuel consumption and emissions. Referring to the pollutant emissions, several studies [3] demonstrate that the transportation sector (including the movement of people and goods by cars, trucks, trains, ships, airplanes and other vehicles) represents one of the major causes for the production of the greenhouse gas as shown in Figure III.

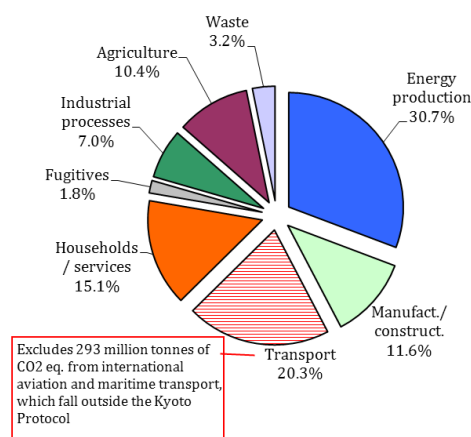


Figure III – EU-27 greenhouse gas emission by source sector (2009).

The majority of greenhouse gas emissions from transportation are CO₂ emissions resulting from the combustion of petroleum-based products, like gasoline, in internal combustion engines. The largest sources of transportation-related greenhouse gas emissions include passenger cars and light-duty trucks, such as sport utility vehicles, pickup trucks, and minivans. For the case of Spark Ignition internal combustion engines, carbon dioxide emission is in strong correlation with the fuel economy and it depends on the engine efficiency. The reduction in CO₂ emissions, or the increase of the SI engine efficiency, has both environment and economic reasons. For the scope of global CO₂ emission, the European Commission has developed an ambitious mandatory CO₂ emission reduction program, with a fleet-average CO₂ emission target of 130 g/km to be reached by 2015, and a long-term target of 95 g CO₂/km to be reached from 2020. As said, internal combustion engines are widely adopted for passenger cars and they are responsible not only for CO₂ emissions but also for the production of other noxious species. In particular, the SI engines, representing the most employed engines for vehicles, show three main pollutant emissions: nitrogen oxides (NO_x), carbon monoxide (CO) and unburned hydrocarbons (HC). These emissions are dangerous for human health [4]. Specific limitations for SI engine emissions have been defined in different countries such as USA, European Union and Japan. In Figure IV emission limitations for passenger cars with SI engines in European Union over the years are presented [5].

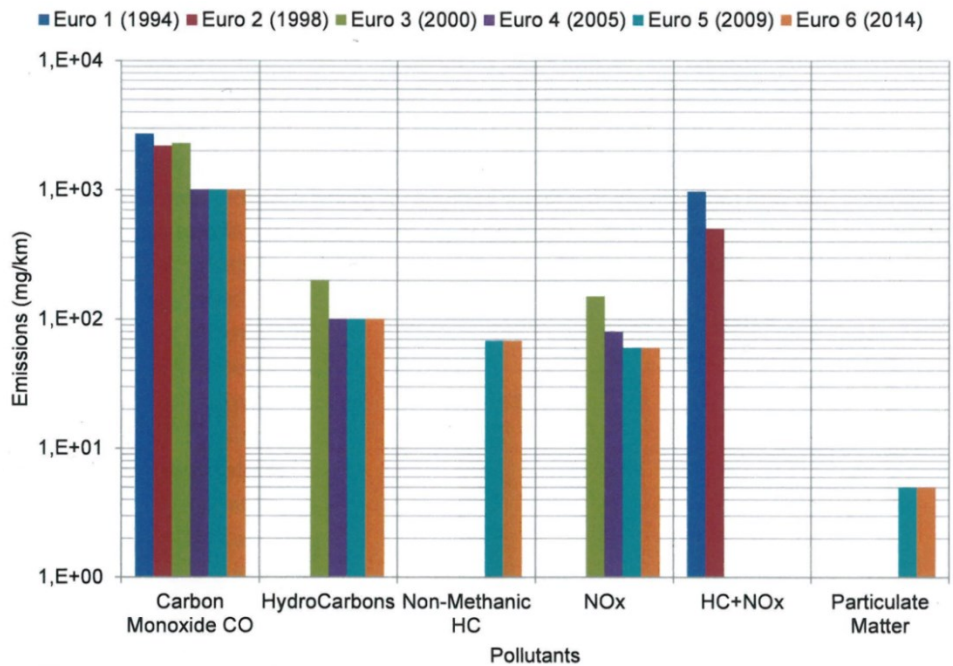


Figure IV – Emission limitations for passenger vehicles with SI engines in European Union [5].

The above Figure IV highlights that the reduction of pollutants emitted by cars equipped with SI engines has been intensified during the years. Indeed, the European Union imposes mandatory emission reduction for new produced vehicles. The direction which may lead to the achievement of this goal together with reduction of fuel consumption is represented by the optimization of the present SI-ICEs technology. Improved gasoline engines are expected to remain competitive in vehicle applications for the near future. If the adopted technologies to improve gasoline engines can obtain a better “cost to benefit” ratio in terms of both pollutant emissions and fuel consumption reduction, it will be commercially attractive to introduce them into the new car fleet mix. In addition, SI engines are more technically mature with respect to hydrogen and electric vehicles and they can be deployed using the existing infrastructure. Furthermore, they can offer near-term solutions to cope with the environmental issues, with affordable costs for customers. Different technologies are currently under study with a greater or lesser interest by various car manufacturers. Some of these technologies can be combined with a synergic approach while others are mutually exclusive. During last years, many OEMs introduced in their fleet Spark Ignition engines with a high level of downsizing, allowing to a lower fuel consumption at part load operation thanks to the shift of load points towards more efficient zones of the engine map, while performance are being preserved or even enhanced despite the smaller displacement by the adoption of a turbocharger. Even if a significant CO₂ reduction on the NEDC cycle is realized, the operation of downsized engine is negatively affected by knocking occurrence that involves substantial efficiency losses. Anyway, this issue can be easily overcome by the employment of other engine sub-systems like EGR systems, water injection technologies and by a proper control of combustion process. Further improvements for downsized engines can be obtained through the adoption of a VVA system applied on the intake camshaft. More recent VVA systems also allow for innovative intake valve lift strategies (*EIVC*, *LIVO*, *Multi-Lift*, *Pre-Lift*). The latter solutions may determine further BSFC reductions at part load operation. In conclusion, the downsized SI engine represents for the coming years one of the more promising engine architecture which, together with other engine sub-systems, will allow the passenger vehicle to meet the stringent limitations on pollutant emissions and to achieve the fuel consumption targets.

CHAPTER 1

Description of characteristics and operation of modern Spark Ignition Engines

1.1 Description of Spark-Ignition internal combustion engine

Internal combustion engines (ICEs) allow to obtain mechanical power from the chemical energy contained in the fuel, which is burned inside the engine itself. Due to this configuration, the working fluids of internal combustion engines are the air-fuel mixture (before the combustion process) and the exhaust gases (after the combustion process); the interaction between these working fluids and the mechanical parts of the engine provides the desired power output.

For their simplicity and favorable power-weight ratio, two types of internal combustion engines have found wide application in transport and power generation sectors: the *spark-ignition* engines (called also Otto engines, or gasoline engines) and the *compression-ignition* or Diesel engines.

The development of internal combustion engines started in the mid of the 19th century but, despite the technological evolution, today the engines are still continuously subjected to improvements related to efficiency, power output and reduction of the emissions, thanks to research activities which keep on providing increasingly efficient technologies and better materials.

There are different types of internal combustion engines. They can be classified according to the main technical differences:

- *Basic design of the engine*: reciprocating engines (in-line, radial or V disposition of the cylinders) and rotary engines (the most famous being the Wankel disposal).
- *Used fuel*: for example, gasoline (or petrol), diesel fuel, hydrogen, natural gas, alcohols (ethanol or methanol).
- *Method of mixture preparation*: carburetion (by means of a carburetor), indirect fuel injection into the intake ports or manifolds and direct fuel injection (directly into the engine cylinder).
- *Method of ignition*: it corresponds to the previously mentioned diversification between petrol engines (spark ignition, SI) and Diesel engines (compression ignition, CI).
- *Method of engine cooling*: water cooled, air cooled (forced convection) or cooling by natural convection and radiation.
- *Working cycle of the engine*: four-stroke cycle, which can be naturally aspirated or turbocharged; two-stroke cycle (crankcase scavenged or turbocharged).

The majority of internal combustion engines are characterized by a *four-stroke working cycle*, where each piston of the engine is subjected to four strokes (corresponding to two revolutions of the crankshaft) for every cycle. As an example, Figure 1.1 depicts the strokes for a SI engine.

The *four-stroke* full cycle is now going to be briefly described, and the theory which will be reported is to be considered valid for both CI and SI engines.

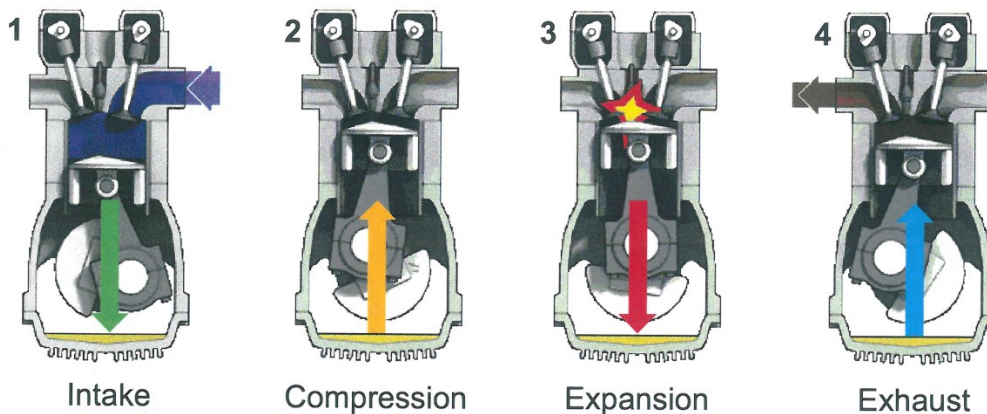


Figure 1.1 – Strokes for a 4-strokes Spark Ignition engine.

Intake Stroke: during this phase the piston moves from the Top Dead Center (TDC) to the Bottom Dead Center (BDC). The opening of the intake valve allows the fresh air/fuel mixture to enter the cylinder. In presence of an Exhaust Gas Recirculation (EGR) system, the exhaust gases from previous cycles and fresh mixture are introduced into cylinder. To optimize the cylinder filling the intake valve opening (IVO) is usually realized before TDC (typically 0-40 degrees) while the intake valve closure (IVC) occurs after the BDC (typically 50 degrees after BDC).

Compression Stroke: this phase starts when the intake valves are closed and the mixture in cylinder is formed by fresh charge of premixed fuel and air and exhaust gases of previous cycles (internal EGR). The piston moves from BDC to TDC by increasing both pressure and temperature of gas inside the cylinder. Towards the end of the compression stroke (some degrees before TDC) the combustion process starts and thus the pressure and temperature inside the cylinder increase even more rapidly.

Expansion Stroke: it begins when the piston is at TDC and finishes when the exhaust valve opens. Expansion stroke allows to obtain useful work thanks to the energy released by the combustion process. Indeed, the chemical energy of the fuel is transformed into mechanical work by the force that the high-pressure gases exert on the piston.

Exhaust Stroke: it starts with the opening of the exhaust valve. Exhaust valve opening (EVO) happens before the piston reaches the Bottom Dead Center (BDC). This phase can be divided into

two sub-phases: spontaneous exhaust and forced exhaust. In the former phase the pressure of the gases within the cylinder is substantially higher than the pressure in the exhaust manifold. For the latter phase, the piston moves from BDC to TDC and pushes the burnt gases to the exhaust valve. As the piston approaches the TDC the inlet valve opens and just after the TDC the exhaust valve closes and the cycle starts again. Figure 1.2, related to a four strokes of a SI engine, shows that an overlap period when both intake and exhaust valves remain opened occurs. As known, this overlap is properly designed for the optimization of the engine exhaust gas process.

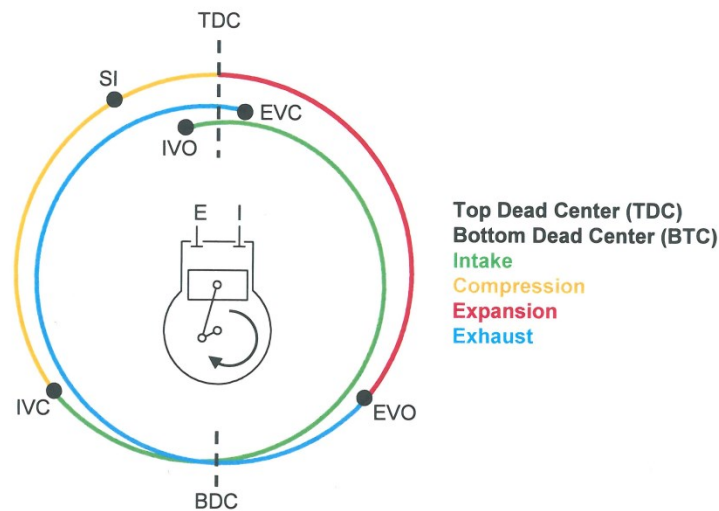


Figure 1.2 – Strokes for a 4-strokes Spark Ignition engine.

Referring to the 4-strokes SI engine cycle, Figure 1.3 shows a typical in-cylinder pressure trace in firing condition (solid line) and in motored condition (dashed line) together with the in-cylinder volume variation and mass fraction burned as a function of the engine crank angle. In the actual engine operation, air and fuel are usually mixed together in the intake system, before entering the cylinder by using a fuel injection system (port injection). The mass flow rate and consequently the engine power is controlled by adjusting the throttle valve. The intake manifold is usually heated to promote faster evaporation of the liquid fuel and to obtain more uniform fuel distribution between cylinders. With port-injection, fuel is injected through individual injectors from a low pressure fuel supply system into each intake port. There are several types of injection systems but the one widely adopted is the electronically controlled injection system.

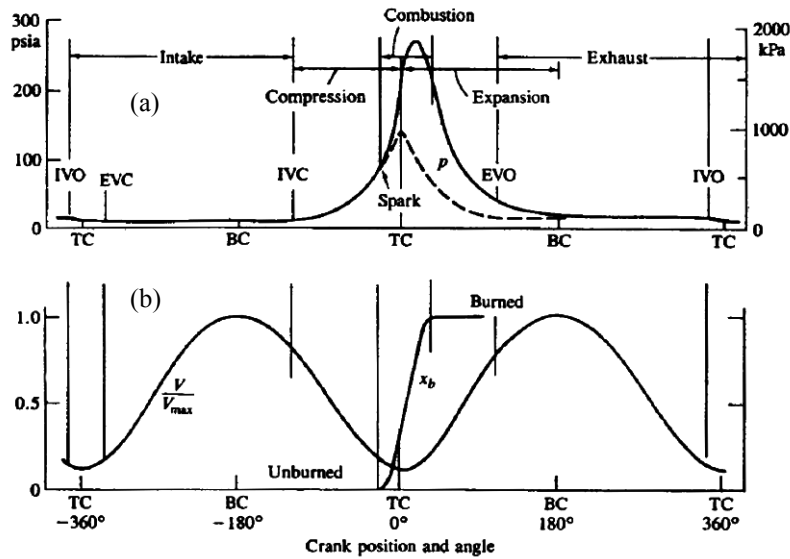


Figure 1.3 – In-cylinder pressure traces (a), volume and mass fraction burned (b) as a function of crank angle for a typical automotive SI engine.

As shown in Figure 1.3a, after the intake valve closure the cylinder contents (air, fuel and residual gases) are compressed and during this phase, heat transfer to the piston, cylinder head, and cylinder walls occurs but it exerts only a modest influence on the unburned gas properties. An electric discharge across the spark plug is realized with a certain advance before the top dead centre (between 10 and 40 degrees), allowing the combustion process to take place within the engine cylinder. A turbulent flame develops from the spark discharge, propagates across the mixture in the cylinder and extinguishes at the combustion chamber wall. The duration of the burning process may vary with engine design and operation but typically it covers a interval between 40 and 60 degrees (Figure 1.3). In presence of combustion the in-cylinder pressure rises above the level due to the sole compression (motored or non-firing condition). In a spark ignition engine, due to differences in flow pattern and mixture composition between cylinders and differences among consecutive engine cycles in a single cylinder, not negligible variations in the development of each combustion process occur. As a consequence, significant variations in combustion process development for consecutive engine cycles in a single cylinder have to be expected. This phenomenon is known as cycle by cycle variation of SI engines. In addition, these engines are also affected by knock occurrence in certain engine operating conditions, especially at high loads and low speeds. Knock phenomenon represents the most important abnormal combustion process for gasoline engines. It derives from the noise which results by the auto-ignition of a part of the gas mixture ahead the advancing flame front. Knocking combustions have to be avoided during the normal engine operation or reduced at a very low level because they cause severe engine damages and reduce the engine efficiency. This

phenomenon bounds the maximum allowable engine compression ratio, especially in the case of turbocharged SI engines, and it causes limitations on the engine efficiency.

1.2 Modern technologies for gasoline engines

Modern gasoline engines are characterized by advanced technologies which involve the adoption of a variety of new components and sub-systems, aiming to improve the fuel consumption and to reduce the noxious emissions. These technical solutions are here listed and will be briefly discussed in the following:

- Downsizing with turbocharging;
- Variable Valve Actuation (VVA);
- Cylinder Deactivation (CD);
- Compression ratio adjustment;
- Stratified charge by direct injection;
- Homogeneous Charge Compression Ignition (HCCI);
- EGR systems and water injection technology;
- Engine friction reduction.

1.2.1 Downsizing with turbocharging

“Downsizing concept” represents one of the most promising solution to reduce the fuel consumption, the CO₂ emissions and to improve the drivability of Spark Ignition engines. Downsizing philosophy consists in the engine total displacement reduction (lower friction surfaces) while the power/torque performance is restored through the adoption of a turbocharger group. This solution causes an increase in the thermo-mechanical load, that involves a more robust engine design. Downsized engine allows for a BSFC reduction at part load with respect to the naturally aspirated engine delivering a similar power output. In fact, for an assigned torque request, a smaller displacement determines a higher Brake Mean Effective Pressure (BMEP) level. In this way, the engine frequently works in a more efficient zone of its operating plane, where the intake throttling is less relevant [6], [7] and the mechanical efficiency is higher, as well. Furthermore, the efficiency of downsized engine may be greatly penalized when the boost level increases, since pre-ignitions or heavy knocking combustions may arise [8], [9]. Knock phenomenon represents the main problem to take into account when supercharging a Spark Ignition engine. This problem is particularly difficult to solve when compression ratio has to be high in order to avoid the lowering of thermodynamic

efficiency of SI engines. However, turbocharged engines have lower geometrical compression ratio than the naturally aspirated engines due to the increased knocking occurrence as the in-cylinder pressure increases. knock phenomenon for downsized engines, which occurs at high load operations, is usually controlled by retarding the combustion phasing in the expansion stroke with efficiency penalizations. In addition, the latter action involves an increase in the turbine inlet temperature that is usually compensated through an enrichment of the air-fuel mixture with further fuel economy penalizations. Another potential benefit for downsized engine can be obtained through the adoption of twin-entry turbine which better utilize the pulsating energy of the exhaust gas [10]. Even if twin-entry turbines present higher cost of production, especially for complex geometry, they allow for reduced turbocharger lag, providing improved vehicle drivability.

1.2.2 Variable Valve Actuation Systems and strategies

Variable Valve Actuation systems allow to control the lift, duration and timing of the intake (or exhaust) valves for air flow adjustment. Furthermore, these systems allow to control the swirl and tumble charge motions in the cylinder by changing the valve lift and timing of the intake valves, thus improving charging and combustion efficiencies over the entire range of engine speeds and loads. Two main variants can be identified: variable valve timing (VVT) systems and variable valve lift (VVL) systems. Referring to VVT system, which is a widely adopted technology for gasoline engines, different types of mechanisms are used to control the timing of the intake and exhaust valves. The employment of VVT systems allows to improve the “full load” volumetric efficiency, which results in increased torque, and to reduce the pumping losses and consequently the fuel consumption at part-load operations. Another advantage of VVT systems is the reduction in CO₂ emissions (1-4%, depending on the VVT design), if compared with fixed valve engines. The variable valve lift (VVL) system controls the valve lift by using two approaches: discrete VVL and continuous VVL. VVL system allows for reduction in pumping losses and improvements in the fuel consumption at low load. A small reduction in valve train friction may be also obtain in the case of low valve lift. Anyway, VVA systems represent a key technology in gasoline engines for their capability to increase engine efficiency, especially at part load. There are many ways in which a VVA can be achieved, ranging from mechanical devices to electro-hydraulic and cam-less systems. Regarding their architecture, VVA systems can be classified as:

- mechanical VVA;
 - electro-mechanical VVA;
 - electro-hydraulic VVA;
- } Equipped with a cam
-
- electro-magnetic VVA;
 - electro-hydraulic VVA
 - pneumatic VVA;
- } Cam-less

Despite their full flexibility the cam-less systems are not yet in production due to their high cost and the difficulties in the management of possible failures. On the other hand, the electro-mechanical and the electro-hydraulic VVAs combine a good valve lift control flexibility with an acceptable cost, and they are therefore currently already being adopted by some OEMs. Since all the experimental and numerical activities of this thesis have been carried out on a *Multi-air* engine, a particular focus is given to this electro-hydraulic system.

MultiAir is an electro-hydraulic system for dynamic and direct control of air and combustion, cylinder-by-cylinder and stroke-by-stroke. The key parameter to control gasoline engine combustion, and therefore performance, emission and fuel consumption is the quantity and the characteristics of fresh air charge in the cylinders. *MultiAir* system is based on direct air charge metering at the cylinder inlet ports by means of an advanced electronic actuation and control of the intake valves, while maintaining a constant upstream pressure. This electro-hydraulic valve actuation technology is based on the interposition, between cam and engine intake valve, of an oil volume (high pressure chamber) that can be adjusted through the adoption of an “on-off” solenoid valve, controlled by a dedicated electronic control unit. The system has been so far applied to the intake valves of gasoline engines, but it could be extended to also actuate exhaust valves and to Diesel engines.

Different valve strategies (Early Intake Valve Closing, Late Intake Valve Opening or Multi-Lift) can be used to optimize combustion efficiency, with notable benefits in terms of brake power, torque, fuel consumption and emissions. Moreover, the constant air pressure upstream the valves and the high actuation dynamics of the system (from partial load to full load in single engine cycle) allow for an increasing and prompt engine torque response, both for naturally aspirated and turbocharged engines, enhancing the so called “Fun-To-Drive”.

MultiAir system includes an actuator activated by a camshaft with an integrated fast-acting solenoid valve and valve control software. The considered system is applied to intake valves and the operating principle is described in the following: a piston, moved by a mechanical intake cam lobe, is connected to the intake valve through an hydraulic chamber, which is controlled by a normally open on/off Solenoid Valve (Figure 1.4).

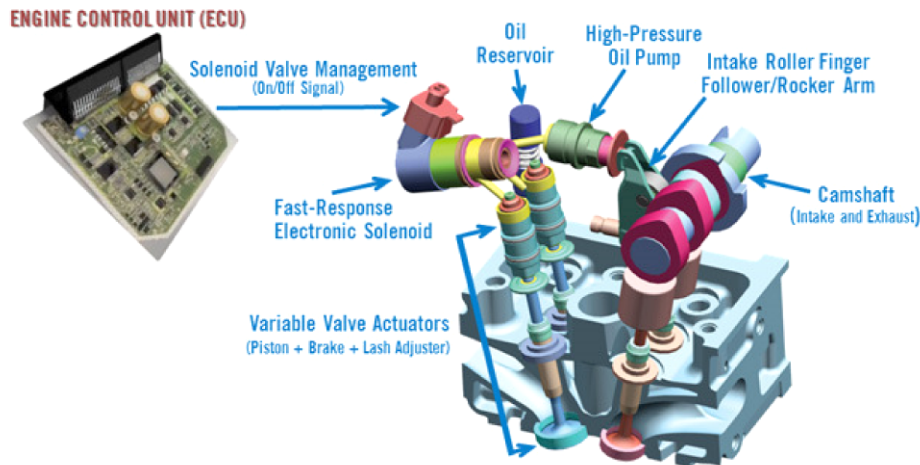


Figure 1.4 – Main Components of MultiAir System.

When the solenoid valve is open, the hydraulic chamber and the intake valves are de-coupled; the intake valves do not follow the intake cam profiles anymore and close under the valve spring action. Shortly before the valve reaches the seat, a hydraulic brake engages to ensure a soft and regular landing phase in any engine operating condition. Through Solenoid Valve opening and closing time control, a wide range of optimum intake valve opening schedules can be easily obtained. This allows cyclical and individual setting of the valve lift curves for the relevant cylinders and intake valves by controlling the solenoid valves. Hydraulic Valve lash Adjustment (HVA) is also implemented in the system. When the solenoid valve is open, the pressure accumulator feeds the retained oil volume back to the high-pressure chamber to refill the chamber and minimize energy losses. For maximum power, the Solenoid Valve is always closed and full valve opening is achieved following completely the mechanical cam, which was specifically designed to maximize power at high engine speed (long opening time). At part load operation, the solenoid valve opens earlier causing partial valve openings to control the trapped air mass as a function of the required torque. Alternatively the intake valves can be partially opened by closing the Solenoid Valve once the mechanical cam action has already started. In this case, the air stream into the cylinder is faster and results in higher in-cylinder turbulence.

The *MultiAir* technology enables an extremely high flexibility in the control of the valve lift, and allows for different strategies to achieve the engine's requirements in all operating conditions. A list of the main valve strategies is proposed below:

- full lift mode;
- early intake valve closing (*EIVC*) mode;
- late intake valve opening (*LIVO*) mode;
- multi lift mode;
- no lift mode.

The above mentioned strategies are described in the following with reference to the valve lift profile and to the solenoid actuation required.

Full Lift (FL) Mode

Full valve lift mode is mainly used at maximum engine power. In this mode, the solenoid valve remains closed during the entire cam lift phase and hence the engine is controlled as a standard one, by means of a throttle valve (Figure 1.5).

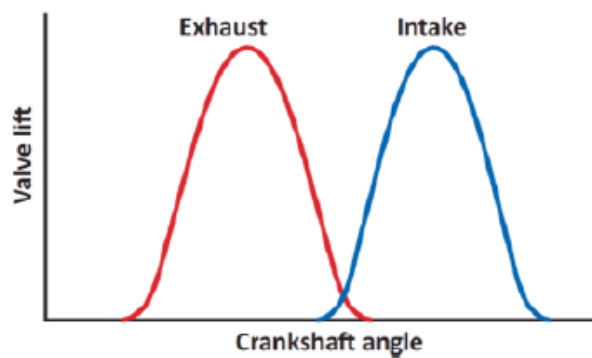


Figure 1.5 – Full Lift Mode.

Early Intake Valve Closing (EIVC) Mode

If the solenoid valve is open before the cam has returned to the base circle, this is called Early Intake Valve Closing (*EIVC*) mode. Here, the engine valve spring forces the valve towards “closing”. The oil is forced out of the high-pressure chamber to the so-called intermediate pressure chamber that is connected with a pressure accumulator. During early intake valve closing (Figure 1.6), the intake valve always performs a ballistic flight phase. This ballistic flight phase is forced by the engine valve spring.

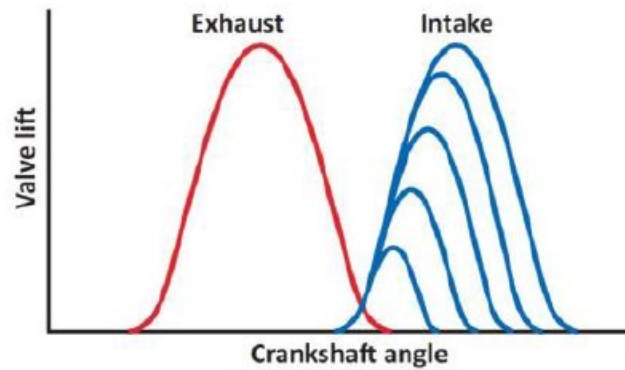


Figure 1.6 – Early Intake Valve Closing Strategy.

The *EIVC* mode is used for engine part-load operation. During this phase only partial valve lifts are performed and the air flow to the cylinder is adjusted according to the torque requirement. *EIVC* is the most promising mode in order to reduce pumping losses. However, the use of *EIVC* strategy suffers from poor in-cylinder turbulence especially at low loads; the dissipation of the kinetic energy of the intake air mainly occurs from the *EIVC* to the BDC, because the intake valves are closed and there is no energy source available to supply the viscosity losses in the trapped air charge. At low loads, the *EIVC* is further advanced towards the TDC, because a lower amount of charge is required, and this results in higher turbulence dissipation if compared with medium-high loads. This is the main drawback of the system, which can be mitigated with combustion chamber modifications, designed to increase the in-cylinder turbulence levels [11].

Late Intake Valve Opening (LIVO) Mode

To enable late opening of the intake valve (*LIVO*), the solenoid valve is not fed with current and remains open. The cam forces oil into the pressure accumulator via the pump piston. The solenoid valve is closed in good time before the engine valve opens. This mode and *Multi-Lift* operations (engine intake valve opens twice in the same cycle) are permitted only at crankshaft speeds up to 3000 rpm (Figure 1.7).

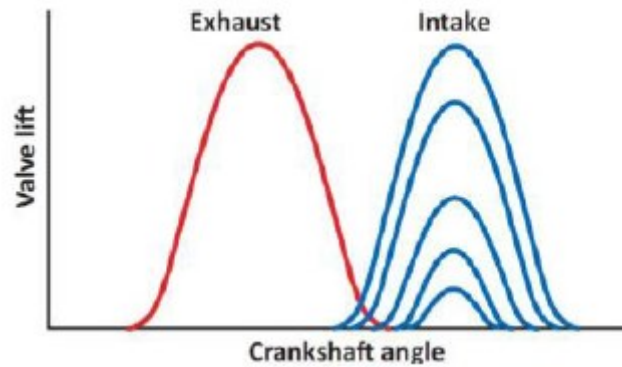


Figure 1.7 – Late Intake Valve Opening Strategy.

Multi-Lift (ML) Mode

Multi-Lift is a combination of the early intake valve closing with another late intake valve opening (Figure 1.8).

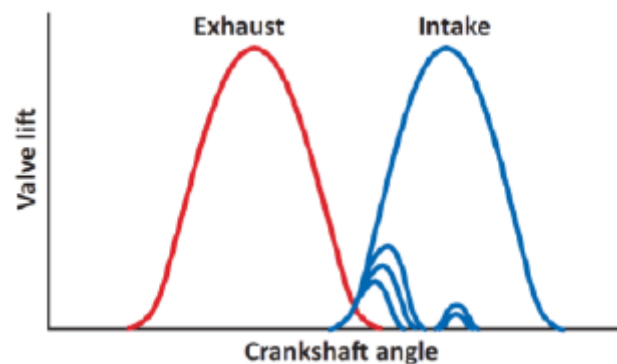


Figure 1.8 – Multi Lift Strategy.

No Lift Mode

In this mode of valve actuation, the intake valve is kept closed during the entire cam-lift phase.

Thanks to the high flexibility offered by this technology, the *MultiAir* system allows to obtain different benefits for gasoline engines which can be summarized as follows:

- ✓ The pumping loss decrease involves a 10% reduction in the fuel consumption and CO₂ emissions on NEDC cycle, both in naturally aspirated and turbocharged engines with the same displacement.
- ✓ On NEDC cycle, *MultiAir* downsized engines can achieve up to 25% of fuel economy improvement over conventional naturally aspirated engines with the same level of performance.

- ✓ Optimum valve control strategies during engine warm-up and internal exhaust gas recirculation, realized by re-opening the intake valves during the exhaust stroke, result in emissions emission reduction from 40% for HC / CO to 60% for NO_x.
- ✓ Constant upstream air pressure, atmospheric for Naturally Aspirated and higher for turbocharged engines, together with the extremely fast air mass control, cylinder-by-cylinder stroke, result in a higher dynamic engine response.
- ✓ High drivability response to the pedal request, better fun to drive and reduced turbo-lag phenomenon for turbocharged engines.

1.2.3 Cylinder Deactivation

It represents a technology allowing an engine to run on a part of its cylinders during part load operation. As an example, a 8-cylinder (V8) engine will run on all cylinders under high load condition or during an acceleration maneuver and a switching to four cylinders will be realized for cruising or low speed drive. The considered technology is very helpful for large capacity engines such as V6, V8 and V12 engines. In this way, pumping losses are significantly reduced during the engine operation in cylinder deactivation mode. The adoption of this technology allows for a CO₂ reduction, too.

1.2.4 Compression ratio adjustment

Variable compression ratio (VCR) system allows the geometrical compression ratio of an engine to be automatically adjusted in order to optimise the combustion process under different load and speed conditions. In general, compression ratio for SI PFI engines varies from 8 to 12. The main solution to prevent knock occurrence during full load operation is to reduce the volumetric compression ratio. However, this method lowers engine efficiency and performance at part load operating points, where pressure and temperature conditions do not favor knocking combustion. VCR system is capable to automatically adjust the compression ratio as a function of the operating point. With the adoption of this system, the compression ratio is limited at high loads, where the probability of knock occurrence is higher, while it is increased at low loads. This technology is still in research stage and it is not commercially available yet due to its mechanical complexity.

Anyway, research done by the European Commission Community showed that VCR engines can achieve a reduction in fuel consumption up to 9%, compared to state-of-the-art turbocharged gasoline engines with a constant compression ratio of 8.9 [12].

1.2.5 Stratified charge by direct injection

Charge stratification within the combustion chamber of a gasoline engine allows to realize a relatively rich mixture close to the spark-plug while the mixture gets progressively leaner in the remainder of the chamber. Charge stratification ensures repeatable ignition without misfire and stable combustion process by using overall very lean air-to-fuel ratio that is otherwise not possible with homogeneous mixture. A typical engine combustion system which allows for stratification of the charge is depicted in Figure 1.9.

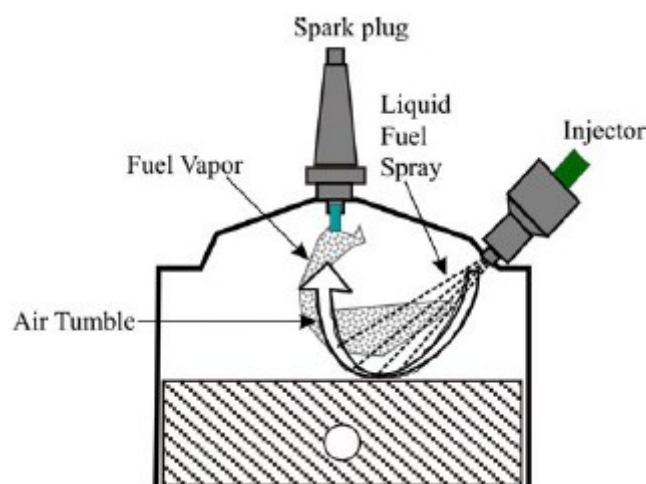


Figure 1.9 – Scheme of direct injection stratified charge (DISC) engine.

Liquid fuel is direct injected into the combustion chamber. Fuel spray is directed by air motion or by the geometry of the piston crown or by the combination of both towards the spark plug. When fuel spray reaches the spark plug electrodes some fuel gets vaporized and forms combustible mixture with air. The vaporized fuel is then ignited by spark, so combustion begins and the flame spreads in the combustion chamber. Anyway, different methods of charge stratification and combustion have been studied and some of these employed in production gasoline engines. Three types of methods can be identified: spray controlled, wall controlled and flow controlled [13]. The

main purpose of the charge stratification is to produce a stratified mixture within the combustion chamber (overall lean mixture) so that the unthrottled operation can be realized and the engine power can be controlled by varying only the injected fuel flow. In this way, the pumping losses are significantly reduced. Stratified charge engine may operate in at least two modes, depending on the load level and speed. During low-load and low-speed operation, the engine runs with a stratified charge and with overall lean mixtures. At high-load and high-speed operation, the engine operates as a stoichiometric (or slightly rich mixture) homogeneous charge DI engine. These engines offer several advantages including:

- ✓ Good ignition characteristics and stable combustion process;
- ✓ Very lean mixture (reaching 50:1), giving high fuel efficiency;
- ✓ Reduced knock tendency, thanks to a lean mixture in end gas zone and to slow precombustion reactions. Hence, higher compression ratio can be adopted with further improvements in the fuel consumption;
- ✓ CO₂ reduction than homogenous charge DI engines, ranging from 8-14% compared to PFI and multi-point injection [14],[15],[16].
- ✓ Faster dynamic response, thanks to the direct injection of gasoline.

1.2.6 Homogeneous Charge Compression Ignition (HCCI)

HCCI represents an alternative engine operating mode which does not need the spark event to initiate the combustion process. In the HCCI engine, fuel and air are premixed in order to form a homogeneous mixture; during compression phase, combustion process takes place by self-ignition at multiple sites [17]. HCCI operates with a very lean air-fuel mixture or with a diluted mixture through exhaust gases [18], [19]. The main advantage of HCCI is the low level of NO_x emissions due to the lower in-cylinder peak temperature. Soot emissions are also very low or negligible due to the homogeneous premixed charge. Conversely, high CO and unburned hydrocarbons emissions can be obtained due to the incomplete reaction in cool wall boundary layers, but conventional three-way catalysts are efficient for the reduction of this emissions. This technology can lead to fuel economy improvement for a simulated European drive cycle, compared to a homogeneous DI gasoline engine. The major challenges of HCCI are the control of ignition timing and the operation over a wide range of engine speed and loads [20]. While in diesel engines auto-ignition and combustion phasing can be controlled by injection timing, HCCI is controlled primarily by in-

cylinder temperature level and distribution. This requires variable exhaust gases recirculation (EGR) rates, as well as sophisticated variable-valve actuation and control systems. The major drawback of HCCI is the reduced operation range. Indeed, this kind of engines operate in a limited speed/load range, and consequently the commercial applications are likely to operate in a “dual-mode” between HCCI and Spark Ignition (SI) application. However, HCCI implementation still requires a lot of time for a high-volume production.

1.2.7 EGR system and water injection technology

Recirculating exhaust gas (EGR) on gasoline engines is employed primarily to reduce throttling loss at part load range in order to reduce fuel consumption, and secondarily, to reduce NO_x emission levels. EGR can also improve fuel economy and inhibit the tendency of engine towards knock. Indeed, cooled EGR reduces the temperature of the charge at beginning of the compression phase and consequently allows to reduce the NO_x emissions. In addition, the reduction in the in-cylinder temperature leads to less risk of knocking combustions. On the contrary, hot EGR favors knock occurrence. Typical mass fraction of recirculated exhaust gas in SI engine ranges from 0 to 15%. However, the maximum possible EGR rate is limited by high cyclic variations, misfire, the decrease of total efficiency and the increase of HC emission. Water Injection (WI) technology represents a promising method for gasoline engines capable to furnish several advantages. In particular, water injection within the intake manifold proves to drastically reduce temperature of the gases within the combustion chamber and at turbine inlet for turbocharged engine. The reduction in gas temperature reduces the knock tendency, mainly thanks to the heat subtracted by the water evaporation. The adoption of port water injection method allows to improve the fuel consumption of turbocharged gasoline engines while preserving engine performance and knock safety margin [21].

1.2.8 Engine friction reduction

Modern technologies for friction reduction include materials, components and sub-systems capable to minimize the friction between the moving parts in the engine. For an internal combustion engine, several friction reduction opportunities can be identified such as piston surface and rings, camshaft design, innovative material coatings and roller cam followers. A reduction in engine friction results in higher efficiency, lower fuel consumption and reduced emissions. These are desirable objectives for today's engine manufacturers as they strive to improve engine performance while trying to meet increasingly stringent emission regulations. As an example, different studies suggest that the potential reduction in CO₂ emissions thanks to the engine friction reduction solutions may vary from 1% to 5 % [14], [16], [22].

1.3 Turbulent combustion in Spark Ignition Engine

In a traditional PFI SI engine the fuel and air are premixed together within the intake system and introduced through the intake valve into the cylinder, where the fresh charge is mixed with the residual gas and then the compression phase takes place. In normal engine operating conditions, combustion process starts before the end of the compression stroke, thanks to the electric discharge in the spark-plug gap. In this phase the flow field inside the cylinder is highly turbulent. A flame kernel is developed within the electrodes of the spark-plug. The flame of the initial kernel is laminar and it grows when interacts with the turbulent flow field. Consequently, the flame gradually becomes turbulent. Turbulence flow field allows to increase the flame speed with respect to the laminar flame and creates wrinkles and corrugations on the flame front. Wrinkles and corrugations increase the flame surface where the chemical reactions occur. Turbulent flame propagates through the combustion chamber until it reaches the wall of the chamber and then extinguishes. Figure 1.10 shows additional features of the combustion process referred to acquired consecutive engine cycles for a Spark Ignition engine.

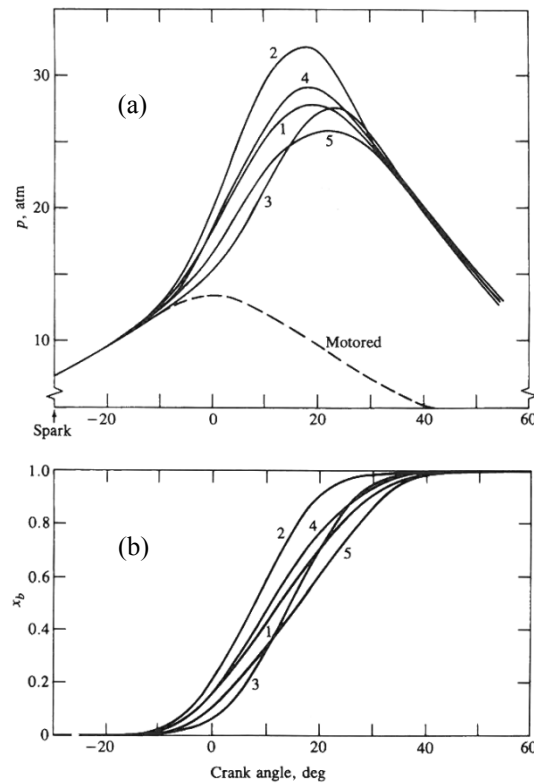


Figure 1.10 –In-cylinder pressure cycles (a) and mass fraction burned (b) for five consecutive engine cycles in a SI engine as a function of crank angle. Ignition timing 30 deg BTDC, WOT, 1044 rpm, $\Phi=0.98$ [23].

Following the spark discharge, initially the energy released by the developing flame is too small for the in-cylinder pressure rise due to the combustion. While the flame continues to grow and it propagates across the combustion chamber the in-cylinder pressure steadily rises above the pressure level related to the motored condition (absence of combustion). The in-cylinder peak pressure occurs after the Top Dead Center but before the mixture is fully burned. In-cylinder pressure level decreases during the expansion phase because of the increase in the cylinder volume. In SI engine, the flame development and propagation show a cycle-by-cycle variation since the in-cylinder pressure traces and mass fraction burned curves significantly differ for consecutive engine cycles. This phenomenon is associated to the growth of the flame which depends on the local mixture motion and composition close to the spark plug. These parameters may vary for consecutive engine cycles referring to a single cylinder and they may vary cylinder-to-cylinder, as well. In particular, mixture motion and composition close to the spark plug at the time of the spark discharge play a very important role for the development of the flame front. Indeed, these phenomena govern the early stage of flame development. A special attention has to be dedicated to cycle-by-cycle and

cylinder-to-cylinder variations because the extreme cycles limit the engine operation. Combustion process for SI engines can be divided into four phases:

1. Spark ignition;
2. Early flame development;
3. Flame propagation;
4. Flame termination.

In order to obtain the maximum brake torque and power the combustion process has to be properly phased, i.e. it has to be located around the TDC. Typical duration of combustion process is between 30 and 90 crank angle degrees. Combustion begins before the end of the compression phase and it continues for the early part of the expansion stroke and finally ends after the crank angle related to the in-cylinder peak pressure. Spark timing has to be properly selected because it exerts a considerable influence on the pressure cycle. The effect of various spark timing values on the pressure cycle is shown in Figure 1.11, allowing to understand why the engine torque varies as the spark timing is modified with reference to the TDC.

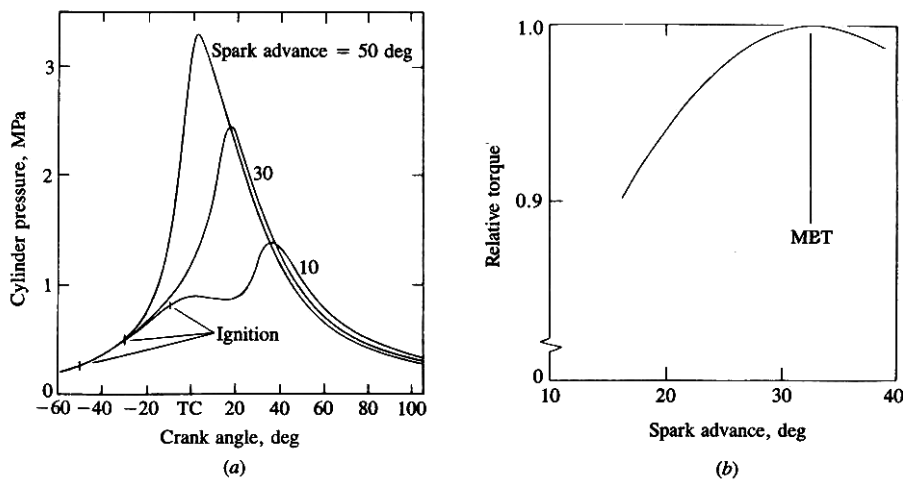


Figure 1.11 – (a) In-cylinder pressure for overadvanced spark timing (50 deg), MBT timing (30 deg) and retarded timing (10 deg); (b) Effect of spark timing on brake torque at constant speed, A/F ratio at WOT [23].

If the start of combustion is progressively advanced before the TDC peak pressure increases and the compression work increases, too. On the other hand, if combustion is delayed by retarding the spark

timing the in-cylinder peak pressure occurs later during the expansion stroke and it is also reduced. The optimum spark timing value, capable to furnish the maximum brake torque (MBT) occurs when the magnitude of this opposite trends just offset each other. Of course, a spark timing different from the MBT involves a lower brake torque. The optimum spark setting depends on the rate of flame development and propagation, length of the flame path across the combustion chamber, the details of the flame termination after it reaches the wall chamber. The latter phenomena depend on the engine design and operation, on the properties of fuel, air and burned gas mixture. For instance, Figure 1.11 shows that for the case of optimum spark timing, the in-cylinder peak pressure occurs at about 16 degrees after TDC while the 50% of the in-cylinder charge is burned at about 10 degrees after TDC. As previously said, in the normal combustion case the flame moves steadily across the combustion chamber until the fresh charge is fully burned. Anyway, different conditions such as engine design and parameters and combustion deposits may cause abnormal combustion. In particular in SI engines two types of abnormal combustion can be identified: knock and surface ignition. Referring to the first phenomenon, it represent the most important abnormal combustion in SI engine which has to be properly avoid in normal engine operating conditions. The name of this phenomenon derives from the noise resulting by the auto-ignition of a portion of the mixture (fuel, air and residual gas) ahead of the advancing flame. During the flame propagation within the combustion chamber, the unburned mixture ahead of the flame (the so called end-gas zone) is compressed and its pressure, temperature and density are increased. Chemical reactions may generate within the air-fuel mixture of the end-gas zone before the normal combustion process. In this way, a rapid and spontaneous release of a part or all of their chemical energy occurs. So the end-gas burns very rapidly and the chemical energy is released at a rate from 5 to 25 times than the characteristic one of the normal combustion. This causes a high frequency pressure oscillations inside the engine cylinder which produce the sharp metallic noise called knock. Knock will not occur if the flame front consumes the un-burned zone before the auto-ignition reactions while it verify if the pre-combustion reactions produce auto-ignition before the normal propagation of the flame front. As said before, another important abnormal combustion is the Surface ignition. It represents the ignition of the air-fuel charge which is not generated by the spark-plug and it is caused by overheated valves or spark plugs, by glowing combustion chamber deposits or by other hot spot within the combustion chamber. Surface ignition may occur before the spark-plug ignites the charge (pre-ignition) or after the normal ignition (post-ignition). Effects of surface ignition are most severe when it results from pre-ignition. Surface ignition may result in knock. More details about knock phenomenon are discussed in following chapter 4.

1.3.1 Turbulence phenomenon

Turbulence represents a complex phenomenon and it is very difficult to simulate even for non reactive flows. As known, turbulent flows are 3D unsteady, rotational and highly diffusive flows. Turbulent flows are characterized by a large spectrum of active scales. As reported in the Figure 1.12, a continuous energy cascade mechanism with a large band of integral length scale is observed. Referring to the spectrum of turbulent kinetic energy k cascade, three different regions can be identified related to specific physical processes. Each considered region has a proper characteristic length scale.

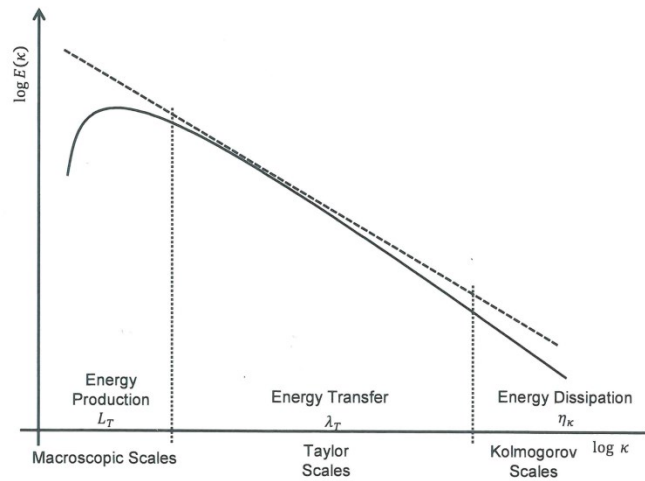


Figure 1.12 – Turbulent energy cascade.

The description of the characteristic length scales is the same for reactive and non-reactive flows. According to the decomposition of Reynolds, turbulent flows are composed by a mean velocity field (\bar{u}) and a turbulent velocity field (u'). In this way the resultant velocity is:

$$u = \bar{u} + u' \tag{1.1}$$

It is well known that the correct prediction of combustion process needs the estimation of the global turbulent intensity (u'). This global property exists only for an homogeneous and isotropic turbulent flow. For the combustion phase of spark ignition engines, turbulence process can be characterized

as homogeneous and isotropic. For this turbulence three characteristic length scales can be identified:

Integral length scale: the eddies of the integral length scale are the largest and they contain most of the turbulent kinetic energy. They are characterized by low frequency and large fluctuations. For the case of internal combustion engine, the integral length scale (L_T) is limited by cylinder head, intake valve geometry and piston position.

Taylor microscale: these eddies dissipate the kinetic energy through Joule effect. Their scale is the Taylor microscale. The eddies of Taylor microscale maintain the greatest part of the flow enstrophy (integral of the square of the vorticity). Taylor length scale can be approximated by the equation:

$$\lambda_T = 15 \sqrt{\frac{L_T \nu}{u}} \quad (1.2)$$

Kolmogorov length scale: this length scale indicates the length of the smallest eddies, which dissipate the turbulent kinetic energy. The considered eddies are characterized of small length and high frequency. The assumption of homogeneous and isotropic turbulent flow is valid for this region of turbulent kinetic energy. These structures are characterized by the Kolmogorov length scale (η_k) which can be defined by the equation (1.3):

$$\eta_k = L_T \left(\frac{u L_T}{\nu} \right)^{3/4} \quad (1.3)$$

In order to reproduce the turbulent combustion, combustion models require a proper estimation of the turbulent intensity (u') and of the integral length scale (L_T). In addition, the main flow pattern of the charge within the engine cylinder has to be properly known to support the development of a simplified yet representative turbulence model for in-cylinder flow field.

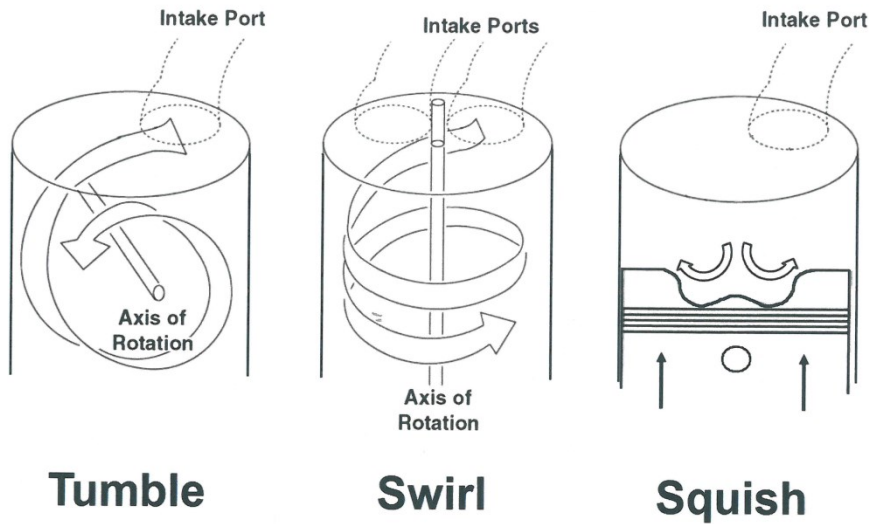


Figure 1.13 – Main in-cylinder motions.

Referring to the case of Port Fuel Injection (PFI) engines, which are those of interest for the purpose of the present thesis work, three main aerodynamic motions within the combustion chamber can be identified: the Tumble, the Swirl and the Squish (Figure 1.13) [24]. It is well known that swirl and tumble flows require energy to generate the vortex during the intake stroke. This energy primarily derives from the kinetic energy of the gases entering by the intake valves into the cylinder. Among the different technologies employed to increase the turbulence levels in the combustion chamber of SI engines, the most usual technology is that capable to amplify the Tumble motion because it allows for the conservation of a high volumetric efficiency [24]. Therefore, tumble motion is predominant for the creation of turbulence in SI engines. Several modeling approaches for the phenomenology of the turbulence are reported in the literature. In this work a 0D K-k modeling approach is chosen since it allows to calculate outcomes near the 3D results by the adoption of a single set of tuning coefficients for different engine operating points. K-k model is specified through two conservation equations: one for the mean kinetic energy (K) and the other one for the turbulent kinetic energy k [25], [26], [27]. These two equations describe the rate of change of the kinetic energy of the mean flow field and the kinetic energy of the turbulent field. More details about this turbulence modeling will be furnished in the following chapter 2.

1.3.2 Turbulent premixed flames

The interaction between the premixed flame and the turbulent flow field can be described through the comparison of characteristic turbulent and chemical length and time scales. This analysis allows to identify different turbulent premixed combustion regimes. Each regime is characterized by different chemical and physical phenomena, controlling the interaction between the flame and the turbulent flow together with the combustion process phenomenology. This schematization for the interaction of the flame with the turbulent flow allows to better understand the actual flame structure. The adoption of diagrams showing the turbulent premixed combustion regimes has been proposed by different researchers and the one widely used is the well known “Borghi” diagram [28]. The reconstruction of the latter diagram requires three non-dimensional numbers:

- Turbulent Reynolds number $Re = \frac{u' L_T}{\nu}$ and if the Schmidt number is assumed equal to unity Reynolds number can be rearranged as $Re = \frac{u' L_T}{s_L \delta_L}$;
- Damköhler number $Da = \frac{\left(\frac{L_T}{u'}\right)}{\left(\frac{\delta_L}{s_L}\right)} = \frac{\tau_T}{\tau_{ch}}$, representing the ratio between the turbulent time and the chemical time;
- Karlovitz number $Ka = \frac{\tau_{ch}}{\tau_K}$, which is the ratio of the chemical time scale and the Kolmogorov time scale. For homogeneous and isotropic turbulence, Karlovitz number can be written as : $Ka = \left(\frac{L_T}{\delta_L}\right)^{-1/2} \left(\frac{u'}{s_L}\right)^{3/2}$.

Turbulent Reynolds number describes the competition between the destabilizing effect of the inertial forces and the stabilizing effect of the viscous forces. Reacting flows having high Reynolds number are characterized by large flow fluctuations, too. Damköhler number correlates the time for the fulfillment of chemical reaction with the time for the turbulent mixing. In this way, flames characterized by low Damköhler numbers are controlled by chemical kinetics of reactions; they are characterized by high mixing rates and are known as “well-stirred reactors”. Conversely, flames with high Damköhler numbers are characterized by very quickly reactions and the limiting factor of the combustion process is the mixing phenomenon. Karlovitz number compares the laminar flame thickness, where the chemical reactions take place, with the smallest turbulent scale i.e. Kolmogorov length scale. Karlovitz number can be considered as an order of magnitude of the flame stretch. Two different ratios are employed to define the well known Borghi diagram, that is

the ratio of the integral length scale to the laminar flame thickness (L_T/δ_L) and the ratio between the turbulent intensity to the laminar flame speed (u'/s_L). The above defined non-dimensional numbers can be adopted to correlate the ratios (L_T/δ_L) and (u'/s_L):

$$\frac{u'}{s_L} = Re \left(\frac{L_T}{\delta_L} \right)^{-1} \quad (1.4)$$

$$\frac{u'}{s_L} = Da^{-1} \frac{L_T}{\delta_L} \quad (1.5)$$

$$\frac{u'}{s_L} = Ka^{2/3} \left(\frac{L_T}{\delta_L} \right)^{2/3} \quad (1.6)$$

The adoption of the above equations (1.4), (1.5) and (1.6) allows to reconstruct the Borghi Diagram (Figure 1.14), in which the turbulent premixed combustion is categorized in different regions.

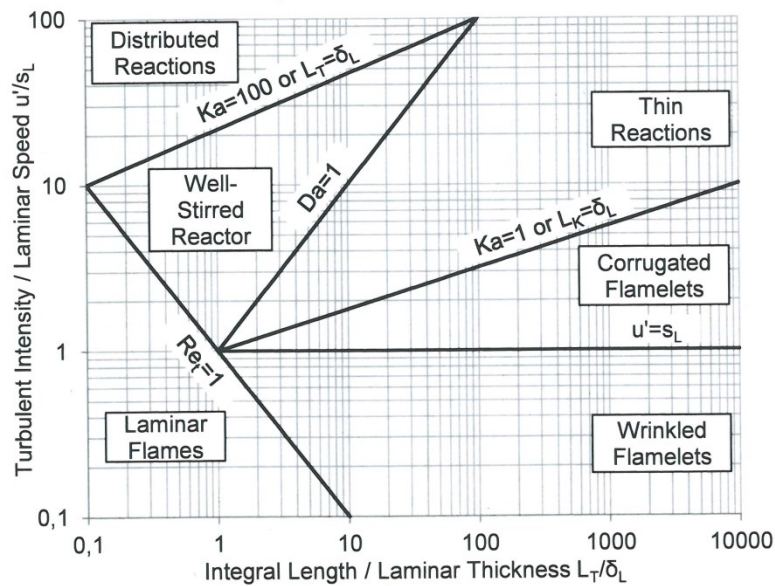


Figure 1.14 – Borghi Diagram of turbulent premixed combustion [29].

As said, various regimes of turbulent premixed combustion can be identify by the Borghi Diagram and they are summarized in the following Table 1.1, reporting the characteristics of each regime. In addition, for each combustion regime a flame depiction is provided. In particular, the flame front (thick black line) propagates from the burnt gases (white region) to the fresh gases (grey region). Flame depictions in Table 1.1 describe the flame morphology according to the combustion regime.

In the following a brief description of combustion regimes showed by the Borghi diagram is reported. In the case of wrinkled flamelets, turbulent intensity is smaller than the laminar flame speed. So the laminar propagation is stronger than the mechanism of corrugations of the flame front. The thickness of the flame front is not altered by the turbulent eddies because the smaller eddies cannot enter the flame front structure since they are greater than flame thickness ($Ka < 1$). In this regime chemical kinetics are not sensitive to the presence of the turbulent flow field. For corrugated flames regime, turbulent intensity is greater than the laminar flame speed. The corrugation mechanism is the strongest. Because of the strong folding of the flame front, pockets of the fresh gases may be detached from the continuous flame front and appear in the zone of the burnt gases. In addition, pockets of burnt gases may appear in zone of the fresh gases. Anyway, turbulent fluctuations do not alter the flame structure which remains quasi-steady. Corrugated flames region expands till the borderline with $Ka=1$. This line defines wrinkled and corrugated flamelet regimes in which chemical kinetics can be described by the laminar flame properties (s_L, δ_L).





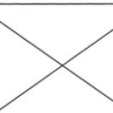
Combustion regime	Re	Da	Ka	Ka_δ	u'/s_L	Flame depiction
Wrinkled flamelets	> 1	> 1	< 1	< 1	< 1	
Corrugated flamelets	> 1	> 1	< 1	< 1	> 1	
Thin reactions zone	> 1	> 1	> 1	< 1	> 1	
Well-stirred reactor	> 1	< 1	> 1	< 1	> 1	
Broken reaction zones	> 1	< 1	> 1	> 1	> 1	

Table 1.1 – Turbulent premixed combustion regimes [29].

Basing on the latter consideration, premixed turbulent combustion of these regions (i.e. corrugated and wrinkled flamelets) can be modeled by the principles of laminar flamelets, since that the interaction between the turbulent flow and the flame front is of kinematic nature. The regime of thin reactions is realized for Karlovitz numbers greater than the unit. In this case, the smallest turbulent

eddies may enter into the pre-heat zone of the flame but they do not enter into the reaction zone. Indeed, turbulent eddies are greater than the thickness of the reaction zone. Heat and mass transfer mechanisms are accelerated within the pre-heat zone thanks to the turbulent convection. In the regime of well-stirred reactor, Damköhler number is smaller than the unit and so the time scale of turbulent mixing is smaller than the chemical time scale. For this reason combustion process is controlled by chemical kinetics. For the considered regime, the turbulent mixing is so intense to cause a perfect stirring between the reactants and the products of combustion. Consequently, no flame front can be distinguished. In broken reaction zones regime ($Ka > 100$), turbulent eddies enter into the reaction zone since turbulent eddies are smaller than flame thickness. High heat loss is obtained from the reaction zone to the preheat zone, due to turbulent convection. The temperature of the reaction zone quickly decreases. For this regime a premixed flame cannot exist and so no flame picture is presented in Table 1.1.

1.3.3 Flame Propagation within the combustion chamber

It is well known that in SI engine the spark discharge generates a high temperature kernel of about 1 mm in diameter between the electrodes of the spark plug [23]. Initial flame kernel is characterized by a quasi-laminar growth and it is highly stretched. The local flow field increasingly distorts the flame front and so a gradual transition to a turbulent flame occurs. The flame kernel is also convected away from the spark plug electrodes [30], [31], [32] by the mean and turbulent flow fields. The flame front is wrinkled by both mean and turbulent flows and its shape may be modified from spherical to elliptical. At the end of the transition stage, the flame kernel is not convected by the flow since the the enflamed mass is too important to be convected by the flow field. At this stage, the heat release rate due to combustion process is very low if compared to the fuel energy content. Consequently, the increase in the in-cylinder pressure is low. With the fully development of the flame, turbulent flow wrinkles the flame front and so the flame propagates throughout the chamber. At this stage the highest part of the fuel energy is released. A microscopic exam of wrinkled turbulent flame shows that its structure is laminar with a thin thickness. Figure 1.15 depicts the turbulent flame front.

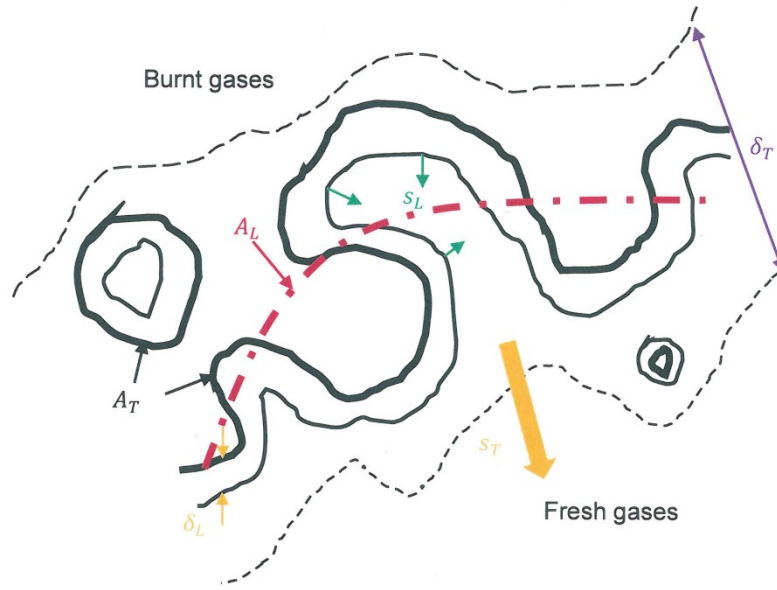


Figure 1.15 – Wrinkled turbulent flame with corrugations [29].

The contour of the turbulent flame front is represented through a reaction sheet characterized by a small thickness. The considered sheet presents intense wrinkles and corrugations at different length scales. The total contour surface is generally called turbulent flame surface A_T , while a fictitious mean flame surface A_L can be defined and spherical assumed for 0D modeling approach. The contours which define the entire flame front allows to identify the turbulent flame thickness δ_T . The speed of the flame propagation in the fresh gases is the turbulent flame speed s_T . Every flame element (i.e. small part of reaction zone) presents a laminar flame thickness δ_L and propagates toward the fresh gases with laminar flame speed s_L . The laminar flame speed depends on the fuel type, the air-to-fuel (A/F) ratio, the in-cylinder pressure p , the temperature of the fresh gases T_u , and the presence of the residual gas. The impact of the flame stretch, that is high at the beginning of the combustion process, on the laminar flame speed has to be properly take into account. The turbulent flame propagation can be observed till it comes in contact with the walls of the combustion chamber and consequently the extinction mechanisms take place till the flame is completely extinguished. During the considered phase the wrinkling of the flame front diminishes under the impact of the flow boundary layer, of the increased heat losses towards the cold wall and of the confinement of the flame by the combustion chamber wall.

1.4 Cycle by cycle variation

In-cylinder pressure measurements of consecutive engine cycles for a Spark Ignition engine show that a not negligible variation on a cycle-by-cycle basis exists. In addition to these variations occurring in each individual engine cylinder, significant differences in combustion process and in-cylinder pressure cycle between the cylinders of a multi-cylinder engine may occur. In particular, cyclic dispersion is caused by variations in the in-cylinder mixture motion at spark time, variations in air flow and fuel flow to the single cylinder at each cycle, variations in the mixing of the fresh charge with residual gas within the single cylinder at each cycle, especially near the spark plug. Cycle-by-cycle variation represents an important phenomenon to properly take into account for two main reasons. First, the optimum spark timing is set for the average cycle, and consequently *faster-than-average* cycles present advanced spark timing while *slower-than-average* cycles have retarded timing and so power and efficiency losses may occur. Second, the extremes of cyclic variations limit the engine operation. Indeed, the fastest burning cycles with its overadvanced spark timing are most likely to knock. These cycles limit the compression ratio and determine the fuel octane requirement. On the other hand, the slowest burning cycles are most likely to burn incompletely and set the practical lean operating limit of the engine. Moreover, too large cyclic variations have a negative impact on the engine drivability. Variations in the in-cylinder pressure reflect in variations of the brake torque which directly relate to vehicle drivability. As an example of cycle-by-cycle variations, Figure 1.16 shows measured 300 consecutive in-cylinder pressure traces as a function of crank angle, with a sampling resolution of 0.2 crank angles, for a point at 7000 rpm and full load of a high performance SI engine.

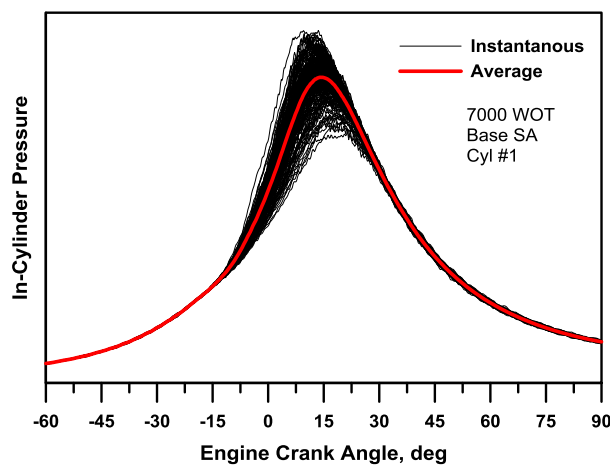


Figure 1.16 – Instantaneous and average in-cylinder pressure cycles at 7000 rpm and Base SA.

It can be noted that the faster burning cycles present higher value of the maximum in-cylinder pressure than the slower burning cycles. In addition, the peak pressure of the faster burning cycle is reached closer to the TDC. Cycle-by-cycle variations are observed in the early stages of the flame development and especially during the rapid burning phase of the combustion process, involving variations in the maximum burning rate. In presence of an excess of air or dilution with high fractions of residual gas the cycle-by cycle variations increases. In this condition some engine cycles are characterized by slower combustion process and partial burning phenomenon may occur (combustion not completed at Exhaust valve opening). For more lean or dilute mixture misfire limit may be reached. Anyway, spark-ignition engine can operate with reduced percentage of cycles showing partial-burn or misfire but these phenomena cause negative effects on engine efficiency, hydrocarbon emissions, torque variations and roughness. Cyclic variation has been observed and intensively studied over the last decades. From an experimental point of view, the study of CCV is typically based on the acquisition and the post-processing of consecutive in-cylinder pressure traces (ranging from 300 up to 2000 cycles, [33]). Moreover, in-depth analyses of the origins of the phenomenon have been performed through optically accessible engines [34], [35], [36], [37] and by 3D-CFD simulations [38], [39]. Cycle-by-cycle variation can be characterized by adopting various measure. In particular, CCV can be defined in terms of variations between different in-cylinder pressure cycles or in terms of variations in parameters of the burning process. The following listed parameters have been adopted to measure the cyclic variation:

1. Pressure related parameters: maximum in-cylinder pressure p_{\max} , crank angle of maximum pressure value $\theta_{p_{\max}}$, maximum rate of pressure rise $(dp/d\theta)_{\max}$, crank angle of maximum rate of pressure rise and IMEP;
2. Combustion related parameters: the maximum heat release rate, maximum mass burning rate, combustion duration (MFB_{10} , MFB_{10-90});
3. Flame front position parameters: flame radius, flame front area, burned volume, all at given times.

Referring to the pressure data, the coefficient of variation of the indicated mean effective pressure and the coefficient of variation of the in-cylinder peak pressure represent relevant measure of cyclic variation. While CoV_{IMEP} clearly affects the engine drivability, a more relevant role is played by $CoV_{p_{\max}}$, since it exerts a direct influence on knock occurrence. Different studies are reported in the current literature to relate the CCV to engine operating parameters such as engine speed, spark advance, equivalence ratio, or fuel properties and combustion parameters (combustion phasing and

duration). As an example, an overview of the spark timing impact on IMEP and p_{max} dispersions (vertical dots) can be noted from the following Figure 1.17 and Figure 1.18, respectively.

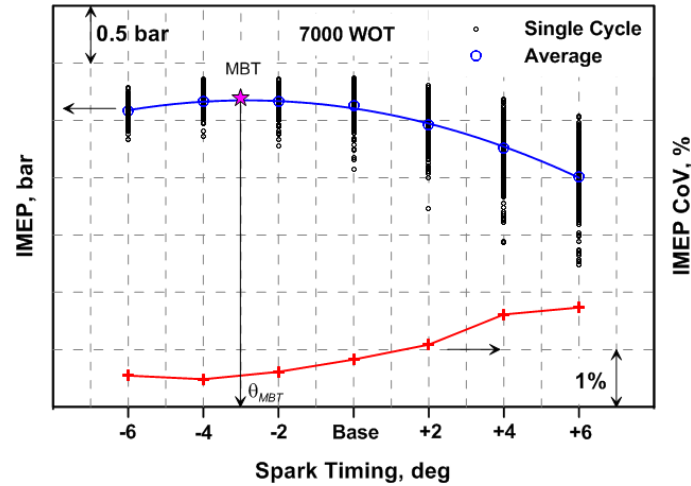


Figure 1.17 – IMEP vs SA, 7000 rpm at full load.

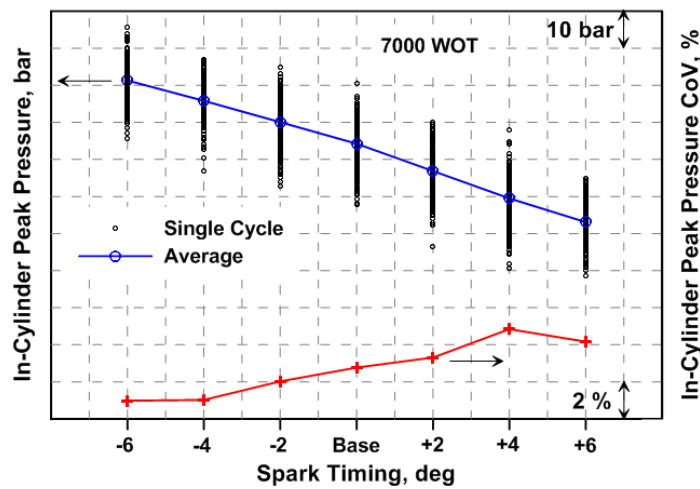


Figure 1.18 – In-cylinder peak pressure vs SA, 7000 rpm at full load.

These figures refer to a high performance naturally aspirated SI engine operating at 7000 rpm and at full load. Related CoVs and average levels are also reported as continuous lines. It can be observed that delayed spark advance ($SA_{base}+6$, late combustion phasing) determines an increase of CoVs level. The Spark advance realizing the Maximum Brake Torque (MBT), can be easily determined as shown in Figure 1.17, and, correspondingly, CoV_{IMEP} attains approximately its minimum. Also the studies by Young [40] underline that CCV is minimized at the ignition timing realizing the MBT. In addition, it is moreover confirmed that p_{max} dispersion (Figure 1.18) is much higher than IMEP one,

for each tested SA. For the same considered engine system, the effect of the engine speed on IMEP and p_{max} distributions can be indeed derived from Figure 1.19 and Figure 1.20, referring to full load operation and Base SA. It is once again confirmed that dispersion of p_{max} is much higher than IMEP one for each tested operating condition. The related CoVs, moreover, do not clearly depend on the engine speed. Higher CoVs are actually detected at 4000 rpm, since Base SA is farther from the angle of MBT (θ_{MBT}), than the other speeds.

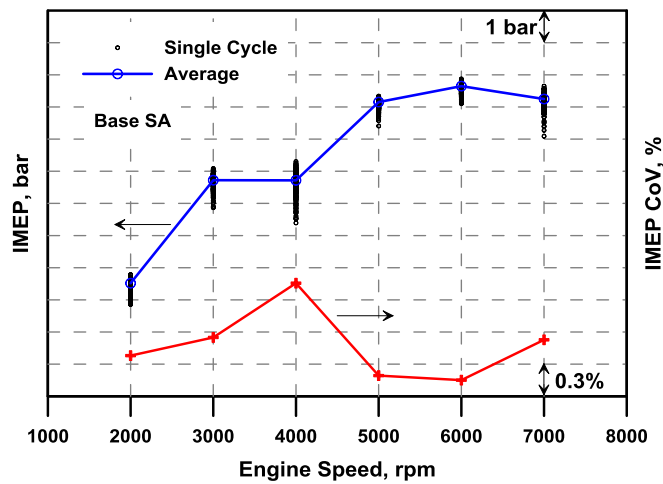


Figure 1.19 – IMEP vs engine speed, Base SA.

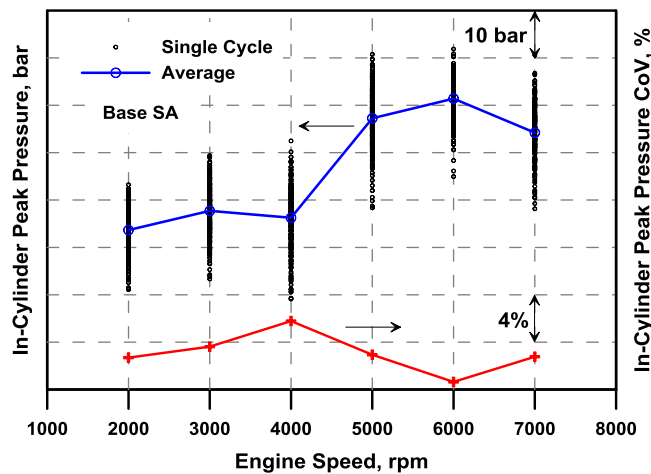


Figure 1.20 – In-cylinder peak pressure vs engine speed, Base SA.

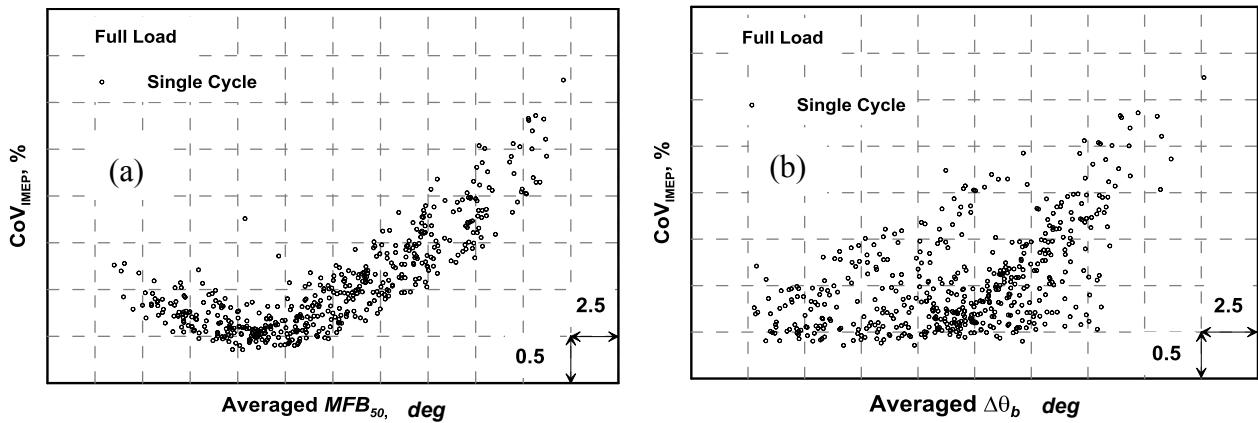


Figure 1.21 – (a) CoV_{IMEP} vs averaged MFB_{50} and (b) CoV_{IMEP} vs averaged combustion duration $\Delta\theta_b$.

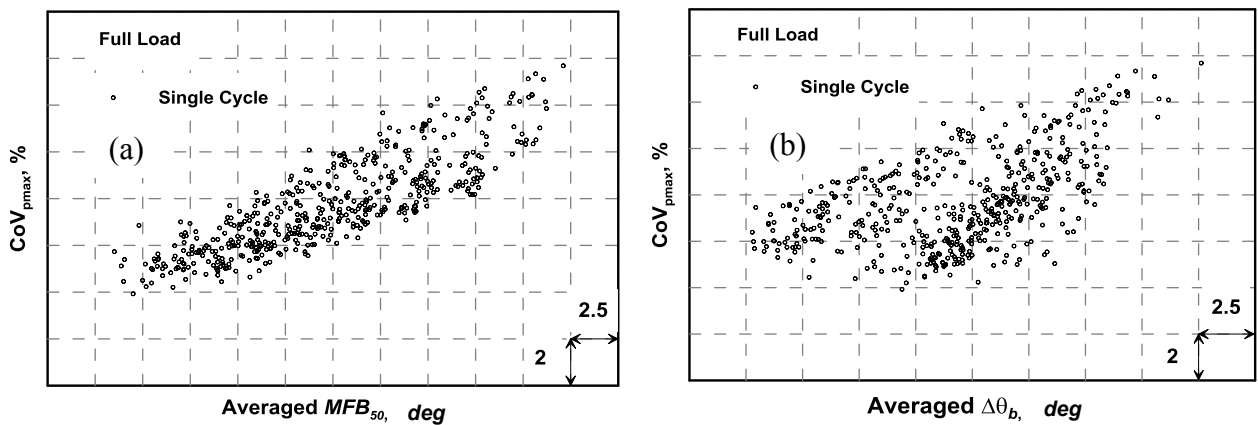


Figure 1.22 – (a) CoV_{pmax} vs averaged MFB_{50} and (b) CoV_{pmax} vs averaged combustion duration $\Delta\theta_b$.

CoV relationship with average combustion-related parameters are also presented in Figure 1.21 and Figure 1.22, once again referring to a high performance naturally-aspirated SI engine [41]. CoV_{IMEP} presents high values for delayed combustions. Its minimum is reached at an angular position roughly corresponding to the θ_{MBT} in each operating condition. The CoV_{IMEP} indeed does not exhibit a well-defined trend with the averaged combustion duration, although it more clearly increases for the slower combustion processes. The CoV_{pmax} , on the contrary, exhibits a clear increasing trend with the combustion phasing, highlighting that a more delayed combustion process leads to higher p_{max} variations. As stated above, a more dispersed trend establishes between CoV_{pmax} and the averaged combustion duration. A longer combustion process however still determines a higher CoV_{pmax} .

Referring to the influence of equivalence ratio on CCV, Pundir et al. [42], as an example, have been observed that the CoV_{pmax} reaches the minimum level when stoichiometric mixtures are adopted, while variations in the equivalence ratio inevitably lead to increased CCV. Hassaneen et al. [43] tested an 8-cylinder natural gas SI engine and found that CoV_{pmax} and CoV_{IMEP} rised by 33% as the equivalence ratio decreased from 1 to 0.6. Ozdor et al. [44] studied CCV for a four-stroke, 4-cylinder engine for various excesses of air, always maintaining the spark timing at MBT. The results showed that CCV were minimum for a stoichiometric mixture. Finally, Maurya and Agarwal [45] investigated the effect of two different fuels (gasoline and ethanol) on CoV_{IMEP} relationship with combustion phasing and combustion duration and for HCCI combustion. The considered fuels shown the same behaviour: longer combustions and late phasing involved higher IMEP variations for both fuels and a second order polynomial correlation between CoV_{IMEP} and combustion duration was developed. To this aim, in order to characterize the CCV phenomenon, different correlation of CoVs with average combustion-related parameters have been investigated and reported in the current literature. As an example, an experimental study on a high performance SI engine [41] showed that the combustion parameters which better correlate with the CoV levels are the combustion phasing and conventional duration (MFB_{50} and $\Delta\theta_b$). In particular, two polynomial correlations have been identified:

$$CoV_{IMEP} = c_0 + c_1\Delta\theta_b + c_2MFB_{50} + c_3\Delta\theta_bMFB_{50} + c_4MFB_{50}^2 \quad (1.7)$$

$$CoV_{pmax} = d_0 + d_1\Delta\theta_b + d_2MFB_{50} + d_3\Delta\theta_bMFB_{50} + d_4MFB_{50}^2 \quad (1.8)$$

where c_i and d_i ($i=0,\dots,4$) are the constants realizing the best fit with the experimental data. The latter correlations allow to take into account the cycle-by-cycle variations from a numerical point of view by computing through a proper engine model (including a refined combustion sub-model) the parameters of correlation (MFB_{50} and $\Delta\theta_b$) referring to the average cycle. In addition, CCV correlations provide the advantage to properly predict the *faster-than-average* pressure cycles allowing to estimate the knock limited spark advance with reference to the more critical pressure cycle.

1.5 Knock phenomenon

Knock phenomenon represents one of the most important abnormal combustion process for Spark ignition engine because it causes limitations on engine performance and efficiency and at the same time imposes restricting constraints to the employed fuels. It is well known that intense knock can cause major engine damages and it represents a source of noise by the engine even in the case of soft knock. Indeed, knock is the name associated to the noise which is transmitted to the engine structure when air/fuel charge molecules in the end-gas zone spontaneously ignite before they have been reached by the propagating flame front. If this abnormal combustion takes place an extremely rapid release of much of the chemical energy in the end gas occurs, causing very high local pressure values and the propagation of the pressure waves of significant amplitude across the combustion chamber. When auto-ignition occurs repeatedly (i.e. more than occasionally) during otherwise normal combustion event, the phenomenon is named “spark knock”. Knock phenomenon may vary substantially cycle-by-cycle and cylinder-by-cylinder in multi-cylinder engines and it does not occur every engine cycle. Spark knock can be controlled by acting on the spark timing. Indeed, an advanced spark timing increases the knock intensity while retarding the spark a decrease in the knock intensity is obtained. Knock may be an outcome following the occurrence of surface ignition, since the latter usually causes a more rapid rise in the end-gas pressure and temperature than the case of normal combustion operation. Anyway while surface ignition represents a problem that can be solved by acting on the engine design, fuel type and lubricant quality, in contrast, knock is an inherent constraint on engine performance and efficiency because it limits the maximum compression ratio for any given fuel. Knock primarily establishes under wide open throttle (WOT) operating conditions, since higher in-cylinder pressure and temperature levels occur. The occurrence and the severity of knock depend on the fuel type (knock resistance) and on the anti-knock characteristics of the engine. Knock resistance of a predefined fuel is measured by the octane number. Higher octane number indicates greater resistance to knock. Gasoline knock resistance can be improved by refining processes such as catalytic cracking and reforming or by the adoption of antiknock additives. Engine design exerts a not negligible effect on the knock occurrence, i.e. combustion chamber, spark-plug position, etc. Besides the quality of the available fuels, knock depends on the ability of the engine designer to ensure the desired normal combustion behaviour reducing the engine knock tendency at minimum. The in-cylinder pressure trace allows to evaluate the actual pressure variation within the cylinder during knocking combustions. As an example, Figure 1.23 shows the in-cylinder pressure variation for three single engine cycles characterized by normal combustion, slight knock and heavy knock, respectively [23].

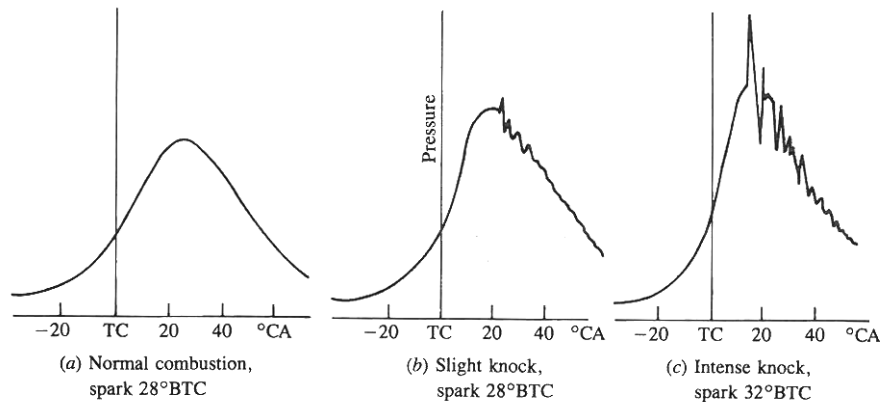


Figure 1.23 – In-cylinder pressure traces of cycle with (a) normal combustion, (b) light knock, and (c) heavy knock (WOT, 4000 rpm, 381 cm³ displacement single cylinder engine) [23].

When knocking combustions occur, high frequency pressure oscillations are observed whose amplitudes are gradually reduced over time. For the considered engine and the tested operating point of Figure 1.23, some engine cycles do not present knock phenomenon (Figure 1.23a) while for the remaining cycles (Figure 1.23b-c) knock phenomena of different intensity occur. In slight knock case (Figure 1.23b), the considered phenomenon occurs late in the burning process and the amplitudes of the pressure oscillations are very small. For heavy knock case (Figure 1.23c), obtained with a more advanced spark timing, knock occurs closer to the TDC and earlier in the combustion process with initial amplitudes of the pressure oscillations more larger than the previous cases. Higher amplitudes of the pressure oscillations are the result of the spontaneous release of a great part of the fuel chemical energy in the end gas zone. The presence of knock involves that the pressure distribution across the combustion chamber is no longer uniform. Consequently, transducers located at different point of the combustion chamber will record different pressure values at a predefined time. To this aim, many methods of knock detection and characterization have been adopted. In particular, knock detection systems usually respond to the vibration driven acceleration of parts of the engine block caused by pressure waves generated by knocking combustion. Optical probes and ionization detectors have been used, too. Indeed, a high intensity flash is observed when knock occurs together with a sharp increase in the ionization. A useful measure of knock intensity is represented by the amplitude of the pressure fluctuations since they depend on the amount of the end-gas which ignites spontaneously. The adoption of this measure of knock intensity allows to highlight that a cycle-by-cycle variation of knock severity exists [23].

Figure 1.24 shows knock intensity for 100 consecutive engine cycles for a single cylinder of a V8 SI engine at WOT and mid-engine speed (2400 rpm).

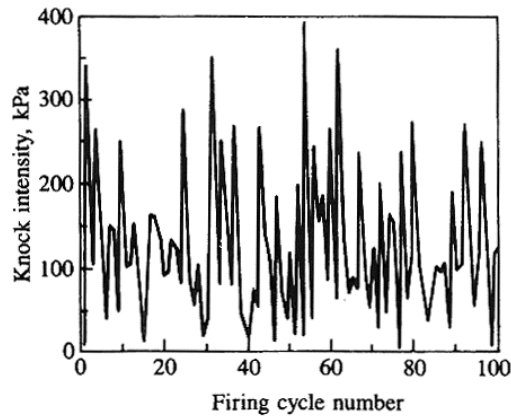


Figure 1.24 – Knock intensity for 100 consecutive engine cycles (single cylinder V8 SI engine at WOT operation and 2400 rpm).

It can be observed that knock intensity varies randomly, covering knock free and heavy knock conditions. In addition, cylinder-to-cylinder variations in knock intensity may occur due to variations in compression ratio, mixture composition, burn rate and combustion chamber cooling. It is the case to underline that knock generates a non-uniform condition within the cylinder and different details of this phenomenon in each cycle and each cylinder are obtained. For this reason, a definition of knock intensity is extremely difficult. A well recognized measure of knock severity is represented by the maximum amplitude of the pressure oscillation occurring in knocking combustion. The in-cylinder pressure signal, measured through an high frequency response pressure transducer, is properly filtered in such a way to obtain only the components of the pressure signal that correspond to the fluctuations due to knock. Knock intensities reported in the previous Figure 1.24 are determined by employing the above discussed method. Since pressure fluctuations are caused by wave propagation phenomenon, the location of pressure transducer with respect to the location of the end-gas zone and the shape of the combustion chamber will affect the maximum amplitude of pressure fluctuation. Knock phenomenon may exerts a significant impact on engine system according to its intensity and duration [23]. Soft knock has not significant effects on engine performance and durability while heavy knock can lead to extensive engine damages. For automotive application, knock characterized by short duration and low intensity (soft knock) is unlikely to cause damages. Instead, heavy knock at constant speed can easily lead to pre-ignition,

runaway knock and gradual erosion of regions of the combustion chamber. The engine can be damaged by knock phenomenon in different ways: cylinder and head erosion, piston crown and top land erosion, piston melting and holing, piston ring sticking, etc. As an example, Figure 1.25 shows component damage due to abnormal engine combustions (pre-ignition and knock). Referring to the mechanisms which cause damages, when heavy knock occurs heat is transferred to the combustion chamber walls together with a rapid overheating of the cylinder head and piston. Under this condition, knock is not stable. Indeed, the overheating increases the knock intensity, making this phenomenon heavier and heavier and without a proper control it can lead to engine failure in a short time. In conclusion, in order to avoid severe engine damages during the engine operating condition, knock phenomenon has to be properly controlled and reduced at very low intensity.

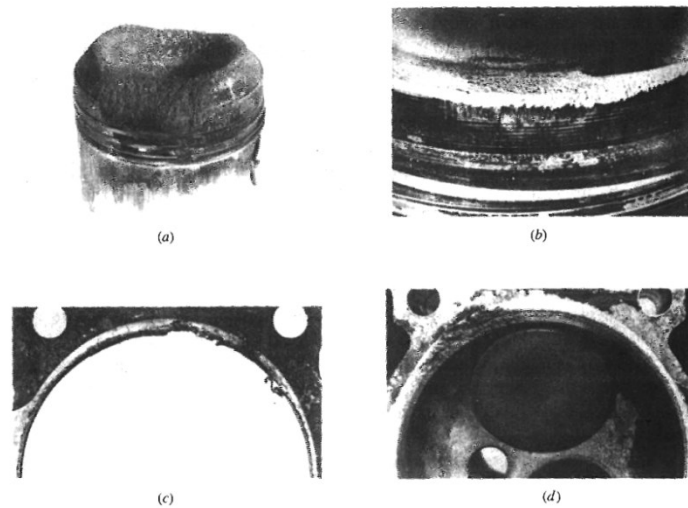


Figure 1.25 – Component damages from abnormal combustion [23]: (a) piston holing by pre-ignition; (b) piston crown erosion after 10 hours of high-speed knocking; (c) cylinder head gasket splitting failure due to heavy knock; (d) erosion of aluminum cylinder head along the top of cylinder liner due to heavy knock.

1.6 Engine system description

The engine under study is a commercial small-size twin-cylinder turbocharged SI engine, representing a typical downsized engine. A simple engine schematic layout is shown in Figure 1.26. Engine system is equipped with gasoline port-fuel injectors and with a variable valve actuation (VVA) module, capable to control the intake valve lift profile. The valve actuation is provided by an electro-hydraulic system that modulates the valve lift according to the operating conditions. In many cases, the valve lift greatly differs from the cam-derived profile. The system consists of a small capacity between the cam and the valve filled with lubricant oil, whose emptying is regulated by an electronically controlled electro-valve [46]. The main features of the tested engine are reported in following Table 1.2. The latter shows that the engine compression ratio is limited to 9.9, in order to avoid the knock occurrence at high load operation. Since the full load performance of a downsized engine is restored by the turbocharger group, as the boost pressure increases knocking combustions may occur. This phenomenon represents one of main problems of the analyzed engine because it limits the specific fuel consumption levels at full load operation.

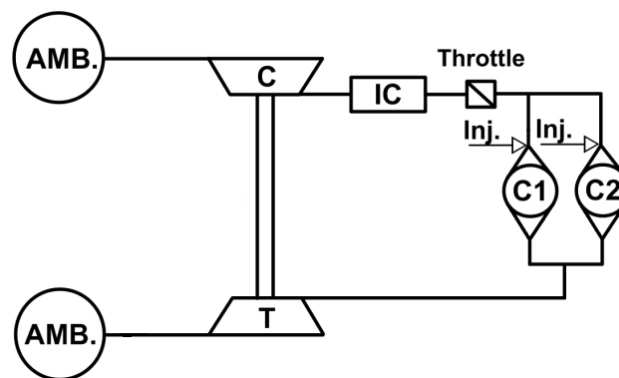


Figure 1.26 – Engine Schematic Layout : C: Compressor, T: Turbine, C_{1,2} :engine cylinders, AMB.: external ambient, Inj.: Fuel injector.

In addition to the discussed BSFC advantages of the downsized architecture at low loads, the adoption of VVA system allows for further improvements at low/medium BMEP operation [47], [48], [49], [50]. Indeed, the flexibility of the VVA systems allows to adjust the engine load with very limited butterfly valve throttling [51], [52], which drastically reduces the pumping work at low/medium load. Moreover, a reduction in NO_x emissions and an improved combustion stability at

idle were experimentally verified [53], [54], [55], [56]. Consequently, reductions in specific fuel consumption may be achieved at part load operation.

Model	2 cylinders, 8 valves, VVA, Turbocharged and Intercooled
Displacement	875 cm ³
Stroke / Bore	86 mm / 80.5 mm
Connecting rod length	136.85 mm
Compression Ratio	9.9
Max Brake Power	64.6 kW @ 5500 rpm
Max Brake Torque	146.1 Nm @ 2500 rpm

Table 1.2 – Main Engine Characteristics.

The intake valve lift strategies which can be realized by the valve actuation system equipping the analyzed engine include Late Intake Valve Opening (*LIVO*), Early Intake Valve Closure (*EIVC*), a combination of the previous ones and a multi-lift (*ML*) strategy. As known, the same load level can be achieved by employing different valve strategies. A typical drawback derived by the VVA system is the worsening of intake gas-dynamic noise emissions at low loads. The reduced throttling of the intake ducts, while allowing a reduction in the pumping work, also results in a less effective attenuation of the pressure wave in the intake system [57], [58]. At very low loads, the decreased duration of the intake phase may determine a reduced turbulence level at the spark time and a slower burning speed. For the above reasons, precise engine control parameter settings must be specified to obtain the best compromise among different objectives.

The analyzed engine presents various degrees of freedom allowing for the opportunity to operate in a specified speed-load point using different control strategies. In particular, it is possible to independently define the following parameters:

- α air to fuel ratio (A/F);
- β throttle opening angle;
- χ spark ignition timing;
- φ_1 intake valve opening angle;
- φ_2 intake valve closing angle;
- WG turbine waste-gate valve opening.

α , β , and χ are traditionally used to calibrate a naturally-aspirated SI engine, while ϕ_1 , ϕ_2 and WG are related to the control of the VVA system and the turbocharger, respectively. This set of parameters has to be properly defined in order to achieve the required performance targets. The experimental identification of this set of engine variables, for a predefined operating condition, poses some problems which can be overcome through the adoption of numerical models and methodologies. This kind of issues will be deeply discussed in the following.

1.6.1 Experimental activities

The considered engine is installed at the test-bench and both high and part load operations are investigated for different speeds (1500-5500 rpm) and intake valve strategies. Acquired data include fuel flow, air flow, power, torque, pollutant emissions and fuel consumption. Instantaneous in-cylinder pressure measurements are also carried out in both cylinders and the indicated parameters (IMEP, maximum pressure, angle of maximum pressure, angles of 10%, 50%, 90% of Mass Fraction Burned – MFB₁₀, MFB₅₀, MFB₉₀, etc.) are derived. In particular, a sequence of 200 consecutive in-cylinder pressure traces are acquired for each tested speed at full load. A sampling resolution of 0.5 crank angles is adopted at each speed. A higher sampling frequency (0.1 deg) is instead specified during combustion angular window (-10 ,75 deg). As an example, cycle-by-cycle WOT pressure measurements at 2100 rpm and 4000 rpm are shown in Figure 1.27a and Figure 1.27b, superimposed with ensemble averaged ones.

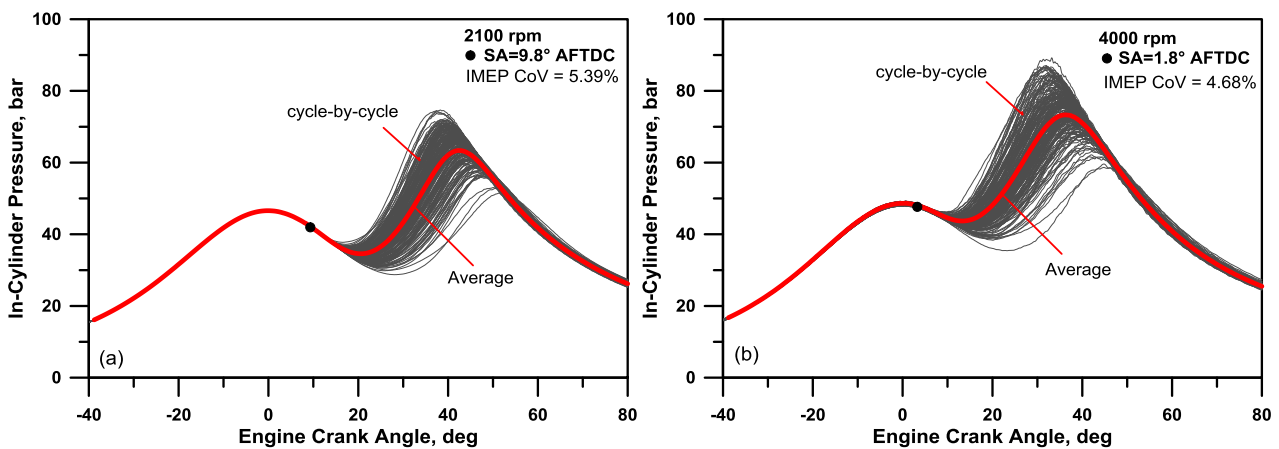


Figure 1.27 – Average and instantaneous in-cylinder pressure cycles at 2100 rpm (a) and 4000 rpm (b) in WOT condition.

A relevant cyclic dispersion can be observed, with differences on the peak pressure of about 20-30 bar, and an IMEP Coefficient of Variation (CoV – defined as the ratio between the standard deviation of the IMEP and the related average level) around 5% in both cases. As said, the electro-hydraulic system equipping the engine allows for different intake valve settings. In order to simplify the experimental investigation, among the various available strategies, only the *EIVC* strategy is tested in the present work. Typical valve lift profiles are shown in Figure 1.28, characterized by a different closure angles, labelled in the following as φ_2 . In particular, in Figure 1.28 the continuous curve represents a *Full Lift* strategy, while dashed ones depict *EIVC* strategy.

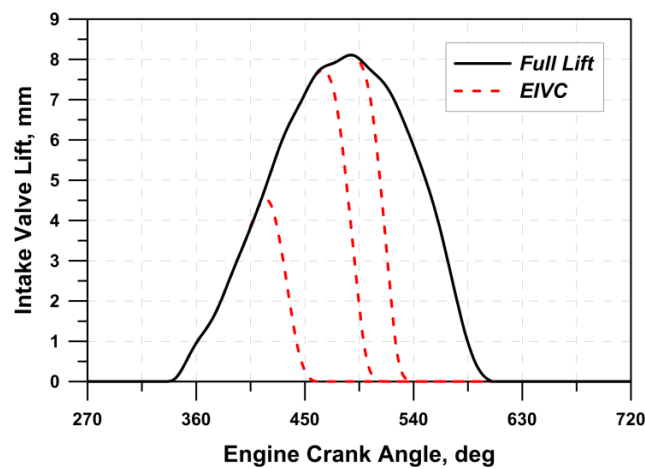


Figure 1.28 – Typical valve lift profiles for different closure angles.

A complete fuel consumption map is collected for a *Full Lift* valve strategy, where the load is adjusted by the throttle valve at low load, and by the waste-gate valve at high load (Figure 1.29a). A second fuel consumption map is measured, where the intake closure angle φ_2 is added as further control parameter (Figure 1.29b). In the latter case, only the region of the operating plane characterized by lower BMEP levels is investigated, where intake throttling and *EIVC* strategy are properly combined to improve the fuel consumption. The *EIVC* strategy is also employed to measure a full load curve, recording a single operating point for each engine speed. In this case, φ_2 angle is adjusted according to the speed in order to realize the highest volumetric efficiency, namely tuning the intake valve closure event with the natural pressure oscillation in the intake line. At medium and low load, the spark advance is set to realize the maximum brake torque, usually corresponding to MFB_{50} of about 4-10 degrees after FTDC (Figure 1.30). The air-to-fuel ratio is fixed at a stoichiometric value, so to guarantee optimal operation for the catalytic converter (Figure

1.31). At high load, a delayed combustion phasing is realized due to knock limitations (Figure 1.30). This is particularly true in case of low speeds, since a higher knock tendency verifies. Air-to-fuel ratio has to be particularly enriched at high engine speeds (Figure 1.31), mainly to maintain the Turbine Inlet Temperature (TIT) below a prescribed threshold level of 950 °C. However, the heat subtracted by the fuel evaporation contributes to reduce knock risks and a more favourable MFB_{50} setting can be set at high speeds. As expected, both the above control strategies, although mandatory, strongly penalize the fuel consumption at high load (Figure 1.29).

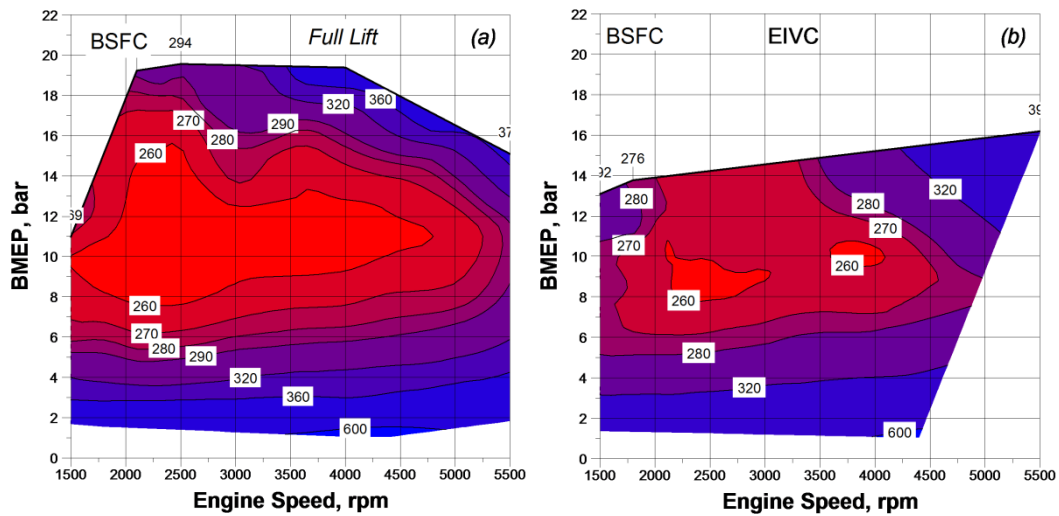


Figure 1.29 – Measured fuel consumption map (g/kWh) for Full Lift (a) and EIVC (b) strategies.

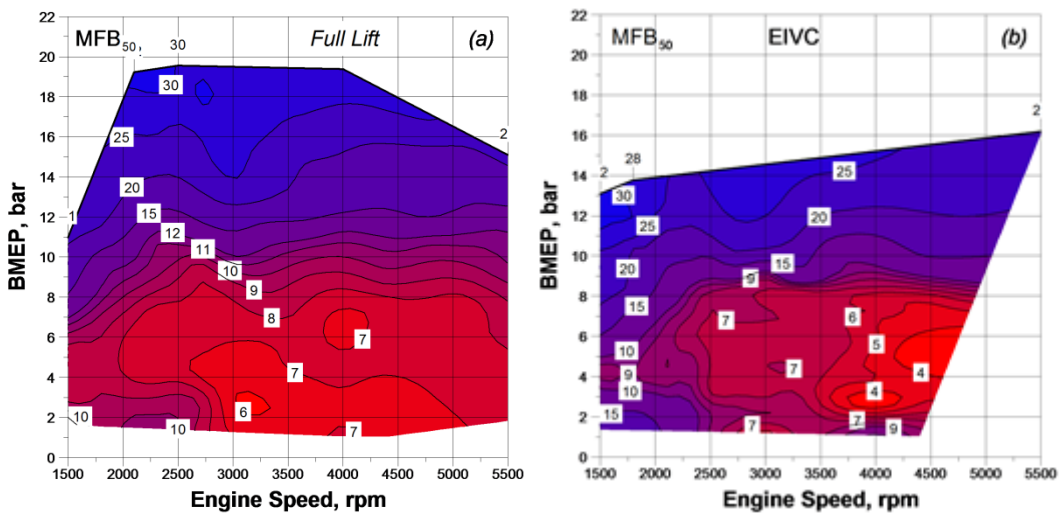


Figure 1.30 – Measured MFB_{50} map (crank angle degree after FTDC) for Full Lift (a) and EIVC (b) strategies.

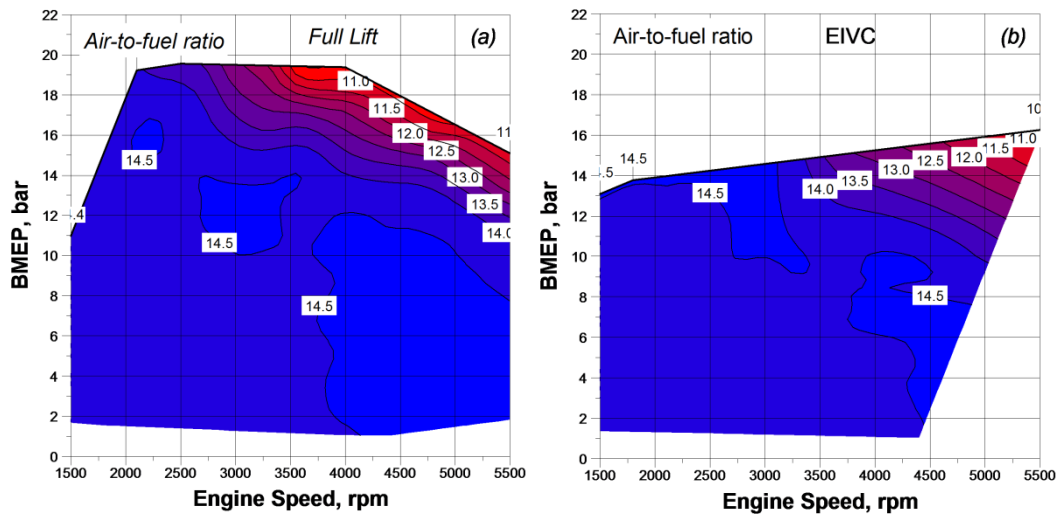


Figure 1.31 – Measured air-to-fuel ratio map for Full Lift (a) and EIVC (b) strategies.

The engine performance are also limited by the compressor operating domain (surge, choke and a maximum speed of 255000 rpm for the compressor of the considered engine). Further limitations are posed for the maximum allowable boost level (2.2 bar), required to guarantee proper operation for the fuel injectors and a certain safety margin for the intake plenum.

1.6.2 Engine calibration issues

Once the engine under study has been deeply specified in terms of sub-systems and all the operating parameters (i.e. degrees of freedom of the engine system) have been properly defined as well as the performance requirements, the engine calibration phase is realized with aim to identify the optimum set of engine variables for various operating conditions by taking into account the system performance targets (minimum fuel consumption and pollutant emissions at part load, maximum power and torque at full load, combustion stability at idle, etc.). As general consideration, modern spark ignition engines are characterized by complex architectures, showing a significant number of sub-systems and operating variables, making the engine calibration a challenging phase during the system development. Indeed, from an experimental point of view, the calibration requires an high number of tests to explore the whole operating domain of the control parameters and the entire engine operating map. This involves a negative impact on the engine development time and costs. In order to avoid the latter problems, the engine calibration phase is often supported by numerical

tools and methodologies. As an example, *Design of Experiment (DoE)* methodologies are successfully employed to reduce the number of experimental tests. A further reduction in the experimental activity can be obtained using proper numerical models that, once tuned, are able to achieve a pre-calibration of the engine, following a fully-numerical approach. Consequently, activity at test-bench can, hence, be limited to verify and refine the desired performance targets. For numerical calibration purposes, among several modeling approaches, 1D engine model, properly validated, coupled to an optimizer tool has been successfully employed to perform multi-objective analyses allowing to numerically identify the optimal set of engine parameters. First, the considered optimization approach shows the capability to reproduce with good accuracy the experimentally advised optimal calibration. Second, for a predefined engine operating point, it is possible to select the new optimal set of engine variables capable to achieve the desired trade-off among different performance requirements. For the downsized engine under study, as said before, the performance at high and full load operation are mainly limited by the knock onset, which influences the engine calibration, causing the adoption of delayed spark timing and over-fuelling mixture. For this reason, the use of proper sub-model for the description of knock phenomenon is mandatory. Only in this way, the reliability of an integrated 1D model/optimizer approach can be ensured and an overall “virtual” calibration of the engine, including all the control variables (i.e. valve strategy, combustion phasing, mixture quality, throttle opening, WG opening) can be accomplished. In particular, the virtual calibration at high loads, for a selected engine speed and intake valve lift strategy, is oriented to the identification of engine parameters allowing to maximize the brake torque while simultaneously minimize the fuel consumption under knock limited condition. In this way, the adopted numerical approach can also underline the potentiality of an engine calibration at high load, based on the actuation of innovative intake valve lift strategies by the VVA sub-system rather than a purely throttle based calibration. A similar virtual engine calibration can be also performed at part load for various VVA strategies. In conclusion, once the 1D engine model is validated against the experimental data, the discussed numerical approach allows for a virtual engine calibration on theoretical basis and it proves to be an useful tool to support and reduce the experimental costs and the engine time-to-market.

1.7 Structure of this work

This work is mainly focused on the study of turbulence, combustion, knock and cycle-by-cycle variation of a downsized VVA Spark Ignition engine. A 0D/1D modeling approach is here adopted to reproduce the engine behavior in different operating conditions. Gas-dynamic noise at intake mouth for the considered engine is also taken into account by testing redesign solutions of the intake system through a 3D CFD model. Engine calibration is also analyzed from a numerical point of view and a proper methodology is presented aiming to perform fully numerical calibrations. Thesis work is organized into eight chapters. A brief description of the content of each of them is reported below:

The present introductory chapter provides a description of characteristics and operation of Spark ignition engines and of the main technologies for SI engines capable to obtain efficiency improvements as well as pollutant emission reductions. Then, a description of SI turbulent combustion process, knock and cycle by cycle variation phenomena is also presented. Finally, the engine under study is analyzed, mainly focusing on the experimental activities and calibration issues. Numerical methodologies to support the calibration phase are discussed, too.

The second chapter furnishes an overview of the modeling approaches for internal combustion engines, with particular reference to the in-cylinder processes. The benefits of a proper integration of modeling approaches are also discussed. The 0D modeling approach is mostly analyzed: factual combustion model and “in-house developed” turbulence model are described in detail as well as the 0D/3D hierarchical approach for turbulence modeling.

The third chapter describes the 0D/1D model of the whole engine, developed in GT-Power™ environment. The single models of the main engine sub-systems and the numerical routines are considered. Once turbulence and combustion sub-models are tuned, the engine model is validated against the experimental data at full and part load operations.

In the fourth chapter various experimental knock detection techniques are analyzed. In particular, two different knock detection methods are utilized to perform a knock analysis for the examined engine. Knock and cyclic dispersion models are discussed and then the knock model taking into account the cycle by cycle variation is validated at full load operation.

The fifth chapter deals with the adoption of an external EGR system for the engine under study. Starting from the validated 1D engine model, a Low pressure EGR circuit is virtually mounted and the new engine configuration is tested by 1D simulations. Numerical results show that the adoption of the EGR circuit allows for fuel consumption reduction at full load points.

In the sixth chapter water injection technique at the engine intake ports is investigated by a 1D approach. The effects of the above technique are studied in various full load knock limited operating points and for various A/F levels and water content. The presented results highlight that the considered solution involves significant BSFC improvements, especially in the operating conditions at medium engine speeds.

In the seventh chapter the gas-dynamic noise emitted at the engine intake mouth is firstly reproduced by 1D and 3D CFD models. Once the models are validated at full load, some redesign solutions for the air-box device are proposed and numerically tested to evaluate the reduction in the gas-dynamic noise.

The eighth chapter deals with virtual engine calibration by employing 1D model coupled to external optimizer. Starting from the model validation for two different intake valve strategies, multi-objective optimizations at part and full load are performed, showing the capability to reproduce the experimentally identified calibrations. The effect of intake valve strategy on the fuel consumption is also discussed for various load levels.

CHAPTER 2

Modeling of Internal Combustion engines and in-cylinder processes

2.1 Modeling Approaches for engine development

In the automobile industry, system modeling and numerical simulation are widely employed for the development of new engines, thanks to the possibility to study different solution with acceptable computational time. During the development phase of an internal combustion engine (ICE) different requirements have to be considered. Indeed, engine manufacturers have to guarantee proper power/torque performance, fuel consumption and pollutant emissions, aiming to comply with the stringent emission limitations and to obtain the desired vehicle drivability. The above tasks, often conflicting, require proper architectures of the ICEs. In order to analyze new engine architectures and to take into account the engine behavior at development stage, virtual design tools and numerical models can be successfully employed to guide and limit the expensive experimental analyses [59], [60], [61]. Numerical simulation and system modeling are utilized at different levels and phases of an ICE developing project. The global engine system, which has to be studied, is usually decomposed into various less-complex sub-systems, on the basis of a functional criterion. In this way, each sub-system can be properly analyzed by evaluating the performance and taking into account the links with the other parts of the system. The main advantage of this kind of approach is that the single sub-system can be modeled separately and subsequently it may be integrated within the entire model of the system. For a given sub-system, several models can be adopted according to the engineering application. Their complexity may vary starting from simple mathematical models to phenomenological and CFD models. As said, system simulation tool may vary significantly according to the engine part which has to be modeled. In particular, in the case of ICEs analysis, three main modeling approaches has been adopted over the time:

- Zero-dimensional models;
- One-dimensional models;
- Three-dimensional models.

In the above classification the level of detail and physical contents increases as one proceeds downward and the complexity of those models increases, too. Zero-dimensional models are the

simplest ones due to their computational speed. Anyway, they present different levels of detail, including mathematical and physical models. They are generally employed to study in-cylinder processes. One-dimensional models are based on the integration of 1D unsteady flow equations and they are usually adopted to study the intake and the exhaust systems of ICEs with good accuracy and reduced computational efforts. One dimensional model can give important information at system levels, i.e about performance and internal flows of the entire system. 3D CFD models, based on the integration of Navier Stokes equations, give detailed fluid-dynamic information for complex 3D domains, allowing to capture the local 3D features of the flow. Anyway, the latter models require higher computational costs. For ICEs study, 3D CFD techniques play an increasingly role during the development phase. As an example, CFD analysis becomes a very powerful tool to analyze the in-cylinder flow structure evolution under actual engine operations, as well as to address the influence of port design on the in-cylinder flow field [62]. Furthermore, they allow for a better understanding of how combustion takes place in new combustion concepts, and consequently low cost testing of different chamber geometries and concepts can be performed in order to design the final product [63]. Although 3D CFD models provide considerable amount of spatial information and allow for a better description of combustion phenomenon and noxious emissions, they still employ phenomenological sub-models and require high computational time and storage. The latter constraints still preclude 3D models from routine use for engine design purposes. On the other hand, 0D and 1D models can be easily used for ICEs modeling because they improve the time delays and diminish the cost of production. 0D-1D models are often used for ICEs modeling either for the engine control or for the optimization of engine performance, fuel consumption and emission. 0D-1D models as support tools for engines development have to cope the challenge of the compromise between the computational time and the accuracy of models. In the following, a brief description of the above listed modeling approaches will be provided.

2.1.1 Zero-dimensional Approach

Zero dimensional model are generally conceived from empirical and semi-empirical approaches. In general, they are considered as simple modeling approach to study different systems and processes. The results obtained from more complex simulations (for example CFD) or from the experimental tests are used for the validation of 0D models. The outcomes of 0D models has to be in good agreement with the experimental or CFD ones. 0D models can present different complexity levels, depending on the modeled system and on the desired outputs. The complexity of the 0D models

may vary from the simple mathematical models to phenomenological models. 0D models are currently employed for the simulation of systems and sub-systems for automobile industry. As an example, 0D models can be adopted for a first satisfactory evaluation of engine performance, consumption, noise or thermal fluxes [29] but they do not take into account the flow modeling i.e. geometric/dimensional features of the flow motion. For the latter reason they are called zero-dimensional. The most important advantage of 0D modelling approach is the very low computational time and it is comparable with the one of the real time application. The latter characteristic makes these models very attractive for automobile industry. Another relevant advantage of this modeling approach is that it can be extended to different sectors, allowing to simulate several types of system, including mechanical, thermal, electrical etc. In the case of internal combustion engines simulation, 0D modeling approach is widely adopted in order to reproduce the in-cylinder phenomena. It is also employed to reproduce the intake and exhaust flow when the wave propagation effects within pipes can be neglected. In many cases a 0D/1D modeling approach is preferred for the simulation of ICEs: 0D model for volume elements (i.e. cylinders) and 1D model for pipes (i.e. intake/exhaust systems). In particular, as said, 0D modeling approach has been widely adopted in the past and it is still used for the simulation of in-cylinder phenomena, including the turbulent combustion process both for Spark-Ignition and Diesel engines and 0D models. Indeed, various 0D phenomenological models have been developed and oriented to primarily reproduce the turbulent combustion phenomenon and then the performance and emissions. As known, with the adoption of a zero-dimensional approach the variables which characterize the thermodynamic state of fluid within the engine cylinder are considered to be uniform in the cylinder volume while they are time-dependent. For the engine cylinder a 0D dimensional model provides the resolution of the mass and energy conservation equations. These equations, for the volume of an engine cylinder, are generally written in terms of crank angle:

$$\text{mass conservation equation: } \frac{dm}{d\theta} = \sum_i \frac{dm_i}{d\theta} - \sum_e \frac{dm_e}{d\theta} \quad (2.1)$$

$$\text{energy conservation equation: } \frac{d(me)}{d\theta} + \frac{dL}{d\theta} + \frac{dQ_{wall}}{d\theta} = \frac{dQ_b}{d\theta} + \sum_i \frac{dm_i}{d\theta} h_i \quad (2.2)$$

where:

$\frac{dQ_b}{d\theta}$ is the heat released by combustion process, $\frac{d(me)}{d\theta}$ is the variation of the internal energy of the system, $\frac{dL}{d\theta}$ represents the mechanical power exchanged by fluid with the piston, $\frac{dQ_{wall}}{d\theta}$ is the heat

exchanged through the walls of the combustion chamber and $\sum_i \frac{d\dot{m}_i}{d\theta} h_i$ is the energy term due to the flux of mass through the control surface.

Normally, the enthalpy term and the system mass variation, due to leakage, are neglected. In this case, $\sum_i \frac{d\dot{m}_i}{d\theta} h_i \cong 0$ and by considering the ideal gas law, the energy conservation equation (2.2) can be rearranged as follows:

$$\frac{dQ_b}{d\theta} = \frac{\gamma}{\gamma-1} p \frac{dV}{d\theta} + \frac{1}{\gamma-1} V \frac{dp}{d\theta} + \frac{dQ_{wall}}{d\theta} \quad (2.3)$$

Once the engine system is assigned, the heat release rate is known, the in-cylinder heat exchange is modeled as reported in the literature [64], [65] and by take into account the ideal gas law, the energy equation allows to obtain the in-cylinder pressure trace as a function of the crank angle. Referring to the in-cylinder models, the zero-dimensional ones are the simplest and most suitable to evaluate the effects of variations in the engine operating parameters on the overall heat release rates and in-cylinder pressure evolutions.

Zero dimensional models are further sub-divided into:

1. Single zone models;
2. Two zone models;
3. Multi-zone models.

In single zone models, the working fluid in the engine is assumed to be a thermodynamic system, which undergoes energy and/or mass exchange with the surroundings and the energy released during the combustion process is obtained by applying the first law of thermodynamics to the system. In two zone models, the working fluid consists of two zones, an unburned zone and a burned zone. These zones are actually two distinct thermodynamic systems with energy and mass interactions between themselves and their common surroundings, the cylinder walls. The mass-burning rate (or the in-cylinder pressure), as a function of crank angle, is then numerically computed by solving the simplified equations resulting from applying the first law to the two zones.

Single zone and to zone models can be employed in two different directions:

1. In one way, both these models can predict the in-cylinder pressure as a function of crank angle from an assumed energy release or mass burned profile (Wiebe equation);

2. Another use of these models lies in determining the energy release/mass burning rate as a function of crank angle from experimental in-cylinder pressure data.

Multi-zone models consider energy and mass balances over several zones, thus obtaining results that are closer to reality. Concerning the modeling of the combustion process, many combustion models have been developed to date and they essentially allow to predict the rate of fuel burning. In the case of Spark Ignition ICEs, various approaches for combustion modeling have been proposed and used trying to reproduce the flame development inside a turbulent flow field [23]. Among the different approaches, the “fractal” combustion model appears to be the one which better describes the turbulent flame propagation phenomenon inside an internal combustion engine [6], [7], [66], [67]. It is based on the hypothesis that aerodynamic turbulence enhances the burn rate by increasing the surface of the flame front with respect the laminar extent and does not alter significantly the inner flame structure. All turbulent length scales are assumed to be larger than the flame front thickness (flame is in the so called “wrinkled flamelet” regime). This combustion model will be described in the following.

2.1.2 One-dimensional Approach

One dimensional modeling is widely adopted for the numerical study of internal combustion engines because it allows for the description of the entire engine system with satisfactory accuracy, lower computational effort and reduced computational time. Indeed, this approach is usually employed during the engine development phase to study the global engine system. The 1D modeling of the entire engine, thanks to the above discussed advantages, allows to analyze (in addition to steady state engine operation) more complex processes such as the transient operation of the engine, unsteady behavior of engine and its sub-systems, including turbocharger group, cooling system behavior, etc. Furthermore, the 1D approach allows to analyze different engine architectures (including VVA/VVT systems, EGR circuits, water injection systems, turbocharging systems, components for the abatement of pollutant emissions, exhaust and muffler systems) and to rapidly test the effects of the modified engine configurations on its overall performances (torque/power, fuel consumption, noxious emissions, gas-dynamic noise, etc.). 1D model also furnishes the possibility to investigate a wide range of engine operating conditions such as engine operations which differ in the air-to-fuel ratio, speed, fuel injection strategies, etc. In particular, as said before,

1D models are usually employed for the description of the unsteady flow within the intake and the exhaust manifolds of internal combustion engines. In this way, the wave propagation within the intake and exhaust systems is taken into account. This approach is particularly suited for the intake/exhaust system design, since that fluid-dynamic effects on intake/exhaust flow and many geometrical variables determining the overall filling/emptying performance can be considered. These variables include length and cross-sectional area of both primary and secondary runners, volumes and locations of plenums or junctions connecting the various runners, entrance and exit angle of runners at a junction, number of cylinders and dimension, intake and exhaust ports and valve design, etc. 1D models consider mass, momentum and energy conservation equations to describe the un-steady flow within the intake/exhaust systems [23]. Normally, the intake and the exhaust flows of a ICE are properly linked by a thermodynamic analysis of the in-cylinder processes performed through the adoption of a zero-dimensional modeling approach. Referring to numerical method, method of characteristics was used in the past to solve the 1D unsteady flow equations. It presents first order numerical accuracy in space and time and requires a large numbers of computational points if the resolution of the short-wave-length variations is important [23]. In recent years, the finite difference techniques are employed for intake and exhaust flow models. They have high order numerical accuracy in space and time and prove to be more efficient: this numerical method is now preferred. The basic assumptions and equations of the 1D models will be now briefly reviewed. The flow through the control volume within a straight pipe (Figure 2.1) is considered. It is assumed that:

- only a reduced change in the area over the length dx of the control volume occurs;
- the length of the pipe is greater than its diameter;
- the radius of curvature of pipe bends is higher than pipe diameter. In these conditions the flow is essentially one-dimensional.

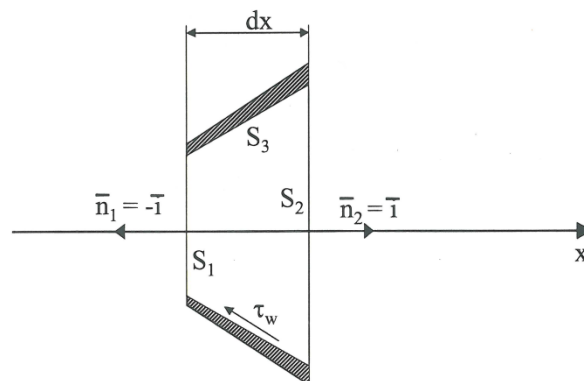


Figure 2.1 – Control volume for unsteady 1D flow analysis.

Under the hypothesis of 1D flow, all the parameters which identify the fluid conditions are considered to be uniform for each cross section of the pipe and consequently these variables depend on a single spatial coordinate (the one along the curvilinear axis of the system) and time. The area of surfaces S_1 , S_2 and S_3 are, less than high order infinitesimal, A , $\left(A + \frac{dA}{dx} dx\right)$ and cdx , respectively. A represents the area of the cross section of the pipe while c is its perimeter. In order to derive the typical equations for one-dimensional flows it has to remember that:

1. Surface S_3 is impervious to the flow;
2. For S_2 and S_3 sections all the variables are uniform and so they can be brought out of the integral sign;
3. For volume integral, all parameters can be brought out of the integral sign, because of the infinitesimal control volume.

Mass conservation requires that the rate of change for mass within the control volume of Figure 2.1 equals the net flow into the control volume:

$$\frac{\partial(\rho A dx)}{\partial t} = \rho A u - \left[\rho A u + \frac{\partial}{\partial x} (\rho A u) dx \right] \quad (2.4)$$

Considering only the first order quantities and imposing $\alpha_A = \frac{1}{A} \frac{dA}{dx}$, equation (2.4) simplifies in:

$$\frac{\partial \rho}{\partial t} + \frac{\partial}{\partial x} (\rho u) + \rho u \alpha_A = 0 \quad (1D \text{ continuity}) \quad (2.5)$$

The momentum conservation equation states that the net pressure forces plus the wall shear force acting on the control volume surface equal the rate of change of momentum within the control volume plus the net flow of momentum out of the control volume.

Pressure forces:

$$pA - \left(p + \frac{\partial p}{\partial x} dx \right) \left(A + \frac{dA}{dx} dx \right) + p \frac{dA}{dx} dx = -A \frac{\partial p}{\partial x} dx \quad (2.6)$$

Shear stress at wall (which opposes to the direction of motion):

$$\tau_{wall} = -\rho \frac{f_a u^3}{2|u|} \quad (2.7)$$

where f_a is the friction coefficient.

Friction forces:

$$\tau_{wall} c dx = -\rho f_a \frac{c}{2} \frac{u^3}{|u|} dx \quad (2.8)$$

The second law of motion by neglecting the weight force of gas is:

$$-\frac{\partial p}{\partial x} A dx - \frac{\rho f_a c}{2} \frac{u^3}{|u|} dx = \frac{\partial(\rho u A)}{\partial t} dx + \frac{\partial}{\partial x} (\rho u^2 A) dx \quad (2.9)$$

By adopting the equation of continuity the above momentum equation (2.9) can be rearranged as reported in equation (2.10):

$$\frac{\partial(\rho u)}{\partial t} + \frac{\partial}{\partial x} (\rho u^2 + p) + \frac{\rho u^2}{A} \frac{\partial A}{\partial x} + \frac{2\rho f_a}{D} \frac{u^3}{|u|} = 0 \quad (2.10)$$

Referring to the energy conservation equation, the energy within the control volume may vary due to the heat transfer and the net flow of total enthalpy through the surfaces of the control volume. The total enthalpy of the fluid is:

$$H = h + \frac{u^2}{2} = e + \frac{p}{\rho} + \frac{u^2}{2} \quad (2.11)$$

where “e” represents the specific internal energy of fluid and in the case of ideal gas $e = c_v T$ while the specific enthalpy for an ideal gas is $h = c_p T$.

The thermal power which is transferred to the working fluid in the control volume is:

$$d\dot{Q}_{wall} = \dot{q} \rho A dx$$

where \dot{q} represents the heat exchange through the wall of the system per unit time and fluid mass.

The temporal variation of the energy within the control volume is:

$$\frac{\partial(\rho A E dx)}{\partial t}$$

$$\text{with } E = e + \frac{u^2}{2}$$

The net flux of total enthalpy through the surface of the control volume can be write as follows:

$$\frac{\partial}{\partial x} (\rho u A H) dx$$

and the energy equation is furnished by the equation (2.12):

$$\frac{\partial(\rho A E dx)}{\partial t} + \frac{\partial(\rho u A H)}{\partial x} dx - \dot{q} \rho A dx = 0 \rightarrow \frac{\partial}{\partial t} (\rho E) + \frac{\partial}{\partial x} (\rho u H) + \rho u H \alpha_A - \dot{q} \rho = 0 \quad (2.12)$$

The one-dimensional unsteady flow equations are given by the system of equations (2.13):

$$\left\{ \begin{array}{l} \frac{\partial \rho}{\partial t} + \frac{\partial(\rho u)}{\partial x} + \rho u \alpha_A = 0 \text{ (I)} \\ \frac{\partial}{\partial t}(\rho u) + \frac{\partial}{\partial x}(\rho u^2 + p) + \rho u^2 \alpha_A + \frac{2\rho f_a}{D} \frac{u^3}{|u|} = 0 \text{ (II)} \\ \frac{\partial(\rho E)}{\partial t} + \frac{\partial}{\partial x}(\rho u H) + \rho u H \alpha_A - \dot{q} \rho = 0 \text{ (III)} \end{array} \right. \quad (2.13)$$

The energy equation (III) in (2.13) can be rewritten by employing both the mass and momentum conservation equations as reported below:

$$\frac{\partial p}{\partial t} + u \frac{\partial p}{\partial x} - a^2 \left(\frac{\partial \rho}{\partial t} + u \frac{\partial \rho}{\partial x} \right) - (\gamma - 1) \rho \left(\dot{q} + 2f_a \frac{u^3}{D} \frac{u}{|u|} \right) = 0 \quad (2.14)$$

where $\gamma = \frac{c_p}{c_v}$ and “a” represents the velocity of sound in fluid medium which for a ideal gas gives:

$$a = \sqrt{kRT} \quad (2.15)$$

The one-dimensional unsteady flow equations can be upgraded by take into account the latter energy equation (2.14). In this way, the one-dimensional flow model is formulated in the primitive variables (ρ, u, p):

$$\left\{ \begin{array}{l} \frac{\partial \rho}{\partial t} + \frac{\partial(\rho u)}{\partial x} + \rho u \alpha_A = 0 \text{ (I)} \\ \frac{\partial}{\partial t}(\rho u) + \frac{\partial}{\partial x}(\rho u^2 + p) + \rho u^2 \alpha_A + \frac{2\rho f_a}{D} \frac{u^3}{|u|} = 0 \text{ (II)} \\ \frac{\partial p}{\partial t} + u \frac{\partial p}{\partial x} - a^2 \left(\frac{\partial \rho}{\partial t} + u \frac{\partial \rho}{\partial x} \right) - (\gamma - 1) \rho \left(\dot{q} + \frac{2f_a u^3}{D} \frac{u}{|u|} \right) = 0 \text{ (IV)} \end{array} \right. \quad (2.16)$$

The above system (2.16) is formed by hyperbolic partial differential equations in the variables (x,t) and it allows to describe the flow field within the space-temporal domain, once the initial and boundary conditions for each instant of time are assigned [68]. For the resolution of the above system (2.16), the equations are set in the conservative form in order to bring their to a formulation and a technique of uniform solution. A typical formulation of the system (2.16), with invariance of molecular species and in absence of thermal flows and friction terms, is reported in the following equation (2.17):

$$\frac{\partial U}{\partial t} + \frac{\partial F(U)}{\partial x} = S \quad (2.17)$$

where U is the vector of the conservative variables, F is the vector of flows and S is the vector of source terms:

$$U = \begin{Bmatrix} \rho \\ \rho u \\ \rho E \end{Bmatrix}; \quad F = \begin{Bmatrix} \rho u \\ \rho u^2 + p \\ \rho u H \end{Bmatrix}; \quad S = - \begin{Bmatrix} \rho u \alpha_A \\ \rho u^2 \alpha_A \\ \rho u H \alpha_A \end{Bmatrix}$$

For the simulation of the flow within the intake and the exhaust pipes of an ICE the above system of equations (2.16) has to be properly generalized, by including the source terms related to the friction and the heat exchange phenomena. For this reason, two further scalar transport equations, one for the exhaust gases and the other one for the fuel, are considered with the aim to take into account the gas composition within the intake and exhaust systems [68].

The system (2.17) is now re-written in (2.18):

$$U = \begin{Bmatrix} \rho \\ \rho u \\ \rho E \\ \rho x_r \\ \rho x_{fu} \end{Bmatrix}; \quad F = \begin{Bmatrix} \rho u \\ \rho u^2 + p \\ \rho u H \\ \rho u x_r \\ \rho u x_{fu} \end{Bmatrix}; \quad S = - \begin{Bmatrix} \rho u \alpha_A \\ \rho u^2 \left(\alpha + \frac{2f_a}{D} \frac{u}{|u|} \right) \\ \left(\rho u H \alpha_A - \frac{4q}{D} \right) \\ \rho u x_r \alpha_A \\ \rho u x_{fu} \alpha_A \end{Bmatrix} \quad (2.18)$$

$x_r = \frac{m_r}{m}$ is the fraction of residual gases, $x_{fu} = \frac{m_{fu}}{m}$ is the fraction of fuel. Concerning the friction coefficient f_a , two different correlations are adopted according to the flow regime. For laminar flows the friction coefficient is:

$$f_a = \frac{16}{Re} \text{ with } Re \leq 2000 \text{ (Poiseuille Formula)}$$

For turbulent flows the friction coefficient is:

$$f_a = \frac{0.0791}{Re^{0.25}} \text{ with } Re > 2000 \text{ (Blasius Formula)}$$

The heat exchange through the system walls is evaluated by the following relationship:

$$q = \frac{1}{2} \rho |u| f_a c_p (T_{wall} - T) \text{ with } \rho \dot{q} = q \frac{4}{D}$$

From an analytical point of view, the integration of the system with five equations (2.18) leads to the determination of the function $U(t, x)$, requiring the assignment of the initial conditions for the entire spatial domain $U_0 = U(0, x)$ and of the boundary conditions such as $U(t, 0)$ and $U(t, L)$. Finally, the considered formulation of system (2.18) is well suited for the numerical integration through finite difference schemes or finite volume schemes.

2.1.3 Three-dimensional Approach

Three dimensional or multi-dimensional models present the capability to reproduce the main chemical and fluid-dynamic (local and temporal) details of the in-cylinder phenomena, including the in-cylinder flow field, combustion and heat exchange process. The increased computational potentialities of modern computers have led to the development of 3D codes capable to furnish acceptable forecasts of the in-cylinder processes, especially for the prediction of the in-cylinder flow field. The comparison of 3D numerical results with experimental outcomes allows for a continuous improvement of codes thanks to the advanced diagnostic techniques. The considered models solve the Navier Stokes equations, based on the resolution of mass (continuity), momentum, energy and chemical species equations, depending on spatial coordinates and time. According to the continuity equation in differential form, the rate of change of mass in a chosen control volume has to be identical to the total mass which flows through said control volume boundaries:

$$\frac{\partial \hat{\rho}}{\partial t} + \frac{\partial}{\partial x_j} (\hat{\rho} \hat{u}_j) = 0 \quad (2.19)$$

The momentum equation, reported below in its differential conservative form, shows that the rate of change of momentum on a fluid elements must be equal to the sum of forces acting on it, according to Newton's second law:

$$\hat{\rho} \frac{D\hat{u}_i}{Dt} = \hat{\rho} \frac{\partial \hat{u}_i}{\partial t} + \hat{\rho} \hat{u}_j \frac{\partial \hat{u}_i}{\partial x_j} = \hat{\rho} g_i - \frac{\partial \hat{p}}{\partial x_i} + \frac{\partial}{\partial x_j} \left[\mu \left(\frac{\partial \hat{u}_i}{\partial x_j} + \frac{\partial \hat{u}_j}{\partial x_i} - \frac{2}{3} \frac{\partial \hat{u}_k}{\partial x_k} \delta_{ij} \right) \right];$$

$$i = 1,2,3 \quad (2.20)$$

where the term in square brackets is the viscous stress τ_{ij} .

The energy equation for an element of fluid states that the rate of change of its total energy must be equal to the net rate of heat and work flow over its boundaries:

$$\hat{\rho} \frac{D\hat{H}}{Dt} = \hat{\rho} \left(\frac{\partial \hat{H}}{\partial t} + \hat{u}_j \frac{\partial \hat{H}}{\partial x_j} \right) = \hat{\rho} \hat{q}_g + \frac{\partial \hat{p}}{\partial t} + \frac{\partial}{\partial x_j} (\hat{\tau}_{ij} \hat{u}_j) + \frac{\partial}{\partial x_j} \left(\lambda \frac{\partial \hat{T}}{\partial x_j} \right) \quad (2.21)$$

For reactive flows, the conservation equation for each individual chemical species has to be considered. The equation for the concentration of the k-th chemical species is:

$$\hat{\rho} \frac{D\hat{c}_k}{Dt} = \hat{\rho} \left(\frac{\partial \hat{c}_k}{\partial t} + \hat{u}_j \frac{\partial \hat{c}_k}{\partial x_j} \right) = \hat{\rho} \hat{r} + \frac{\partial}{\partial x_j} \left(D \frac{\partial \hat{c}_k}{\partial x_j} \right) \quad (2.22)$$

For the equations (2.20), (2.21) and (2.22), g_i represents the component of the gravity acceleration along the axis x_i , \dot{q}_g is the floating term, and \hat{r} represents the source term of the considered chemical species. All the other terms which appear in equations (2.20), (2.21) and (2.22) are reported in Table 2.1.

\hat{T}	Temperature
\hat{c}_k	Concentration of the k-th chemical species
\vec{q}	Heat flux
λ	Thermal conductivity
D	Molecular diffusivity coefficient for single chemical species
τ_{ij}	Viscous Stress
μ	Dynamic viscosity
$I = \delta_{ij}$	Unit tensor
$S_{ij} = \frac{1}{2} \left(\frac{\partial \hat{u}_i}{\partial x_j} + \frac{\partial \hat{u}_j}{\partial x_i} \right)$	Mean rate of strain

Table 2.1 – Terms in the conservation equations.

The above discussed equations represent a non-linear system of partial differential equations with respect to the time and the three spatial coordinates [69]. This set of equations accurately describes the flow (both laminar and turbulent) of a Newtonian fluid. Such a system is difficult to be analytically solved, since it is non-linear and coupled. So *Numerical methods*, must be used. However, the resolution of this system requires several information as reported in the following list:

- Working fluids, their properties and state equations;
- Chemical reactions among the considered species;
- Initial and boundary conditions.

Three dimensional models also include different phenomenological sub-models because of wide spatial and temporal scales related to chemical and physical processes to be simulated [70]. Main characteristic sub-models of 3D codes for the simulation of typical phenomena of internal combustion engines are listed below:

- turbulence;
- spray evolution (both for gasoline and Diesel engine);

- combustion and knock processes;
- generation of pollutant emissions.

In general, a 3D CFD analysis for a predefined system requires the definition of a proper computational grid. Indeed, the 3D volume of interest has to be divided into a discrete number of elements with selected shape and consequently a certain number of nodes are defined, too. In this way, the computational mesh associated to the system under study is realized. Partial differential equations are discretized on the computational grid, by adopting a combination of formal integration and approximation within each volume element, in such a way to transform system of differential equations in a system of algebraic equations. The latter system of mathematical equations is solved through a proper iterative numerical algorithm. For 3D CFD analyses, computational grid generation represents a relevant step during pre-processing phase. Indeed 3D results are affected by the resolution of the computational grid. A fine mesh which presents a high number of nodes and elements allows for accurate solutions but conversely it involves greater computational efforts or high performance workstation. For these reasons, in general, a preliminary grid invariance analysis has to be performed with the aim to select a proper mesh for the analyzed system which simultaneously shows an acceptable computational effort and a good accuracy for numerical findings. The computational grid has to be realized by taking into account, in addition to the geometrical features of the considered system, the characteristics related to the system operation, too. For instance, if the examined system does not present moving parts a static mesh has to be properly realized. On the other hand, dynamic grid has to be employed to simulate moving computational domains. The latter case is usually for the simulation of ICE phenomena such as the in-cylinder flow field and processes, turbocharging group operation, etc. A moving mesh takes into account the the motion of certain boundaries which refer to moving mechanical parts. As an example, in the case of simulation of the in-cylinder processes a moving grid allows to consider the motions of intake and exhaust valves and the piston motion. In the case of moving mesh, the computational domain for the numerical integration of the above discussed equations is continuously modified. In order to avoid a greater cells deformation a mesh upgrade during the simulation is mandatory. The updating operation mainly consists in a new distribution of cells and this process is well known as “rezone” of mesh. 3D code geometrically interpolates the different generated grids allowing the continuous deformation of the mesh. In addition, during the rezone process a re-mapping of numerical variables on the new grid is realized. Summarizing a dynamic mesh requires particular attention to be properly realized with respect to the generation of a static mesh. Referring to the definition of the fluid-dynamic problem before starting with the running

phase, proper selection of surfaces is needed in order to define the boundary conditions. Computational domain has to be associated to a well defined fluid, the desired phenomenological sub-models have to be enabled to describe fluid-dynamic processes of interest and the case under study requires a proper fluid-dynamic initialization. Finally, an appropriate solution method has to be selected for the numerical integration of Navier Stokes equations.

2.2 *Integration of Modeling Approaches: 1D/3D methodology*

For the numerical simulation of ICEs behavior, as discussed before, several modeling approaches can be adopted according to the analysis type, the desired results and their level of detail. During the last years, three-dimensional codes have been more and more used to describe various thermo-fluiddynamic processes, allowing for detailed and accurate prediction of fluid-dynamic conditions within the intake and exhaust manifolds and engine cylinders. In particular, 3D analyses are very helpful to study the in-cylinder phenomena, including turbulence and combustion processes, abnormal combustion (knock phenomenon), fuel spray evolution, fuel evaporation, mixing process and pollutant species generation. Even if 3D CFD models allow to be closer to the actual engine fluid-dynamic behavior, they still require high computational times, which grows with the engine dimensions, making the considered models not compatible with the development phase of ICEs. For this reason, the employment of a sole 3D CFD model for ICEs is limited to few cases and oriented to better understanding the physical phenomena and to find information which cannot be easily obtained with the experimental tests. On the other hand, 0D/1D models allow to describe the whole engine system (including external sub-systems such as turbocharger) with reduced computational times and satisfactory accuracy. With this modeling approach, virtual analyses of new engine configurations can be performed. The main drawbacks of 0D/1D models are usually represented by the description of the in-cylinder phenomena, because an inadequate formulation of in-cylinder processes (especially for combustion process) leads to not correct assessment of engine performance and engine-turbocharger matching. A very promising numerical methodology showing the potentialities to support the engine development phase and to overcome the limits of both 0D/1D and 3D models, is represented by a proper integration of these types of models. The role of each model within the integrated 0D-1D/3D methodology is univocally identified. As an example, a brief description of an integrated procedure for the simulation of SI ICEs performance is here reported and it is adopted within this work. The considered integrated method requires, as the initial step, the engine geometrical data provided by the manufacturer. They are used to build the 1D

model of the whole engine and to carry out preliminary 1D simulations under motored operations. Then, multi-cycle motored 3D analyses, applying 1D computed time-varying pressure and temperature traces as boundary conditions, are performed. Detailed information about the in-cylinder mean and turbulent flow fields are extracted from the 3D analyses over a whole engine cycle. The results obtained by the latter analyses are utilized to calibrate a 0D turbulence model coupled to a proper phenomenological combustion model, which will be discussed in detail in the following paragraph. Once the turbulence sub-model is tuned, the 1D engine simulation is carried out under fired operations. The combustion process description is properly linked to the previously tuned in-cylinder turbulence model. The combustion model is tuned in order to fit the in-cylinder pressure cycles at full load operation. Once validated, the 1D model is capable to reproduce the engine performance and it can be employed for further numerical analyses, including the description of knock occurrence and cycle-by-cycle variations. In Figure 2.2, a flowchart of the described integrated 1D/3D methodology is fully summarized.

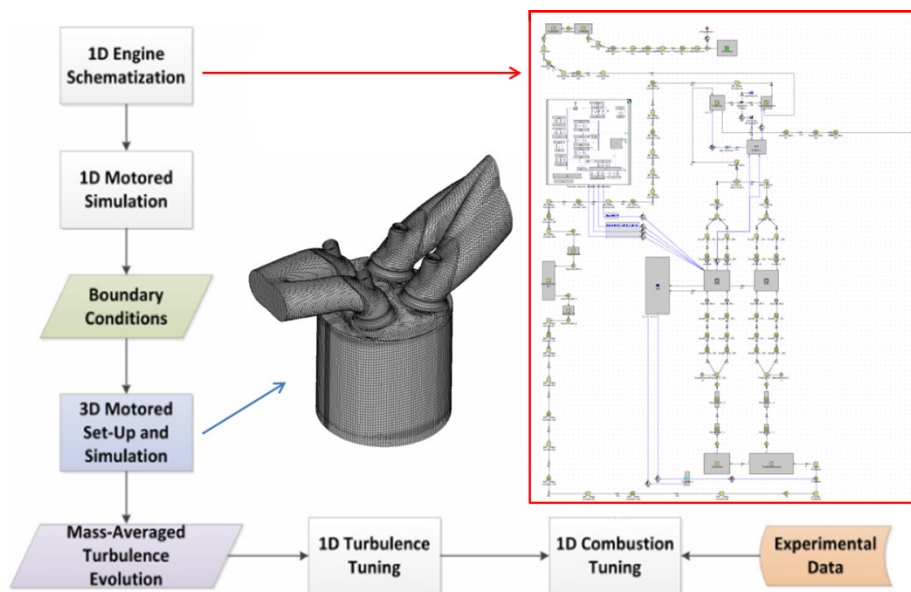


Figure 2.2 – Flowchart of the integrated 1D/3D hierarchical methodology.

2.3 0D Combustion Modeling: “Fractal Combustion Model”

Fractal Combustion Model is a phenomenological 0D model, based on the fractal description of the flame front and it is able to sense both the combustion system geometry and the operating parameters, such as air-to-fuel ratio, spark advance, boost level, residual gas content etc. This model is capable to take into account the in-cylinder turbulence evolution thanks to a proper 0D turbulence sub-model. Referring to the 0D combustion modelling, in the wrinkled-flamelet regime of combustion occurring inside an ICE [71], [72], [73], the burning rate can be expressed as:

$$\frac{dm_b}{dt} = \rho_u A_T S_L = \rho_u \left(\frac{A_T}{A_L} \right) A_L S_L \quad (2.23)$$

ρ_u being the unburned gas density. Equation (2.23) puts into evidence that the burning rate is mainly increased by the wrinkling of the flame surface A_T determined by the turbulent flow field, with respect to the corresponding smooth surface A_L , occurring in a laminar combustion process. Flame propagation indeed locally proceeds at the stretched laminar flame speed, S_L , which is a function of the fuel type, air-to-fuel ratio and residual gas fraction. The employed correlation also accounts for flame stretch mainly occurring during the first phase of burning process [74]. Under this schematization, moreover, the burning rate can be easily computed once the increase in flame area has been established. Basing on the concepts of the fractal geometry, the latter can be easily expressed as a function of a minimum and maximum flame wrinkling scales, L_{\min} - L_{\max} , and to its fractal dimension D_3 as reported in equation (2.24):

$$\frac{A_T}{A_L} = \left(\frac{L_{\max}}{L_{\min}} \right)^{D_3-2} \quad (2.24)$$

L_{\min} is assumed equal to the Kolmogorov length scale, η_k which, under the hypothesis of isotropic turbulence, follows the expression (2.25):

$$\eta_k = \frac{L_T}{Re_t^{3/4}} \quad Re_t = \frac{u' L_T}{\nu_u} \quad (2.25)$$

ν_u being the kinematic viscosity of the unburned mixture. The turbulent intensity u' and the integral length scale L_T are given by the K-k model described in the following. L_{\max} , indeed, representing the dimension of the maximum flame front wrinkling, is related to some characteristic dimension the

flame front, such as the flame radius or the square root of the laminar surface. In the present version of the model, the latter choice is followed, and the L_{max} is computed according to equation (2.26):

$$L_{max} = c_{wrk} \sqrt{A_L} \quad (2.26)$$

c_{wrk} being a tuning constant. The D_3 dimension only depends on the ratio between the turbulence intensity u' and the laminar flame speed S_L , reported in [73].

The above described fractal model is really valid for a fully developed and freely expanding turbulent flame. During both early flame development and combustion completion, a different approach is required. Initial flame development is in fact dominated by the kernel formation phase; its duration is calculated by an Arrhenius-like formulation, also accounting for residual fraction contents. At the end of the kernel formation time, the computation of the combustion process starts with a stable and spherically-shaped smooth flame, of radius r_0 . Flame wrinkling process also starts at a rate, ω_{wr} (equation (2.27)), which increases with the normalized elapsed time after the combustion start.

$$\omega_{wr} = \frac{t - t_{start}}{t_{trans}} \quad (2.27)$$

The transition time, t_{trans} , in the above equation (2.27) is hence considered as a time scale during which the flame front evolves from an initial smooth surface – corresponding to a laminar-like combustion – to a fully developed turbulent wrinkled flame. The transition time is assumed proportional to a characteristic turbulent time scale, calculated as reported in equation (2.28):

$$t_{trans} = c_{trans} \frac{k}{D_r} \quad (2.28)$$

c_{trans} being a tuning constant, while k and D_r are the turbulence kinetic energy and its dissipation rate. Flame wrinkling rate ω_{wr} affects the calculation of the maximum fractal dimension of the flame, according to equation (2.29):

$$D_{3,max} = 2.00(1 - w_1) + 2.35w_1 \quad w_1 = W_F \omega_{wr} \quad (2.29)$$

W_F being the well-known Wiebe function. In this way, the D_3 expression in [73] is redefined as:

$$D_3 = \frac{D_{3,max}u' + 2.00S_L}{u' + S_L} \quad (2.30)$$

With this formulation, the first phase of the combustion process ($w_1 \sim 0$) is characterized by a fractal dimension close to 2.00, corresponding to an initial laminar burning process.

A different combustion rate is also specified when the flame front reaches the combustion chamber walls (wall combustion phase). Wall-combustion burning rate is simply described by an exponential decay, as reported in equation (2.31):

$$\left(\frac{dm_b}{dt}\right)_{wall-combustion} = \frac{m-m_b}{\tau} \quad (2.31)$$

τ being the characteristic time scale of the above process. The overall burning rate is consequently defined as a weighted mean of the two described combustion rates in (2.32):

$$\left(\frac{dm_b}{dt}\right) = w_2 \left(\frac{dm_b}{dt}\right)_{fractal} + (1 - w_2) \left(\frac{dm_b}{dt}\right)_{wall-combustion} \quad (2.32)$$

The switch between the two combustion modes gradually starts when a threshold value, c_{wc} , of the burned gas fraction is reached (transition time, t_{wc}). At this time, the characteristic time scale in equation (2.31) is computed assuming that the wall combustion burning rate equals the one derived from the fractal model, equation (2.23), hence:

$$\tau = \frac{(m-m_b)_{t_{wc}}}{(\rho_u A_T S_L)_{t_{wc}}} \quad w_2 = \frac{m-m_b}{(m-m_b)_{t_{wc}}} \quad (2.33)$$

The above τ value is then kept fixed during the subsequent wall combustion process. The weight factor w_2 indeed increases with time, depending on the instantaneous unburned mass ($m - m_b$), compared to the one occurring at the transition time, t_{wc} . In this way, a smooth transition between the two modes is easily obtained. It is important to note that the above schematization of the wall combustion, based on the analysis of typical heat release data, does not include any additional tuning constant. Finally, two corrections are introduced in the turbulent flame front area calculation, as shown in equation (2.34):

$$\frac{A_T}{A_L} = \left(\frac{L_{max}}{L_{min}}\right)^{D_3-2} [1 + c_{enh1}(Ka - 1)] \left[1 + c_{enh2}W_1 \frac{U_{flow}}{S_T}\right] \quad (2.34)$$

Ka in the above equation is the Karlovitz number which is computed as reported in equation (2.35):

$$Ka = \left(\frac{\delta_f}{\eta_k}\right)^2 \quad \delta_f = \frac{v_u}{S_L} \quad (2.35)$$

δ_f being the flame front thickness. The first correction accounts for the enhanced species mixing in the flame front and is activated only when the $Ka > 1$ inequality verifies. In this case, in fact, the flame thickness is larger than the Kolmogorov turbulence micro-scale and turbulent eddies are able to enhance the burning speed. This verifies in the case of high turbulence levels (high engine speed) or slow laminar flame speed (large amount of trapped EGR, very lean or very rich mixtures, for instance). Simultaneously, at very high Karlovitz numbers, the flame deformation determined by the turbulent flow field can be so intense to produce a multiple connected flame front, with “islands” of unburned mixture trapped within the burned gas zone. This is mainly due to the increased convective action of the turbulent field, that can stretch and break the flame, determining pockets of unburned mixture within the burned gas zone. As a consequence, the reaction surface and the burning speed increase.

The second correction term is justified by the possibility of a flame front distortion, that may occur when an intense mean flow is present in the cylinder. Each term is weighted by additional tuning constants, c_{enh1} and c_{enh2} .

2.4 Turbulence modeling in 3D codes: RANS technique and $k-\varepsilon$ model

As said before, the description of the turbulent flow fields inside internal combustion engines is obtained through the solution of Navier Stokes equations, as well. Regarding the turbulent flows, various resolution methods are available and adopted according to the simulation application. To this aim, three turbulence modeling approaches can be identified:

- *Direct Numerical simulation (DNS)*: it represents the most detailed approach, since it resolves the complete equations locally and without any modeling for the reactive flows. This approach requires a very high number of grid points and accurate schemes for numerical discretization. DNS approach is rarely adopted into the industrial sector, due to its very high computational costs. Consequently, DNS is limited to university research to reproduce very difficult experimental tests and to understand the involved physical phenomena.
- *Reynolds Averaged Navier Stokes (RANS)*: it is an ensemble average approach, based on

the assumption that the flow field variables can be expressed as a sum of mean value and the fluctuation value. The ensemble average method is applied to the usual Navier Stokes equations and consequently additional terms containing the fluctuation value appears and need to be modeled. Since every length scales of turbulence is modeled, RANS technique offers a correct description of the mean flow field with a relatively low computational needs. For these reasons, RANS is well suited for industrial use.

- *Large Eddy Simulation (LES)*: this technique offers a compromise between computational efforts and description of physical phenomenon. In this case, Navier Stokes equations are solved for large eddies while small eddies are modeled. Indeed, large scale eddies are highly anisotropic and so difficult to be modeled while small scale eddies enhance the dissipation and they may be modeled similarly to the RANS approach. LES technique is capable to furnish a description of the flow field close to the DNS response but the computational time is close to the RANS technique. Anyway, LES calculation still remains expensive for industrial practice.

The above classification highlights that the RANS approach is the most simple one and it is widely utilized for the study of the mean flow characteristics of turbulent flow inside the ICEs. For this reason, among the discussed turbulence modeling techniques, RANS model is here analyzed in more detail with respect to the other models. According to Reynolds decomposition, the mathematical description of turbulent flow field is obtained by expressing the single instantaneous property (i.e. velocity, pressure, density, temperature, etc.) as sum of mean part Ω and the fluctuation part ω :

$$\hat{\omega} = \Omega + \omega \quad (2.36)$$

where the mean part is defined by the integral:

$$\Omega(\bar{x}, t) = \frac{1}{\delta t} \int_{t_0}^{t_0 + \delta t} \omega(\bar{x}, t) dt \quad (2.37)$$

where δt is a sufficiently long interval of time compared to the fluctuation period of variable Ω . According to the Reynolds decomposition the instantaneous velocity, temperature, pressure and enthalpy are expressed as follows:

$$\left. \begin{aligned} \hat{u}_i &= U_i + u_i \\ \hat{T} &= T + \theta \\ \hat{p} &= P + p \\ \hat{h} &= H + h \end{aligned} \right\} \quad (2.38)$$

The well known Reynolds-averaged equations can be obtained by applying the averaging operation to mass, momentum, energy and chemical species equations. The latter are reported below:

Averaged mass equation in the case of incompressible flows:

$$\frac{\partial u_j}{\partial x_j} = 0 \quad (2.39)$$

Averaged Momentum equation:

$$\rho \frac{DU_i}{Dt} = \rho \frac{\partial U_i}{\partial t} + \rho U_j \frac{\partial U_i}{\partial x_j} = \rho g_i + \frac{\partial}{\partial x_j} (\tau_{ij} - \rho \overline{u_i u_j}) \quad (2.40)$$

Averaged energy equation:

$$\rho \frac{DH}{Dt} = \rho \left(\frac{\partial H}{\partial t} + U_j \frac{\partial H}{\partial x_j} \right) = \rho \dot{q}_g + \frac{\partial P}{\partial t} + \frac{\partial}{\partial x_i} (U_j \tau_{ij}) + \frac{\partial}{\partial x_j} \left(\lambda \frac{\partial T}{\partial x_j} \right) \quad (2.41)$$

Averaged equation for single chemical species:

$$\rho \frac{DC}{Dt} = \rho \left(\frac{\partial C}{\partial t} + U_j \frac{\partial C}{\partial x_j} \right) = \rho \dot{r} + \frac{\partial}{\partial x_j} \left(D \frac{\partial C}{\partial x_j} - \rho \overline{c u_j} \right) \quad (2.42)$$

where the terms of diffusive transport due to the turbulence are represented by:

$$\tau_{ij} = \rho \overline{u_i u_j} \text{ turbulent stress tensor}$$

$$\rho c_p \overline{\theta u_j} = q_s \text{ turbulent heat flux vector}$$

$$\rho \overline{c u_j} = m_i'' \text{ turbulent mass flux vector of the individual chemical species}$$

It can be noted that the above Reynolds averaged equations contain unknown variables as a consequence of the averaging operation [69]. In order to close the set of equations, these variables require additional equations to derive the solution for the turbulent flow field. This issue is well known as ‘‘Turbulence closure’’ problem. Further algebraic or differential equations have to be added to the Reynolds averaged equations. A set of mathematical equations involving the unknown

variables, resulting from the averaging operation, is usually called closure model for the turbulence.

Two different types of closure models are mainly adopted:

- ✓ First Order closure models, i.e. Eddy Viscosity/Diffusivity Models (EVM);
- ✓ Second Moment Closure models (SMC).

Concerning the first order closure models, the turbulent stress tensor depends on the turbulent viscosity (the so called Eddy viscosity) and on the gradient of average velocity; for the second order closure models, transport equations are solved for the individual turbulent flux of momentum and scalars which appear in the mean flow equation. Second order models are expensive with respect to the first order models. Consequently, the latter models are often employed for 3D CFD simulations of turbulent flows in many industrial applications, including the automotive ones. Even if various forms of eddy viscosity model exist, the widely adopted is represented by the two equations Standard k-ε model. In this case, transport equations for turbulent kinetic energy k and dissipation rate ε are solved. The equations of Standard k-ε model can be applied for near equilibrium flows and characterized by high Reynolds numbers:

$$\rho \frac{Dk}{Dt} = \rho \frac{\partial k}{\partial t} + \rho U_j \frac{\partial k}{\partial x_j} = P + G - \varepsilon + \frac{\partial}{\partial x_j} \left(\mu + \frac{\mu_t}{\sigma_k} \frac{\partial k}{\partial x_j} \right) \quad (2.43)$$

$$\rho \frac{D\varepsilon}{Dt} = \left(C_{\varepsilon 1} P + C_{\varepsilon 3} G + C_{\varepsilon 4} k \frac{\partial U_k}{\partial x_k} - C_{\varepsilon 2} \varepsilon \right) \frac{\varepsilon}{k} + \frac{\partial}{\partial x_j} \left(\frac{\mu_t}{\sigma_\varepsilon} \frac{\partial \varepsilon}{\partial x_j} \right) \quad (2.44)$$

P represents the term of production of turbulent kinetic energy k, due to the deformation of the mean flux [69], G is the production or destruction of turbulent kinetic energy k due to mass forces (gravity):

$$P = -2\mu_T S : S - \frac{2}{3} [\mu_T (trS) + k] (trS) \quad (2.45)$$

$$G = -\frac{\mu_T}{\rho \sigma_\rho} \nabla \rho \quad (2.46)$$

S represents the strain tensor. Finally, the constant values of k-ε model are recommended by Launder and Spalding (1974) and they are reported in Table 2.2.

Cμ	Cε ₁	Cε ₂	Cε ₃	Cε ₄	σ _k	σ _ε	σ _ρ
0.09	1.44	1.92	0.8	0.33	1	1.3	0.9

Table 2.2 – Constants of k-ε turbulence model.

2.4.1 0D/3D hierarchical approach for turbulence modeling

It is commonly recognized that for ICEs applications, 3D turbulence models are capable to describe the evolution of the in-cylinder flow field and the sub-sequent combustion process with good accuracy. However, 3D models require too high computational time to analyze the in-cylinder flow characteristics, turbulence levels and the engine performance for the whole operating domain. On the other hand, this task is easily accomplished by 1D codes, where, the combustion process is usually derived from experimental in-cylinder pressure measurements (Wiebe correlation). This method is poorly predictive for the simulation of operating conditions relevantly different from the experimental ones. To overcome the above issue, 1D code has to include enhanced physical models for the description of in-cylinder turbulence evolution and combustion. Referring to the phenomenological turbulence sub-model to be implemented in 1D engine model, once it has been fully developed, a proper tuning is required. To this aim, reference in-cylinder turbulent variables are needed and they are not easily derived by experimental tests. On the contrary, the turbulence phenomenological model can be validated against in-cylinder results provided by 3D CFD analysis carried out for a limited number of engine operating conditions. In the latter case, a hierarchical 1D/3D approach for the description of in-cylinder turbulence is identified. Indeed, information from 3D CFD analyses, in terms of temporal evolution and spatially averaged in-cylinder flow fields, both mean and turbulent, are utilized to set-up and calibrate the phenomenological 0D turbulence model. The discussed methodology, once tuned, shows the potentialities to accurately estimate the temporal evolution of the in-cylinder turbulence according to the engine operating conditions with reduced computational time.

2.5 0D Turbulence modeling: K-k model

A 0D turbulence model aiming to synthesize very complex 3D phenomena based on the assumption that turbulence is both homogenous (i.e. equally distributed in the space) and isotropic (i.e. without a preferential direction in space). Several 0D turbulence models are available in the technical literature. The so called K-k model family describes the energy cascade mechanism from the average flow field kinetic energy (K) to the turbulence fluctuation kinetic energy (k) by an ordinary derivative two-equation system [75]. In other cases, macro-scale kinetic energy is imposed [76], while balance equations are solved for the turbulence fluctuation kinetic energy and the dissipation rate [77], [78]. Further approaches require the computation of the ordinated flow fields (swirl and

tumble), apart from the turbulent kinetic energy and the dissipation rate [79], [80]. Referring to K-k turbulence model, it describes the temporal rates of the mean and turbulent kinetic energies as reported in equations (2.47), (2.48):

$$K = \frac{1}{2}m_{cyl}U_{flow}^2 \quad \frac{dK}{dt} = \left(\frac{dK}{dt}\right)_{valve} - P_K + c_{tumb,K}K \frac{\dot{\rho}_{cyl}}{\rho_{cyl}} - K \frac{\dot{m}_{ex}}{m_{cyl}} + K \frac{u_{pist}}{\bar{u}_{pist}} \frac{du_{pist}}{\bar{u}_{pist}} \quad (2.47)$$

$$k = \frac{3}{2}m_{cyl}u'^2 \quad \frac{dk}{dt} = \left(\frac{dk}{dt}\right)_{valve} + P_k + c_{tumb,k}k \frac{\dot{\rho}_{cyl}}{\rho_{cyl}} - k \frac{\dot{m}_{ex}}{m_{cyl}} - D \quad (2.48)$$

The first term in both equations accounts for the kinetic energy produced by the flow through the valves (both intake and exhaust). P_K and P_k represent the K decay and the k production term, respectively. In both the equations, the third term accounts for the kinetic energy production due to the piston motion close to compression TDC; in particular, in equation (2.47), this term mimics the tumble macro-vortex compression responsible for the increase of the mean-flow velocity, while, in equation (2.48), it simply describes an isotropic compression according to the theory [81], [82]. The compression terms are multiplied by the constants, $c_{tumb,K}$ and $c_{tumb,k}$, respectively. They depend on a single tuning constant, c_{tumb} , and on the maximum valve lift, h_{max} according to:

$$c_{tumb,k} = c_{tumb} * h_{max} \quad c_{tumb,K} = \frac{1}{3}c_{tumb,k} \quad (2.49)$$

The fourth terms accounts for the convective flow through the exhaust valves. Last term in equation (2.47) takes into account the effects of piston motion, at velocity u_{pist} , on the mean flow field. As shown below, this contribution is relevant especially during the expansion stroke, while in the remaining portion of the cycle it is masked by the other effects. The D term in equation (2.48) is the dissipation rate of k into heat, derived as follows:

$$D = m_{cyl}\varepsilon \quad \varepsilon = 0.09^{3/4} \frac{k^{3/2}}{L_T} \quad (2.50)$$

L_T being the integral length scale. The production term related to the flow through the valves in equation (2.47) is calculated as:

$$\left(\frac{dK}{dt}\right)_{valve} = \left(c_{in} \frac{1}{2} \dot{m}_{in} u_{in}^2 + c_{ex} \frac{1}{2} |\dot{m}_{ex}| u_{ex}^2\right) + c_{inv} \frac{1}{2} \dot{m}_{ex} u_{cyl}^2 \quad (2.51)$$

being \dot{m}_{in} , \dot{m}_{ex} , u_{in} , and u_{ex} the mass flow rates and the flow speeds through the intake and the exhaust valves, respectively. The above terms are taken into account only when the gas flows from the ports towards the cylinder (i.e. direct intake flow and reverse exhaust flow). Direct flow through the exhaust valve is indeed considered in the last term, with reference to an exhaust flow related mean velocity u_{cyl} , evaluated as follows:

$$u_{cyl} = \frac{\dot{m}_{ex}}{\rho_{cyl} A_{pist}} \quad A_{pist} = \frac{\pi B^2}{4} \quad (2.52)$$

Concerning the equation of turbulent kinetic energy (2.48), the valve related production term is more simply computed as:

$$\left(\frac{dk}{dt}\right)_{valve} = \frac{k}{K} \left(c_{in} \frac{1}{2} \dot{m}_{in} u_{in}^2 + c_{ex} \frac{1}{2} |\dot{m}_{ex}| u_{ex}^2 \right) \quad (2.53)$$

c_{in} , c_{ex} and c_{inv} parameters in equations (2.51) and (2.53) are tuning constants; the only one given as an input is c_{in} , while the others are derived from:

$$c_{ex} = 0.1 * c_{in} \quad c_{inv} = c_{in} \quad (2.54)$$

The terms P_K and P_k are calculated according to:

$$P_K = c_{pkap} \frac{K}{t_K} \quad P_k = c_{pkey} \frac{k}{t_k} \quad (2.55)$$

c_{pkap} and c_{pkey} being additional tuning constants. t_K and t_k are the characteristic time scales of K decay and of k production, evaluated as:

$$t_K = \frac{L_T}{U_{flow}} \quad t_k = \frac{L_T}{u'} \quad (2.56)$$

Previous investigations [26] showed that the time evolution of the integral length scale L_T is only slightly depending on engine operating conditions. It can be hence prescribed as an assigned sequence of Wiebe-like functions (see 0D turbulence model validation in chapter 3). The control points of these equations are given as an input; they represent additional tuning constants for the turbulence model.

As said before, information from 3D CFD analyses, in terms of the in-cylinder mean and turbulent flow fields, are utilized to set-up and calibrate the examined turbulence model. In particular, the mass averaged integral length scale, specific turbulent kinetic energy and mean flow kinetic energy, equation (2.57) are calculated all over the 3D domain.

$$L_T = \frac{\sum_{CYL-CELL} \rho_i V_i L_{T,i}}{\sum_{CYL-CELL} \rho_i V_i} \quad TKE = \frac{\sum_{CYL-CELL} \rho_i V_i k_i}{\sum_{CYL-CELL} \rho_i V_i} \quad MKE = \frac{\sum_{CYL-CELL} \frac{1}{2} \rho_i V_i U_i^2}{\sum_{CYL-CELL} \rho_i V_i} \quad (2.57)$$

ρ_i , V_i , U_i , k_i , and $L_{T,i}$ are the density, the volume, the mean flow velocity, the specific turbulent kinetic energy and the integral length scale within the i -th cell, respectively. $L_{T,i}$ is defined as a function of the local dissipation rate ε_i , while the mean flow velocity accounts for its three local components, u_i , v_i , w_i :

$$L_{T,i} = 0.09^{3/4} \frac{k_i^{3/2}}{\varepsilon_i} \quad U_i = \sqrt{u_i^2 + v_i^2 + w_i^2} \quad (2.58)$$

In order to compare 3D and 0D results, the following 3D-derived mean flow and turbulent velocities are defined:

$$u'_{3D} = \sqrt{\frac{2}{3} TKE} \quad \rightarrow \quad U_{flow,3D} = \sqrt{2MKE} \quad (2.59)$$

CHAPTER 3

Engine Model Validation

3.1 0D-1D Models Description

A one-dimensional model of the considered engine has been developed with the aim to faithfully reproduce the behavior of different engine parts. The commercial software adopted for 1D fluid-dynamic simulation of the considered engine is the well-known GT-Power™ software of *Gamma Technologies*. Single parts of the engine system will be deeply described in the following, including intake/exhaust sub-systems, turbocharger group, intercooler, injection system, cylinders, valves and User *Subroutines*. The latter have been employed to include the user sub-models within the whole engine model.

3.1.1 Air Intake System

As shown in Figure 3.1 the ‘Air Intake system’ is made up of the elements between the external ambient and the Compressor inlet. The considered system is reproduced by:

- ✓ the intake (ambient) environment with air temperature at 20°C;
- ✓ seven pipes located upstream the air-filter box; they allow the ambient air to be introduced into the filter box component;
- ✓ air-filter box, which is modeled by two “Flow-Split” objects (IN and OUT);
- ✓ five pipes, located downstream the filter box (convergent section up to the Compressor inlet). They allow the clean air to be elaborated by Compressor.

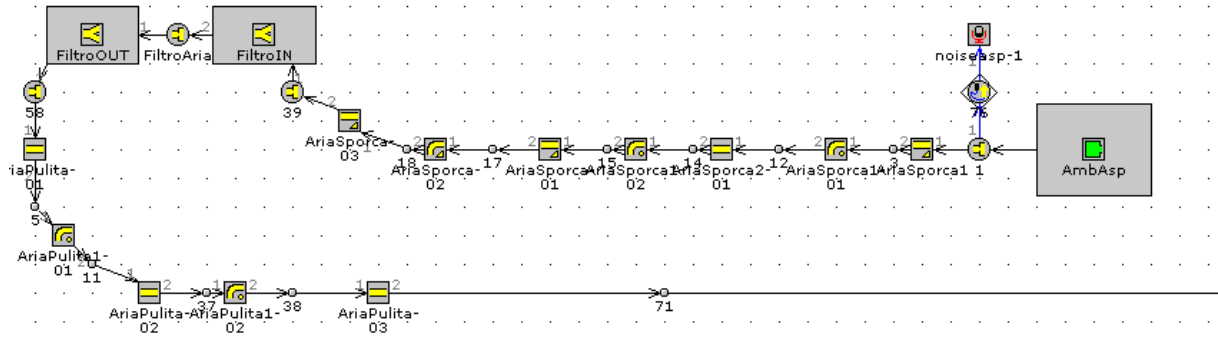


Figure 3.1 – Air Intake System including the filter box.

3.1.2 Compressor

The air flow is introduced at Compressor inlet through a proper air intake system described before. Compressor performances are reproduced by adopting a “Map Based” approach. In particular, the experimental compressor maps, in terms of pressure ratio (Figure 3.2a) and efficiency (Figure 3.2b) as a function of corrected mass flow rate are specified for this component by “Map object attribute”. As known, a proper mechanical link between Compressor and Turbine components is considered through the object named ‘Alberino Turbo’ (Figure 3.3).

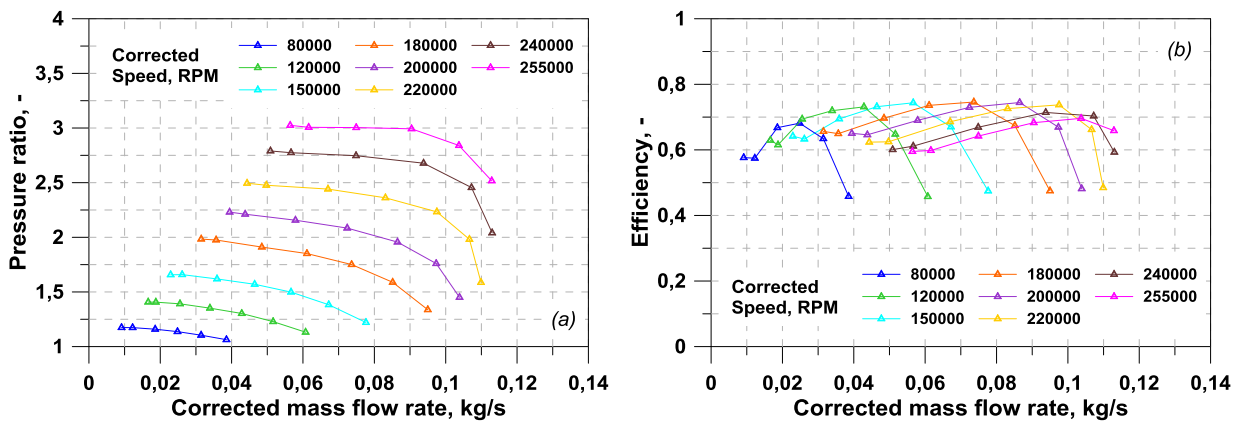


Figure 3.2 – Compressor pressure ratio map (a) and Compressor efficiency map (b).

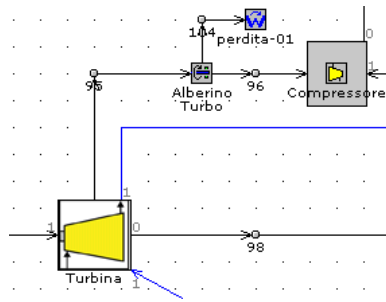


Figure 3.3 – Turbocharger group schematization.

3.1.3 Intercooler

The air compression involves an increase in the air temperature and a reduction in the air density. In addition, the exhaust gas processed by the turbine causes a further increase in the air temperature within the intake system, because of the heat exchange. Consequently, a reduced engine filling has to be expected. Intercooler represents a system which allows for a reduction in the air temperature, through a proper cooling circuit. Consequently, an increase in the air density and improved engine filling performances are obtained. The engine model includes an intercooler device which is properly schematized. The inlet and outlet pipes of intercooler object are modeled, too. Inlet pipes connect the compressor outlet to the intercooler while the outlet pipes allow the intake manifold to be reached by the air flow. The actual intercooler is schematized as a simple pipe of rectangular section, presenting a wall temperature equal to 50°C.

3.1.4 Intake Manifold and Runners

The air flow at intercooler outlet is introduced within the intake manifold through the throttle valve. The latter presents a reference diameter of 57.5 mm while the throttle angle can be controlled in order to obtain a prescribed load level. For this type of engine, load level can be also adjusted by controlling the intake valve lift profile. The intake manifold located downstream the throttle valve is schematized by two volume elements (named “*FarfallaRunner*” and “*Runner2*”), presenting 0.85 liters and 0.67 liters, respectively. In addition, proper Runners (named *Runner1_1*, *Runner1_2*, *Runner2_1*, *Runner2_2*) allow the air flow to be directed towards the engine cylinders. Runners

showed in Figure 3.4 are characterized by converging section and each of them presents a total length equal to 34 mm.

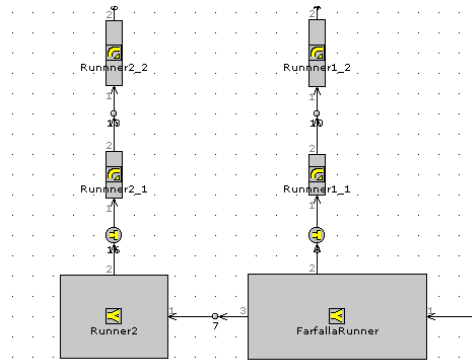


Figure 3.4 – Intake Manifold and Runners.

3.1.5 Intake pipes and Fuel Injectors

Fuel injection is realized within the intake system through proper injectors, located at junction elements (named “FSAsp_IT_R1” and “FSAsp_IT_R2” in Figure 3.5) for the pipes at cylinder entrance. Starting from the single junction element, the gas flow is splitted in two different intake pipes, allowing the air-fuel mixture to enter into the cylinder. For the single injector (named ‘Iniettore’), the following parameters have to be specified: average speed of injection, air-to-fuel ratio, injection timing angle, fuel temperature (equal to 50°C), type of fuel and fraction of vaporized fuel.

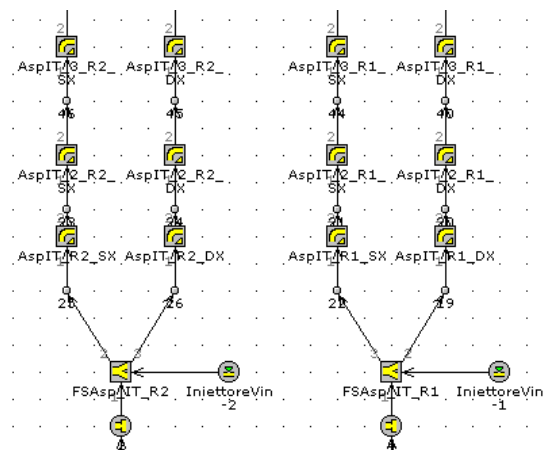


Figure 3.5 – Intake Pipes and fuel injectors.

3.1.6 Engine Cylinders and Intake/Exhaust Valves

As stated before, the engine under study presents a port fuel injection system and once the air-fuel mixture is formed, thanks to the interaction of the air flow with the injected fuel, it is introduced into the cylinder through intake valves while the exhaust gases are discharged by exhaust valves. As shown in Figure 3.6, two intake and exhaust valves are specified for each cylinder. Cylinders and valves allow the engine thermodynamic cycle to be realized.

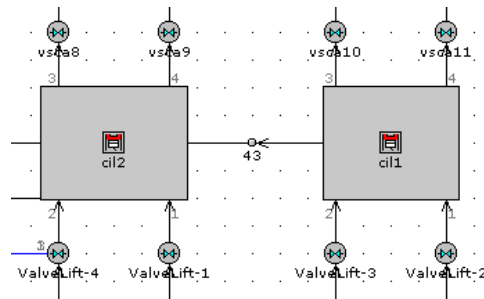


Figure 3.6 – Engine cylinders and valves.

Concerning the intake valves, the reference diameter (diameter equal to 26 mm) and the lift profile have to be specified. Since the examined engine is equipped with a VVA system at the intake side, the intake valve lift profile is defined through a proper ‘user model’ named “ValveLift”. Instead, the exhaust valves present fixed valve timing and a lower reference diameter (21.5 mm). Referring to the cylinder object, turbulence, combustion, heat transfer, fuel evaporation and knock models have to be defined. All the above models represent user sub-models.

3.1.7 Exhaust system and Turbine Object

As shown in Figure 3.7 the exhaust gases, coming out from the valves of each cylinder, are introduced into the exhaust manifold through two pipes. Each exhaust pipe is schematized by two elements (as an example, “ScaIT_R1_DX” and “ScaIT_R1_DX-1” for cylinder #1). The exhaust manifold allows the flow connection of two exhaust branches in order to direct the exhaust flow at turbine inlet through a single pipe named ‘MonteTurbo’.

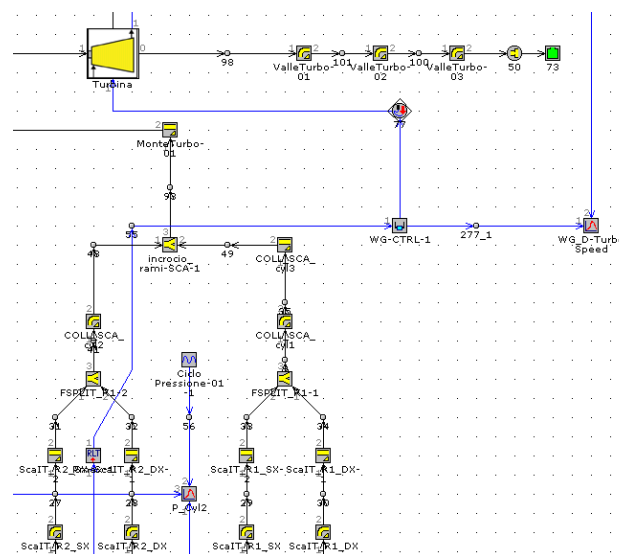


Figure 3.7 – Exhaust Manifold and Turbine.

Similarly to the Compressor object, turbine performances are modeled by adopting a “Map Based” approach. The reduced turbine maps in Figure 3.8 are obtained by experimental tests and they are employed within the 1D engine model. Turbine model shows flow connections, the mechanical link with Compressor object and the connection with the Waste-gate valve controller. The latter is utilized to adjust the waste-gate diameter in order to reproduce the experimental value of the in-cylinder peak pressure in WOT operation. Instead, at part load operation the prescribed load level is obtained by controlling the throttle valve angle.

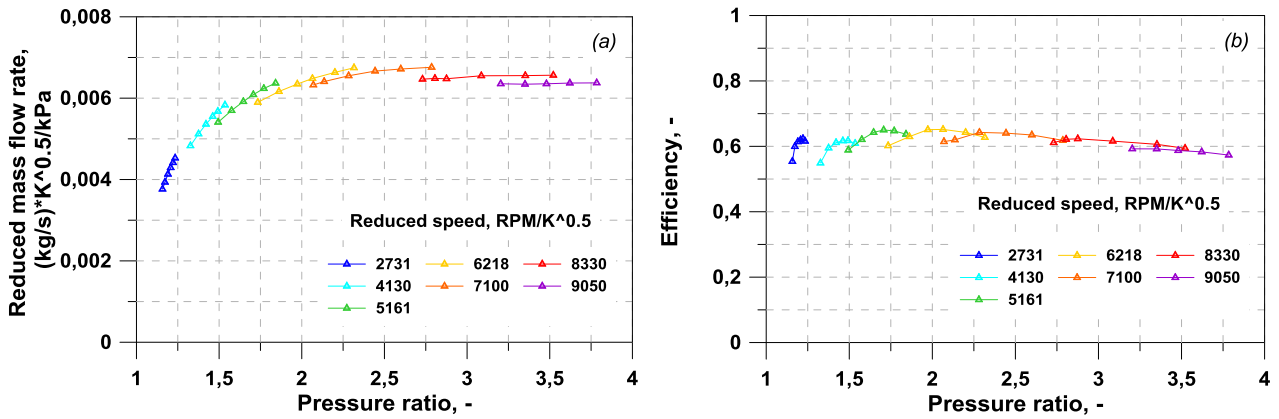


Figure 3.8 – Turbine pressure ratio map (a) and turbine efficiency map (b).

3.1.8 Model Subroutines

1D engine model presents different *UserSubroutines*, whose output are used both during data processing both during simulation phase. *UserSubroutine* object allows the model to invoke an externally developed routine. It is adopted to transfer the processed signals between GT-Power model and routines. Routine input signals can be control signals or parameters defined in the object *UserModel*. Output values of *UserSubroutine* can be sent to other control objects or to *RLTcreator*.

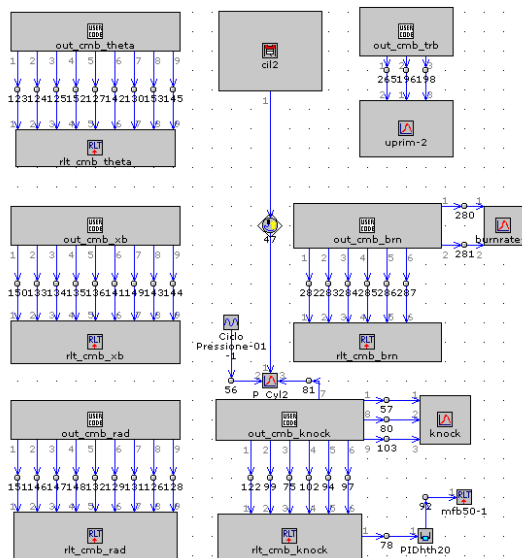


Figure 3.9 – Model Subroutines.

The above Figure 3.9 shows the *Subroutines* reported in the model. They recall the fractal combustion model and the corresponding data are sent to other objects to be processed. In particular, these *Subroutines* allow to evaluate several parameters, including characteristic combustion angles, burned mass fractions at the above angles, burn rate $\frac{dm_b}{d\theta}$, knock index, angle of knock occurrence, volume chamber at knock occurrence V_{knock} , mass fraction which instantly burns at knock occurrence, burned gas temperature T_b , unburned gas temperature T_u , etc.

3.2 0D Turbulence model validation

Turbulence model is tuned against 3D-CFD motored findings for different speeds and intake valve closure angles typical of full and part load operations, as well (Table 3.1).

Case Number	Engine speed, rpm	Intake valve closure angle, deg after CTDC	Label
1	2500	560	2500FL
2	5100	548	5100FL
3	2000	462	2000PL
4	3000	448	3000PL

Table 3.1 – Tested engine points.

First of all, a reliable time evolution of the integral length scale must be assigned. This is done by employing a sequence of Wiebe-like functions passing through specified control points. In particular, 3D results show that the mass averaged L_T , starting from a very low TDC level, L_{T3} , continuously increases during the intake stroke and reaches its maximum during the compression stroke. The location of the above maximum is prescribed in the 0D model in terms of angular position, $\Delta\theta$, and height, L_{T2} . Then, the integral scale reduces, reaching a minimum at the compression TDC (L_{T1}). During the expansion and exhaust strokes, L_T mainly follows the in-cylinder height above the piston, increasing once again up to the L_{T2} level at the expansion BDC and reducing down to the L_{T3} level at the valve overlap TDC.

Figure 3.10 shows the above described phases, connected through a sequence of Wiebe-like functions. Parameters L_{Tj} , ($j=1, 2, 3$), and $\Delta\theta$ represent of course, further unknown constants.

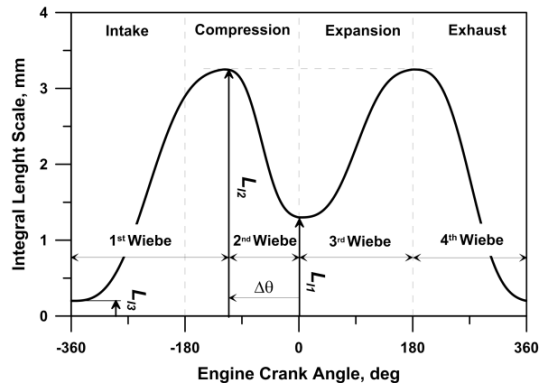


Figure 3.10 – Integral length scale reconstruction.

L_{T1}	1.3 mm	L_{T2}	3.25 mm	L_{T3}	0.2 mm	$\Delta\theta$	120 deg
c_{in}	0.7	c_{tumb}	0.19	c_{pkey}	0.03	c_{pkap}	0.05

Table 3.2 – Optimal values of turbulence model constants.

Once the integral length scale is formally identified, each tuning constant of the 0D model has to be set to fit the actual results provided by the 3D-CFD calculations [83]. Through a simple trial and error procedure, a single set of optimal constants is selected as listed in Table 3.2.

It is not worthless to emphasize that, for all the considered cases, the tuning constants are kept unchanged to demonstrate the generality of the proposed model.

Figure 3.11 shows the comparison between 3D and 0D results, for the integral length scale and for all the operating points. For sake of clarity, the attention is focused on the intake, compression and half expansion stroke portion of the cycle. The agreement is satisfactory for all the cases. It is confirmed that the trends of 3D computed integral length scale depend only slightly on the engine operating conditions, especially in the neighbourhood of the compression TDC. This allows the use a unique L_T reconstruction for all the considered operating points.

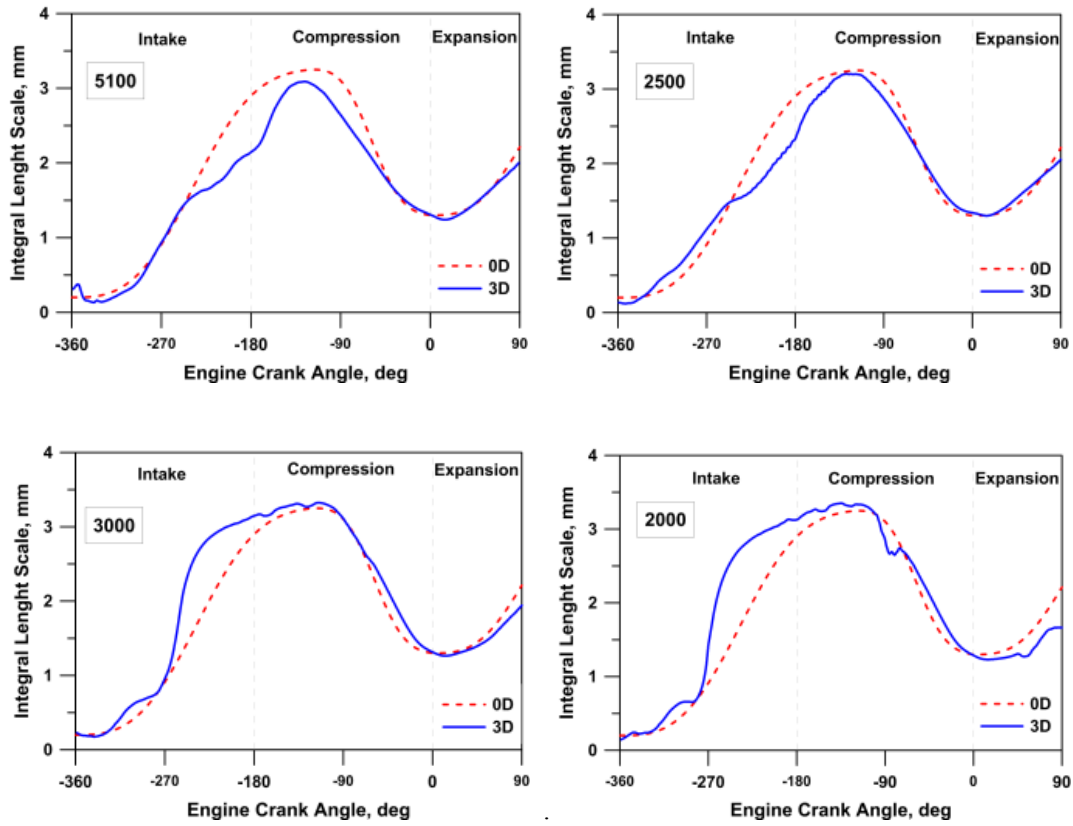


Figure 3.11 – 0D/3D comparison of the integral length scale.

Figure 3.12 highlights that the proposed model is able to forecast the in-cylinder turbulence levels during the combustion relevant portions of the cycle, i.e. intake, compression and expansion phases. This mainly depends on the model capability to sense the different durations of the intake phases for the considered cases. The different turbulence levels at the compression TDC are very well predicted thanks to the compression term in turbulent kinetic energy equation, which properly accounts for the different valve lift profiles, mainly through the maximum lift correction term included in the definition of the tuning constant $c_{tumb,k}$.

The turbulence fluctuation (Figure 3.12) and the mean flow velocity (Figure 3.13) are normalized with the piston mean speed.

Since equations of 0D turbulence model are strongly coupled, it is also important to verify the accuracy in the prediction of the mean flow velocity, reported in Figure 3.13. It can be appreciated that a good agreement is reached, especially during the compression and expansion strokes.

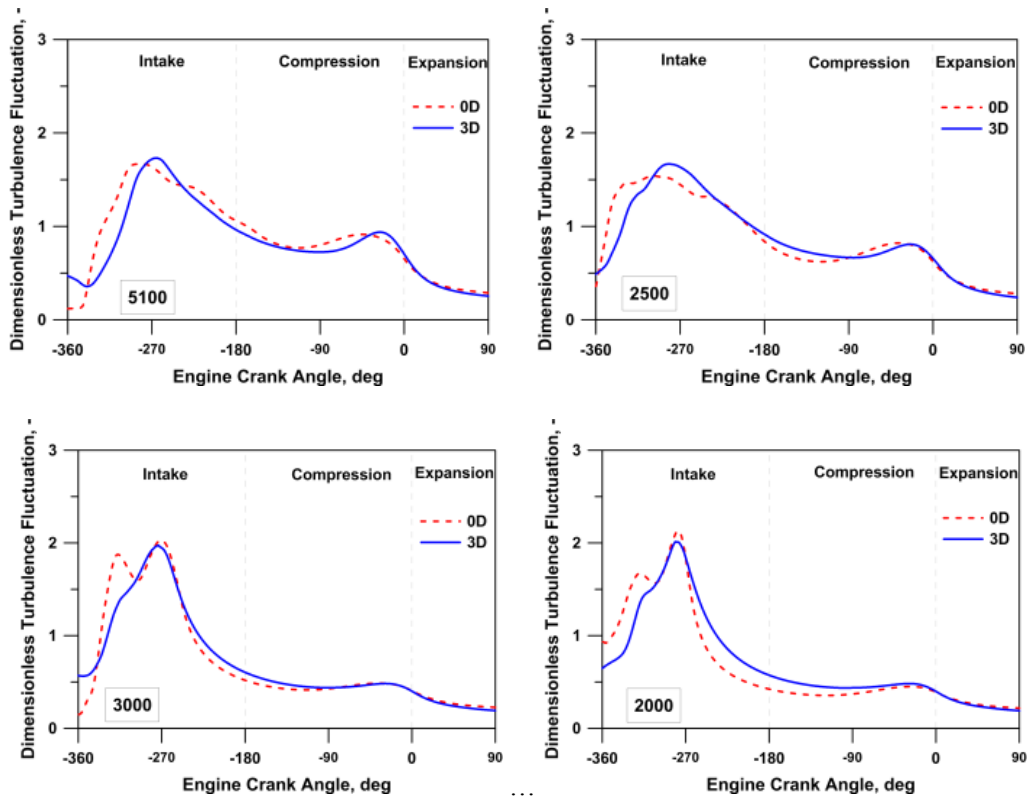


Figure 3.12 – 0D/3D comparison of the dimensionless turbulence fluctuation.

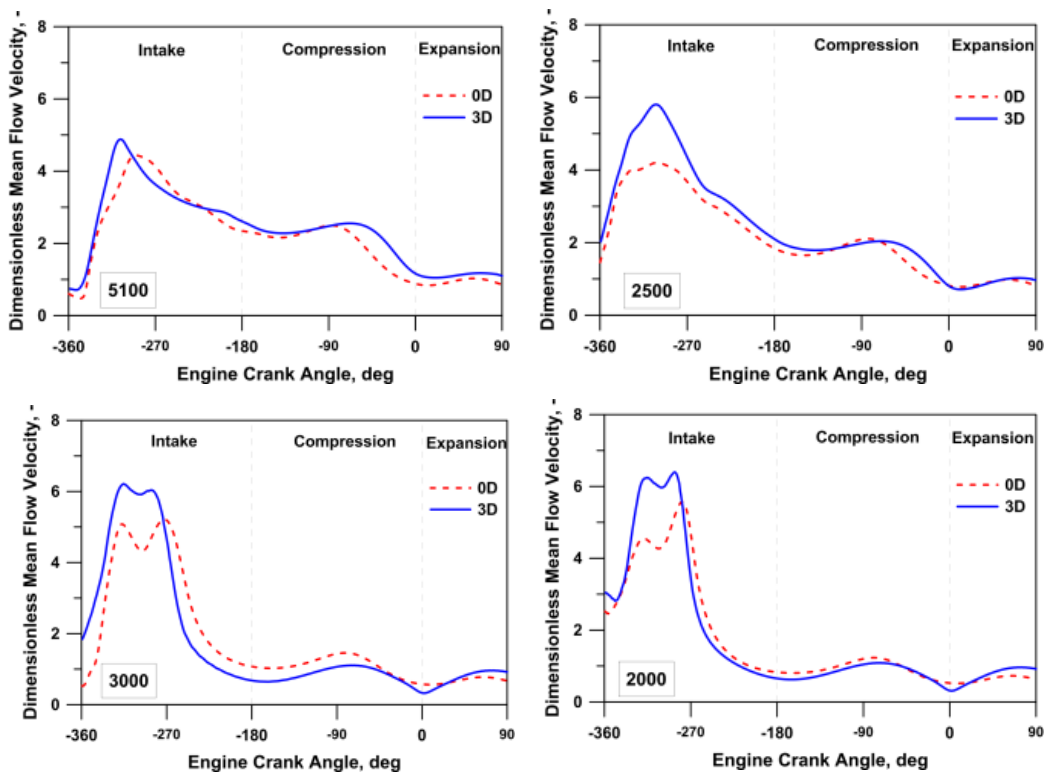


Figure 3.13 – 0D/3D comparison of the dimensionless mean flow velocity.

Concerning the compression stroke, the density-dependent term of the equation for mean kinetic energy is able to capture the local maximum before TDC, while the local maximum during the expansion is described by the term related to the piston movement.

Simultaneously looking at Figure 3.11, Figure 3.12 and Figure 3.13 it is demonstrated that the 0D turbulence model successfully describes the energy cascade mechanism from the mean to the turbulent flow and it represents the basis for an accurate development of the combustion model.

3.3 Engine Model Tuning at Full Load Operation

The operating parameters given as an input to the GT-PowerTM engine model are the intake valve closure, the A/F ratio and the spark advance. Since information about the experimental turbine waste-gate valve openings are not available, the latter have to be indirectly evaluated using a PID controller and a target experimental datum, like the boost level, the mass flow rate or the turbocharger speed. The adoption of the experimental boost level may introduce some inaccuracies in the simulations, since at low-speed/full-load the compressor operates in close-to-surge map region, where iso-speed slopes are very reduced. Consequently, the map-derived mass flow rate cannot be precisely identified. On the other hand, the experimental mass flow rates or the turbocharger speeds are usually affected by higher uncertainties. For this reason, an alternative strategy is proposed, aiming to identify the waste-gate opening realizing the experimental pressure level at the firing TDC for the cylinder #2. This level is in fact representative of the actual in-cylinder filling conditions since, at full-load, the combustion process, to avoid knocking combustions, always begins after the TDC. The proposed strategy provided the best agreement with experimental data.

c_{wrk}	0.5	c_{trans}	0.4	c_{wc}	0.8	c_{enh1}	0.5	c_{enh2}	0.1
-----------	-----	-------------	-----	----------	-----	------------	-----	------------	-----

Table 3.3 – Combustion model tuning constants.

Results shown in Figure 3.14 are obtained after the tuning of the combustion model parameters (Table 3.3). They are kept constant for each analyzed operating condition. In particular, the Figures show the numerical/experimental comparison in terms of brake power, brake torque, air mass flow rate, BSFC and turbocharger speed. The agreement of the engine overall performance is satisfactory, with the exception of the higher engine speeds. This is probably due to uncertainties in the Amesim-computed lift profiles, affecting the volumetric efficiency and the pumping work. In

addition, because of the two-cylinder arrangement, large mass flow rate and pressure ratio oscillations are expected. Engine-turbocharger matching is hence a critical issue for this engine, since a strongly unsteady operation is expected for the turbocharger. This may also affect BSFC predictions at higher engine speeds.

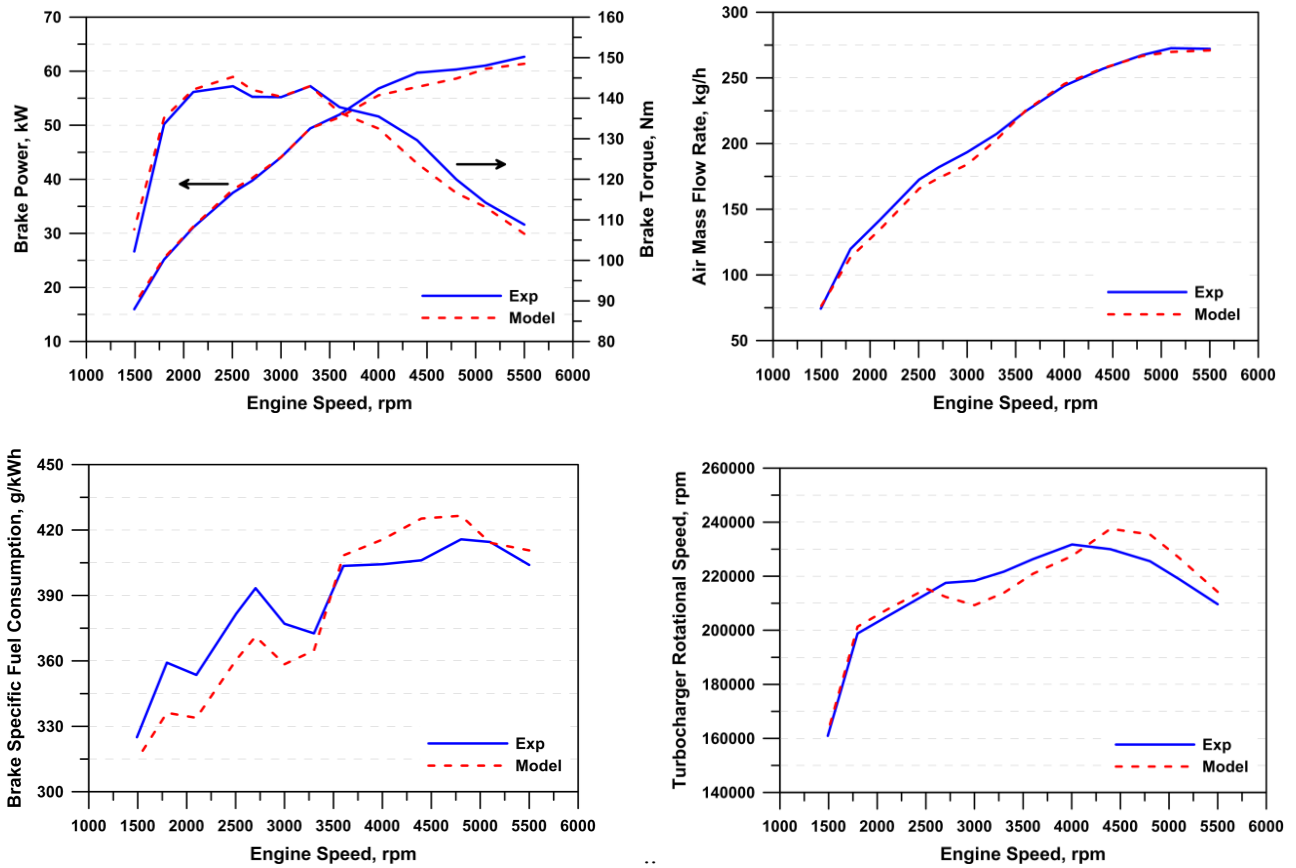


Figure 3.14 – Engine performance at full load: 1D numerical/experimental data comparison.

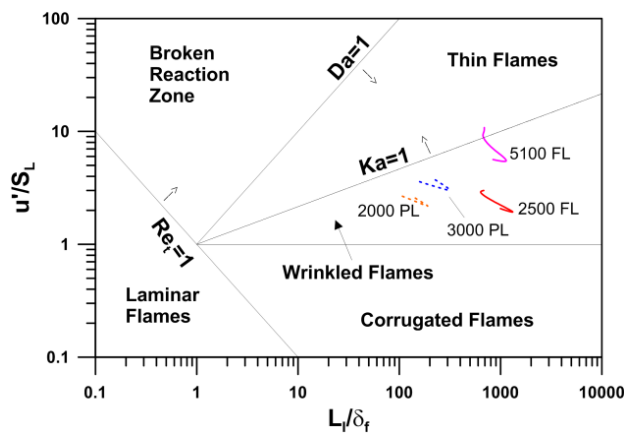


Figure 3.15 – Borghi Diagram.

In order to verify that model results are consistent with the theoretical hypotheses, the combustion regime establishing at different engine speeds is analyzed. This can be accomplished looking at two typical dimensionless parameters extracted from the simulations, namely the ratio between the integral length scale and the flame thickness, L_T/δ_f , and the ratio between the turbulent intensity and the laminar flame speed, u'/S_L . These parameters are reported on the well-known Borghi Diagram in Figure 3.15, identifying the different combustion regimes occurring at different Reynolds, Karlovitz and Damkholer numbers, [84].

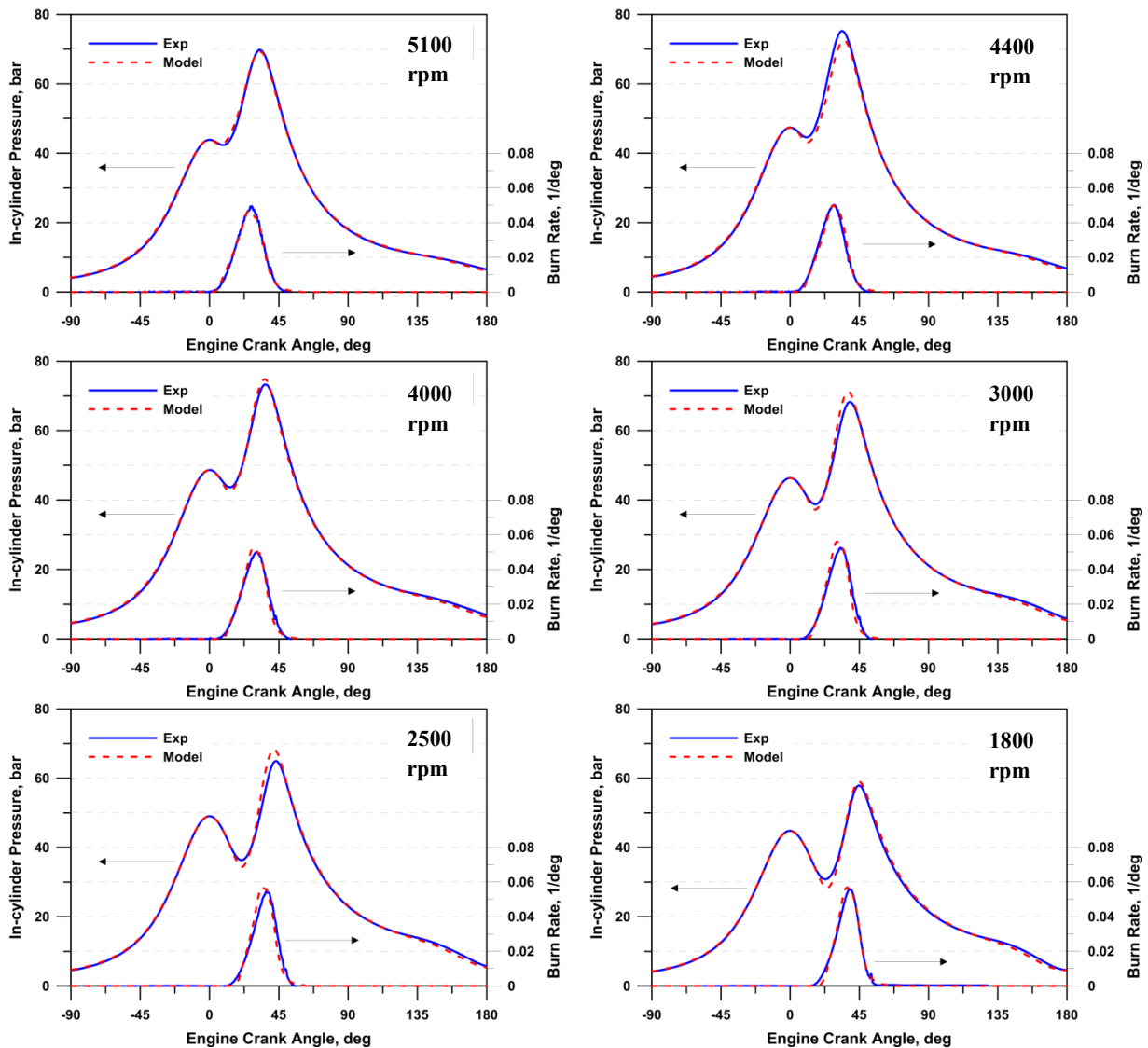


Figure 3.16 – Numerical/Experimental comparison of the in-cylinder pressure cycle and burn rate.

It is verified that, at each speed-load condition, the instantaneous trajectory on the Borghi plane always belongs to the wrinkled-flamelets regime, with the exception of the highest speed, where a local $Ka > 1$ value may occur at the beginning of the combustion process. At spark time, in fact, u'

is still high, while S_L is reduced, due to intense flame stretch at small flame radius. Correction in equation (2.34) roughly takes into account the above phenomena.

Figure 3.16 shows the experimental/numerical comparison of pressure cycles and burn rates for various engine speeds, during the compression and combustion/expansion phases. Especially at low engine speeds, the spark timing occurs late after the TDC, determining the displayed double-peak pressure cycles; this choice, although hardly penalizing IMEP and BSFC, is necessary to avoid knocking occurrence. Anyway, the accuracy of the in-cylinder pressure cycle prediction is very high. Burn rates are also very well predicted, and the model properly describes the initial and the final combustion evolutions.

3.4 Engine Model Validation at part load

After the above described tuning process at full load, the capability of the model in predicting the engine performance in terms of BSFC at part load is tested. In this case, the simulations are carried out by imposing the experimentally actuated spark advance, the air-to-fuel ratio and the early intake valve strategy (*EIVC*). The latter is qualitatively depicted in Figure 3.17. As can be observed, the advanced closure is also coupled to a reduction of the maximum lift, with respect to the *Full-Lift* profile (lost-motion principle).

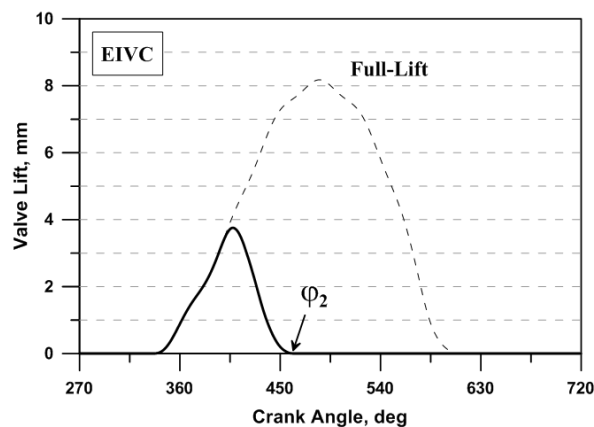


Figure 3.17 – *EIVC* valve lift profile.

The waste-gate opening is instead automatically selected by a PID controller aiming to reproduce the measured turbocharger rotational speed, while the throttle opening targets the predefined loads. Figure 3.18, Figure 3.19 and Figure 3.20 show the fuel consumption variation against the BMEP, for different engine speeds. It can be observed that the numerical results are in a very good

agreement with the measurements, especially for the low-medium loads. Thanks to the *EIVC* strategy, the fuel consumption levels are substantially low and they only increase at very low loads. This is mainly due to a more relevant incidence of the pumping losses, and to a worsening of the combustion process efficiency, as well. The reduced intake phase duration (Figure 3.17) in fact produces a moderate turbulence level at the compression TDC, coupled to the well-known syringe effect. Both affect the combustion speed, mainly during its early stage. The latter phenomena are very well captured by the employed turbulence/combustion sub-models, as demonstrated by the highlighted results and by the next detailed combustion analysis. The worsening of the fuel consumption for the higher loads is indeed related to the relevant mixture enrichment necessary to decrease the exhaust gas temperature at the turbine inlet. In addition, a further penalty is determined by the specification of a reduced (sometime negative) spark advance, required to avoid knocking phenomena. Also in this case, the model shows the capability to capture the described trends, except for the engine speeds of 4400 and 5500 rpm. To further highlight the predictiveness of the combustion model at part load operations, in Figure 3.21 the angular positions of 10%, 50% and 90% of the MFB are compared with the experimental data for an engine speed of 3000 rpm. It can be appreciated that the combustion center is correctly forecasted by the model for all the considered loads with a maximum error lower than 3 degrees. The combustion duration (10-90% MFB) is well captured for the medium and higher loads, while for the lower loads it is overestimated, mainly due to a longer combustion tail. However, as shown in Figure 3.19 for the case at 3000 rpm, this error has a negligible effect on the fuel consumption prediction.

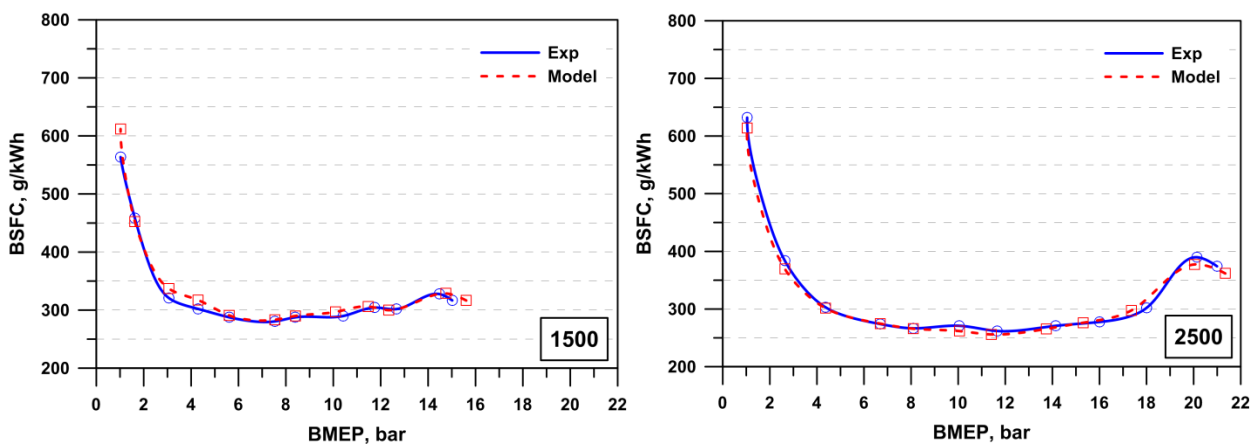


Figure 3.18 – BSFC vs. BMEP at 1500 rpm and 2500 rpm.

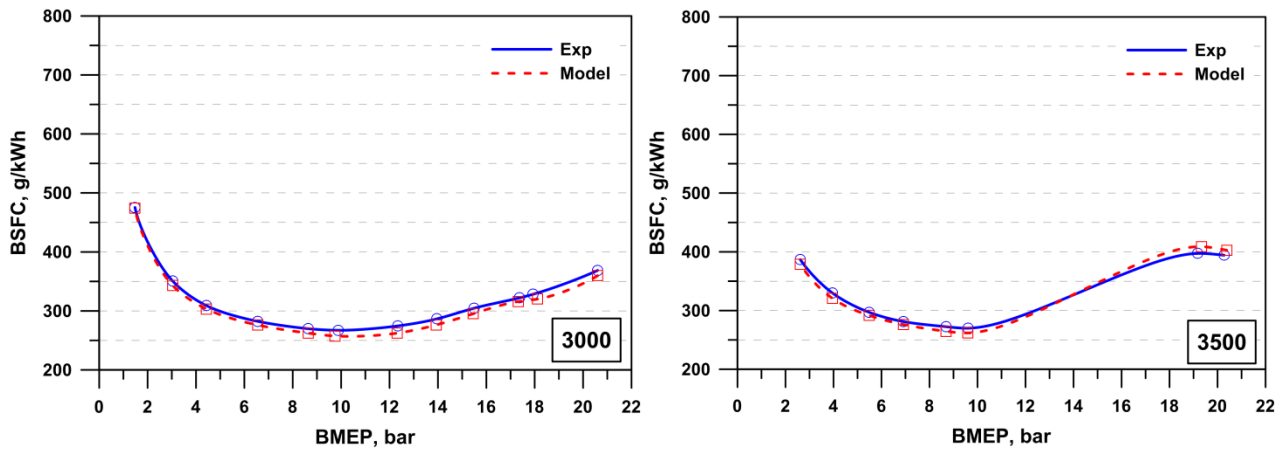


Figure 3.19 – BSFC vs. BMEP at 3000 and 3500 rpm.

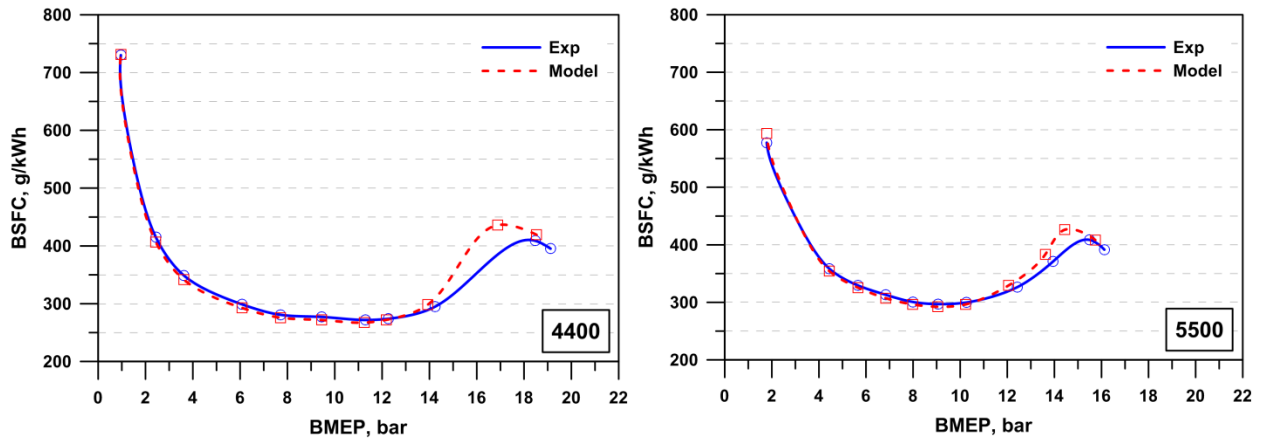


Figure 3.20 – BSFC vs. BMEP at 4400 rpm and 5500 rpm.

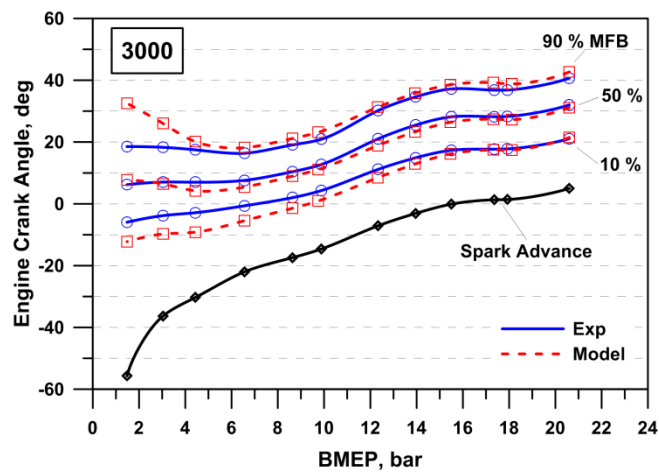


Figure 3.21 – Spark advance and 10%, 50%, 90% MFB vs. BMEP at 3000 rpm.

CHAPTER 4

Experimental Knock detection and modeling

4.1 Overview of Knock detection

It is well known that the combustion process represents a key phenomenon to be optimized during the design phase of internal combustion engine. Indeed, engine performance in terms of power output, fuel consumption and noxious emission are strongly affected by the development of the combustion process. Referring to the Spark-ignition engine, combustion process has to be properly controlled in order to avoid the abnormal combustion. Knock phenomenon arises when a portion of the fuel charge within the combustion chamber spontaneously ignites after the spark event, but before it has been reached by the flame front propagating from the spark plug position [23], [85]. This phenomenon most likely occurs within fuel charge particles burning late during the combustion process (end-gas auto-ignition). The strong heat released by the sudden oxidation of the end-gas produces a system of pressure waves moving and colliding each other within the combustion chamber, at a frequency ranging from 6 to 10 kHz [86], [87], which is sometimes audible (pinging knock).

knock represents one of the most difficult aspects to recognize and properly set up for the engine control system. If left untreated or if the engine control system does not properly recognize the knock occurrence, over time, a severe engine damage will occur. Such damage includes piston-ring failure, piston failure and valve damage, mainly due to increased cylinder temperature / pressure induced by a severe knock condition [88], [89], [90]. As shown in the current literature [9], different knock suppression methods can be adopted. However a simple way to avoid knock is to bound the compression ratio and/or the spark advance. The latter approach hardly reduces the potential in gaining a lower fuel consumption and a higher power output. As a consequence, an ideal engine control system has to be able to operate as close as possible to knocking, without really moving inside it. The above consideration is remarkably true in a “downsized” turbocharged spark-ignition engine, where the in-cylinder temperature and pressure are higher.

To avoid knock, in fact, a turbocharged SI engine always operates at full load with a particularly rich air-to-fuel ratio and a very reduced spark advance. At low speed a negative value of the spark advance is sometimes required (the combustion begins after the TDC). In these conditions, the

pressure cycle assumes a double-peak shape, like the one depicted in Figure 4.1. The first peak, located at TDC, is due to volume variation during compression-expansion strokes, while the second one is due to the combustion process. The latter hence completely develops during the expansion stroke.

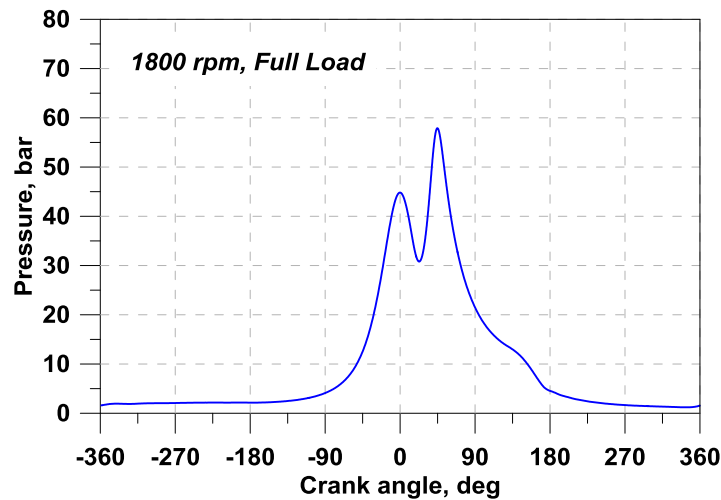


Figure 4.1 – In-cylinder pressure cycle at 1800 rpm, full load, for a turbocharged SI engine.

A negative spark advance, although hardly penalizing the fuel consumption is the only solution in these operating conditions to limit the peak temperature and pressure during combustion and avoid knocking occurrence. It is once again clear that the engine control system must be able to select the maximum allowable spark advance with the smallest knock safety margin. An additional problem is moreover related to cycle-to-cycle variations, which are commonly observed during the combustion process of a SI engine. They mainly cause unpredictable and stochastic fluctuations in the rate of heat release, turning in fluctuations in the in-cylinder pressure cycle. As a consequence, faster-than-average cycles are most likely to knock. Therefore the optimal “knock-limited” spark advance must be accurately chosen taking into account cycle-to-cycle variations [91].

From an experimental point of view, the identification of the “knock-limited” spark advance is a complicated task, requiring the measurement of numerous instantaneous pressure cycles, at a high crank angle resolution (usually 0.1 deg). In addition, a careful treatment of the measured data must be performed to extract the high frequency components from each instantaneous pressure cycle [92], [93].

The typical high frequency knock signature is related to the combustion chamber resonant frequencies [94], excited by the knock-induced pressure wave propagation. Wave amplitudes of the high frequency filtered pressure are used to define a great variety of knock indices [95], [96], [97]. However, these indices are affected by the pressure sensor type, by its position inside the combustion chamber [93], [96], and by the engine operating conditions [98], [99]. Because of the cycle to cycle variation, the knock extent is usually quantified following a statistical approach. In fact, a certain operating condition is assumed as “knocking” when a prefixed percentage of individual cycles (around 2-3%) is characterized by a knock index overtaking a predefined threshold level (usually depending on the engine speed). Its determination comes out from a number of considerations based on extensive engine calibration at the test-bench, manufacturer know-how, durability tests, etc. However, the whole process is affected by a certain arbitrariness according to the filtering technique and pass-band, proper definition of the threshold level, accepted percentage of knocking cycles, etc.

A number of techniques aimed at the experimental identification of the knocking onset in Spark-Ignition (SI) Internal Combustion Engines have been proposed and reported in the current literature. They can be classified into two broad categories, namely direct and indirect methods. Non-conventional techniques have been also attempted. A brief description of most popular detection techniques is reported in the following [9].

Direct Methods – They are mainly based on in-cylinder pressure measurements and are able to detect the typical high-frequency knock signature, related to the combustion chamber resonant frequencies. The latter depend on radial or circumferential vibration modes, which establish at a frequency depending on the speed of sound inside the combustion chamber and the cylinder bore.

Knock signature is identified through a proper analysis of the in-cylinder pressure signals in the frequency domain. After being processed in a band-pass filter (4–20 kHz), the pressure signals are rectified and processed to give proper knock indices. Among these, *MAPO* and *IMPO* indices are frequently used [97]. The first indicator measures the Integral of Modulus of Pressure Oscillations (*IMPO*). It hence accounts for the energy contained in the high frequency oscillations of the cylinder pressure signal, which occurs due to knock. The second one indeed estimates the Maximum Amplitude of Pressure Oscillations (*MAPO*). It is related to the peak of the knock-related pressure oscillations. *IMPO* and *MAPO* can be evaluated for each cycle and are then averaged over at least 100 consecutive cycles. Both are calculated on a prescribed crank angle window (usually 40-60 deg), starting at the spark timing. Knock occurrence is identified when *IMPO* or *MAPO* exceed a certain threshold level.

The typical drawback of such indices is that they are sensitive to local information provided by the pressure transducer. As knock occurs, however, huge pressure non-homogeneities take place inside the combustion chamber [96]. So, the measured pressure wave amplitude has only a local meaning, and cannot be considered as the maximum value of the whole combustion chamber pressure wave. Oscillations detected by the pressure transducer actually depend on relative distance between the sensor and the knocking sites within the combustion chamber. Amplitudes may be increased or smoothed, due to pressure waves reflections on combustion chamber walls. In addition, the threshold level of the knock index closely depends on engine features and operating conditions, as well [93], [100]. Due to the short lifetime expectancy and costs of pressure transducers, direct methods are moreover restricted to test-bench engine analyses.

Indirect Methods – Advanced signal processing techniques have been developed, as well, employing the cylinder block vibration signals, provided by accelerometers [90]. Although characterized by a lower signal-to-noise ratio, these sensors have a lot of advantages, in terms of excellent durability, sensitivity and low-cost. For this reason they are becoming the most practical solution for mass-production engines. Their application within on-board control systems requires however the development of reliable and precise procedures, able to detect cycle-by-cycle and cylinder-by-cylinder knocking conditions. Great care must be moreover devoted to identify the most favorable sensor locations, especially for multi-cylinder engines.

Methods based on the exhaust gas temperature – It is widely recognized that the exhaust gas temperature reduces in knocking conditions as a consequence of increased wall heat fluxes inside the cylinder. Therefore the exhaust gas temperature measurement can be utilized to identify knocking combustions. This technique, moreover, is not affected by mechanical noise, and can be applied for all types of engines [101]. Main drawbacks are related to the need of compare the temperature level provided by the thermocouple to the one stored in a map, representative of a knock-free operation in the same speed, load and air-fuel ratio operating conditions.

Methods based on intermediate radicals and species analysis – Nowadays, chemical luminescence emissions of end-gas can be used to analyze the chemical reactions caused by the end-gas autoignition [102]. Spectroscopic and chemiluminescence measurements allow identifying radicals as markers of different combustion phases. For instance, HCHO is built up in the unburned gas zone, while CH and OH radicals can be markers of normal combustion reaction and burned zone, respectively. The above measurements give the possibility to identify knocking zones inside the combustion chamber. However, they can be only carried out in optically accessible engines, and the related detection techniques are once again restricted to test-bench analyses.

4.2 Experimental Approaches for knock detection

As previously said, knock detection can be accomplished through different methods. In particular, two approaches are here proposed and analyzed: MAPO and A/R techniques. In-cylinder pressure traces are mandatory in order to utilize the above mentioned methods. For this reason, measurements of instantaneous in-cylinder pressure cycle are realized in each cylinder of the considered engine. As said in chapter 1, 200 consecutive pressure cycles are acquired for each operating condition. A sampling resolution of 0.5 crank angles is adopted at each speed. A higher sampling frequency (0.1 deg) is instead specified during combustion angular window (-10, 75 crank angle degrees). For sake of brevity, the acquired data for a single cylinder (cyl #2) are considered.

4.2.1 Maximum Amplitude of Pressure Oscillations (MAPO) Analysis

This method of knock detection requires an high-frequency filtering of pressure traces and it allows to evaluate the maximum amplitude of pressure oscillations (i.e. MAPO Index). The considered knock index is defined as reported in the following equation (4.1):

$$MAPO = \max(|\hat{p}|) \quad (4.1)$$

where \hat{p} is the in-cylinder pressure, filtered within the crank angle window of knock occurrence (-10, 75 degrees). For the filtering operation an high-pass filter with cut-off at 6 kHz is employed. An overview of the results obtained for each of the 200 experimentally acquired pressure cycles (vertical dots), is shown in Figure 4.2, at each engine speed.

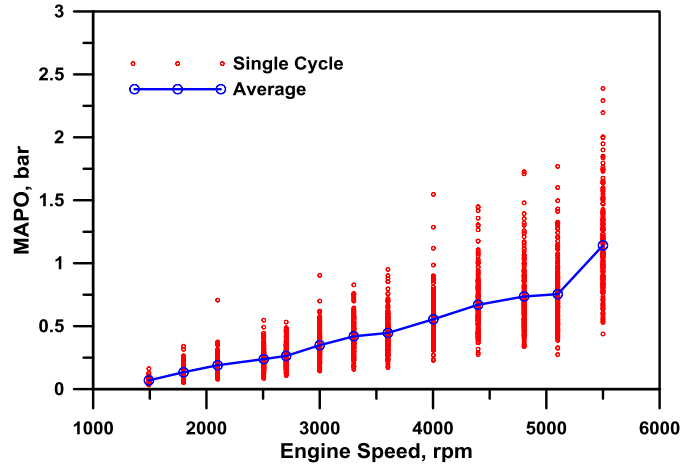


Figure 4.2 – MAPO Index as a function of the engine speed.

Huge cycle-by-cycle variations of the MAPO index are obtained in each condition, while the average level, reported as a continuous line, is always well below the maximum ones at each speed. For a prefixed speed, the knock indicators are in many cases distributed around the most frequent value in an almost symmetric way and without “high level” isolated points. For this reason, MAPO analysis, for the tested conditions, does not allow to easily identify individual knocking cycles.

4.2.2 ARMA Technique

An alternative ARMA approach is applied, which was proven to better perform particularly under soft-knock conditions [103]. Objective of an ARMA model is to predict the actual value of time signal x_t , based on its past history (AR property) and adding a prediction error (e_t) in the form of a Moving Average (MA) The following equation (4.2) hence defines an ARMA model with an AR order of n and a MA order of m :

$$x_t + a_1x_{t-1} + \dots + a_nx_{t-n} = e_t + b_1e_{t-1} + \dots + b_me_{t-m} \quad (4.2)$$

An ARMA(n,m) model is hence constituted by $n+m$ coefficients, which must be selected to minimize the prediction error, e_t . Different techniques can be followed to estimate the above coefficients. Among these, Yule-Walker functions or a least-squares polynomial regression are the most employed ones [104]. The accuracy level of the ARMA model is then synthesized in terms of variance of the error function, or Noise Variance (NV), defined in equation (4.3) as the sum of the squared distances of each term in the error function series from the mean (μ), divided by the number of samples, N :

$$\sigma^2 = \frac{\sum(e_t - \mu)^2}{N} \quad (4.3)$$

The smaller NV, the better the estimated model fits the time series. On the contrary, changes in the variance of the prediction error identify the presence of physical phenomena altering the characteristics of the time series. This property is here utilized to identify knocking phenomena. In particular, the in-cylinder data represent the time series (x_t), directly affected by uncorrelated disturbances (knocking, e_t). Knock phenomena will cause substantial deviations of the error function from its mean value. By monitoring the NV level, it is hence definitely possible to detect the knock occurrence and its intensity, even in the case of incipient knocking conditions.

It must be stressed however that a suitable ARMA model should be made up of the smallest number of adjustable parameters ($n+m$) that can achieve the desired accuracy. For this reason, it is very important to also define a criterion for the selection of the optimal model orders, n and m [105], [106]. In the present analysis, the Akaike Information Criterion (AIC) is used [107], given by equation (4.4):

$$AIC = \log[\sigma^2] + \frac{2(n+m)}{N} \quad (4.4)$$

In the above definition, the first term is a decreasing function of the model orders, while the second has an opposite trend, and represents a penalty adjustment. Since a proper ARMA(n,m) model should realize the lowest variance with the minimum number of parameters, the AR and MA orders reaching the lowest AIC level must be searched. In particular, the order selection is performed as follows:

1. The ranges of the ARMA model orders to be considered are selected (e.g. $1 \leq n \leq n_{max}$ and $1 \leq m \leq m_{max}$); in this case $n_{max} = m_{max} = 8$;
2. For each order pair (n,m), the coefficients of the ARMA model are estimated;
3. Based on the selected AIC criterion, the prediction error variance is calculated for each pair;
4. Finally, the (n,m) order pair that yields the lowest value of the selected criterion is chosen as the optimal pair.

A Matlab™ routine was in house developed in order to identify the best model order. The method has been applied to a complete time series, involving more than 200 cycles in a single operating condition (1500 rpm, cylinder #2). To exclude knock unrelated phenomena, each individual cycle is only processed in the crank angle window (10, 75 degrees).

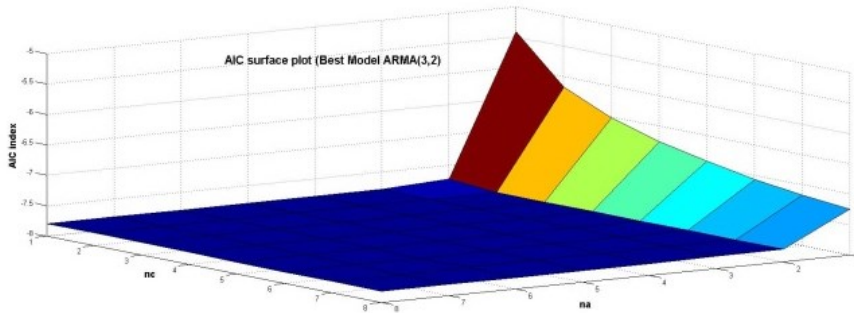


Figure 4.3 – AIC Surface plot.

Figure 4.3 shows the obtained AIC surface plot. Initially, by increasing both n and m , the AIC index rapidly reduces, while further increases in both orders only realize negligible improvements. The minimum AIC value is obtained with $n=3$ and $m=2$, which hence represent the proper orders to be selected.

Once set up, the ARMA(3,2) model is applied to all the investigated operating conditions. A complete picture of the model outcomes is given in Figure 4.4: it displays, at each engine speed, the cycle-by-cycle noise variance levels resulting from the processing of each individual cycle. A predefined null offset threshold level is also reported. Due to the presence of background pressure fluctuations at high speeds, a linearly increasing threshold would seem to be appropriate [108]. Its slope cannot be not fully rigorous and mainly comes out from the analysis of some individual cycles exhibiting noise variance peaks [95], [98].

It can be noted that cylinder #1 presents knock free operations for almost all the considered speeds, while cylinder #2 shows a certain number of cycles above or very close to the threshold for all the considered speeds. The more critical speed is 2100 rpm, where the maximum percentage of knocking cycle occurs.

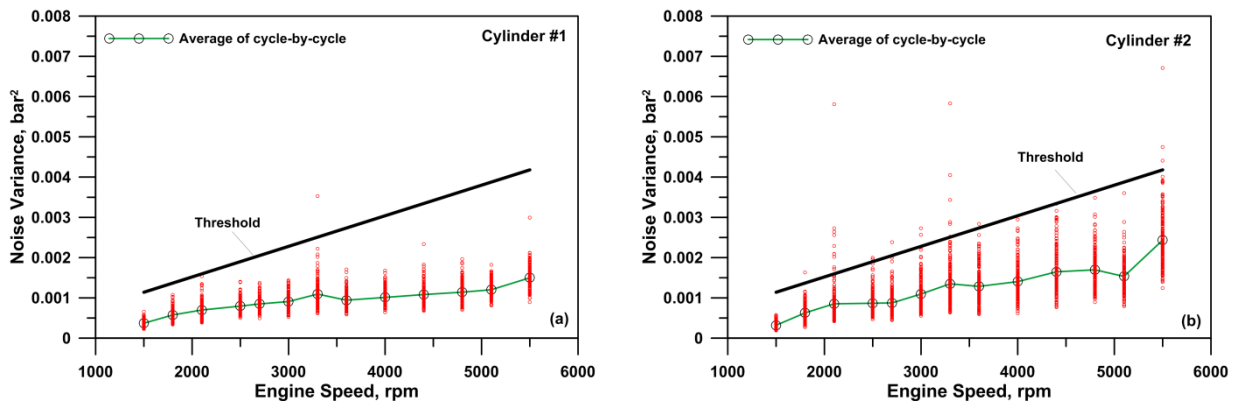


Figure 4.4 – Cycle-by-cycle noise variance for all investigated engine speeds, (a) cylinder #1, (b) cylinder #2.

It is well known that the knocking combustions most likely occur when high in-cylinder pressure and temperature peaks are attained. Based on this consideration, it appears possible to find a correlation between the assigned NV threshold and a peak pressure value above which knocking combustions begin to arise. With reference to the more critical speed of 2100 rpm, it can be observed in Figure 4.5 that the cycles characterized by a NV above the threshold also present a peak pressure exceeding the value of 68 bar.

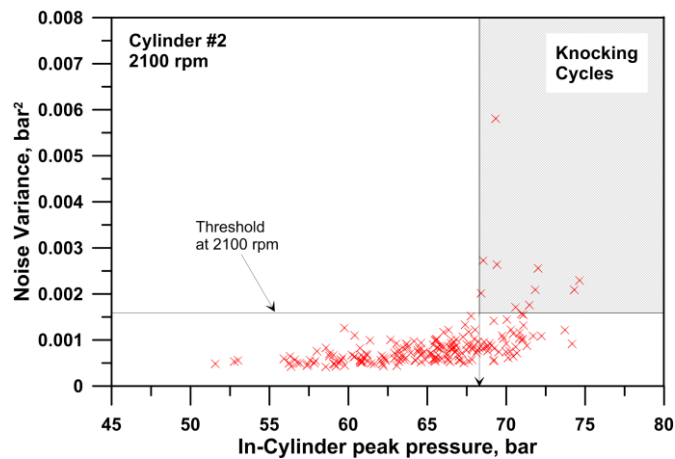


Figure 4.5 – ARMA analysis of the experimental pressure cycles at 2100 rpm.

4.3 Cyclic dispersion through random perturbation of combustion parameters

Based on a 1D methodology, the cycle-by-cycle variation can be imposed through a perturbation of the parameters controlling the combustion phase. A basic method [109] consists in modeling of the combustion by means of the a Wiebe function, whose coefficients are randomly varied to reproduce the experimental cyclic dispersion. A more physical approach is here considered, by employing phenomenological models for the description of the in-cylinder turbulence and combustion processes and taking into account the CCV by introducing proper variations on a number of parameters that affect the combustion process. To this aim, a random perturbation is introduced on the parameters (listed in Table 4.1) that mainly affect the combustion onset and development.

Perturbed parameter	Range of variation
Δ Spark advance, deg	± 2.5
Δ Intake valve closure, deg	± 1.0
Δ Air-to-fuel ratio, -	± 0.1
Variation of turbulence intensity, %	± 17
Variation of flame kernel radius, %	± 50

Table 4.1 – Range of variation of the cycle-by-cycle model parameters.

In the employed quasi-dimensional combustion model, the flame kernel radius defines the duration of the early stage of the combustion. The air to fuel ratio and turbulence intensity indeed influence the laminar flame speed and the turbulent flame area, respectively. The intake valve closure angle affects the cylinder filling, while the spark advance defines the start of the simulated combustion. At the beginning of each engine cycle, each parameter is randomly perturbed within a prescribed range. The superimposition of these perturbations non-linearly affects the heat release and the pressure cycle, and consequently determines cycle-by-cycle variations. The variation range of the considered parameters is specified in order to realize an IMEP standard deviation similar to the one observed in the experimental data. The experimental/numerical comparisons between the averaged IMEP and the related standard deviation are shown in Figure 4.6, denoting a good agreement.

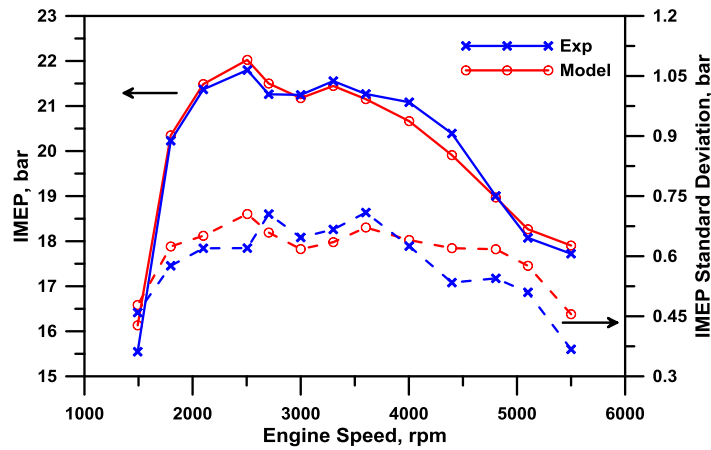


Figure 4.6 – Comparison between the experimental and computed averaged IMEP and IMEP standard deviation [103].

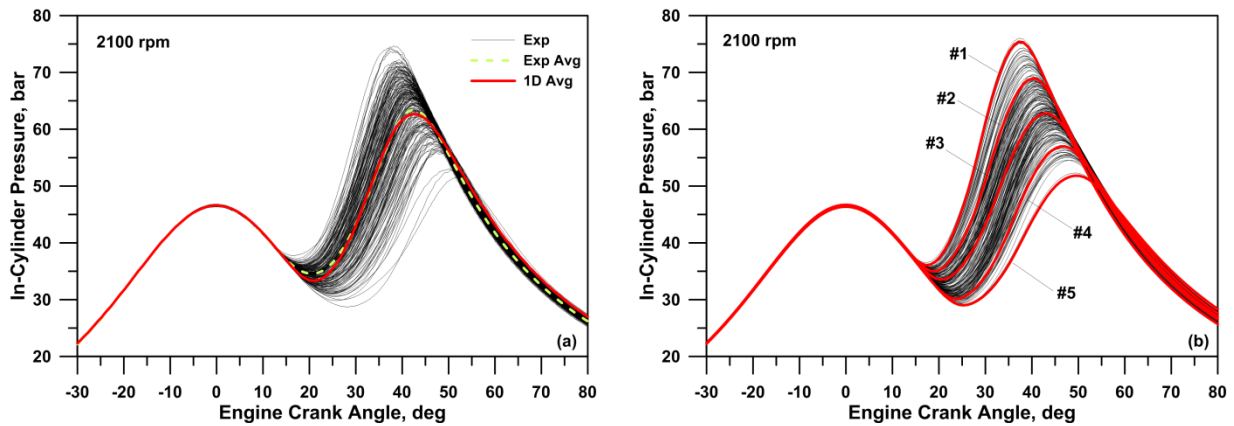


Figure 4.7 – Sequence of experimental pressure traces, its ensemble average and 1D mean pressure cycle (a), 1D simulated pressure cycles including cycle-by-cycle variation (b).

In Figure 4.7a, the comparison between the measured and simulated ensemble-averaged pressure cycles at 2100 rpm are shown. This last speed, as stated above, is identified by the ARMA analysis as the most critical operating condition in terms of percentage of knocking cycles. The related train of 200 consecutive experimental cycles is also plotted Figure 4.7a, to be compared to the simulated data set in Figure 4.7b. Five modelled cycles are selected, characterized by a different peak pressure. In particular, cycles #1, #3 and #5 correspond to the maximum, mean and minimum peaks, respectively, while cycles #2 and #4 represent intermediate conditions.

4.4 Cycle by cycle variation model and validation

The above discussed results (Figure 4.7) take into account the typical approach to model CCV in 1D simulations [110], [111]. As previously said, the cycle by cycle variation phenomenon is introduced in the model through a perturbation of the parameters (Table 4.1) controlling the combustion phasing and duration (turbulence intensity, air-to-fuel ratio, residual fraction, etc.). However, the above approach, while providing encouraging results in CCV simulation, of course requires an increased computational effort because of the necessity to compute a large number of cycles to obtain a statistically significant test sample and adequately characterize the cyclic variations. This may undermine the typical simplicity and efficiency of 1D modelling. For this reason, a different approach is here proposed in order to overcome the limits of the previous one and to properly consider the cycle by cycle variations phenomenon. Referring to the proposed alternative approach, the effects of the experimentally observed cyclic dispersion are introduced through the computation of representative *faster-than-average* and *slower-than-average* in-cylinder pressure cycles. In particular, the experimental values of the CoV of the in-cylinder peak pressure are available for the engine under study and they are imposed as input parameter for the 1D engine model. A proper algorithm is adopted to numerically evaluate two cycles, representative of *faster-than-average* and *slower-than-average* cycles, belonging to a sequence of consecutive pressure cycles. The above algorithm starts from the average, fractal-predicted, burnt profile of the previous cycle ($x_{b,avg}^{i-1}$), and it allows to derive the faster and slower burning fractions ($x_{b,h}^i$ and $x_{b,l}^i$) at the current i_{th} computing cycle. To this aim, at each crank angle, θ , the $x_{b,avg}^{i-1}$ profile is inquired at angular positions θ_h and θ_l , given by the following equation (4.5) and (4.6):

$$\theta_h = \theta_{spark} + (\theta - \theta_{spark})s_h \quad (4.5)$$

$$\theta_l = \theta_{spark} + (\theta - \theta_{spark})s_l \quad (4.6)$$

$s_h > 1$ and $s_l < 1$ being “stretch factors”, allowing to derive the burned fractions of the *faster* and *slower* cycle, as synthesized by equations (4.7) and depicted, as an example, in Figure 4.8.

$$x_{b,l}^i(\theta) = x_b^{i-1}(\theta_l) \rightarrow x_{b,h}^i(\theta) = x_b^{i-1}(\theta_h) \quad (4.7)$$

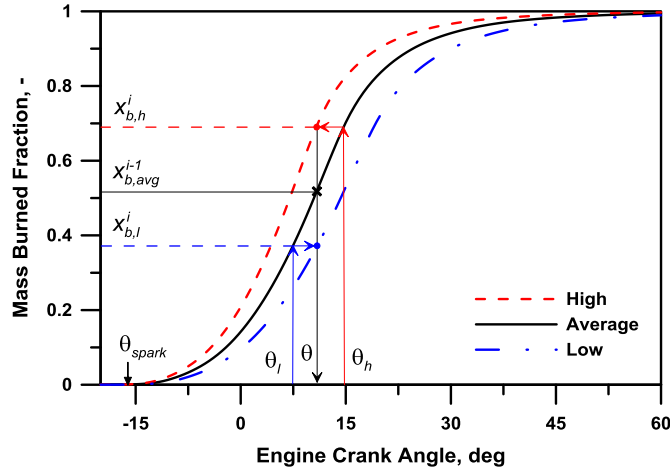


Figure 4.8 – Procedure for the identification of “slower-than-average” and “faster-than-average” burning profiles.

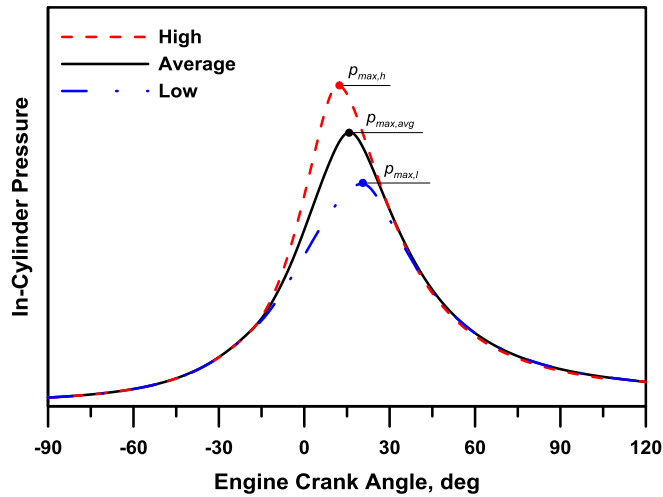


Figure 4.9 – Typical pressure cycle obtained by the cycle-by-cycle variation model.

Starting from the three burnt profiles showed in Figure 4.8, three pressure cycles are actually computed (Figure 4.9), and the related maximum pressures ($p_{max,h}$, $p_{max,avg}$, $p_{max,l}$) are estimated. At the end of the i_{th} computing cycle, the stretch factors s_h and s_l are automatically adjusted until $p_{max,h}$ and $p_{max,l}$ reach the related target values, realizing the value of CoV_{pmax} given as input parameter. Target values for maximum pressures of high and low cycles are evaluated by equations (4.8) and (4.9).

$$p_{max,h,target} = p_{max,avg} (1 + N_{\sigma} CoV_{pmax} / 100) \quad (4.8)$$

$$p_{max,l,target} = p_{max,avg} (1 - N_{\sigma} CoV_{pmax} / 100) \quad (4.9)$$

In the above equations , the parameter N_σ has been fixed to 2, to get a 95% of cycles lying within the $[p_{max,h}, p_{max,l}]$ interval.

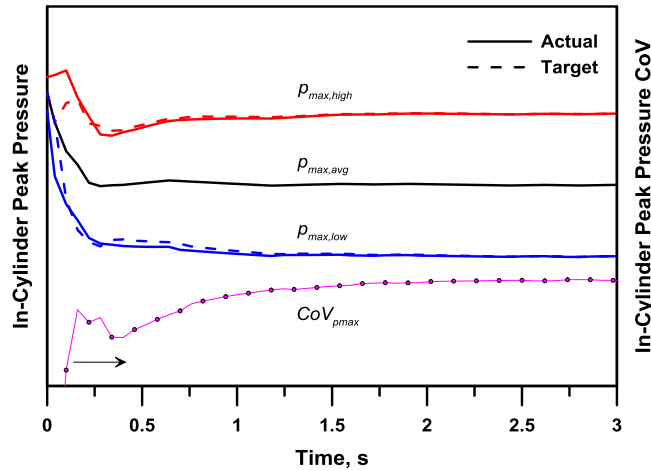


Figure 4.10 – Time history of the peak pressures of the average, “high” and “low” cycles.

This means that the computed *high* and *low* cycles are representative of the 2.5% faster and slower cycles, belonging to the whole experimental dataset. Figure 4.10 depicts, as an example, a typical time evolution of the in-cylinder peak pressures during a simulation in presence of CCV. It can be observed that the application of the CCV model starts after few simulation cycles, before that steady state operation for the average pressure cycle is reached. In addition, it can be noted that the actual peak pressures of the *high* and *low* cycles very quickly attain the related targets, not requiring the computation of a relevant number of pressure cycles as the more common methods discussed above. Those aspects, of course, contributes to make the proposed CCV model very efficient in terms of computational effort. Without requiring any additional tuning, the CCV model is applied for all the full-load operating points. The computed cycles, representative of the cycle-by-cycle variations, are compared to the sequence of 200 pressure traces measured at the test bench. Figure 4.11 shows the experimental/numerical comparisons for the full load points at different engine speeds (1500, 2100, 2500, 3300, 4400 and 5500 rpm). For each operating point, the base spark timing is considered. The experimental/numerical comparisons put into evidence that the computed *high* and *low* cycles well agree in most of tested conditions with the extreme faster and slower measured cycles, respectively, proving the consistency of the proposed CCV modelling. Also the shape of the computed *high* and *low* cycles closely resembles in many cases the experimental data, thus supporting the simplified hypothesis that a “stretched” burnt rate profile is enough to well reproduce the CCV.

In some points of Figure 4.11, however, the experimental/numerical agreement is less satisfactory, and some underestimation on *high* cycles and overestimation on *low* cycles can be observed. Actually, any error in the computation of the average cycle also reflects on CCV. Moreover a non-perfectly Gaussian distribution of the in-cylinder peak pressure may occur, as well.

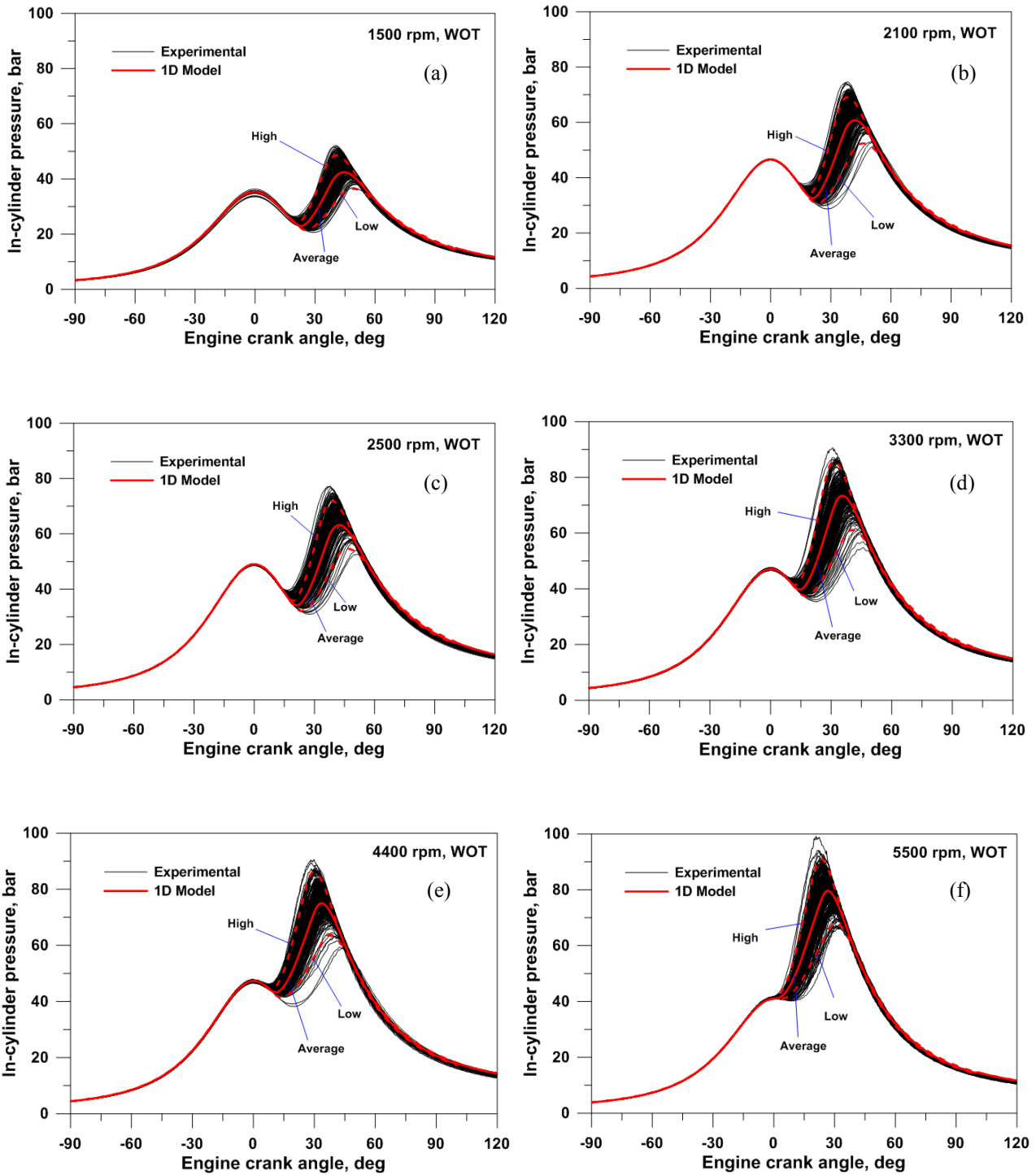


Figure 4.11 – Numerical vs. experimental pressure cycles at full load; (a) 1500 rpm, (b) 2100 rpm, (c) 2500 rpm, (d) 3300 rpm, (e) 4400 rpm, (f) 5500 rpm.

4.5 Knock Model Description and Validation

The knock phenomenon is modelled by the computation (CHEMKIN) of a chemical kinetic scheme, able to detect the presence of auto-ignition reactions in the end-gas zone. In particular, a semi-detailed kinetic mechanism for the oxidation of a blend of a three-component surrogate fuel, consisting of toluene, n-heptane and iso-octane (TRF mechanism), is specified [112], [113], [114]. The kinetic scheme here adopted was developed by Liu et al. [114] and includes 5 elements, 56 species and 168 reactions. The mechanism handles both low and high temperature reactions and is tuned to well reproduce the ignition delay and evolution of most important species. Amount and composition of inert gases in the combustion chamber hence affect the TFR kinetics and hopefully capture the EGR and water effects on the knock event better than the simplified correlations employed in the revised literature [115], [116].

Knock event is recognized as the condition when “high temperature” reactions activate in the unburned zone, resulting in a sudden jump in the unburned temperature and pressure profiles during the final stage of the combustion process. The considered knock index is the pressure increase, Δp_{knock} , computed assuming an instantaneous isochoric combustion of the end-gas still unburned at knock event:

$$\Delta p_{knock} = \frac{R}{c_v} \frac{x_{u,knock} m_f LHV}{V_{knock}} \quad (4.10)$$

R and c_v being the average gas constant and the constant volume specific heat of the in-cylinder gases, m_f and LHV being the mass and the low heating value of the fuel, V_{knock} and $x_{u,knock}$ being the in-cylinder volume and end-gas unburned fraction at the knock event. In the proposed approach, while the engine performance are computed with reference to the experimental ensemble average pressure cycle, the knock evaluation refers to cycles that are representative of the faster ones, within a measured sequence. The latter are in fact supposed to most likely exhibit knocking combustions [41], [117]. To this aim, computed burning rates are properly “stretched” to statistically mimic the experimental cyclic variability. The above approach is described in detail in [118], [119].

In addition, special attention is devoted to the heat transfer modelling because of its crucial influence on the knock prediction. An almost standard Woschni correlation is implemented, while piston, cylinder liner and head temperatures are calculated by the finite element approach of GT-

Power. The heat transfer coefficient on the coolants side (water and oil) is derived by simulations of the coolant circuits and adjusted according to the engine speed [120]. The knock model, described above, is validated through the numerical identification of the knock limited spark advance at full load operation. The KLSA is searched by means of an automatic and iterative procedure. In particular, the identification strategy acts by delaying the spark timing in 0.1 degrees steps when the knock index, Δp_{knock} , exceeds the prescribed threshold level, otherwise the timing is advanced. It is the case to underline that, exactly the same threshold for the MAPO index derived by experimental knock analysis, is also adopted in the present simulations. It is characterized by a linearly increasing trend with the engine speed. To better understand the automatic procedure for the KLSA identification, in Figure 4.12 the time evolution of the knock index and of the spark advance are reported.

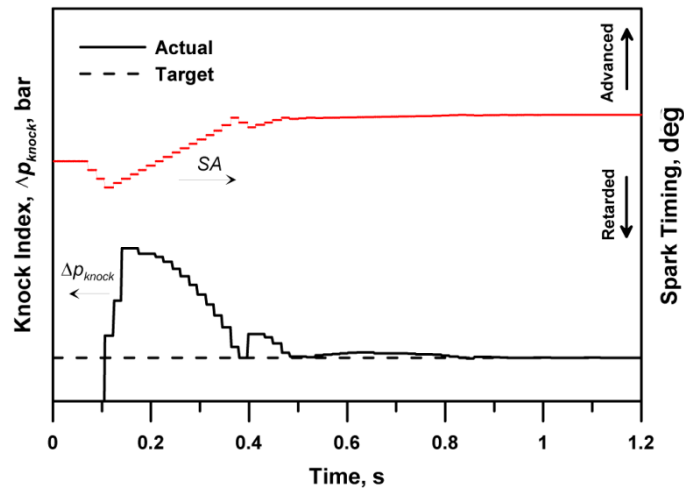


Figure 4.12 – Time history of SA and Δp_{knock} parameters during a simulation for KLSA determination.

It can be observed that, after a numerical transient, the spark advance reaches a constant value when the knock index stabilizes on the prescribed threshold level, providing the numerical KLSA. The above procedure is performed with reference to the *faster-than-average* pressure cycle, rather than the average cycle. This choice is widely confirmed by experimental observations suggesting that knock most likely occurs for the faster cycles of a sequence. In addition, based on the choice of the N_σ parameter in equations (4.8) and (4.9), only 2.5% cycles are expected to be even faster than the computed *high* cycle. Hence, when KLSA is searched with reference to the latter, a 2.5% knocking

cycles are roughly expected in the same operating condition on the real engine. The numerical KLSA is finally compared with the experimental data at full load (Figure 4.13).

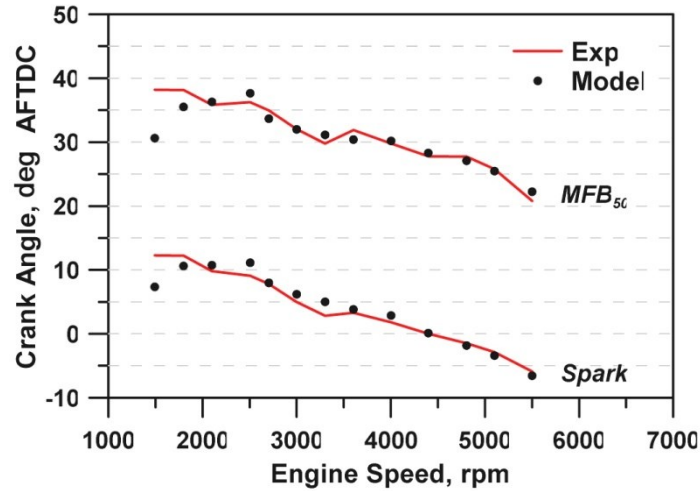


Figure 4.13 – Comparison of experimental and numerical MFB_{50} and spark timing at the knock onset.

Figure 4.13 also shows the numerical/experimental comparison in terms of combustion phasing (MFB_{50}). It can be noted that a good agreement is assessed, confirming the accuracy of the adopted knock model. Greater errors can be observed only at the lowest engine speed. In conclusion, a proper integration of experimental data and refined models of combustion, cyclic dispersion and knock, finally allows for a KLSA identification on a completely theoretical basis, opening the opportunity to perform a reliable “virtual calibration” of the engine at full load operation.

CHAPTER 5

EGR System Employment to reduce the fuel consumption and the knock occurrence

5.1 Adoption of EGR Systems for SI Engine

Turbocharged spark ignition engines are becoming increasingly popular in the worldwide market because of their compactness and high power density. However, knocking combustions and high exhaust gas temperatures constitutes a very important problem at high loads. For these reason, one of the major goals for manufacturers of turbocharged SI engines is to increase knock resistance at high load. Indeed, when the engine goes into knocking operation at high load, the spark timing has to be retarded in order to move out of knock. This represent an effective method to eliminate the knock but the negative effects of retarding the spark timing are, however, multiple [67]: the thermodynamic efficiency of the engine decreases while the in-cylinder gas temperature at exhaust valve opening increases. As a consequence, the thermal stress of the exhaust components, such as the exhaust valve, turbocharger and the catalyst increases. In order to reduce the gas temperature and to suppress knock, excessive amounts of fuel have traditionally been used. Unfortunately, fuel enrichment has a detrimental effect on the fuel consumption and on the exhaust emissions, since the three way catalyst is unable to oxidize CO and HC under fuel-rich conditions. So far this has not been considered as a problem due to the relatively short time the engine is running at full power. However, new legislation is expected, which will regulate high load emissions. Consequently, fuel enrichment during full load has to be reduced in order to meet the new legislation. Therefore, there is a need for finding alternative strategies for knock control. Several knock suppression methods have been studied. These methods can be divided into two categories. The first one consists in the modification of charge composition and the second one consists in decreasing the effective compression ratio. However, if the expansion ratio also is decreased, the exhaust gas temperature is increased. Reduced compression, with a maintained expansion ratio, can be achieved by advancing or retarding inlet valve closing times [121], [122], [123]. By reducing the compression ratio the peak compression temperature of the charge is reduced, and hence knock is suppressed. The charge composition has typically been altered by introducing anti-knock additives to the fuel, for example more recently different ethers, methyl tertiary butyl ether (MTBE) or ethyl tertiary butyl ether (ETBE), or alcohols. However, the composition of the charge can also be varied by introducing

water, additional air or by recycling exhaust gas (EGR). In particular, several studies demonstrate that a promising technology to limit knocking through dilution is the cooled exhaust gas recirculation (EGR), which represents a suitable candidate for replacing fuel enrichment. In Cooled EGR system exhaust gas temperature is reduced through an EGR cooler.

EGR technique was firstly adopted in diesel engines in order to limit thermal NO_x formation rate by reducing combustion chamber temperature thanks to the dilution of fresh charge with a certain amount of exhaust gases recycled at engine intake. Some studies also suggest that appropriate EGR ratio can reduce combustion noise by lowering the pressure rise rate and the pressure high frequency oscillation magnitude [124], [125]. But with the growing of energy and environmental issues, various countries in the world have developed more stringent regulations on vehicle emission and fuel economy to drive gasoline engine to be developed towards downsizing direction. Downsizing philosophy consists in the reduction of the total engine displacement while the adoption of a turbo-charger group allows to achieve the required power/torque performance. Downsized SI engine presents improved BSFC at part load operation but, on the other hand, the BSFC is penalized at high/full load operation because of the knock occurrence and of further limitations on the Turbine Inlet Temperature (TIT). For this engine configuration, the use of cooled EGR represents an effective measure to avoid abnormal combustion. Cooled EGR systems have already been introduced and mass-produced in naturally aspirated (NA) gasoline engines. Generally, there are two methods to introduce cooled EGR in turbo-charged engines. One is the high pressure EGR (HP-EGR), in which the exhaust gas is recirculated from the exhaust pipe upstream of the turbine to the intake pipe downstream of the compressor. The second one is the low pressure EGR (LP-EGR), in which the exhaust gas is recirculated from the exhaust pipe downstream of the turbine to the intake pipe upstream of the compressor [126], [127], [128]. (Figure 5.1):

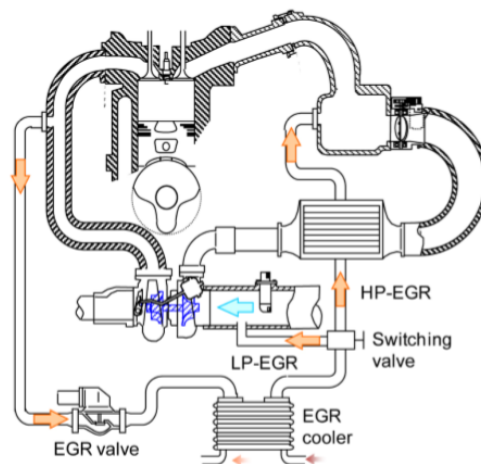


Figure 5.1 – Example of Experimental setup with actual EGR.

The HP-EGR system has been partially introduced since the structure and mechanism of EGR are similar to those in NA SI engines. However, a sufficient EGR amount cannot be provided in turbo-charged operation especially in the low engine speed region, which leads to higher fuel consumption.

On the other hand, the LP-EGR system has a long flow path and needs a complex control system. Therefore, it has not been put to practical use at the moment. However, since a higher EGR ratio could be set in turbo-charged operation, it has been focused on as an effective method for realizing fuel-efficient combustion in heavily downsized and highly boosted gasoline engines.

As said before, current literature is plenty of studies (papers) experimentally demonstrating the potential of EGR in improving fuel economy [128-132]. Bourhis et al. [129] analyzed the effects of internal and external EGR in turbocharged SI engines at moderate load. In particular, the first solution allows an Indicated Specific Fuel Consumption (ISFC) improvement of 8% at 1500 rpm and 8 bar Indicated Mean Effective Pressure (IMEP) with an EGR increase from 5% up to 8%. Through the second strategy, a ISFC reduction of 4% is obtained at 2000 rpm and 10 bar IMEP.

In [130], indeed, high load operation was mainly addressed, showing fuel consumption improvements ranging from 6% at high speed, up to 17% at low speed. Cairns et al. [128] performed a comparison of excess fuel, excess air, and cooled external EGR charge dilution, revealing that cooled EGR is the most effective knock suppressant among the other investigated strategies. Experimental work of Grandin et al. [67] confirmed that cooled EGR is the most effective replacement of fuel enrichment, especially if a three-way catalytic converter has to be used at all operating conditions. Potteau et al. [131] measured BSFC reductions up to 14% and an exhaust gas temperature decrease up to 100°C. Similar advantages were claimed in [132], once again emerging from a decrease in knock tendency allowing for a better combustion phasing, as well as from reductions in exhaust temperatures that eliminated the necessity of over-fuelling.

The above results, as said, were demonstrated by extensive experimental analyses at the test bench, requiring a complete engine recalibration to fully exploit the EGR advantages. Of course, the possibility to recover similar outcomes through numerical 1D or 3D analyses [133-135] would be very helpful to reduce the development costs, the time-to-market and to also analyze the trade-offs among different architectures (low-pressure or high-pressure EGR, recycled gas temperature, etc.). However, the complex interactions among different driving parameters affecting the fuel consumption - namely the mixture composition, the auto-ignition chemistry, the flame speed, the heat transfer, the boost level, etc. - imply the need of employing very accurate numerical tools. In addition, since the whole engine system has to be characterized, a 1D model, enhanced to properly furnish a satisfactory description of combustion and knock phenomena, appears to be the more

suitable numerical tool. EGR potential in mitigating knock phenomena are analyzed with reference to a small turbocharged VVA engine through the employment of a commercial 1D code (GT-PowerTM). High-pressure and Low-Pressure (LP) circuits are initially considered. However, preliminary calculations for the former solution highlighted the presence of intense pressure fluctuations within the high pressure branches of the intake and exhaust circuits (mainly due to the twin-cylinder architecture), responsible for frequent flow reversals within the EGR circuit. The above problems are indeed drastically mitigated in the second solution, because of the damping effect exerted by the turbocharger. For this reason, the LP cooled EGR system is only analyzed in the following. Model predictivity is greatly improved by “in-house developed” sub-models for the description of combustion [136] and knock [91] processes. The base engine model has been in fact already extensively validated at full and part load operation [137], [138], as well.

5.2 Numerical analyses description

Starting from the validated engine model (base engine configuration), an external EGR (*EGR, Exhaust Gas Recirculation*) circuit is virtually mounted. In particular, a Low Pressure (LP) Cooled EGR circuit is taken into account (Figure 5.2).

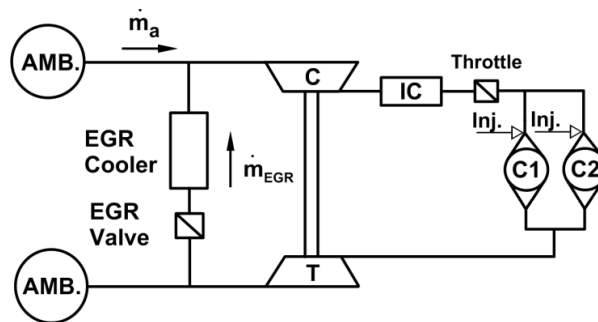


Figure 5.2 – Engine schematic layout.

As known, the adoption of LP cooled EGR circuit allows for a reduction in BSFC. Indeed, the higher amount of inert gas involves a decrease of the in-cylinder peak pressure which diminishes the knock risk and allows for an optimization of combustion phasing (MFB_{50}) and an air/fuel mixture (A/F ratio) leaning. LP cooled EGR circuit is schematized as a circular pipe of a constant diameter, that links the ducts upstream the compressor and downstream the turbine. Recycled gas flow rate and temperature are controlled by an EGR valve and a cooler device, respectively.

Figure 5.3 shows the EGR circuit modeled by five elements, whose flow connections are reported in red line. Concerning the considered EGR circuit, the main geometrical characteristics are reported below:

- ✓ EGR-Valve presents a reference diameter of 17 mm;
- ✓ EGR cooler represents a cylindrical pipe with diameter of 24.22 mm and length of 150 mm; it allows to realize a recycled gas temperature of 433 K; the selected EGR temperature is similar to real applications described in [67], [139].
- ✓ EGR pipes located upstream and downstream the EGR cooler; each element presents cylindrical section with diameter of 24.22 mm and total length of 150 mm;
- ✓ Two Flow splits TRight: “FS-monte-compressore” having a total length of 40 mm and a diameter of 33.2 mm while “FS-valle-turbina” presents a total length of 30 mm and a diameter of 64 mm.

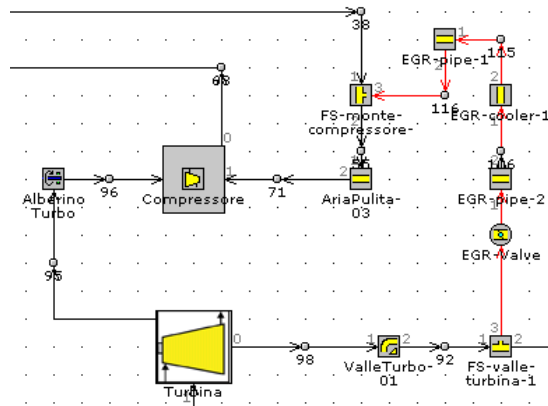


Figure 5.3 – Low Pressure EGR circuit.

Case #	Case label	Engine Speed, rpm	BMEP, bar
1	5500@16	5500	15.96
2	4400@18	4400	18.53
3	3300@21	3300	20.78
4	2500@21	2500	20.60
5	2100@20	2100	20.42
6	1500@17	1500	16.62

Table 5.1 – Summary of the analyzed operating points.

Referring to the numerical analyses, six operating conditions are investigated (Table 5.1) at full load. For each case, different simulations are performed with various A/F ratios and EGR valve openings (ranging from 0 to 90 degrees). In this way, different EGR rates are obtained as defined in the following equation (5.1):

$$EGR\ rate = \frac{\dot{m}_{EGR}}{\dot{m}_{air} + \dot{m}_{EGR}} \cdot 100 \quad (5.1)$$

In all analyses, the spark timing is automatically modified to realize operation at the knock onset. The same knock threshold adopted for the model validation in the base configuration is also applied in presence of EGR. The waste-gate valve opening is adjusted by a PID controller targeting the prescribed load levels of Table 5.1. Numerical results are then post-processed to verify the respect of the following constraints:

- boost pressure, below 2.6 bar;
- turbocharger speed, below 255000 rpm;
- in-cylinder peak pressure, below 90 bar.

TIT and speed limitations are required to preserve the turbocharger safety, while, for the considered engine, the boost pressure needs to be controlled to ensure proper operation of the fuel injectors for the intake manifold. Since the 1D model shows a certain inaccuracy in the prediction of the TIT (Figure 5.4), a case-dependent TIT threshold is assumed, corresponding to the numerical TIT attained in the base engine configuration. The boost pressure has to be controlled to provide proper operation for the injectors and for the intake manifold. The maximum in-cylinder pressure has to be limited below the prescribed threshold to preserve engine mechanical safety. Although a value of 90 bar represents the maximum allowable peak pressure level suggested by the engine manufacturer, in the standard calibration of the considered engine the peak pressure never exceeds 80 bar. The numerical results exceeding one of the above limits are discarded and labelled as “not allowable” in the next section.

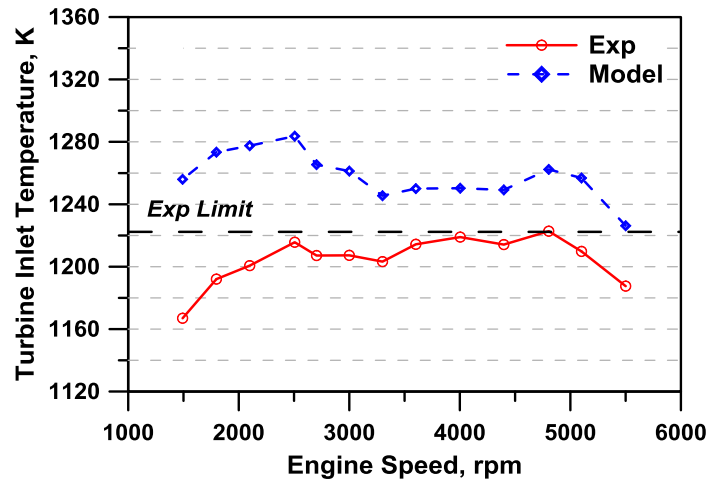


Figure 5.4 – Experimental/numerical comparison of Turbine Inlet Temperature in WOT as a function of the engine speed.

5.3 Results of Cooled EGR Analyses

The numerical results show that the EGR adoption involves BSFC reductions for all the examined operating points. Maximum improvements strictly depend on the possibility to modify the monitored parameters up to their prescribed limits. First, a detailed description of the outcomes of the parametric analysis for two operating points, namely 2100@20 and 5500@17 will be presented. Then a summary of the BSFC advantages related to the considered techniques will be reported, describing the re-calibration of the engine control parameters capable to furnish the above benefits.

For the first considered operating point, i.e. 2100@20, an increase in the EGR rate always involves a better fuel consumption (Figure 5.5a). Similarly, the BSFC reduces as the A/F ratio increases, reaching minimum values at the stoichiometric A/F ratio. The latter, however, also affects the combustion phasing (Figure 5.5b) since less over-fuelling determines more critical knock conditions. Dashed lines in the Figure 5.5a and Figure 5.5b indicate operating conditions which do not respect one or more limitations. Referring to Figure 5.5a, the “Best” allowable solution (denoted by a star) is obtained at about 20% of EGR rate, where a BSFC improvement of about 88 g/kWh is achieved with respect to the “Base” calibration (square symbol). The latter corresponds to no-external EGR operation, at the experimentally imposed A/F ratio.

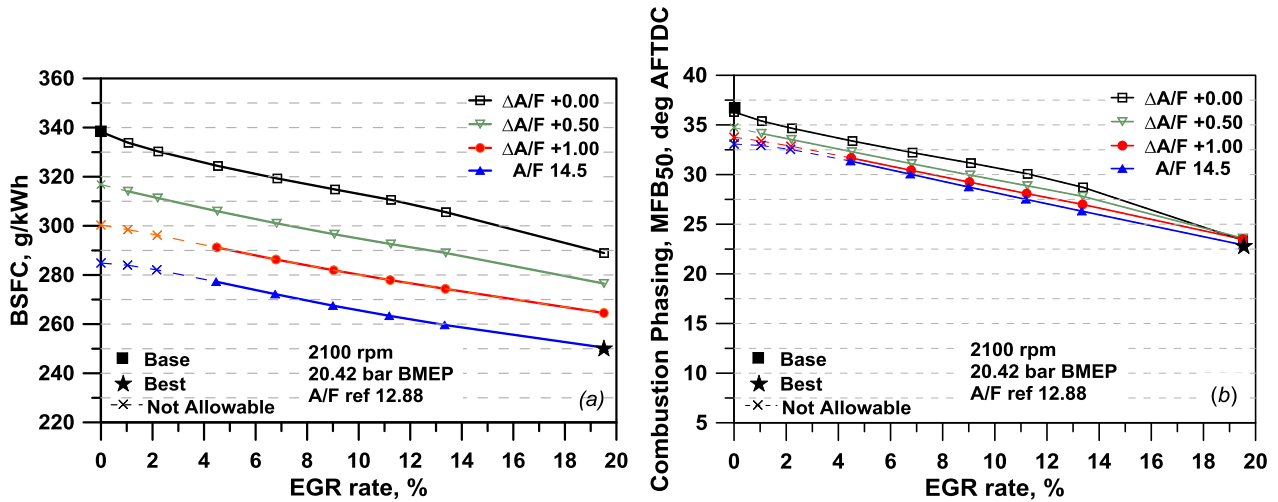


Figure 5.5 – BSFC vs. EGR rate (a) and MFB_{50} vs. EGR rate (b) at 2100 rpm.

Figure 5.6a underlines that an increase in boost pressure is required to recover the cylinder filling penalties induced by the EGR. Figure 5.6b shows that a reduction in the TIT occurs at increasing EGR [131] rates, while the A/F ratio has an opposite effect. The TIT exceeds the assigned constrain at low EGR levels and reduced mixture fuelling, determining unallowable conditions. Figure 5.7a highlights the effects on combustion duration caused by the introduction of inert gases. As expected, the latter increases with the EGR content, due to a lower laminar flame speed [130], [140]. Despite the higher boost level and the more advanced combustion, a less relevant increase in the in-cylinder peak pressure is attained, that remains below the prescribed limit of 90 bar (Figure 5.7b). The overall BFSC improvements actually arise from the balance among main “pros” (better combustion phasing and reduced over-fuelling) and “cons” (slower combustion, higher peak pressures). Summarizing, at 2100@20, fuel economy gains result from both a mixture dilution (Figure 5.5a) and a combustion phasing advance (Figure 5.5b). Since the boost pressure never reaches the considered limit, a wide open EGR valve can be specified and the maximum EGR rate can be admitted (about 20%).

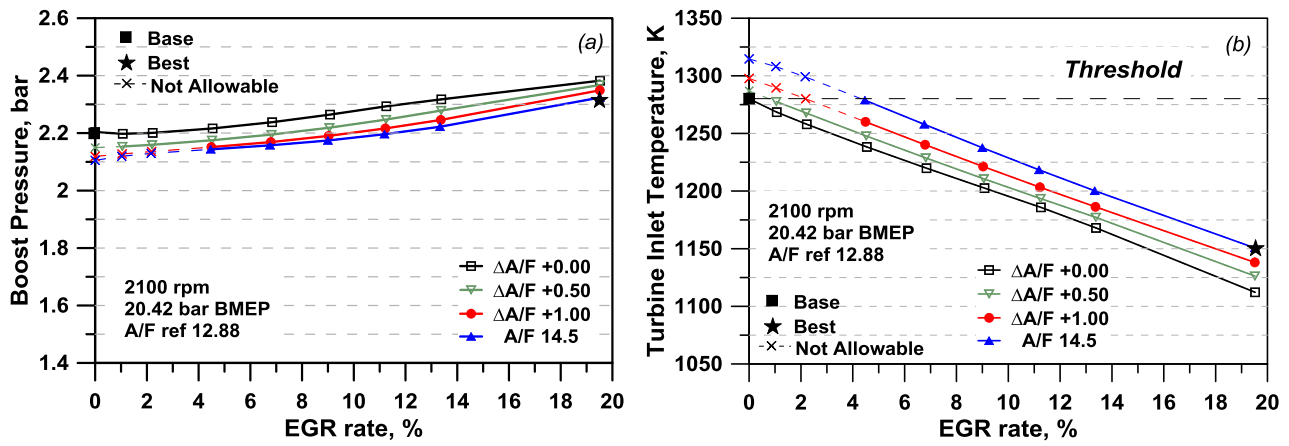


Figure 5.6 – Boost pressure vs. EGR rate (a) and TIT vs. EGR rate (b) at 2100 rpm.

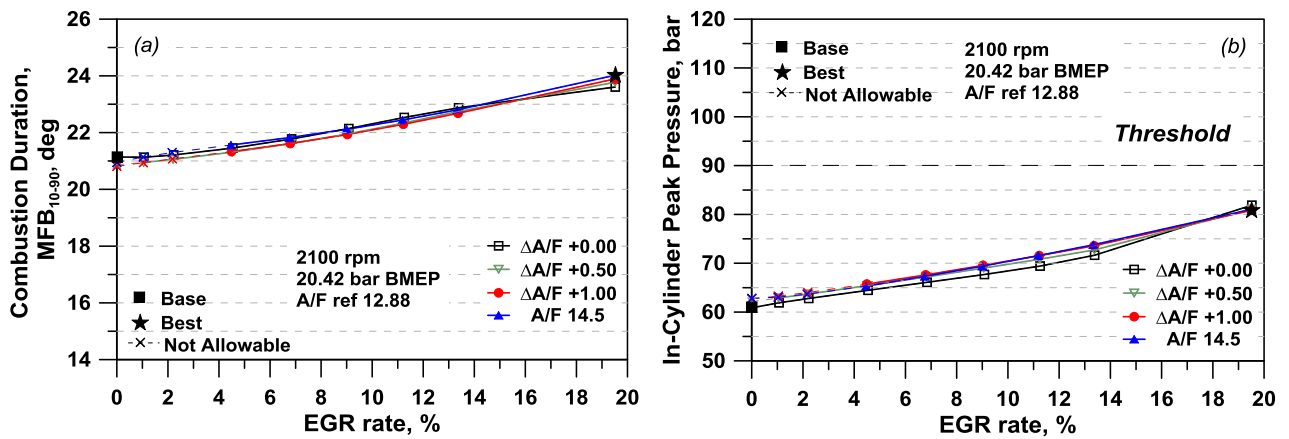


Figure 5.7 – Combustion duration vs. EGR rate (a) and in-cylinder peak pressure vs. EGR rate (b) at 2100 rpm.

To deepen the understanding of EGR effects on knock resistance, the in-cylinder pressure and temperature cycles in the Base and Best EGR calibrations are depicted in Figure 5.8a and Figure 5.8b, respectively. Looking at Figure 5.8a, the increased boost level caused by the EGR adoption determines a higher pressure at the TDC. However, the peak pressure does not present an excessive increase with respect to the Base case, due to the slower burning rate. On the other hand, the peak temperatures in the unburned zone for the Base and Best EGR calibrations are almost the same during the last stage of combustion, since both corresponds to operation at knock onset (Figure 5.8b). With reference to the Best EGR calibration, the increased heat capacity of the in-cylinder mixture caused by the higher inert content is compensated by the higher boost level, determining almost the same temperature profiles in the unburned zone during the compression stroke.

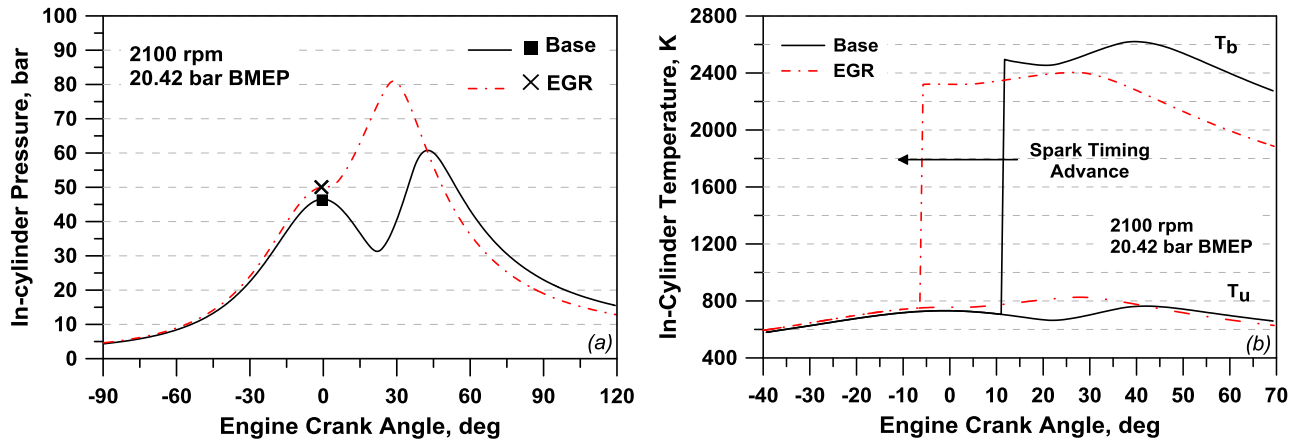


Figure 5.8 – Comparison of in-cylinder pressure (a) and temperature (b) cycles for base and Best EGR calibrations at 2100 rpm.

As said, the second operating point discussed in detail in this section is 5500@15. BSFC curves in Figure 5.9a denote a more flat trend with EGR, mainly depending on the more relevant incidence of the pumping losses (Figure 5.9b). The comparison of Figure 5.9a and Figure 5.10a highlights that at 5500@15, the main path to reduce the fuel consumption is the mixture leaning, rather than combustion phasing advance. In fact, thanks to an A/F ratio increase of 1.50, a BSFC improvement of about 61 g/kWh is reached, with a combustion phasing advance of only 2 degrees. The fuel economy improvements are limited by the boost level (Figure 5.10b) and by the in-cylinder peak pressure (Figure 5.11b) at the highest EGR rate, and by the TIT (Figure 5.11a) at the higher A/F ratios.

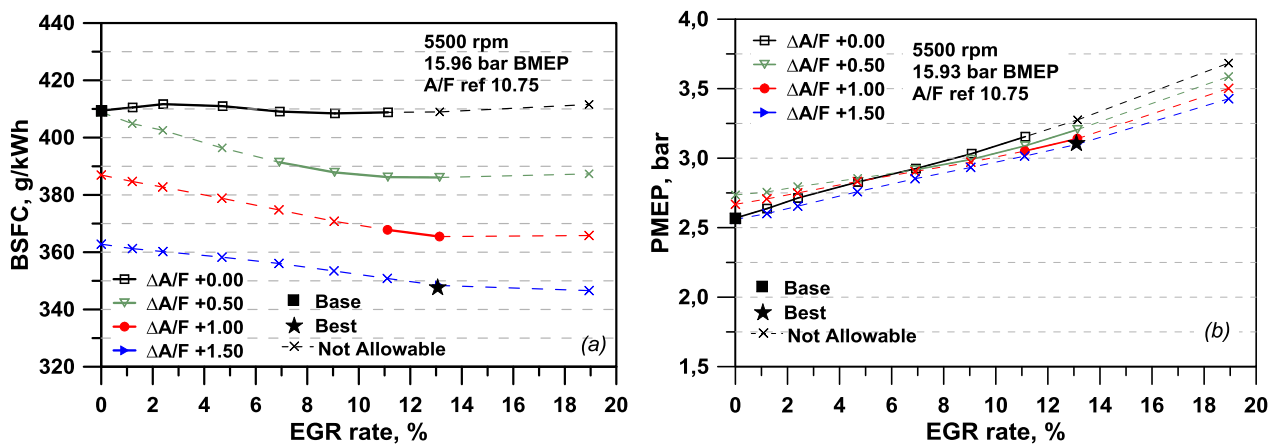


Figure 5.9 – BSFC vs. EGR rate (a) and PMEP vs. EGR rate (b) at 5500 rpm.

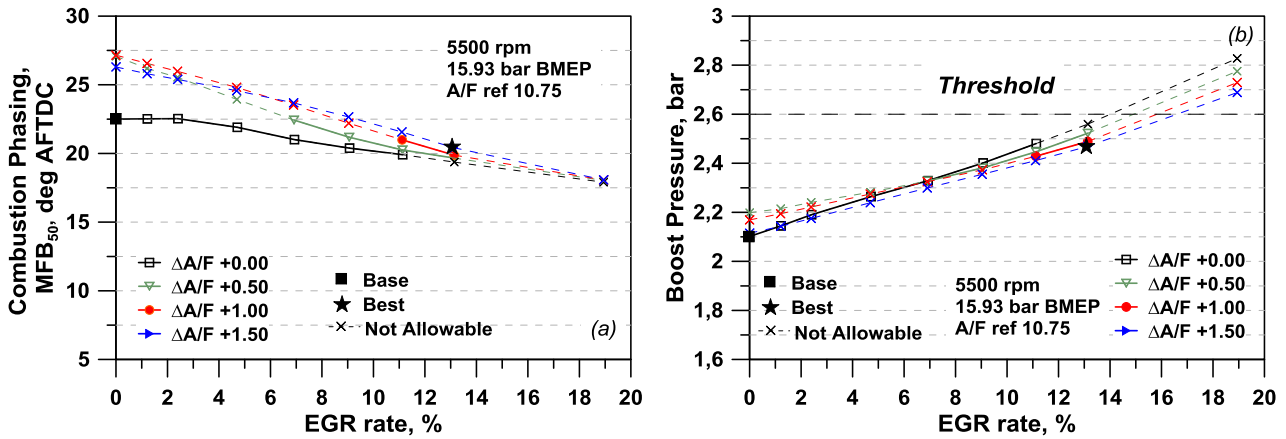


Figure 5.10 – MFB_{50} vs. EGR rate (a) and Boost pressure vs. EGR rate (b) at 5500 rpm.

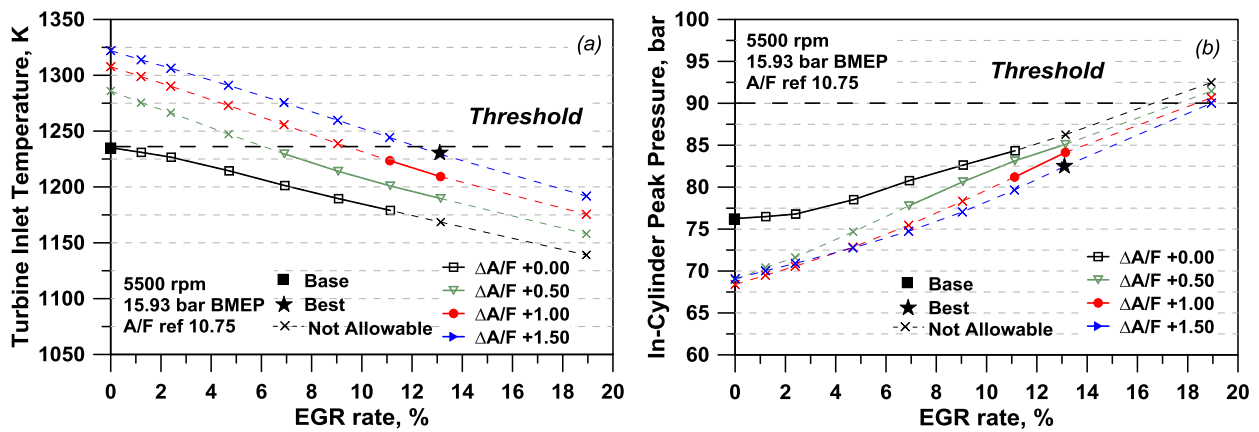


Figure 5.11 – TIT vs. EGR rate (a) and In-cylinder peak pressure vs. EGR rate (b) at 5500 rpm.

In the operating points 2500@21, 3300@21 and 4400@18, as expected, an intermediate behaviour between the discussed results at 5500@16 and 2100@20 is observed, while at 1500@17, where the A/F is almost stoichiometric in the Base calibration, the BSFC improvements mainly come out from a re-phasing of the combustion process.

Table 5.2 summarizes the “Base” and “Best” operating points here analyzed. It can be noted that the maximum BSFC improvement (32.8%) is obtained at 2500 rpm. The latter point shows a similar behavior of the first examined point (2100@20), where both a reduced over-fuelling and a more advanced combustion phasing can be actuated without exceeding the prescribed limitations on TIT, boost level, or compression-ignition occurrence.

As a final consideration, it should be recognized that, on the real engine, any increase in the residual gas causes a higher cycle-by-cycle variation. The latter can only be roughly taken into account in a

1D modeling environment [103], [109]. However, experimental observations showed that IMEP cyclic fluctuations should remain under an acceptable level, provided that the EGR percentage does not exceed 25-30% [130]. The best solutions identified in the proposed analyses never approach the above critical range, thus preserving the consistency and reliability of the presented results.

Operating condition		no-EGR (“Base” points)			Optimal EGR (“Best” points)				
Engine Speed, rpm	BMEP, bar	BSFC, g/kWh	MFB50, deg	A/F,-	BSFC, g/kWh	MFB50, deg	A/F,-	EGR, %	BSFC improvement, %
1500	16.62	289.1	30.6	14.32	254.7	21.9	14.5	17.1	11.9
2100	20.42	338.2	36.3	12.88	250.4	22.9	14.5	19.3	25.9
2500	20.6	376.7	38.2	12.06	250.0	22.3	14.5	19.5	32.8
3300	20.77	372.4	31.1	11.25	257.3	24.2	14.5	18.2	30.9
4400	18.53	429.5	29.5	10.60	429.5	29.5	10.60	0	0
5500	15.96	409.4	22.5	10.75	348.4	20.4	12.25	13.1	14.9

Table 5.2 – Summary of the engine performance in the base and EGR-optimized calibrations.

CHAPTER 6

Port Water Injection to improve fuel economy and reduce knock occurrence

6.1 Employment of water injection technique for Spark Ignition engine

As known, spark ignition engines may exhibit knock or even pre-ignition phenomena at high loads operation. Both phenomena have to be avoided to preserve the engine safety. To this aim, different knock suppression techniques have been proposed and analysed in the current literature. Among the proposed methods [9], a very interesting technique is represented by the water injection in addition to the previously discussed external cooled EGR. Concerning the water injection technique, it can be adopted for a modern SI engine involving minor modification to its architecture and employing components of well assessed technology, such as a low pressure injector. The introduction of inert, due to water injection (WI), in the engine combustion chamber reduces the knock tendency mainly thanks to a lowering in the charge temperature during the compression stroke, related to the increased heat capacity of the charge. The reduction in the gas temperature is drastically enhanced in the case of WI, due to the heat subtracted by the water evaporation [141]. In the current literature, several papers have shown from an experimental point of view the potential of water injection technique in terms of knock mitigation at full load. Soyelmez et al. [142] experimentally studied its effects on the performance of a naturally aspirated 4-cylinder LPG SI engine at a constant throttle valve setting. In particular, five different water-to-fuel (W/F) ratios, namely 0, 0.125, 0.2, 0.33 and 0.5, at various engine speeds, ranging from 1000 to 4500 rpm, were considered. The spark timing was always set at the maximum brake torque (MBT) value. The results pointed out that the engine torque, power and brake thermal efficiency improved as the W/F ratio increased, attaining maximum benefits at the maximum investigated W/F ratio. The results also showed that the BSFC and the exhaust gas temperature decreased as the W/F ratio increased. In [143], Busuttil and Farruggia experimentally investigated the water injection effects with reference to a single cylinder SI engine for various spark timings, engine speeds and pressure levels in the intake manifold. The proposed results showed that a maximum torque improvement of 16 % is obtained with a fuel-to-water ratio of 4.65 by volume. In [141], a single cylinder research engine equipped with two direct water-injectors is tested. A potential increase in the efficiency of 3.3% – 3.8% was found in the region of the minimum BSFC through a combination of water injection, Miller cycle and cooled

external EGR. More significant efficiency improvements around 16% were obtained at low speed and high load, mainly thanks to a combustion phasing optimization. Concerning the study of water injection from a numerical point of view, very few papers are indeed available in the current literature. In [21], a high performance turbocharged engine was analysed by a 3D approach, where the water was port injected to replace mixture enrichment, while preserving the indicated mean effective pressure and the knock safety margin. The proposed results highlighted that the water injection allowed the spark advance to be increased, while maintaining the load target with a simultaneous relevant reduction in the BSFC. Boretti [144] analysed by a 1D model the effects of WI for a turbocharged SI engine fuelled with pure ethanol. Numerical findings highlighted that the port-injection of liquid water involved the possibility to apply higher compression ratios and/or boost levels, and/or spark advances closer to the MBT. Both combustion and knock phenomena were modelled by simplified approaches (Wiebe-like function and Douaud and Eyzat model [116], respectively), which do not directly take into account the influence of operating parameters such as the A/F ratio and the inert content. Based on the above literature overview, 3D approaches prove to be very useful in better understanding and predicting with higher accuracy the effects of inert (water) on the in-cylinder 3D phenomena (inert and fuel spatial distribution, flame front distortion, etc.). On the other hand, in order to foresee the actual advantages of the WI technique, a 1D model of the whole engine appears to be a more suitable numerical tool. In this case, however, more advanced combustion and knock models with respect to those employed in the previously recalled literature are mandatory. Water injection exerts thermal and chemical effects on combustion and auto-ignition phenomena, since it modifies the in-cylinder temperature and composition, as well. In addition, especially in a turbocharged engine, application of water injection substantially changes the boost pressure, the air flow rate, the TIT and hence relevant adjustments of spark advance, A/F ratio, waste-gate opening, etc, are expected in a prefixed torque-speed operating point. The effects of the above parameters modify the combustion speed, the maximum temperature, while the knock occurrence has to be hence directly included in the phenomenological combustion through a proper knock model. Only in this way, a preliminary calibration of the engine with an enhanced knock resistance can be numerically identified, together with realistic expected BSFC improvements. In the following, 1D numerical analyses of water injection strategy for the considered turbocharged SI engine are realized with the aim to improve the BSFC under knock-limited operation, through refined “in-house developed” turbulence, combustion and knock models. In particular, the tested engine is re-calibrated in terms of spark timing, boost level, A/F ratio and inert content. The main focus is in fact the application of the recalled numerical model to highlight the BSFC benefits with

WI strategy. The potential of the above methodology, together with the identification of the related optimal engine calibration, will be discussed in the next sections.

6.2 Numerical set-up for water injection investigation

Once verified the consistency of the 1D schematization and of the combustion and knock sub-models, the engine architecture is virtually modified to investigate the effects of the water injection on the engine behaviour, with the aim of improving the BSFC at full load. Starting from the 1D schematization in the base configuration a further 1D engine model is set-up. A water injector is virtually installed in each intake runner (Figure 6.1). A discontinuous injection of water liquid at 25 °C is realized. It is assumed that 30% of total mass of water vaporizes immediately upon the injection. Water condensation and evaporation are also enabled within the intake pipes, depending on the actual pressure and temperature of gas. Once entered the cylinder, liquid water evaporates according to an assigned profile, so to have a complete transition in vapour phase at the combustion start.

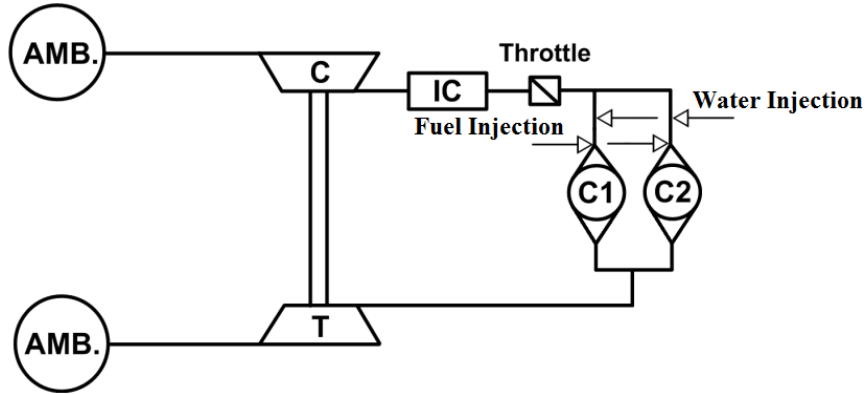


Figure 6.1 – Engine layout with water injectors.

As an example, Figure 6.2 shows the installation of the water injector (called “iniettore water”) for each intake runner within the whole 1D engine model. The single water injector requires the definition of location along the pipe, the nozzle characteristics, the injection timing, the specification of “fluid object” (water species) and the injected fluid temperature. In addition, the ratio between air mass flow rate and water flow rate has to be specified for the water injector:

$$\alpha_w = \frac{\dot{m}_{air}}{\dot{m}_w} \quad (6.1)$$

The latter can be easily adopted to define a more suitable parameter, representing the ratio between the water mass flow rate and fuel mass flow rate:

$$W/F \text{ ratio} = \frac{\alpha}{\alpha_w} \quad (6.2)$$

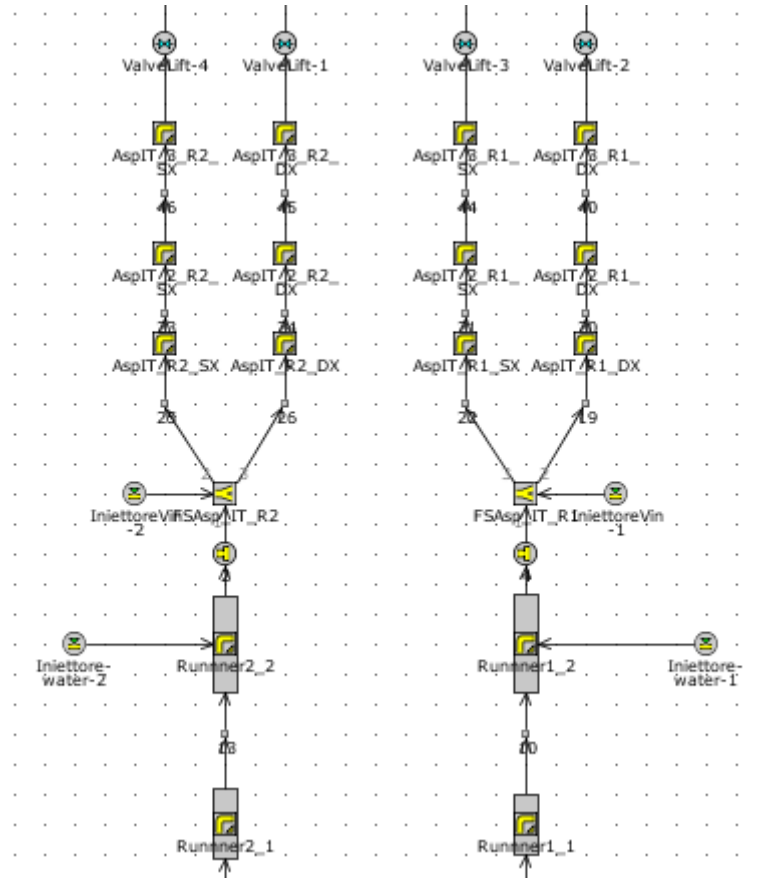


Figure 6.2 – Installation of water injectors in 1D engine model along the intake runners.

For the modified engine configuration, parametric analyses are carried out at various A/F ratios and inert content in six operating points at full load, as reported in Table 6.1. In the WI configuration, the duration of the water injection is selected in order to realize seven different water-to-fuel ratios, ranging from 0 up to 0.5. The upper limit for the W/F ratio is chosen according to the maximum experimentally investigated values in [141], [142]. The above small value should guarantee that all the injected water actually evaporates, hence contributing to the in-cylinder charge cooling.

Case #	Case label	Engine Speed, rpm	BMEP, bar
1	5500@16	5500	15.96
2	4400@18	4400	18.53
3	3300@21	3300	20.78
4	2500@21	2500	20.60
5	2100@20	2100	20.42
6	1500@17	1500	16.62

Table 6.1 – Summary of the considered operating conditions.

In all the simulations, the spark timing is automatically modified to realize operation at the knock onset. The same knock threshold assumed for the model validation in the base configuration is also applied in presence of water. The waste-gate valve opening is adjusted by a PID controller targeting the prescribed load levels of Table 6.1. Numerical results are then post-processed to verify the respect of the following constraints:

- boost pressure, below 2.6 bar;
- turbocharger speed, below 255000 rpm;
- in-cylinder peak pressure, below 90 bar.

The boost pressure has to be controlled to provide proper operation for the injectors and for the intake manifold. The maximum in-cylinder pressure has to be limited below the prescribed threshold to preserve engine mechanical safety. Although a value of 90 bar represents the maximum allowable peak pressure level suggested by the engine manufacturer, in the standard calibration of the considered engine the peak pressure never exceeds 80 bar. The mechanical and thermal safety of the turbine moreover obliges to control the turbocharger speed and the turbine inlet temperature (TIT). A case-dependent TIT threshold is assumed, corresponding to the numerical TIT attained in the base engine configuration.

6.3 Results discussion

The numerical results show that the introduction of water within the combustion chamber involves BSFC reductions for all the examined points. Once again, maximum improvements strictly depend on the possibility to modify the monitored parameters (TIT, boost pressure, in-cylinder peak pressure) up to their prescribed limits. In this paragraph, the outcomes of the parametric WI analysis for two selected operating points, namely 2100@20 and 5500@17, are firstly discussed in detail. Then, a summary of the BSFC advantages for all the examined points with the considered technique is reported, describing the re-calibration of the engine control parameters required to get the above benefits. For the first considered operating point, i.e. 2100@20, an increase in the W/F ratio always involves a better fuel consumption, (Figure 6.3). Similarly, the BSFC reduces as the A/F ratio increases, reaching minimum values at the stoichiometric A/F ratio. The latter, however, affects the combustion phasing (Figure 6.3), since less over-fuelling determines more critical knock condition. Dashed lines in the Figures indicate operating conditions which do not respect one or more limitations. Referring to Figure 6.3a, the “Best” allowable calibration (star symbol) is realized with a W/F ratio of 0.3, resulting in a BSFC benefit of about 100 g/kWh with respect to the “Base” calibration.

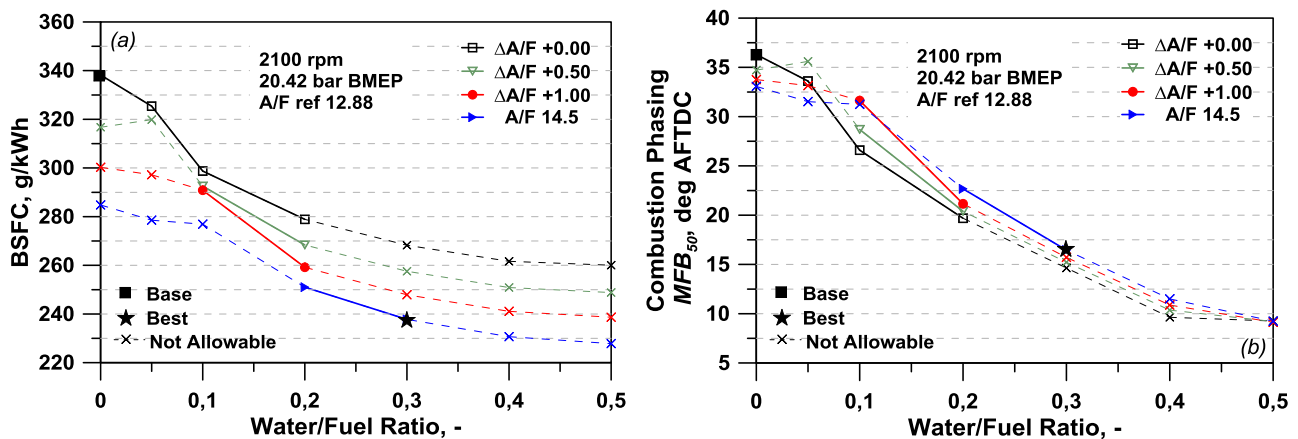


Figure 6.3 – BSFC vs. W/F ratio (a) and MFB_{50} vs. W/F ratio (b) at 2100 rpm.

The injection of liquid water does not substantially affect the cylinder filling, and hence no boost recovery is required (Figure 6.4a). On the contrary, a much better combustion phasing (Figure 6.3b) and an increased amount of working fluid during the expansion stroke involve a reduction in the boost level to maintain the assigned load, as confirmed by the experimental observations in [141].

Figure 6.4b shows that a reduction in the TIT occurs at increasing W/F rates, while the A/F ratio has an opposite effect. The TIT exceeds the assigned constrain at low W/F levels and reduced mixture fuelling, determining unallowable conditions. Figure 6.5a highlights the effects on combustion duration caused by the introduction of inert content (due to water injection). As expected, the latter increases with the water injection content, due to a lower laminar flame speed [130], [140]. In the present case, it must be considered that even a W/F ratio of 0.5, for a stoichiometric mixture, corresponds to an inert rate, $\dot{m}_W/(\dot{m}_{air} + \dot{m}_W)100$, of about 3.5%, thus affecting the laminar speed in a negligible extent. On the other hand, a better combustion phasing determines an opposite prevailing effect, thus finally resulting in a shorter combustion duration (Figure 6.5a) [141]. The latter causes pressure cycles characterized by an increased peak pressure with respect to the Base calibration (Figure 6.6a), that exceeds the assigned threshold, hence limiting the BSFC advantages at the higher W/F ratio (Figure 6.5b). The overall BFSC improvements actually arise from the balance among main “pros” (better combustion phasing and reduced over-fuelling) and “cons” (slower combustion, higher peak pressures). At 2100@20, fuel economy is improved thanks to both a mixture dilution (Figure 6.3a) and a combustion phasing advance (Figure 6.3b). The BSFC advantages related to the WI technique are limited by the in-cylinder peak pressure, resulting in a maximum W/F rate of 0.3.

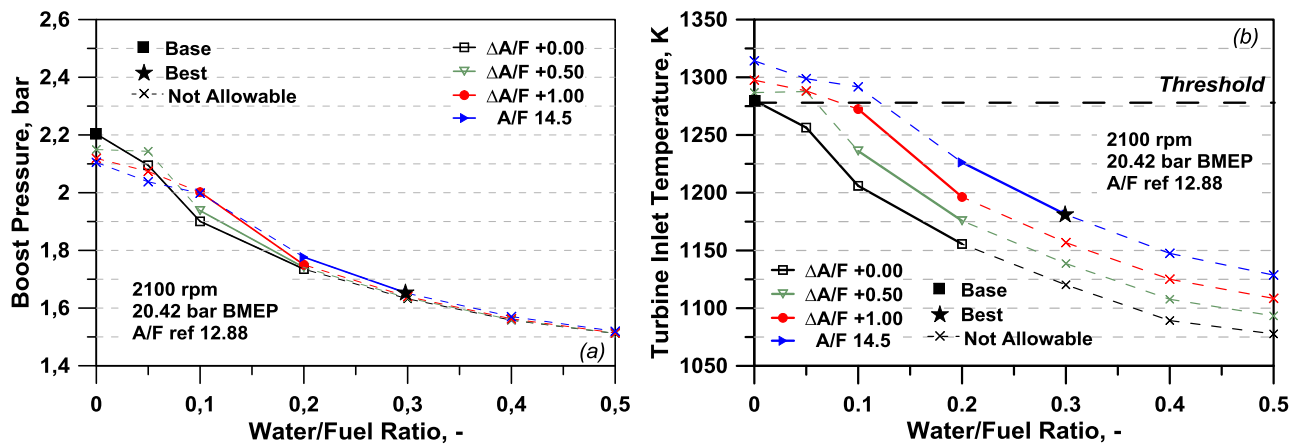


Figure 6.4 – Boost pressure vs. W/F ratio (a) and TIT vs. W/F ratio (b) at 2100 rpm.

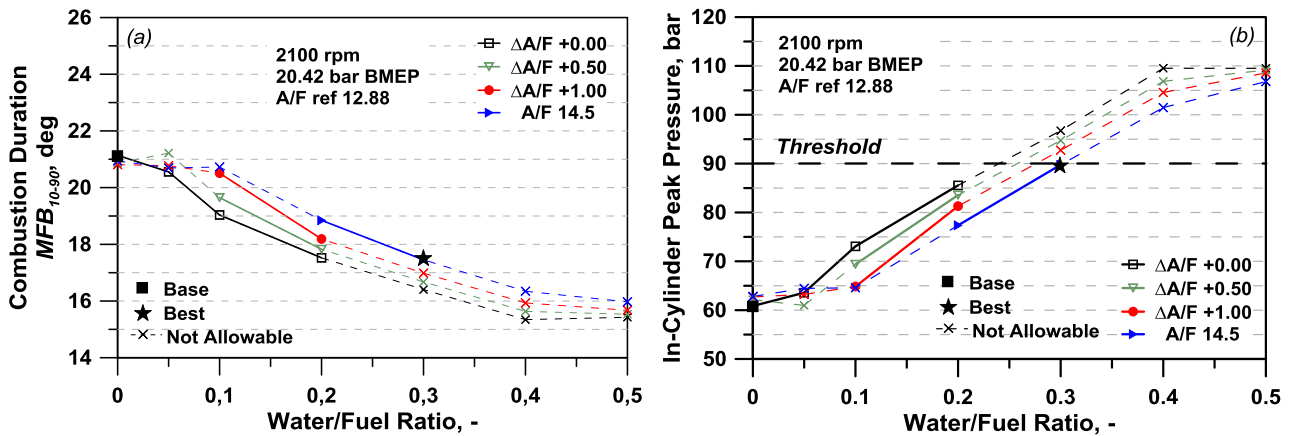


Figure 6.5 – Combustion duration vs. W/F ratio (a) and In-cylinder peak pressure vs. W/F ratio (b) at 2100 rpm.

To deepen the understanding of inert effects on knock resistance, the in-cylinder pressure and temperature cycles in the Base and Best WI calibrations are depicted in Figure 6.6a and Figure 6.6b, respectively. With reference to the Best WI calibration, the heat subtracted by the water evaporation causes a lower temperature during the compression stroke (Figure 6.6b). This of course reduces the knock tendency, allowing an advanced combusting phasing with respect to the Base case. The latter, together with a faster combustion process, causes a higher peak pressure as shown in Figure 6.6a. The constraint on the maximum allowable in-cylinder peak pressure limits the advance in the spark timing and reduces the BSFC potential benefits.

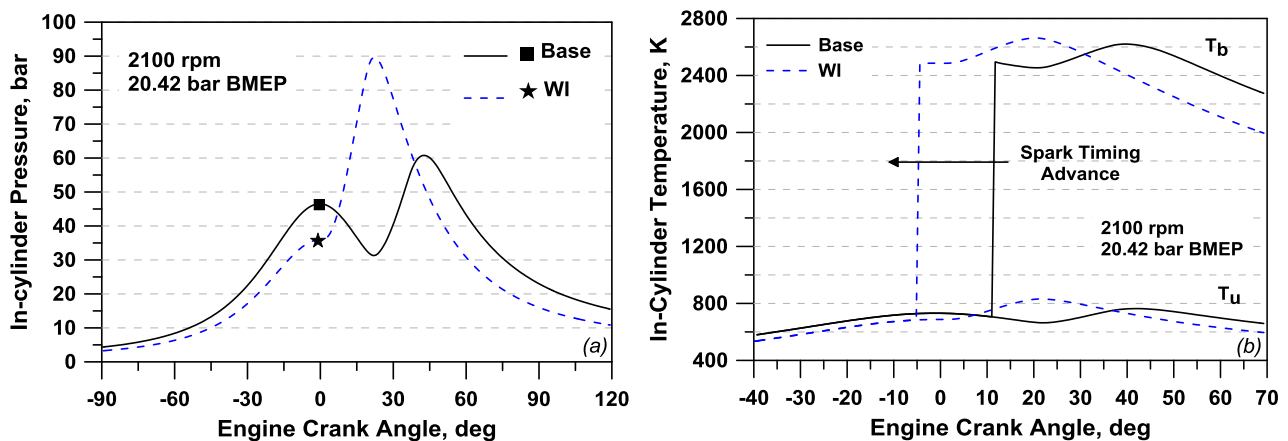


Figure 6.6 – Comparison of in-cylinder pressure (a) and temperature (b) cycles for base and Best WI calibrations at 2100 rpm.

As said, the second operating point discussed in detail in this section is 5500@15. As shown in Figure 6.8a, a W/F ratio of 0.2 is enough to reach an optimal combustion phasing of 9 degrees after the firing TDC. As a consequence, any further increase in the water amount does not involve significant BSFC improvements (Figure 6.7a). The potential fuel economy advantages are restricted by TIT (Figure 6.9a) and the maximum allowable in-cylinder peak pressure (Figure 6.9b), that limit the maximum allowable W/F ratio to 0.05. Consequently, just a reduced increase in the A/F ratio is permitted, resulting in a BSFC saving of about 59 g/kWh. As expected the boost pressure reduces with the allowable increase in the W/F ratio (Figure 6.8b), without any problem on the prescribed threshold. The pumping work also reduces with an increase in the W/F ratio and for lower over-fuelling (Figure 6.7b). Although the WI result for this operating point is practically the same obtained with EGR strategy, the identified calibrations are very different: while for EGR technique, a large mixture leaning and a small combustion advance are required, for WI the opposite occurs.

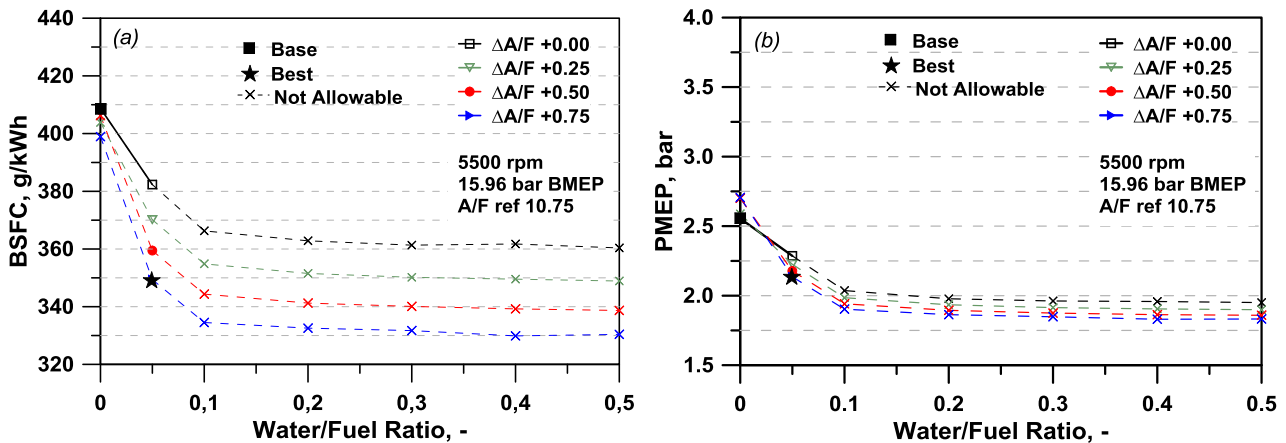


Figure 6.7 – BSFC (a) and PMEP (b) vs. W/F ratio at 5500 rpm.

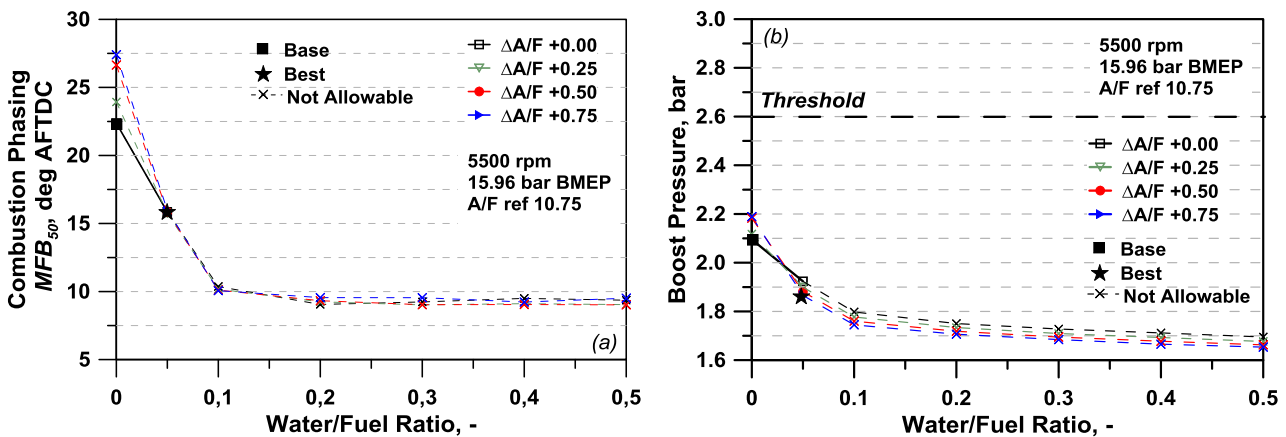


Figure 6.8 – MFB_{50} (a) and Boost pressure (b) vs. W/F ratio at 5500 rpm.

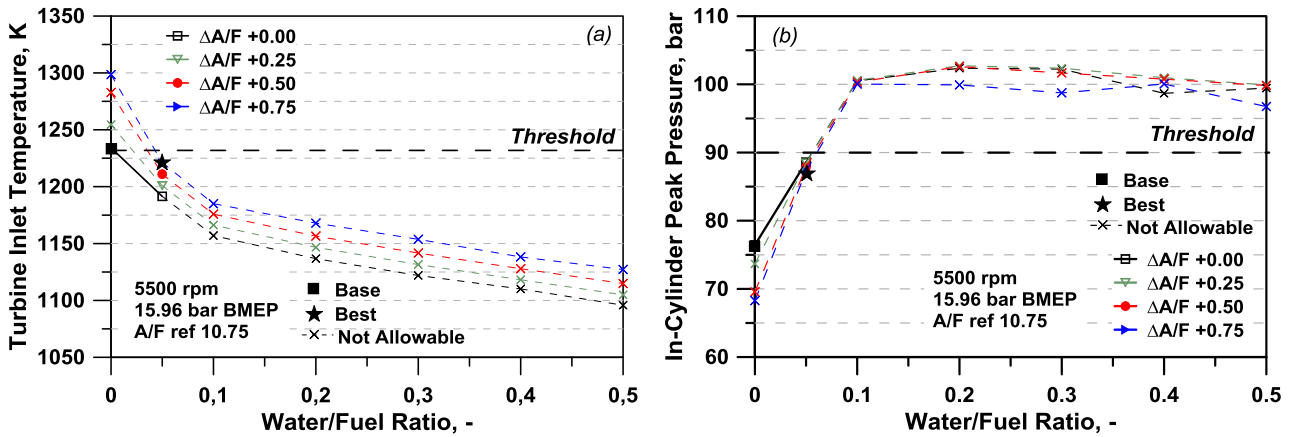


Figure 6.9 – TIT (a) and In-cylinder peak pressure (b) vs. W/F ratio at 5500 rpm.

Table 6.2 reports a summary of the results obtained by WI analyses for the considered operating points. In particular, for each operating condition, base and best WI calibrations are shown. It can be noted that at the lowest engine speed point (1500@17) BSFC improvements are mainly ascribed to an advanced combustion phasing since that the A/F ratio is almost stoichiometric in the base calibration. At higher engine speeds (i.e 4400@18 and 5500@16) the allowable water/fuel ratio and consequently the BSFC improvements are limited by the constraints on the TIT and on the in-cylinder peak pressure. Therefore, more reduced BFSC benefits are achieved, mainly due to a better combustion phasing and limited mixture leaning. Finally, for the operating points 2500@21, 3300@21 and 4400@18, BSFC reductions are obtained thanks to both a better combustion phasing and a reduced over-fuelling.

Operating condition		no-WI (“Base” points)			Optimal WI (“Best” points)				
Engine Speed, rpm	BMEP, bar	BSFC, g/kWh	MFB50, deg	A/F,-	BSFC, g/kWh	MFB50, deg	A/F,-	Water/fuel ratio, -	BSFC improvement, %
1500	16.62	289.1	30.6	14.32	239.1	10.0	14.5	0.4	17.3
2100	20.42	338.2	36.3	12.88	237.7	16.45	14.5	0.3	29.7
2500	20.6	376.7	38.2	12.06	247.6	21.5	14.5	0.2	33.8
3300	20.77	372.4	31.1	11.25	247.7	18.3	14.0	0.2	33.5
4400	18.53	429.5	29.5	10.60	374.4	21.0	10.85	0.05	11.6
5500	15.96	409.4	22.5	10.75	349.4	16.0	11.5	0.05	14.5

Table 6.2 – Summary of the considered operating conditions.

6.4 Comparison between cooled EGR and WI techniques

A comparison between the results, deriving from the previous 1D analyses with the adoption of the cooled EGR system and the water injection technique, is here discussed for the full load cases of the tested SI engine. Figure 6.10-Figure 6.13 summarize the BSFC and the main calibration parameters in the Base, Best EGR and Best WI solutions obtained in each considered operating point. Referring to those Figures, the BSFC advantages related to both EGR and WI techniques (Figure 6.10) arise from the possibility to reduce or even cancelling the mixture over-fuelling (Figure 6.11a) and to advance the combustion process (Figure 6.11b). The latter effect is enhanced with the WI technique, where the heat subtracted by the water evaporation more highly reduces the knock tendency, especially at lower engine speeds. Indeed, at the higher engine speeds the imposed constraints on the TIT and on the in-cylinder peak pressure oblige to still adopt a rich air-to-fuel ratio, with smaller BSFC improvements.

Figure 6.12 shows the EGR and W/F percentages in the best calibrations at each considered operating point. The latter underlines that the EGR level can always reach the amount corresponding to a fully opened EGR valve, excepting the points at higher speeds, where the constraint on the boost pressure obliges to recirculate lower percentages of exhaust gases, hence limiting the fuel economy. Concerning the WI solution, a decreasing water amount is admitted as the engine speed increases, mainly due to the limit on the in-cylinder peak pressure.

BSFC results presented in Figure 6.10 are also depicted in Figure 6.13b in terms of percent variation with respect to the Base calibration, denoting improvements in the range 25-30% in the operating points at low/medium speeds, namely 2100@20, 2500@21 and 3300@21. As clearly pointed out by the previous discussion, the above values strictly depend on the constraints posed by the engine and turbocharger safety. As an example, if the limit on the in-cylinder peak pressure decreases from 90 bar down to 80 bar, less important BSFC improvements can be obtained, as shown in Figure 6.13a. On the contrary, if the allowable maximum in-cylinder pressure raises up to 100 bar, more enhanced advantages on BSFC can be obtained, especially with the WI technique at the higher speeds. Of course, in the latter case a redesign of the cylinder head and piston will be required to preserve their mechanical safety.

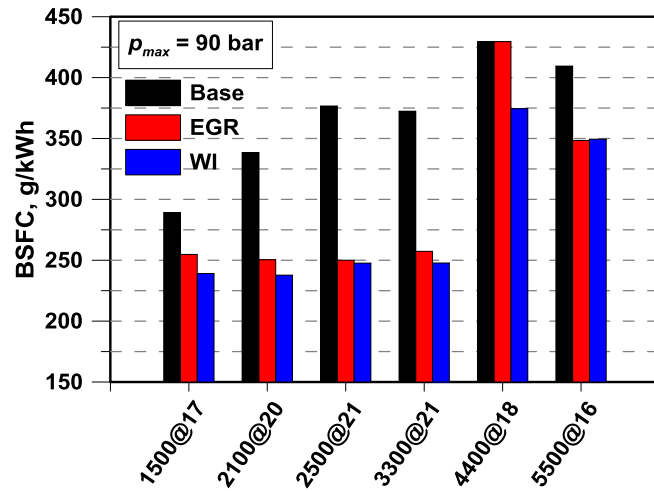


Figure 6.10 – Comparison among Base, Best EGR and Best WI calibrations.

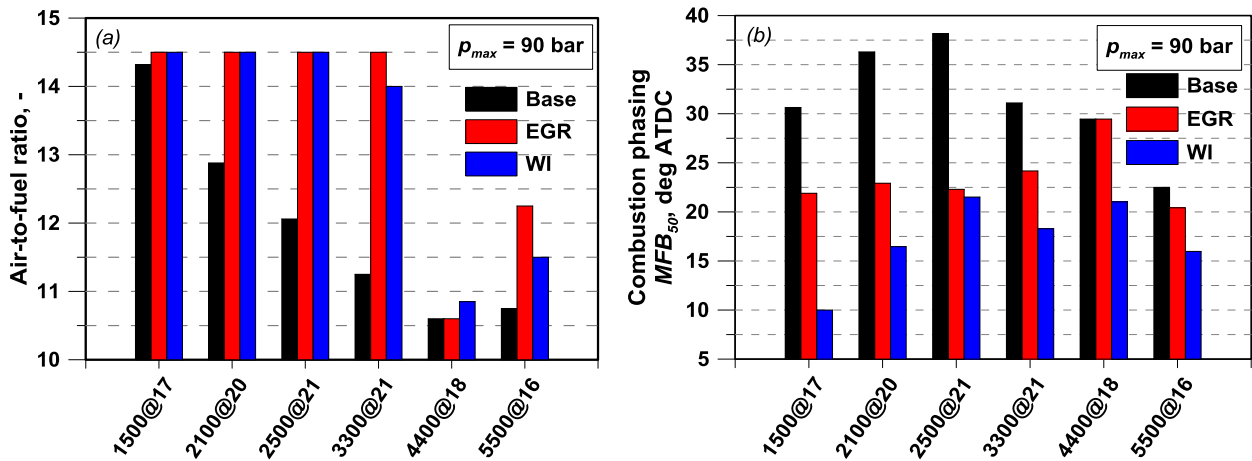


Figure 6.11 – A/F (a) and MFB₅₀ (b) comparison among Base, Best EGR and Best WI calibrations.

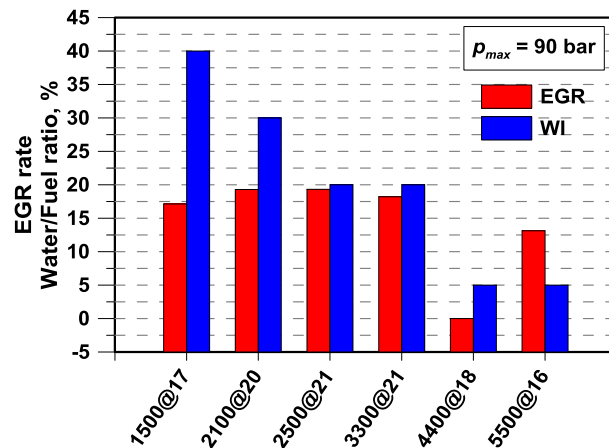


Figure 6.12 – EGR rate and water-to-fuel ratio in Best EGR and Best WI calibrations.

It is the case to underline that the above huge BSFC improvements are not ensured in practical applications, since they would require a perfect control system, able to operate the engine always as close as possible to prescribed TIT, boost pressure and in-cylinder peak pressure constraints. As an example, with reference to the Best EGR calibration at 5500@16 (Figure 5.9a), if the EGR percentage becomes higher (lower) than 13%, the constraint on the boost pressure (on the TIT) is violated. A very reduced EGR operating domain is hence admitted. This issue becomes even more felt in the case of transient manoeuvres. As a consequence, an engine calibration less close to the prescribed constraints is recommended, although resulting in lower BSFC improvements. Similar problems occur in the Best WI calibration at 5500@16 (Figure 6.7a), as soon as the W/F ratio moves from 0.05.

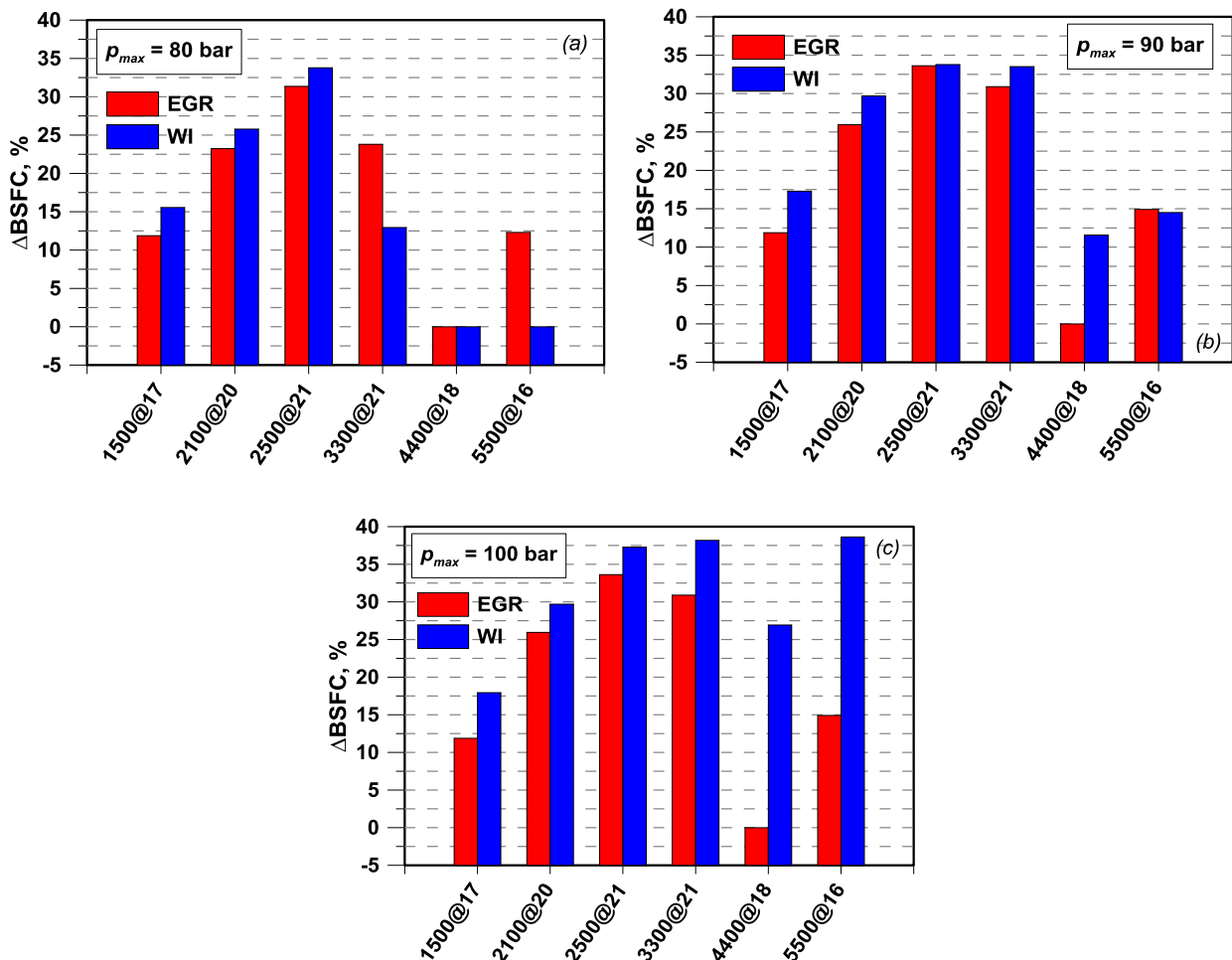


Figure 6.13 – Percent BSFC improvement of Best EGR and Best WI calibrations with respect to the Base one with a maximum in-cylinder pressure of 80 bar (a), 90 bar (b) and 100 bar (c).

Summarizing, for the downsized engine under investigation, a huge mixture enrichment (Figure 6.11a) and a delayed combustion (Figure 6.11b) are the only operating parameters that allow to respect TIT constraints and a knock free operation in the standard configuration. The analyzed strategies, both EGR and WI, demonstrate to have the potential to mitigate the knock tendency, allowing an engine re-calibration that produces very high BSFC improvements, while respecting the prescribed limitations. This may be not the case for other engine architectures, even considering similar operating conditions.

Concerning the practical application of EGR and WI techniques, it should be recognized that, on a real engine, any increase in the inert gas causes higher cycle-by-cycle variations. The latter can only be roughly taken into account by a 1D modelling approach [110], [145]. However, experimental observations showed that IMEP cyclic fluctuations should remain under an acceptable level, provided that the EGR percentage does not exceed 25-30% [130]. The Best EGR solutions identified in the proposed analyses never approach the above critical range, thus preserving the consistency of the presented results. For the WI technique, no critical problem, both in terms of combustion stability and completion of the water evaporation, is pointed out in the experimental analyses in [141], [142], where W/F ratios up to 0.6 are considered. Since the presented WI results refer to a maximum W/F ratio of 0.5, also the results in presence of WI can be deemed reliable. As far as engine layout issues are concerned, a cooled EGR circuit only requires a water/gas heat exchanger and a recirculation valve. The above components of course contributes to increase the engine complexity and weight. In addition, both may clog up after a certain period, affecting the engine operation and control. In the case of a low pressure EGR circuit, as the one here considered, the impurity and the combustion residuals in the evolving gas may also damage the compressor blades.

On the other hand, the WI technique requires less severe modifications of the engine layout. In fact, only a low pressure ported injector (similar to the fuel injector) has to be installed along the intake runners. Of course, the installation of an additional tank for the water storage would be required, with the consequent need of a periodic supplying. However, its volume will be much smaller than the gasoline tank, since the WI has to be actuated only when the engine works under knock-limited operation and, in those cases, the water amount will be just a fraction of the fuel, at maximum one half. The need of a periodic supplying can be moreover overcome by the concept proposed in [146], where the water vapour in the exhaust gas condensates to supply a buffer tank. Anyway, once again a more complex exhaust system architecture would be necessary, including the installation of a condenser. This solution appears hence attractive only if coupled to a further waste heat recovery

system, such as an ORC system [147]. Summarizing, both the solutions pose practical issues to deal with for their in-series application. The modifications and technologies related to the EGR solution have been successfully developed in the past years for diesel engines, hence appearing of straightforward application to gasoline engines, too. The WI involves the installation of components (tank and injector), whose technology is once again well assessed. In this case, additional issues related to system reliability in terms of corrosion, ice formation, etc., require further experimental analyses.

CHAPTER 7

Gas-dynamic noise prediction and re-design of the air-filter box to improve the acoustic performance

7.1 Introduction

Nowadays the transportation systems are recognized as the main source of the air pollution and a special attention is devoted to this issue in the urban areas where a very high concentration of vehicles occurs. In particular, vehicles equipped with the internal combustion engines (ICEs) are responsible not only for the increase in the noxious emission but also for contributing to the noise pollution. Different noise sources can be identified in a vehicle such as the engine, the intake and exhaust systems, the mechanical transmission, the tires etc. In the automotive field, significant efforts are being made, especially during the design phase, to improve the acoustic performance of vehicles and to ensure a better comfort within the car interior. Indeed, the vehicle components are designed also considering the noise level that they generate during the engine operation together with the optimization of the energy conversion process.

The intake system gives an important contribution to the vehicle noise, since it is usually responsible for 25-50% of the overall radiated noise [148]. The design of the intake system for an ICE takes into account, in addition to an acceptable acoustic performance, the delivered power, the mechanical functionality and the geometrical constraints imposed by the layout of the engine space. Concerning the engine power, the intake system design affects the pressure losses along the circuit and, consequently, the volumetric efficiency. The mechanical design, in terms of layout and material, has to guarantee sufficient reliability and resistance to the mechanical stress and to the corrosion. Concerning the acoustic behavior, the intake system should be designed in order to properly attenuate the pressure waves induced by the alternate opening and closing of the intake valves. In fact, when these pressure oscillations reach the inlet section of the system, they radiate noise to the external environment, determining the so called gas-dynamic noise. Its reduction can be obtained by adopting new design solutions of the intake system, including parallel resonators (Helmholtz and column). In particular, Helmholtz resonators are acoustic attenuation devices at low

frequencies consisting of a neck and a cavity. They can be easily installed along the pipes of the intake system, without incurring in layout constraints.

Currently, 1D and 3D fluid-dynamic simulation codes represent very useful tools to design and optimize the intake air-box system. In fact, they are commonly used to predict the overall system performance, including the gas-dynamic noise emission through a suitable post-processing of the results. In the study of new configurations of the intake system, a pure 1D approach presents some limitations due to a rather rough schematization of the air-box that often presents a complex 3D geometry. However, a refined 1D schematization of the intake system, formed by a network of 0D and 1D components, may provide reliable results.

Anyway, 1D models can be successfully employed to get a first estimation of acoustic performance, while the 3D approach is very powerful to investigate the flow field within complex geometries, allowing for a more accurate prediction of the gas-dynamic noise. In addition, 3D models take much better into account the effect of resonators design. An integration of 1D and 3D CFD models can be employed to improve the design of the intake air-box, with a reduced computational time. In this way, the advantages of two previous approaches can be properly combined.

In the following paragraphs, 1D and 3D CFD analyses for the air filter box of the examined SI- ICE are reported with the aim to identify new configurations of the intake system, capable to ensure a gas-dynamic noise reduction. As said in chapter 1, the considered engine is equipped with a VVA system which controls the lift profile of the intake valves. In this type of engine, the VVA system involves an increased gas-dynamic noise emission at low load, since the reduced throttling of the intake pipes determines a lower attenuation of pressure wave in the intake system. At part load, alternative engine control strategies allow for a reduction in the noise emissions, with some penalties on the fuel consumption, determining a typical trade-off between noise and fuel consumption performance [138]. A reduced gas-dynamic noise emission can be, indeed, obtained through a proper re-design of the air-filter box.

Initially, a proper experimental campaign is performed to measure the gas-dynamic noise at the intake mouth of the air-filter box. Gas-dynamic noise is measured during an engine run-up test at full load and varying the engine speed from 1100 rpm to 6000 rpm. According to the standard ISO, measurements are carried out by using a microphone placed at 1 cm of distance from the intake mouth, as shown in Figure 7.1.

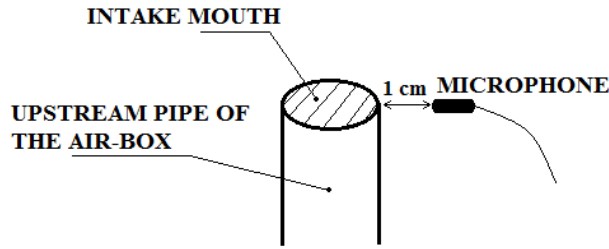


Figure 7.1 – Scheme of the experimental layout.

The microphone signal is acquired by a multichannel system triggered by the rotational speed, in order to perform a tracking analysis. The run-up test is realized at full load with the aim to determinate the nature of frequency peaks in a noise signature and by observing how they change throughout the engine operating speed range. This experimental approach is named “Order Tracking”, whereby the influence of a particular speed-related frequency can be observed. The overall SPL and the first 15 engine orders - defined as multiples of the revolving frequency, rpm/60 - are acquired during the run-up test in dBA scale.

Numerical analyses are performed on the above described engine to compute the overall sound pressure level (SPL) at the intake mouth by using a 1D approach. 1D model is tuned, in terms of the gas-dynamic noise, through the comparison with experimental data. This model overestimates the experimental the gas-dynamic noise. The limitations related to the 1D schematization of the engine, with particular reference to the air-box device, need to be overcome thanks to a more refined 3D CFD approach. 3D simulations, performed with the FLUENT™ package [149], are limited to the air-filter domain. The time-varying pressure profile, derived from the 1D model in the section located just upstream the turbocharger compressor, is used as a boundary condition for the 3D CFD unsteady analysis. The previous numerical and experimental analyses highlight that the maximum radiated noise is reached in a defined frequency range (350-450 Hz). The air-box component is hence re-designed by virtually installing an external resonator and an internal one with the aim to reduce the sound pressure level (SPL) in the frequency range previously identified.

The transmission loss (TL) profiles of the base and re-designed air-box configurations are firstly computed, by using a 3D FEM model, developed within the FEM module of ANSYS™ package.

3D CFD analyses of the re-designed intake systems are performed at different engine operating conditions. A comparison between the two proposed solutions is finally carried out.

7.2 Air-box device: 1D/3D Models Description

The air-box device of the examined engine system is firstly studied by a 1D model. Then a more refined 3D CFD model is considered. Both models are obtained starting from the 3D geometry of the sole air-box device. Detailed descriptions of the above models are reported in the following.

7.2.1 1D Model

A one-dimensional schematization of the original air-box device is developed within the well known GT-PowerTM code [150]. Starting from CAD geometry of the considered system, a proper 1D schematization of the air-filter box geometry is realized. Referring to the previous chapter 3, Figure 3.1 shows the adopted 1D schematization of the air-box device. It is the case to underline that a ‘virtual microphone’ is also taken into account. The latter is located at 1 cm of distance from the intake mouth, according to the actual microphone position during the experimental campaign. As previously said, this object has the function to compute the overall sound pressure level at the intake mouth.

A pure 1D approach presents some limitations due to a rather rough schematization of the air-box, because of its complex 3D geometry. However, a refined 1D schematization of the intake system, formed by a network of 0D and 1D elements, may provide reliable results. Anyway, 1D models can be successfully employed to get a first estimation of the acoustic performance, while the 3D approach is very powerful to investigate the flow field within complex geometries, allowing for a more accurate prediction of the gas-dynamic noise emission.

7.2.2 3D Model

The air-box device of an internal combustion engine is usually a complex 3D component, whose shape is often imposed by the space available within the engine bay. The 1D model of the air-box device involves relevant geometrical approximations which also affect the prediction of the gas-dynamic noise. The described limitations of the 1D schematization can be overcome by means of a 3D CFD model which is able to reproduce in detail the unsteady flow field inside the air-filter box [57] and to perform a more refined acoustic analysis [151]. The CAD model used for the 3D CFD analyses is shown in Figure 7.2. It is obtained by removing from the constructive CAD drawing, the geometrical details not relevant for the 3D analyses.

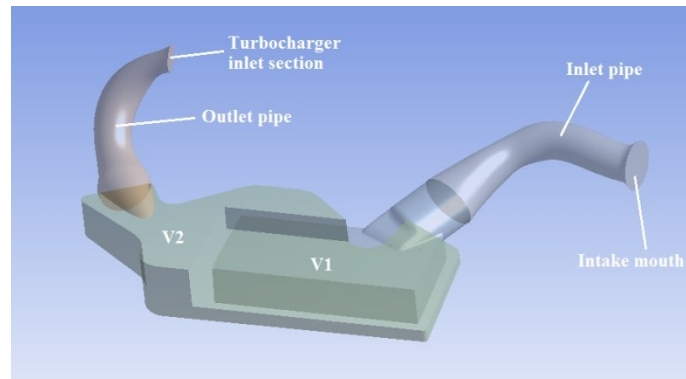


Figure 7.2 – CAD drawing of the original air-box device.

As shown in Figure 7.2, the air box device includes two main volumes, the former (V_1) is substantially a parallelepiped volume connected to the upstream pipe and containing a thin filtering element; the latter (V_2) is connected to the outlet pipe and it presents a more complex shape. An unstructured mesh (Figure 7.3) is realized for the original device within ANSYSTM environment, consisting of 65906 nodes and 201992 elements. A preliminary grid invariance analysis is also performed and the corresponding results are not reported here for sake of brevity. The computational domain includes, in addition to the component geometry, also a spherical shaped volume, centered on the axis of the inlet pipe. The spherical domain allows to compute the pressure field at the virtual microphone, located in the same position as the actual microphone. Concerning the boundary conditions, ambient temperature and pressure are applied all over the spherical surface (pressure-inlet BC), while a time-varying static pressure, derived by the 1D engine model, is imposed in the downstream section (pressure-outlet BC). Referring to the initial conditions, zero velocity, ambient pressure and temperature are specified all over the 3D domain.

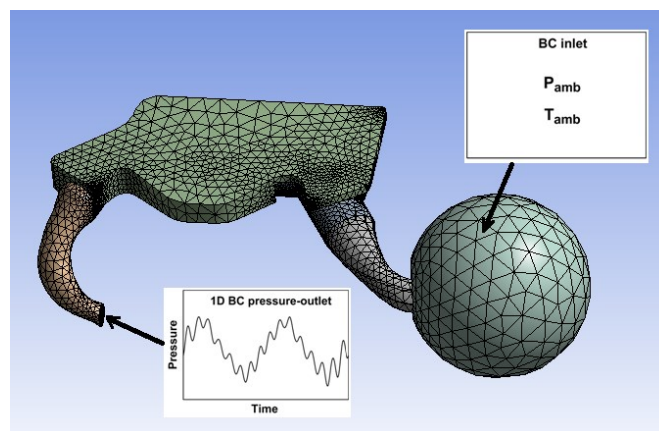


Figure 7.3 – Unstructured mesh of the original air-box device.

Concerning the modeling of the flow field within the air- box device, Reynolds averaged Navier-Stokes (RANS) equations are solved, considering the standard $k-\varepsilon$ turbulence model and adopting a second order upwind discretization in space and time. Pressure and velocity coupling is based on the SIMPLE algorithm [149]. Ten consecutive engine cycles are computed to ensure an accurate periodic solution of the pressure signal at the virtual microphone. The post-processing of the time-varying pressure signal at the microphone allows to compute, by means of a discrete Fourier transform (DFT), the root mean square amplitudes of the pressure signal and the SPL in the frequency domain.

7.3 Refined Turbocharger modeling

In the 1D codes the compressor and turbine behavior is usually described following a quasi-steady map-based approach. The latter is proved to be able to properly reproduce the engine performance both in terms of overall parameters and in-cylinder pressure cycle. On the other hand, the standard methodology does not take into account the dynamic effects inside the turbocharger (wave propagation and the mass and energy storage) and, for this reason, some inaccuracies commonly arise in the modeling of the passive acoustic properties of the compressor and of the turbine. Consequently, the gas-dynamic engine emission may be estimated by a 1D simulation with a unsatisfactory accuracy.

To overcome this issue, several methodologies have been proposed [152], [153]. Most of them includes a detailed 1D schematization of the device [154], [155]. However, these approaches, while improving the wave propagation and the noise passive attenuation inside the device, require the definition of several geometrical data, usually unavailable. In addition, the computational effort is significantly increased because of the fine spatial discretization required for the small pipes that schematize the compressor and/or the turbine.

In this thesis, an enhanced map-based approach is proposed for the description of the turbocharger: it employs the experimental maps, measured under steady state operation, with the introduction of two 0D capacities placed upstream and downstream the compressor and turbine object. The latter are included to take into account the mass and energy storage inside the device. The volumes of the 0D capacities are evaluated by the geometrical module of the turbocharger model developed by researchers of University of Naples in the recent years [156]. In the case of the compressor, the upstream volume coincides with the volume of the inlet duct, while the downstream capacity

includes the volume of the wheel, of the diffuser and, mostly, of the volute. The proposed turbocharger model is implemented in the GT-Power™ environment as a further user routine. The map is inquired based on the pressure ratio between the upstream and downstream capacities and the rotational speed, while the output parameters are the mass flow rate, the exchanged mechanical work and the enthalpy variation across the device.

7.4 Gas-dynamic noise: Validation at Full Load

In a first stage, 1D analyses are realized to evaluate the gas-dynamic noise emission at intake mouth and a standard approach is considered for the description of compressor performance within the 1D engine model. The original air-box device is properly schematized. Gas-dynamic noise is predicted by 1D model at full load operation in the whole engine speed range. 3D analyses are also carried out to estimate the gas-dynamic noise of the original intake system. The unsteady 3D CFD simulations of the original air-box device are performed at full load operation and for the whole engine speed range. In each operating condition, 3D analysis allows to predict the gas-dynamic noise, in terms of the overall SPL and the frequency spectrum, as well. In Figure 7.4, a comparison between the experimental, 1D and 3D computed overall SPL at full load operation is reported.

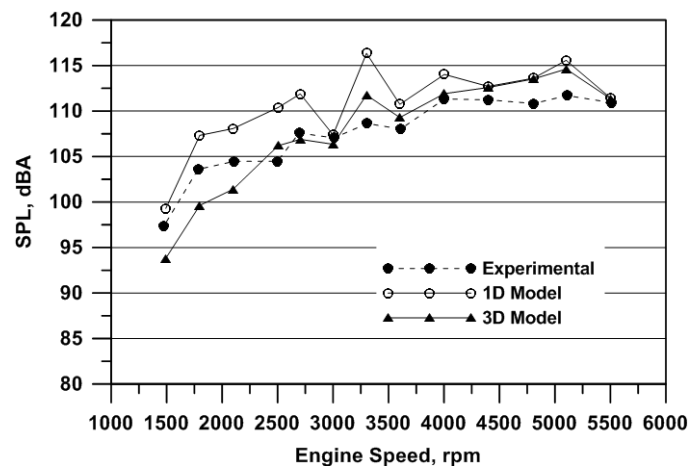


Figure 7.4 – Comparison among the experimental, 1D and 3D Overall SPL at full load.

It can be observed that the trend of 1D results is close to the experimental one, although a significant overestimation is realized, especially for low speeds. This is partly due to the standard

“map-based” description of compressor behavior within the 1D model. According to the 1D approach, the compressor is represented by a volume-less interface where the steady-state compressor map data are applied. The compressor map is obtained from steady-state flow tests and it does not include the effects exerted by pressure waves travelling through the component [149]. This approach, in fact, does not allow to take into account the internal geometry of the compressor and its noise attenuation characteristics [157]. Since the 3D model utilizes a 1D derived BC, the compressor modeling inaccuracies also affect the 3D results. However, significant improvements can be obtained with the 3D model, especially in the medium-high speed range. In Figure 7.5a, Figure 7.5b and Figure 7.5c the frequency spectra of the pressure signal to the microphone are reported for three engine speeds at full load operation, namely 2100, 3000 and 5100 rpm. For each engine speed, the first 15 engine orders are considered in the numerical analysis since they contain most of the gas-dynamic noise energy. As shown in Figures 7.5a, 7.5b, 7.5c, a satisfactory agreement is obtained between the 1D computed SPL and the measurements. 3D results indeed realize a better matching with experimental data in the medium-high frequency range. For each engine speed, the maximum SPL is always reached within the 350-450 Hz frequency range. It should be considered that the latter refers to the gas-dynamic noise resulting from the coupled engine-air-box system. The acoustic performance of the isolated device, obtained by a TL analysis, may actually exhibit a different behavior. In addition to a standard turbocharger model, an advanced user model for turbocharger group has been developed and consequently integrated within the whole 1D engine model with the aim to evaluate the gas-dynamic noise at the intake mouth. In Figure 7.6, the gas-dynamic noise results obtained with the standard and refined turbocharger models are compared with the measured data. In the second case, a more accurate noise prediction is realized, while the standard compressor sub-model furnishes an overestimation of the SPL, especially at low engine speeds. The refined turbocharger model is hence able to better account for noise attenuation exerted by its internal geometry (in particular, the compressor volume) [157].

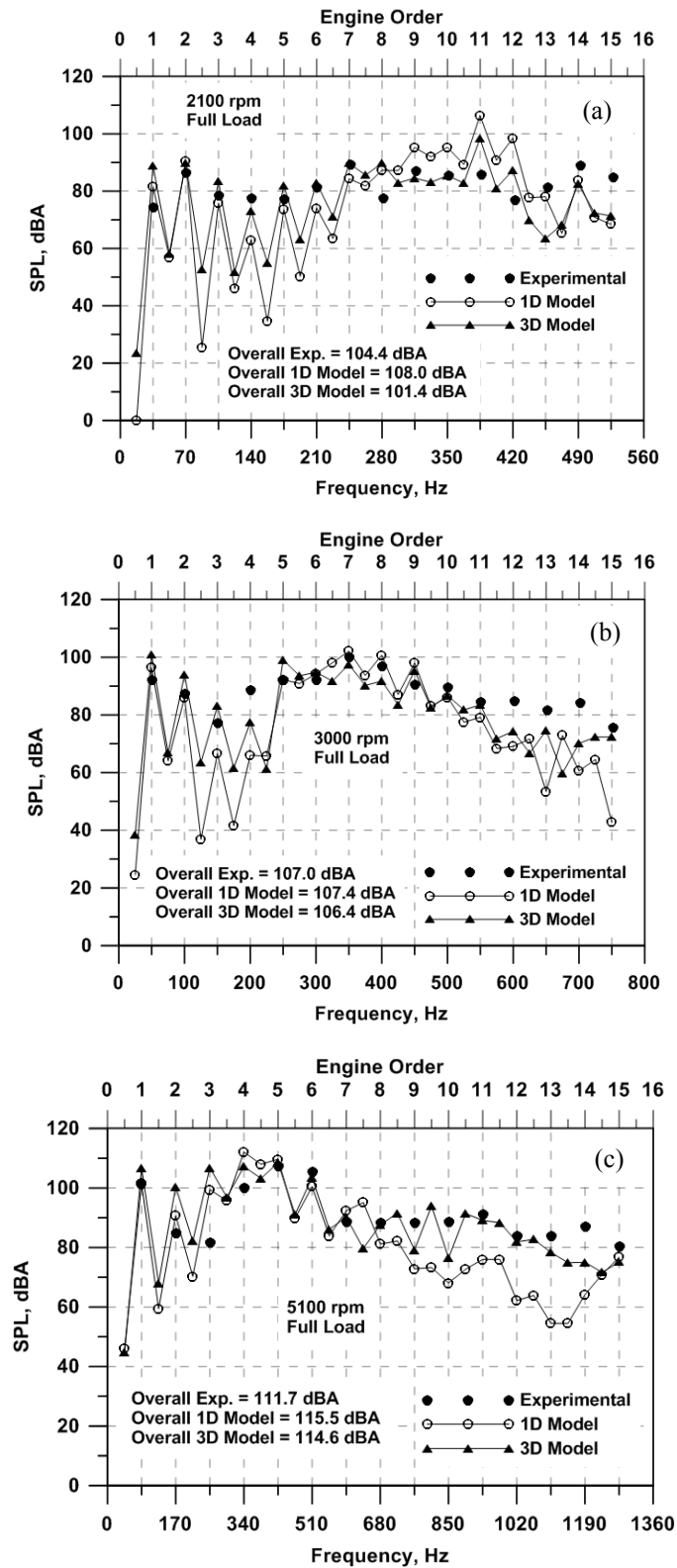


Figure 7.5 – Frequency spectra of the pressure signal to the microphone; (a) : 2100 rpm; (b) : 3000 rpm; (c) : 5100 rpm.

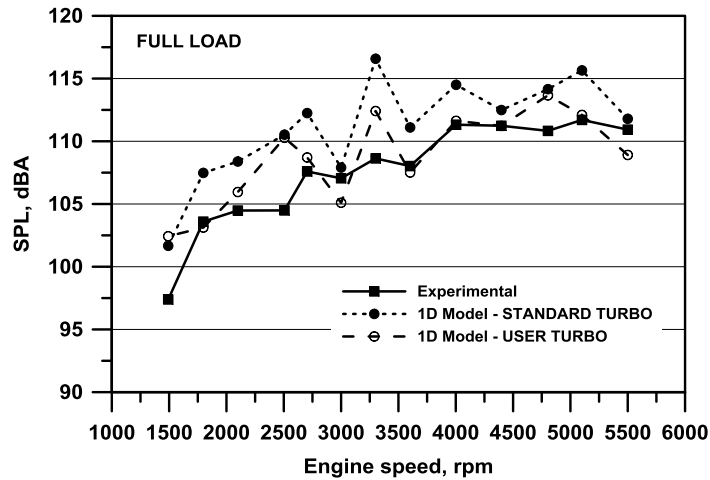


Figure 7.6 – Experimental overall SPL, 1D overall SPL with standard turbo and user one.

As stated above, in a first stage, 3D CFD analyses are performed to evaluate the acoustic behavior of the sole air-box device in the base configuration. To this aim, the model results are validated against the experimental data in terms of gas-dynamic noise at the engine intake mouth (overall SPL and frequency spectrum). The unsteady 3D simulations are still carried out at full load operation for different engine speeds. Figure 7.7 reports the comparison between the experimental and 3D computed overall SPL with standard and refined turbocharger models.

The comparison between Figure 7.6 and Figure 7.7 highlights that the 3D approach improves the gas-dynamic noise prediction. In particular, an accurate agreement between 3D computed overall SPL and experimental one is obtained at medium engine speed, while more relevant errors at low engine speeds occur. However, in the medium-high speed range a slight better noise prediction is achieved by the 3D model with user turbo boundary conditions.

In Figure 7.8, the frequency spectra of the pressure signal at the microphone predicted by the 1D and 3D models employing the refined turbocharger approach, are reported for two engine speeds, namely 2100 and 5100 rpm. In both cases, the first 15 engine orders are considered in the numerical analysis. The latter in fact contain most of the gas-dynamic noise energy.

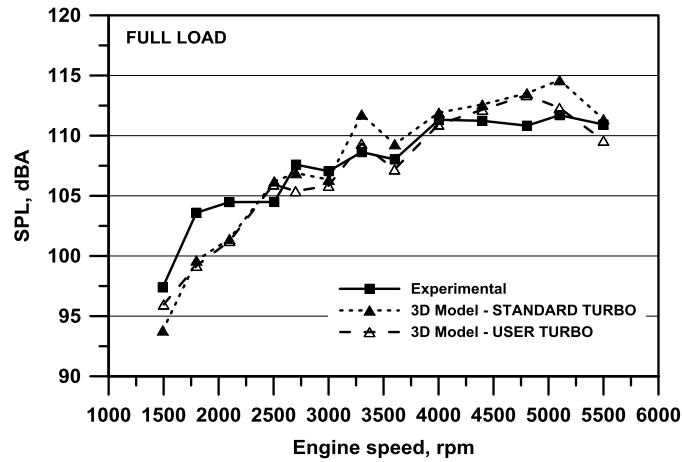


Figure 7.7 – Experimental overall SPL, 3D overall SPL with standard turbo and user one.

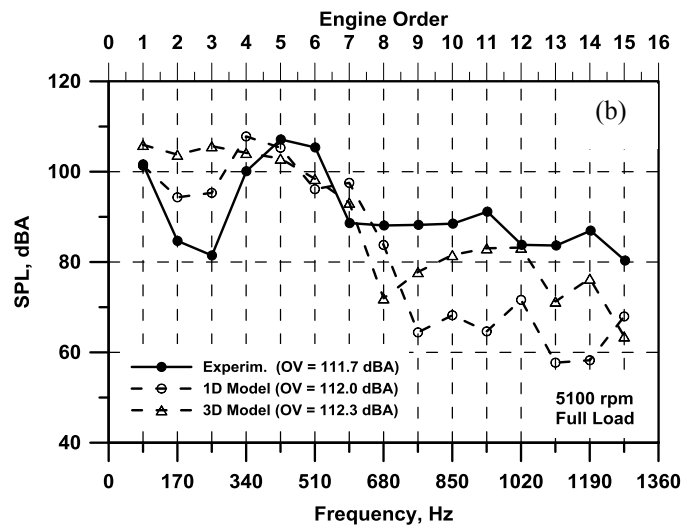
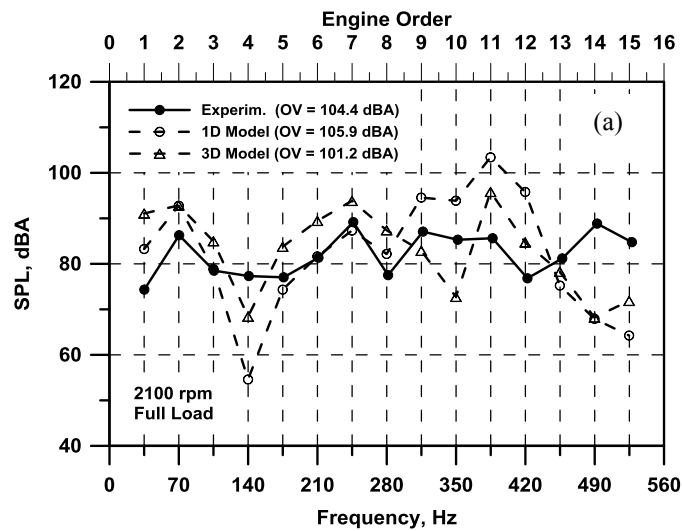


Figure 7.8 – Frequency spectra of the pressure signal to the microphone; (a): 2100 rpm; (b): 5100 rpm.

As shown in Figure 7.8, a satisfactory agreement between the 1D computed and the experimental SPL trends is obtained especially for the lower frequencies, while the 3D model allows to realize an improved matching with experimental data in the medium-high frequency range, as well. For each engine speed, the maximum SPL is always reached within the frequency range 350-450 Hz. Both the internal and external resonators introduced in the subsequent sections will be hence designed to provide substantial noise abatement in the above identified range.

7.5 Air Box redesign

The acoustic performance of the original air-box device is improved through a partial re-design of the component. Two different geometrical configurations of the air-filter box are proposed and subsequently numerically analyzed. The first configuration is obtained by virtually installing an external Helmholtz resonator along the inlet pipe of the air-box, while the second one considers the introduction of an internal resonator within the base air-box. The Helmholtz resonator represents a simple acoustic device formed by a rigid cavity (in the following analyses, only spherical cavities will be considered) and a cylindrical neck which communicates with the inlet pipe (Figure 7.9). It is capable to realize an acoustic attenuation at its natural frequency. The latter depends on the cavity and neck geometries and can be computed by equation (7.1):

$$f = \frac{a}{2\pi} \sqrt{\frac{k_f}{V_c}} \quad (7.1)$$

where a is the speed of sound, V_c is the volume of the cavity and k_f is the fluid-dynamic conductivity of the element that connects the cavity and the pipe [70].

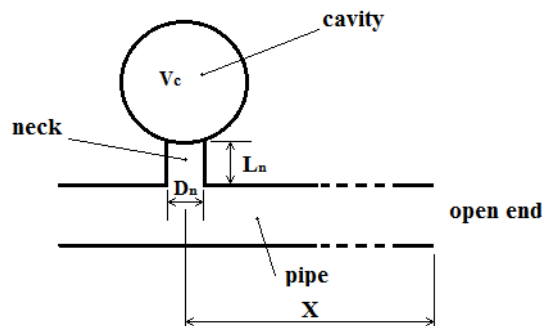


Figure 7.9 – Scheme of a side-branch Helmholtz resonator.

The conductivity k_f of a neck with circular cross-section of diameter D_n and length L_n is given by the equation (7.2):

$$k_f = \frac{\pi \frac{D_n^2}{4}}{L_n + \pi \frac{D_n}{4}} \quad (7.2)$$

An Helmholtz resonator is characterized by different noise attenuation at the resonance frequency, according to the efficiency parameter G_E [70]. The latter parameter is defined by equation (7.3):

$$G_E = \frac{\sqrt{k_f V_c}}{2S_n} \quad (7.3)$$

where S_n is the section of the neck.

A higher value of G_E involves a greater noise attenuation at the resonance frequency and an enlargement of the working bandwidth, as well. As stated above, the Helmholtz resonator is designed with the resonance frequency in the identified critical range, 350-450 Hz (Table 7.1). In addition, the resonator geometry is defined with the aim to maximize the efficiency parameter, while respecting the constraint imposed by the layout of a typical engine bay.

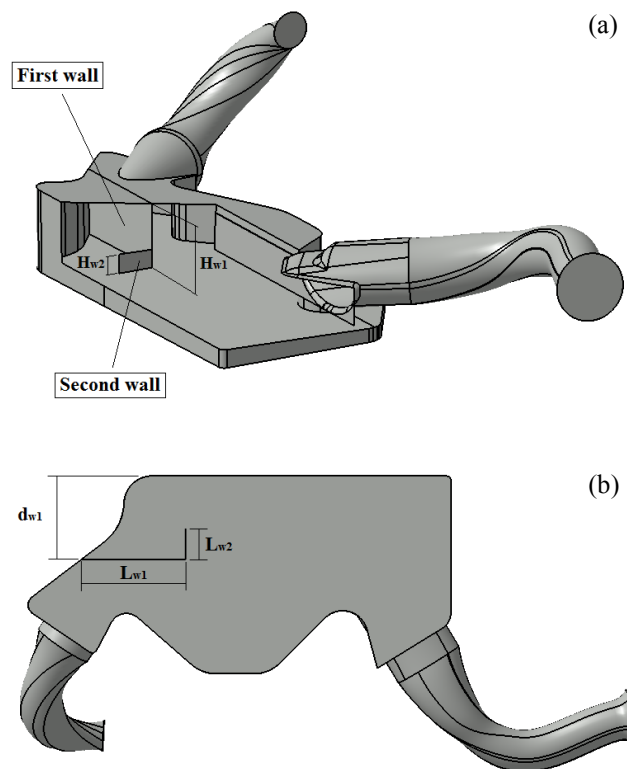


Figure 7.10a-b – Internal walls within the original air-box configuration.

As previously stated, a different path to improve the acoustic behavior of the air-box is the introduction of an internal resonator [148]. It is obtained by the insertion of two rigid internal walls in the base air-box configuration (Figure 7.10a-b). The walls extension and location are identified by preliminary parametric TL analyses, described in the following sections. They are not reported in the paper for sake of brevity. The results shown in the following refer to the configuration that guarantees the best acoustic behavior in the frequency band of interest. It is not worthless to emphasize that this solution does not require an increase in the air-box size, unlike the external Helmholtz resonator solution. Once defined the main design data for the considered resonators, 1D analyses of the whole engine are performed at full load operation in order to verify the absence of relevant influence of the re-designed intake systems on the overall engine performance. 1D results show that a negligible effect on the engine power is obtained by adopting the modified configurations of the air-box device with respect to the base system.

Resonator Type	External	Internal
Configuration	cylindrical neck and spherical cavity	Two internal walls
Position	neck distance from the intake mouth $X=50$ mm	walls installed within the volume V_2 of the air-box
Geometrical Data		
Volume Cavity V_c , mm ³	435864	439360
neck diameter D_n , mm	30	
neck length L_n , mm	4.8	
fluid-dynamic conductivity k_f , mm	24.9	24.24
First wall		
length L_{w1} , mm		113.4
height H_{w1} , mm		58.85
distance d_{w1} , mm		88.9
Second wall		
length L_{w2} , mm		33
height H_{w2} , mm		17.6
Operating parameters		
resonance frequency f , Hz	416	402
resonator efficiency parameter G_{E_s} -	2.33	1.75

Table 7.1 – Characteristic data of the tested resonators.

The effects generated by the new intake system configurations are also studied through 3D CFD analyses, limited to the air-box domain, under steady-state conditions for six engine operating points at full load and various speeds. The same analyses are carried out for the base configuration, too. The results are compared in terms of pressure loss across the device (Figure 7.11). As expected, the total pressure drop exhibits a quadratic trend with respect to the mass flow rate and the presence of a resonator (both internal and external) involves an increase in the total pressure drop. In particular, the internal resonator involves higher losses than the external one because of the restriction of the flow cross section near to the outlet pipe. Nevertheless, the increased losses are considered to only introduce negligible penalties in the overall engine performance.

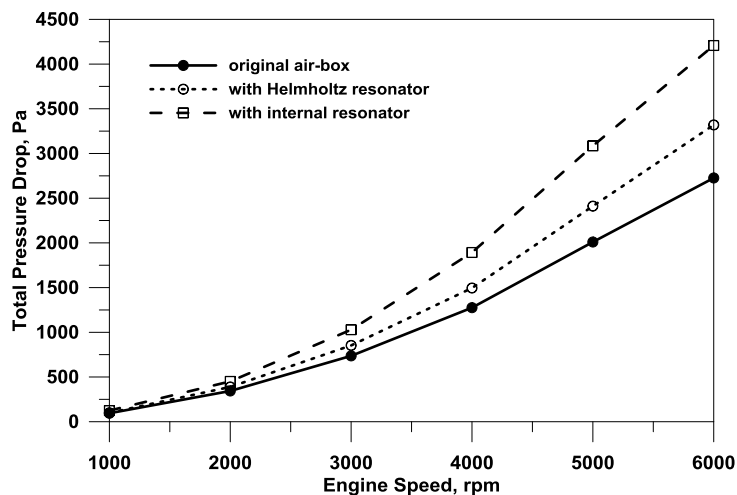


Figure 7.11 – 3D computed total pressure drop as function of the engine speed at full load operation.

3D CFD analysis also allows to investigate the flow field within the air-box device. As an example, in Figure 7.12 the velocity streamlines within the original and modified air-filter box are depicted, for the case at full load and 6000 rpm operation. For each configuration, it can be observed the presence of vortexes near the corners not interested by the main flow coming out from the inlet to the outlet pipe (Figure 7.12a-b). Instead, regarding the modified system (Figure 7.12b), a low velocity flow is established in the neck and in the cavity of the Helmholtz resonator. This determines a localized pressure loss which affects the global fluid-dynamic performance of the whole device. Anyway, 3D analyses of the modified air-box substantially confirm the results

obtained by the 1D simulations, denoting a negligible influence of an Helmholtz resonator on the global engine filling performance.

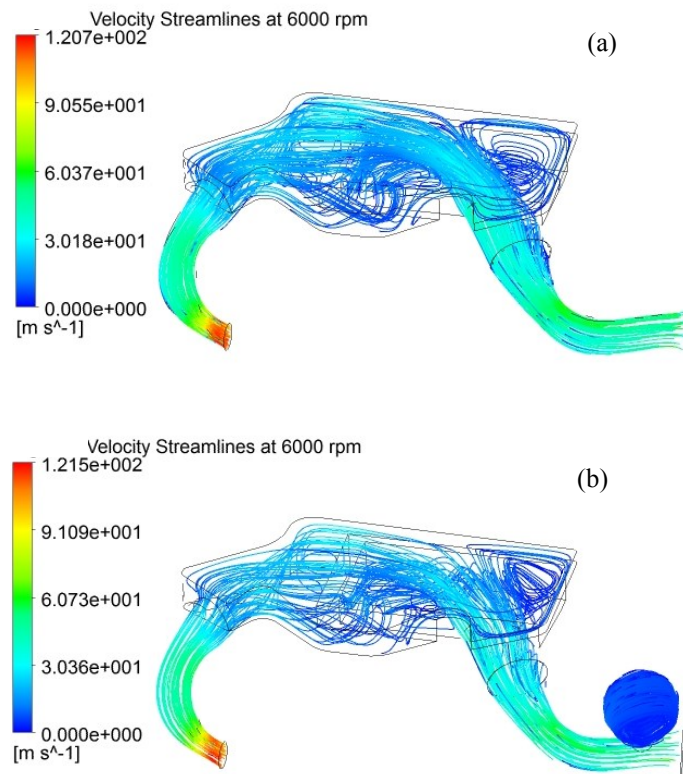


Figure 7.12 – Velocity streamlines for the original air-box device (a) and the modified one (b), at full load and 6000 rpm.

7.6 Transmission Loss: 3D FEM Model and Results

A 3D FEM model for the air-filter box is developed in order to evaluate the acoustic performance of the isolated component in zero-mean flow condition. Concerning the TL calculation, the Helmholtz equation (7.4) is solved:

$$\nabla \left(\frac{1}{\rho_0} \nabla p - q \right) + \frac{k_{wav}^2 p}{\rho_0} = 0 \quad (7.4)$$

where p is the sound pressure, $k_{wav} = \frac{2\pi f}{a}$ is the wave number, ρ_0 is the fluid density and a is the speed of sound. q represents a dipole source term corresponding to acceleration/unit volume, which can be here put to zero.

TL analyses are realized for the original air-box device and for the considered modified configurations of the system, as well. First, a computational mesh is generated for each air-box device configuration. The meshes are obtained by using default elements with properly controls applied to achieve the required consistency in terms of size and distribution. In particular, the grid is made up of linear tetrahedron elements. As an example, the mesh adopted for the air-filter box including the external and internal resonators are depicted in Figure 7.13 and Figure 7.14, respectively. The first grid consists of about 207000 total elements, while the second one is made up of 179400 total elements. For each tested configuration, the TL profile is computed in the frequency range 0-500 Hz with a step of 2 Hz.

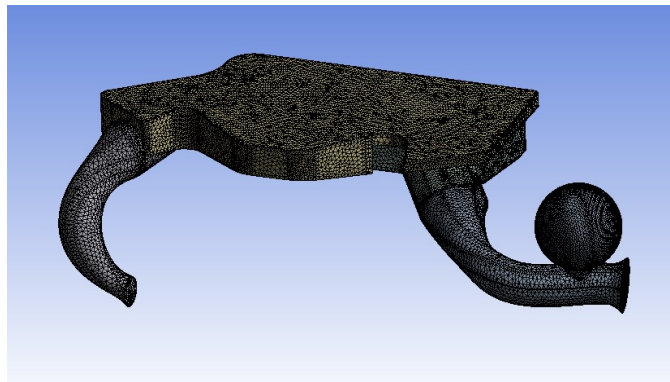


Figure 7.13 – Mesh of the air-box device with the external Helmholtz resonator for 3D TL analysis.

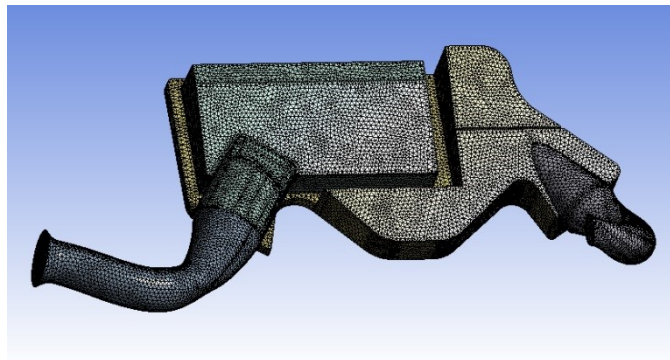


Figure 7.14 – Mesh of the air-box device with internal resonator for 3D TL analysis.

Concerning the numerical results with the above discussed models, Figure 7.15 shows the comparison among the TL parameters of the original air-box system and the modified ones. Concerning the base configuration, the TL presents a double shaped profile with local maxima depending on the volumes of the first and second connected chambers (Figure 7.15). The second

maximum, of lower intensity, is located exactly in the frequency range of the maximum gas-dynamic emission for the considered engine. This highlights a correct design of the air-box in the base configuration. Of course, the noise attenuation is improved through the introduction of properly dimensioned external and internal resonators, as discussed above. Figure 7.15 also highlights the effectiveness of the proposed external and internal resonators within the frequency range of interest (350-450 Hz). Referring to the external resonator, it is designed with a high value of the efficiency parameter G_E , and this allows to obtain a high TL peak together with a wider working frequency band. However, it is well known that the mean flow velocity exerts a not negligible influence on the resonator performance [70]. For this reason, TL analysis has to be extended to evaluate the engine behavior in terms of gas-dynamic noise, with the aim to directly consider the effects of the actual operating conditions when the air-box is coupled to the engine.

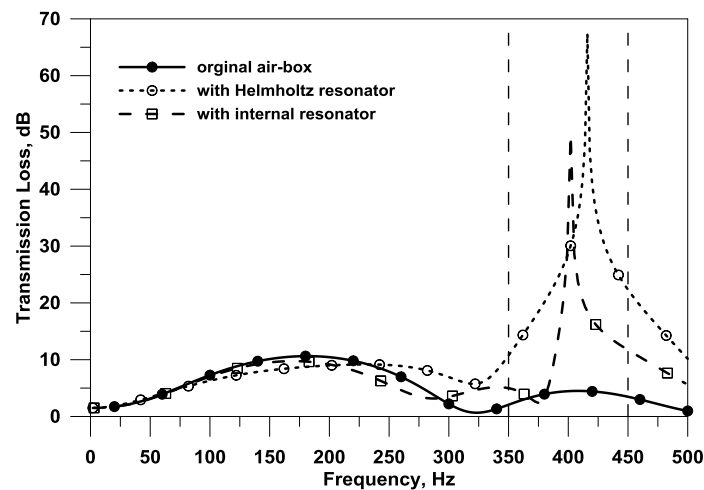


Figure 7.15 – Comparison among the Transmission Loss profiles of the original and modified air-box configurations.

7.7 Gas-dynamic noise: 3D CFD results at full and part load operation

3D analyses are performed for the modified air-box device including both the external resonator and the internal one to estimate the gas-dynamic noise emitted by the engine intake mouth at full load operations for various engine speeds. The radiated gas-dynamic noise is once again predicted in terms of the overall SPL and frequency spectrum. Proper grids are defined for the modified air-box configurations. In particular, the same modeling approach used for the analysis of the original air-

box is considered. Indeed the computational domain of each modified configuration is provided with a spherical-shaped volume, centered on the inlet section, in order to compute the pressure field at the virtual microphone. The boundary conditions for the new 3D analyses of each modified air-box device are derived by the corresponding 1D engine model which includes the 0D/1D schematization of tested resonators. Two different operating conditions are selected and the related gas-dynamic noise results are analyzed in detail. In Figure 7.16 the frequency spectra for the modified air-box devices are shown, for the engine speeds of 2100 rpm and 3300 rpm. For the considered cases, the external Helmholtz resonator allows for a more significant reduction in the SPL within the frequency range of interest. However, a certain noise attenuation is also obtained outside the above range. A lower noise reduction within the critical frequency band is indeed observed for the modified air-box that includes the internal resonator. This may be due to both the reduced internal resonator efficiency (G_E parameter in Table 7.1) and to the presence of a more intense mean flow ahead the resonator within the air-box volume. Similar results are obtained for the other operating points. Concerning the frequency spectrum at 2100 rpm (Figure 7.16a), the SPL reduction at 11th order (385 Hz) is equal to 4.6 dBA for the Helmholtz resonator and 2.3 dBA for the internal one, while at 3300 rpm (Figure 7.16b) the SPL reductions at the same frequency (7th order) are 4.3 dBA and 1.3 dBA, respectively. In the other analyzed operating conditions, a greater noise reduction is always obtained with the installation of the Helmholtz resonator, with an average SPL improvement of 4.15 dBA. Figure 7.16a and Figure 7.16b also show a high improvement at high engine orders (14th and 15th). However, since the above levels are well below the maximum ones, this improvement is not reflected in the overall noise emission. The Figure 7.17 in fact shows the comparison of the overall SPLs for the original and the modified configurations of the air-box. It can be observed that, a Helmholtz resonator added to the base intake system leads to an overall SPL reduction ranging from 0.9 up to 4.2 dBA within the whole speed range, except the case at 3000 rpm. On the other hand, the internal resonator allows for a decrease in the overall SPL only at low engine speeds (1.7 dBA at 1500 rpm), while a null noise abatement is realized at higher engine speeds.

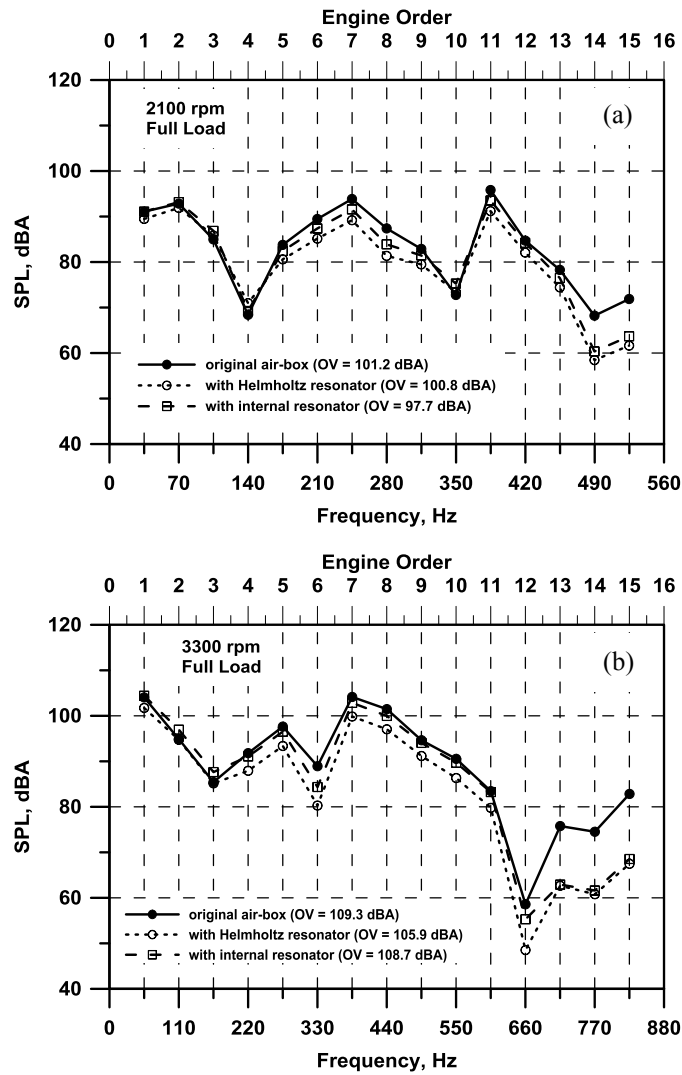


Figure 7.16 – Comparison of the frequency spectra of the original and modified air-box device for two different engine operating points, 2100 rpm (a) and 3300 rpm (b).

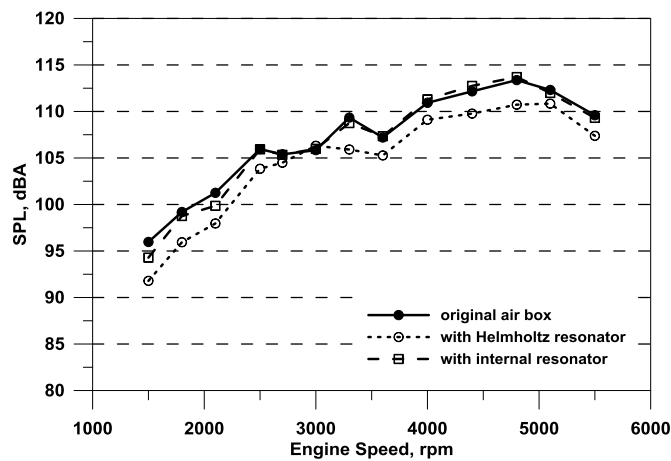


Figure 7.17 – Overall SPL comparison between the original air-box and the modified configurations.

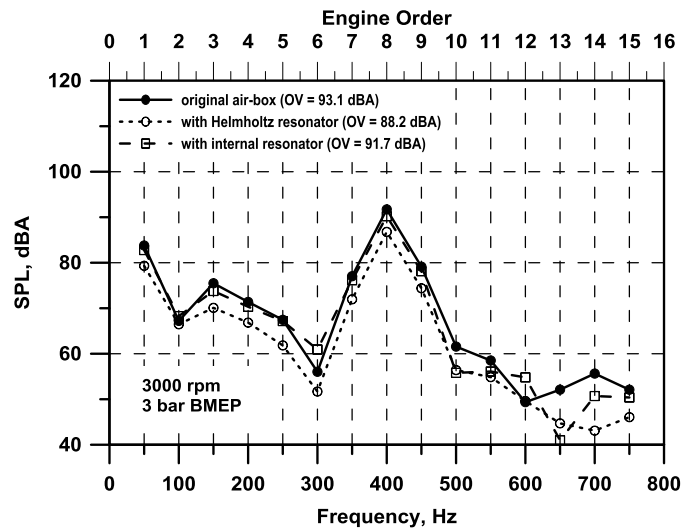


Figure 7.18 – Comparison of the frequency spectra for the operating point at 3000 rpm and 3 bar of BMEP.

In order to also verify the air-box attenuation efficiency at low load, further 3D CFD analyses for the modified air-box configurations are performed at a predefined operation (i.e. 3000 rpm and 3 bar of BMEP). Figure 7.18 shows the predicted results in the above operating point. The SPL reduction at the most important order (8th order at 400 Hz) is here equal to 4.9 dBA with the external resonator and 1.5 dBA with the internal resonator. The above improvement almost exactly reflects on the overall sound pressure levels, as well. Based on the presented results, it is hence confirmed that the redesigned air-box configurations reveal the capability to improve the acoustic engine behavior even at part-load operation.

CHAPTER 8

Virtual Engine Calibration through optimization code

8.1 Introduction and formulation of Multi-objectives Optimization

Many real engineering problems actually do have multiple objectives, i.e., minimize cost, maximize performance, maximize reliability, etc. Genetic algorithms (GA) are popular meta-heuristic particularly well-suited for this kind of problems. There are two general approaches to multi-objectives optimization. The first general approach is to combine the individual objective functions in a single composite function. In this case the determination of a single objective is possible with proper methods such as utility theory, weighted sum methods, etc. but the considered problem involves a proper selection of weights or utility functions in order to characterize the decision-maker's preferences. Actually, it can be very difficult to accurately select these weights. In addition, this approach will return a single solution rather than a set of solution which can be examined for trade-offs.

The second general approach is to determine an entire Pareto optimal solution set or a representative subset. A Pareto optimal set is a set of solutions that are non-dominated with respect to each other. While moving from one Pareto solution to another, there is always a certain amount of sacrifice in one objective to achieve a certain amount of gain in others. Pareto optimal solution sets are often preferred to single solutions because they can be practical when considering real-life problems since the final solution of the decision-maker is always a trade-off. Pareto optimal sets can be of varied sizes, but the size of the Pareto set usually increases with the increase in the number of objectives.

Concerning the formulation of a multi-objective optimization, an optimization problem with N objectives is considered. For the decision maker, the objectives are not commensurable and a not clear objectives preference exists. In these conditions, all the objectives are considered of minimization type without loss of generality for the optimization problem. Indeed, a minimization type objective can be easily converted into a maximization type one. A minimization multi-objective problem with N objectives is so defined: for a n -dimensional decision variable vector $X = \{x_1, x_2, \dots, x_n\}$ in the solution space X , find a vector x^* which minimizes a given set of N objective functions $z(x^*) = \{z_1(x^*), z_2(x^*), \dots, z_N(x^*)\}$. The solution space X can be restricted by several constraints $g_j(x^*) = v_j$ for $j=1,2,\dots,m$ and bounds on the decision variables.

In many problems the objectives under study are in conflict each other. So the optimization with respect to a single objective often results in unacceptable results for the other objectives. Consequently, a perfect multi-objective solutions that simultaneously optimizes each objective is almost impossible. A reasonable solution of a multi-objective problem is represented by a set of solutions capable to satisfy the objectives at an acceptable level without being dominated by any other solution. When all objective functions are for the minimization, a feasible solution x dominates another feasible solution y , if and only if $z_i(x) \leq z_i(y)$ for $i=1,2,\dots,N$ and $z_j(x) < z_j(y)$ for least one objective function j . A Pareto optimal solution is not dominated by any other solution within the solution space X . A Pareto optimal solution cannot be improved with respect to any objective without worsening at least one other objective. Pareto optimal set represents the set of all feasible not dominated solutions in X and for a given *Pareto Optimal Set* the corresponding values in the objective space are the so-called "Pareto front". The goal of a multi-objective optimization algorithm is to identify the solutions in the Pareto optimal set. For many multi-objective problems, the identification of the entire Pareto optimal set is practically impossible, because of its relevant size. A practical approach to multi-objective optimization is to investigate a set of solutions that represent the Pareto optimal set as well as possible. A multi-objective optimization approach should achieve three conflicting goals:

1. The best-known Pareto front should be as close as possible to the true Pareto front. Ideally, the best known Pareto set should be a subset of the Pareto optimal set.
2. Solutions in the best-known Pareto set should be uniformly distributed and diverse over the Pareto front in order to provide the decision-maker a true picture of trade-offs.
3. The best-known Pareto front should capture the whole spectrum of the Pareto front. This requires the investigation of solutions at the extreme ends of the objective function space.

For a given computational time limit, the first goal is best served by focusing the search on a particular region of the Pareto front. On the contrary, the second goal demands the search effort to be uniformly distributed over the Pareto front. The third goal aims at extending the Pareto front at both ends, exploring new extreme solutions. The algorithms usually adopted to solve a multi-objective optimization problem will be discussed in the following.

8.1.1 Description of Genetic Algorithms for Multi-objectives optimization

The concept of GA was developed by Holland et al. in the 1960s and 1970s [158]. GA are inspired by the evolutionist theory explaining the origin of species. In nature, weak and unfit species within their environment are faced with extinction by natural selection. The strong ones have greater

opportunity to pass their genes to future generations via reproduction. In the long run, species carrying the correct combination in their genes become dominant in their population. Sometimes, during the slow process of evolution, random changes may occur in genes.

If these changes provide additional advantages in the challenge for survival, new species evolve from the old ones. Unsuccessful changes are eliminated by natural selection.

In GA terminology, a solution vector is called a “chromosome”. Chromosomes are made of discrete units called “genes”. Each gene controls one or more features of the chromosome. Normally, a chromosome corresponds to a unique solution in the solution space.

GA operates with a collection of chromosomes, called a “population”. The population is normally randomly initialized. As the search evolves, the population includes fitter and fitter solutions, and eventually it converges, meaning that it is dominated by a single solution.

GAs use two operators to generate new solutions from existing ones: “crossover” and “mutation”. The first one is the most important operator of GA. In crossover, generally two chromosomes, called “parents”, are combined together to form new chromosomes, called “offspring”. The parents are selected among existing chromosomes in the population with preference towards fitness so that offspring is expected to inherit good genes which make the parents fitter. By iteratively applying the crossover operator, genes of good chromosomes are expected to appear more frequently in the population, eventually leading to convergence to an overall good solution.

The mutation operator introduces random changes into characteristics of chromosomes. Mutation is generally applied at the gene level. In typical GA implementations, the mutation rate (probability of changing the properties of a gene) is very small and depends on the length of the chromosome. Therefore, the new chromosome produced by mutation will not be very different from the original one. Mutation plays a critical role in GA. As discussed earlier, crossover leads the population to converge by making the chromosomes in the population alike. Mutation reintroduces genetic diversity back into the population and assists the search escape from local optima.

Reproduction involves selection of chromosomes for the next generation. In the most general case, the fitness of an individual determines the probability of its survival for the next generation. There are different selection procedures in GA depending on how the fitness values are used.

Proportional selection, ranking, and tournament selection are the most popular selection procedures. The procedure of a generic GA [159] is given as follows:

Step 1: Set time $t=1$. Randomly generate N solutions to form the first population, P_1 . Evaluate the fitness of solutions in P_1 .

Step 2: Crossover: Generate an offspring population Q_t as follows:

2.1. Choose two solutions x and y from P_t based on the fitness values.

2.2. Using a crossover operator, generate offspring and add them to Q_t .

Step 3: Mutation: Mutate each solution x of Q_t with a predefined mutation rate.

Step 4: Fitness assignment: Evaluate and assign a fitness value to each solution $x \in Q_t$ based on its objective function value and infeasibility.

Step 5: Selection: Select N solutions from Q_t based on their fitness and copy them to P_{t+1} .

Step 6: If the stopping criterion is satisfied, terminate the search and return to the current population, else, set the time $t = t+1$ go to Step 2.

Genetic algorithms are well suited to solve multi-objective optimization problems. Jones et al. [160] reported that 90% of the approaches to multiobjective optimization aimed to approximate the true Pareto front for the underlying problem. A majority of these used a meta-heuristic technique, and 70% of all metaheuristics approaches were based on evolutionary approaches.

The first multi-objective GA, called vector evaluated GA (or VEGA), was proposed by Schaffer [161]. Afterwards, several multi-objective evolutionary algorithms were developed including Multi-objective Genetic Algorithm (MOGA) [162], Niche Pareto Genetic Algorithm (NPGA) [163], Weight-based Genetic Algorithm (WBGA) [164], Random Weighted Genetic Algorithm (RWGA) [165], Nondominated Sorting Genetic Algorithm (NSGA) [166], Strength Pareto Evolutionary Algorithm (SPEA) [167], improved SPEA (SPEA2) [168], Pareto-Archived Evolution Strategy (PAES) [169], Pareto Envelope-based Selection Algorithm (PESA) [170], Region-based Selection in Evolutionary Multiobjective Optimization (PESA-II) [171], Fast Nondominated Sorting Genetic Algorithm (NSGA-II) [172], Multi-objective Evolutionary Algorithm (MEA) [173], Micro-GA [174], Rank-Density Based Genetic Algorithm (RDGA) [175], and Dynamic Multi-objective Evolutionary Algorithm (DMOEA) [176].

Although there are many variations of multi-objective GA in the literature, these cited GA are well known and credible algorithms that have been used in many applications and their performances were tested in several comparative studies.

Among the above cited GAs, a special attention is devoted to the MOGA-II algorithm, since it is implemented in the commercial software ModeFrontier.

MOGA-II is an improved version of Multi-Objective Genetic Algorithm, developed by Poloni et al. [177]. It uses a smart multi-search elitism for robustness and directional crossover for fast convergence. The efficiency of MOGA-II is controlled by its operators (i.e. classical crossover, directional crossover, mutation and selection) and by the use of elitism. The latter plays a crucial role in multi-objective optimization because it helps to preserve the individual that are closest to the Pareto Frontier and the ones that have the best dispersion. MOGA-II uses four different operators

for reproduction: one point crossover, directional crossover, mutation and selection. At each step of the reproduction process, one of the four operators is chosen and applied to the current individual.

One point or classical crossover represent the most classical operator for the reproduction. Two parents are chosen and some portion of genetic materials (i.e design variables) is exchanged between parent variables vectors (Figure 8.1). The point of the crossing site is randomly chosen and the binary strings are cut at that point. The resulting two head pieces are swapped and rejoined with the two tail pieces. The obtained individuals are usually called children and one of them is randomly selected to be the new individual.

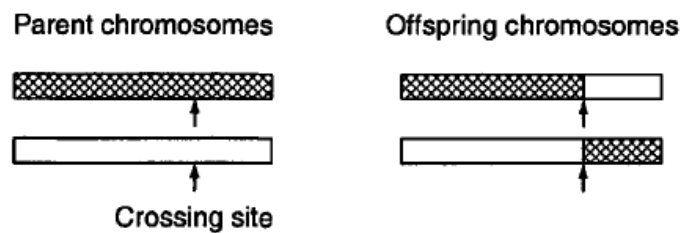


Figure 8.1 – Illustration of one-point crossover operation.

Directional crossover is slightly different and assumes that a direction of improvement can be detected comparing the fitness values of two reference individuals. In [178] a novel operator called evolutionary direction crossover was introduced and it was shown that even in the case of a complex multi-modal function this operator outperforms classical crossover. The direction of improvement is evaluated by comparing the fitness of the individual Ind_i from generation t with the fitness of its parents belonging to generation $t-1$. The new individual is then created by moving in a randomly weighted direction that lies within the ones individuated by the given individual and his parents (Figure 8.2). A similar concept can be however applied on the basis of directions not necessarily linked to the evolution but detected by selecting two other individuals Ind_j and Ind_k in the same generation (like shown in Algorithm 1).

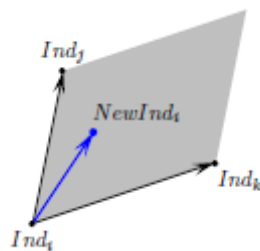


Figure 8.2 – Directional Crossover between individuals Ind_i , Ind_j and Ind_k .

The *selection* of individuals Ind_j and Ind_k can be done using any available selection schema. In MOGA-II local tournament with random steps in a toroidal grid is used. First of all, the individual subject to reproduction is chosen as the starting point. Other individuals met in a random walk of assigned number of steps from that starting point are then marked as possible candidates for the first "parent" Ind_j . The list of all possible candidates for the second "parent" Ind_k is selected in the same way in a successive (and generally different) random walk from the same starting point. When the set of candidates is generated, the candidate with the best fitness is chosen. The number of steps N in the random walk remains fixed during the entire optimization run and is proportional to the population size.

Mutation is an operator that ensures diversity from one generation to the next. *Mutation* guarantees the algorithm robustness. In MOGA-II it is possible to define the value of the so-called DNA String Mutation Ratio. This value gives the percentage of the binary string that is perturbed by the mutation operator.

In the following, after a brief description of the engine model validation at high and part load operations, multi-objective optimizations for the considered engine system, will be discussed in detail by employing a proper Genetic Algorithm, available within the adopted optimization code.

8.2 Engine Model Validation for Full Lift and EIVC Strategies

Turbulence and combustion models have been widely validated at full load [83], [118], both in terms in-cylinder turbulence intensity, combustion evolution and overall engine performance (BMEP, BSFC, air flow, etc.) The knock model has been validated through the automatic identification of the knock limited spark advance at full load by means of a controller targeting a single threshold level for the knock index [179]. In this work, the engine model is applied to describe the engine behaviour at both high and part load for an engine speed of 3000 rpm. The numerical findings are validated against the experimental data collected for both *Full Lift* and *EIVC* valve strategies. The measured values of MFB_{50} and air-to-fuel ratio assigned in the simulations. The spark advance is automatically adjusted by a controller implemented in the "user routine" to match the imposed MFB_{50} . Since the actual waste-gate flow area is not available in the experiments, it is indirectly set in a 1D simulation through a PID controller targeting the measured turbocharger rotational speed. The experimental BMEP is matched at low loads by a further PID controller adjusting the throttle valve opening. In the case of medium and high loads, the throttle valve is set at

a fully opened position. For the sole *EIVC* strategy, the experimentally actuated values of φ_2 are also imposed as an input.

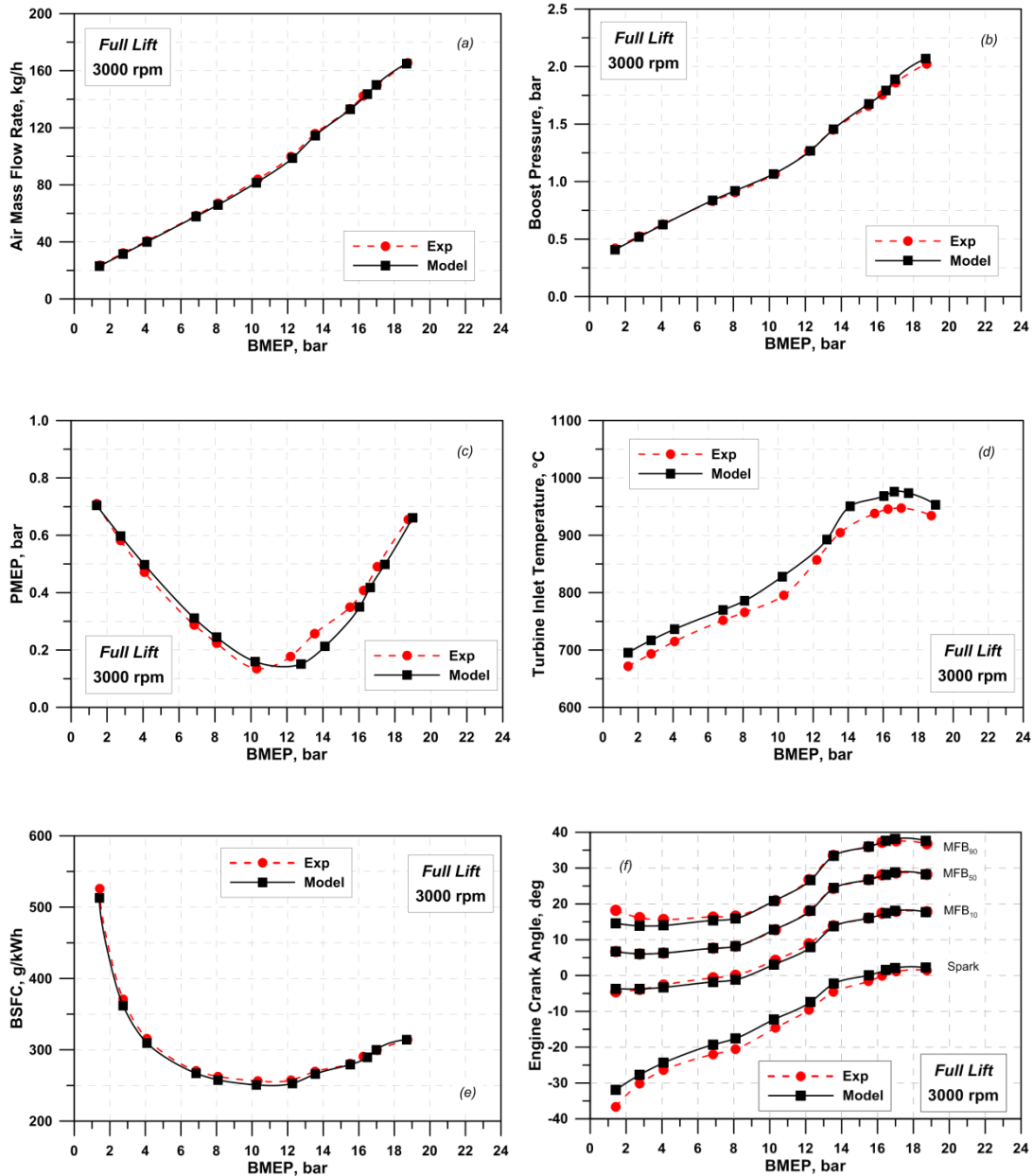


Figure 8.3 – Experimental vs. numerical air mass flow rate (a), boost pressure (b), pumping work (c), turbine inlet temperature (d), BSFC (e) and combustion characteristic angles (f) as a function of the BMEP for the Full Lift strategy.

As said, turbulence, combustion and knock models have been tuned in author works with reference to full load operation. It is not worthless to emphasize that the same tuning constants suited for full load operation, are here adopted, without requiring any adjustment. Results of Figure 8.3 and Figure

8.4 show the numerical/experimental comparison in terms of air flow, boost pressure, Pumping Mean Effective Pressure (PMEP), TIT and characteristic combustion angles as a function of the engine load, both for *EIVC* and *Full Lift* and strategies, respectively.

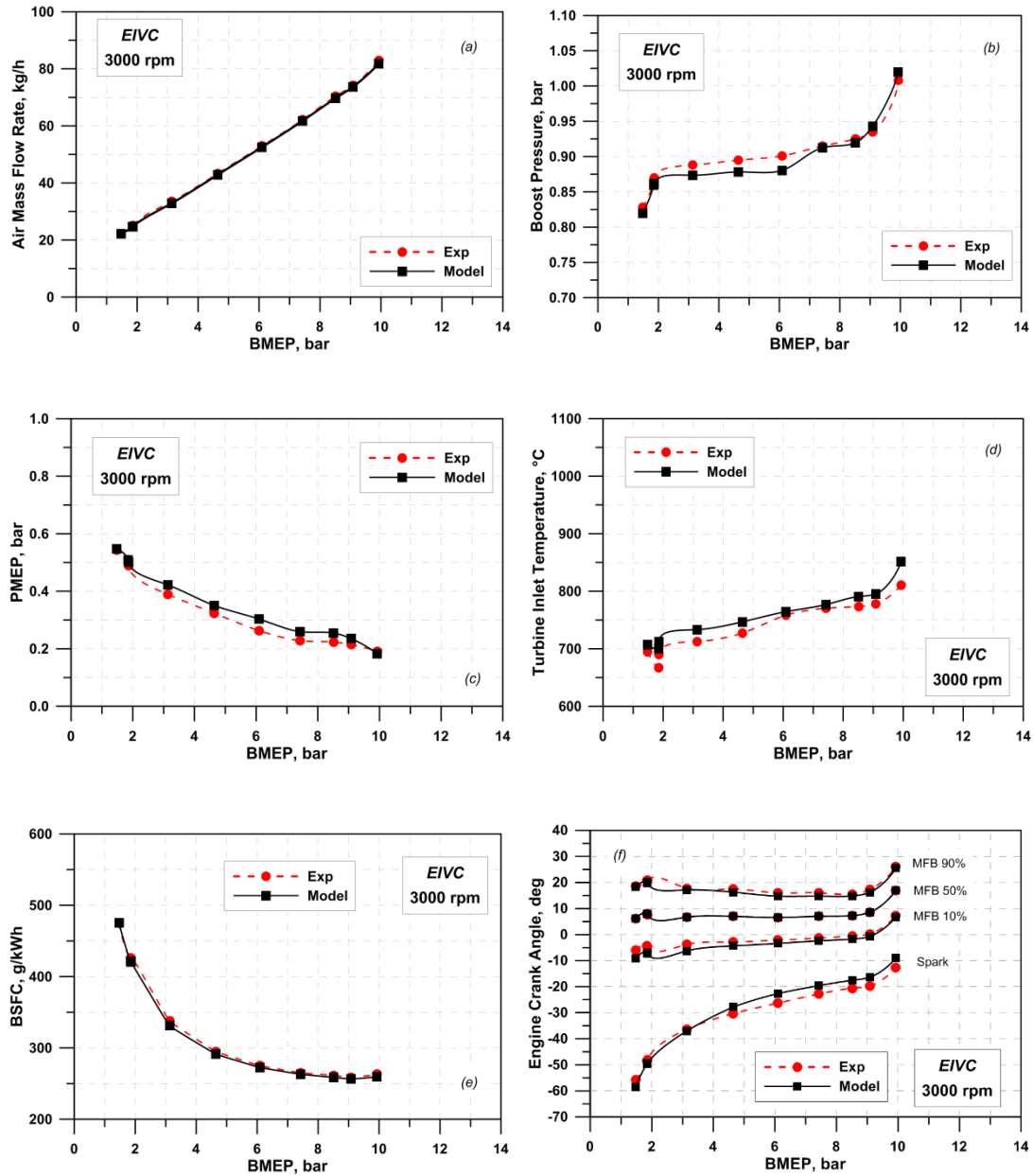


Figure 8.4 – Experimental vs. numerical air mass flow rate (a), boost pressure (b), pumping work (c), turbine inlet temperature (d), BSFC (e) and combustion characteristic angles (f) as a function of the BMEP for the EIVC strategy.

Numerical air flow, boost and PMEP results mainly underline the accuracy of the geometrical schematization of the engine, in addition to the reliability of the turbocharger modelling. Computed TIT correctly follows the measured trend, even if a systematic overestimation occurs, quantified in about 20 °C on average. The latter error can be mainly ascribed to some inaccuracy in the heat

exchange modelling within the cylinders, especially during the expansion stroke, and within the exhaust ducts upstream the turbine. The satisfactory numerical/experimental agreement in the BSFC and combustion findings mainly depends on the accuracy of the considered combustion and turbulence modelling. In fact, it can be observed that the adopted approach is able to adequately catch the combustion lengthening as the load decreases, mainly regarding the beginning of the process (from spark event up to MFB_{10}). This can be ascribed to the capability of the model to sense the reduced in-cylinder turbulence, temperature and pressure levels occurring at very low load. This is particularly true in the case of *EIVC* strategy, where, however, the model is able to adequately locate the spark advance at about 60 degrees before the FTDC. It is not worthless to point out that the above validation at high and part loads represents a fundamental prerequisite to guarantee the reliability of the optimization procedure described in the next section.

8.3 Optimization Procedure Description at Full Load

1D model represents the core of the optimization process aiming to define the engine calibration that simultaneously minimize BSFC and maximize the BMEP at high load operation (BMEP higher than 10 bar), where engine performance are limited by the knock onset. The parameters for the engine calibration are the MFB_{50} angle, the waste-gate valve opening and the air-to-fuel ratio. Since high load operation is studied, the throttle valve opening is assumed completely opened, while load control is mainly demanded to the waste-gate opening.

Figure 8.5 illustrates the logical scheme of the optimization procedure, developed in the modeFRONTIER environment. The optimization process, which is based on the genetic algorithm MOGA-II, iteratively selects the values of the above listed control parameters; they are written in the input file of the GT-PowerTM model and the related 1D analysis is performed at the predefined engine speed of 3000 rpm. At the end of each simulation, the computed BSFC and BMEP are passed back to the optimizer for the next iteration, until optimal values are identified. The experimental constraints are also imposed in the optimization procedure, namely 2.2 bar for the boost pressure and 255000 rpm for the turbocharger speed. The experimental limit of turbine inlet temperature is increased in the simulations from 950°C up to 970 °C to take into account the model inaccuracies on the TIT prediction, already discussed in the previous section. If one or more constraints are violated, the related solution is considered unfeasible.

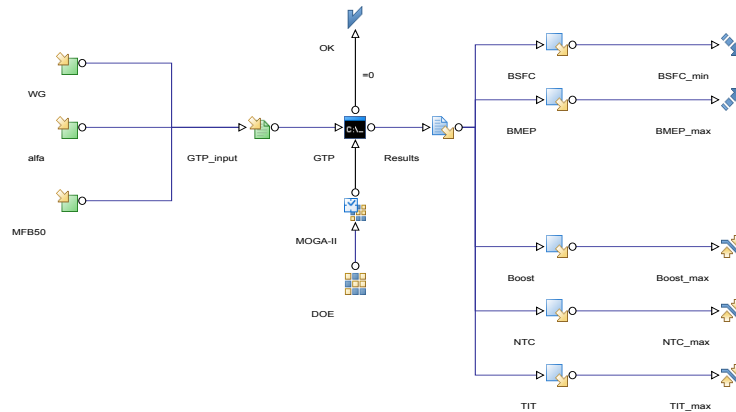


Figure 8.5 – Flowchart of the optimization process implemented in modeFRONTIER environment.

As usual, in a multi-objective optimization, the optimal solutions define the “Pareto-frontier” in the BSFC-BMEP plane, expressing the trade-off between the two objectives. A further optimization is set up, where the intake valve closure angle is added as an additional control variable, so to investigate the potential advantages of *EIVC* strategy at high load. The logical scheme of the optimization is the same of Figure 8.5, with an additional input parameter corresponding the φ_2 angle.

8.4 Results Discussion at Full Load

Figure 8.6a and Figure 8.6b collect all the engine calibrations investigated by the optimizer in the BSFC vs. BMEP plane both for *Full Lift* and *EIVC* strategy. In the Figures, green rhombuses correspond to “Feasible” solutions which, as said, respect the constraints on the maximum allowable boost level, turbocharger speed and TIT, while red crosses represents “Unfeasible” solutions. The optimal solutions are depicted by black rhombuses, connected by a continuous black curve, denoting the “Pareto” frontier. Figures also shows the numerical results obtained by imposing the experimental calibration, depicted by a blue dashed line with circles. As a general consideration, the closer the experimental data are to the various Pareto lines, the higher is the accuracy of the numerical optimization. In particular, it can be observed in Figure 8.6a that the Pareto frontier for *Full Lift* strategy satisfactorily resembles the optimal calibration results measured at the test bench, even if slightly lower BSFC values are generally identified. The latter occurrence

can be mainly ascribed to some incongruence in the calibration settings, as better explained in the following. For the *EIVC* strategy, a very good agreement verifies for the unique experimental point available at full load (Figure 8.6b).

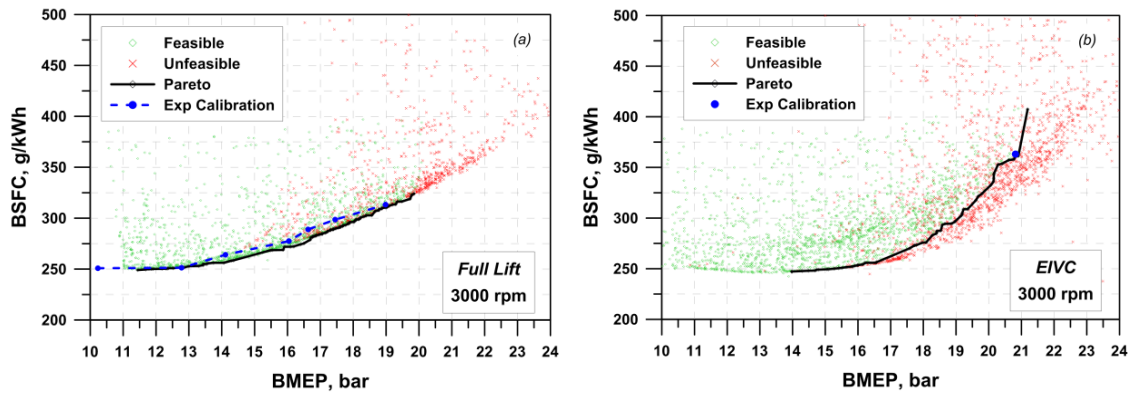


Figure 8.6 – BSFC vs. BMEP trade-off for Full Lift (a) and EIVC (b) strategy.

The decreasing trends of the Pareto frontier in Figure 8.7 underline the necessity of a mixture over-fuelling as the load increases. The irregularities in the above trend are due to inability of the optimizer in perfectly identifying a smooth Pareto line for each control parameter. Its overall tendency however clearly highlights that a richer and richer mixture is selected as optimal solution as the load increases. This is in fact the path identified by the optimizer to limit the TIT (Figure 8.8), in accordance with the strategy followed in the experimental activity. On the other hand, the mixture enrichment also contributes to mitigate the knock intensity, by reducing the in-cylinder temperatures thanks to the heat subtracted by the fuel evaporation. However, as the BMEP increases, the other path detected by the optimizer to limit the knock is a delay in the combustion phasing (Figure 8.9).

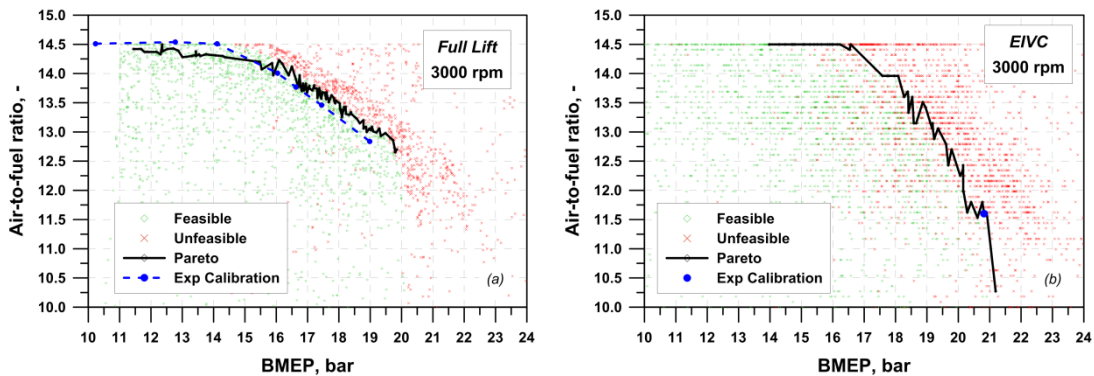


Figure 8.7 – Air-to-fuel ratio vs. BMEP for Full Lift (a) and EIVC (b) strategy.

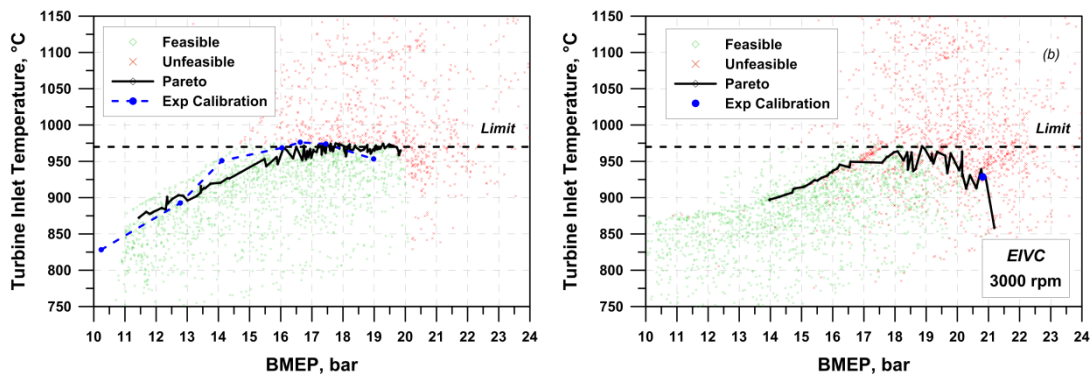


Figure 8.8 – TIT vs. BMEP for Full Lift (a) and EIVC (b) strategy.

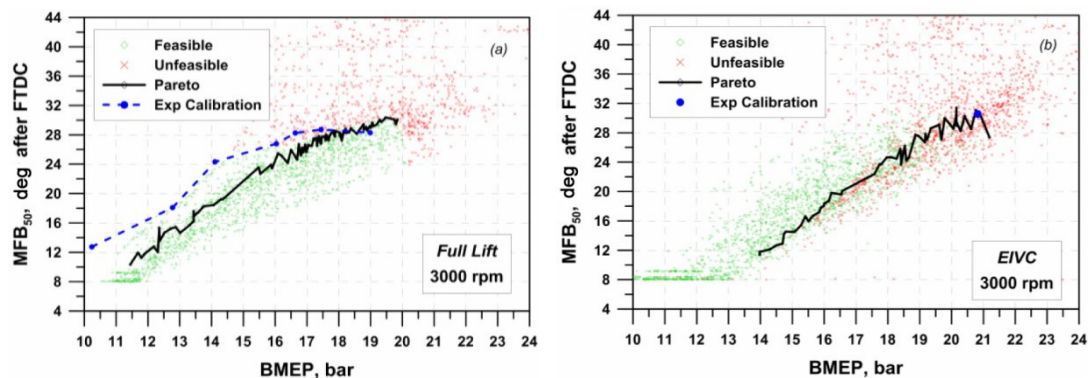


Figure 8.9 – MFB_{50} vs. BMEP for Full Lift (a) and EIVC (b) strategy.

Concerning the *Full Lift* strategy, even if the experimentally-derived trends of the operating parameters are properly captured by the numerical procedure, a certain disagreement can be observed, especially in terms of MFB_{50} , that is sometimes in advance at an assigned load level with respect to the measured data. The above inaccuracy is the main cause of the BSFC difference of Figure 8.6a. This incongruence may be justified by a certain difference in the knock intensity accepted at high load and full load from an experimental point of view. On the other hand, in the simulations, exactly the same knock threshold is assigned regardless the load level, being the knock limit tuned for full load operation. However, the above issues only partially undermine the model reliability, that, based on the proposed results, can be considered very satisfactory.

Figure 8.10 points out that for the Full Lift strategy, a load increase is mainly driven by the boost level, while for an *EIVC* approach, the boost has to be always maintained at the maximum allowable level, while the load can be adjusted by the intake valve closure angle (Figure 8.11). The

congruence between the experimentally and numerically-identified calibrations is further proved by the PMEP comparisons of Figure 8.12, mainly deriving by a proper setting of the waste-gate valve opening.

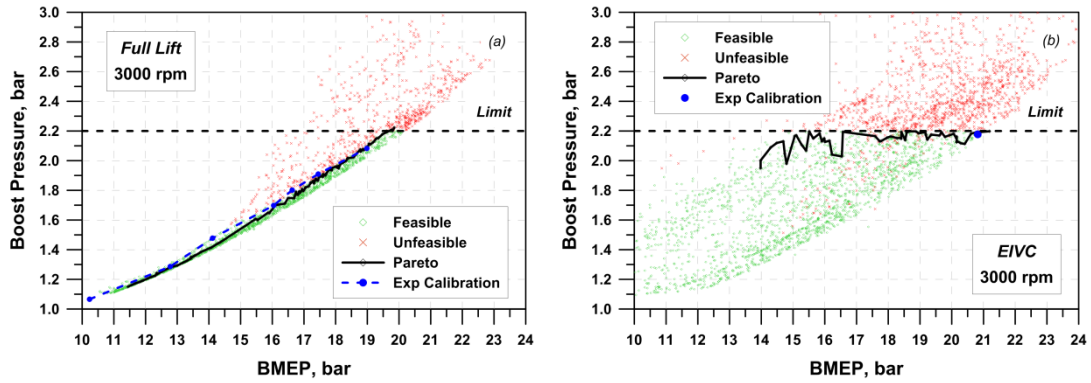


Figure 8.10 – Boost Pressure vs. BMEP for Full Lift (a) and EIVC (b) strategy.

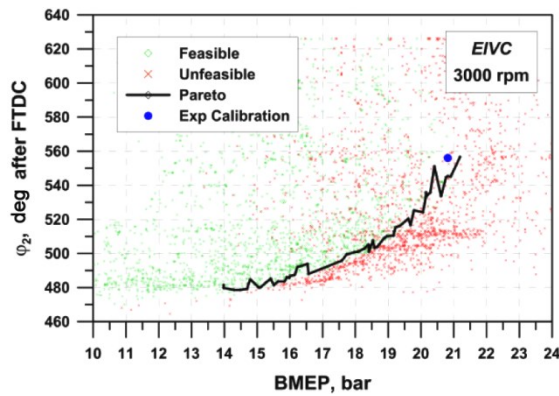


Figure 8.11 – ϕ_2 vs. BMEP for EIVC strategy.

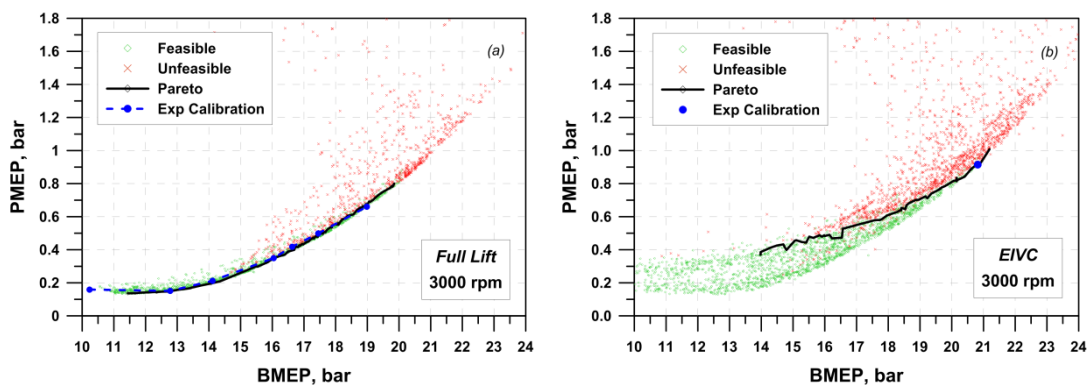


Figure 8.12 – PMEP vs. BMEP for Full Lift (a) and EIVC (b) strategy.

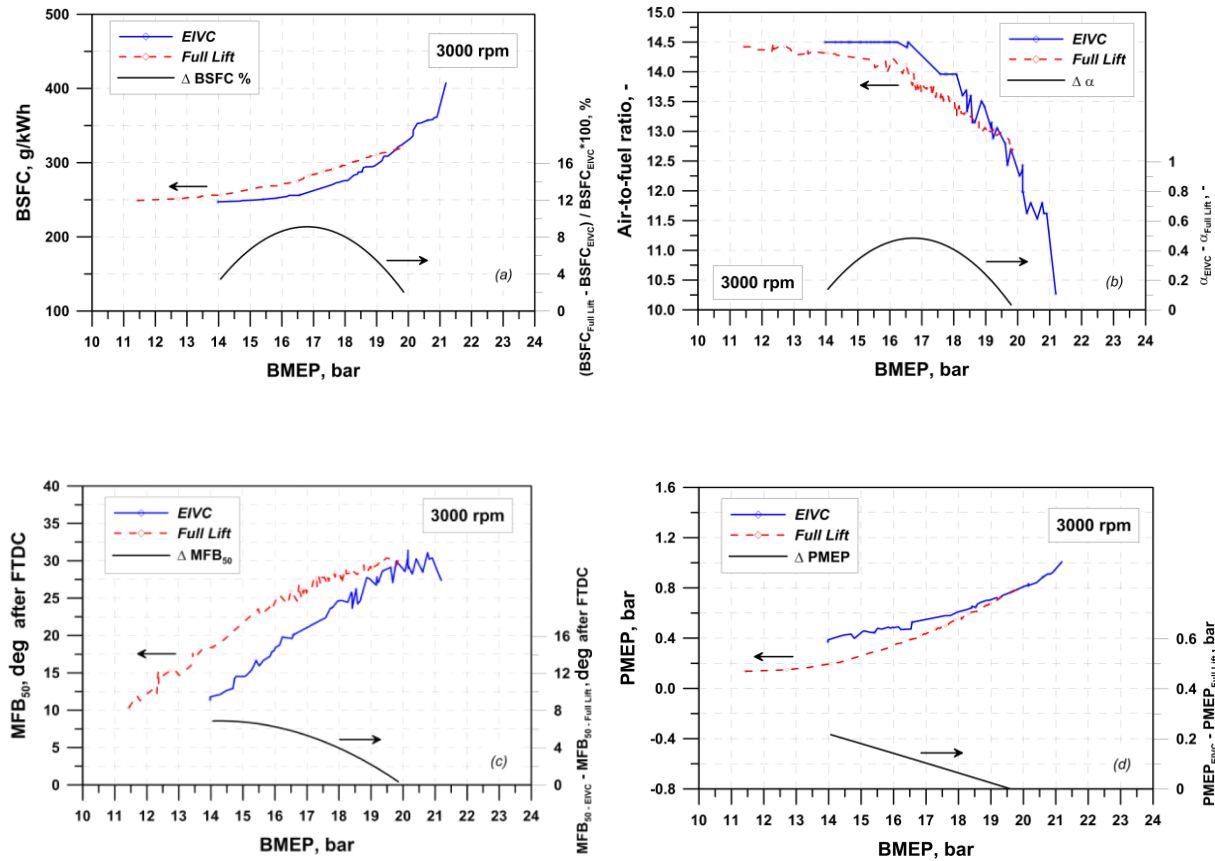


Figure 8.13 – Comparison of optimal calibration for Full Lift and EIVC strategies in terms of BSFC (a), air-to-fuel ratio (b), MFB₅₀ (c) and PMEP (d).

A deep insight on the considered valve strategies can be realized looking at Figure 8.13, comparing optimal BSFC, air-to-fuel ratio, MFB₅₀ and PMEP as a function of the load. It can be observed that the *EIVC* strategy guarantees a lower BSFC (Figure 8.13a), with a maximum BSFC improvement of about 9% at 17 bar of BMEP. This is mainly due to less severe request of mixture over-fuelling (Figure 8.13b) and combustion phasing delay (Figure 8.13c). However, a partial compensation of the above advantages is exerted by a higher pumping work (Figure 8.13d), required to reach the maximum allowable boost pressure at each load. The *EIVC* advantages become less relevant at medium loads, where the knock intensity is less severe and consequently the MFB₅₀ delay and the fuel enrichment are not required. Similarly, close to full load, the ϕ_2 angle is set with a reduced advance (Figure 8.11) to guarantees the maximum cylinder filling and, consequently, the *EIVC* benefits are less significant. The above discussed *EIVC* advantages can also be explained looking at Figure 8.14a and Figure 8.14b, reporting the unburned/burned temperatures evolution near to the FTDC and the in-cylinder pressure vs. volume cycle, respectively, at a BMEP of 16.5 bar. It can be noted that an early closure of the intake valve determines lower temperatures during the

compression stroke (about 20 K), thanks to the so-called “syringe effect”, clearly depicted in Figure 8.14b at the end of the intake stroke. In this way, the knock risk is mitigated and, consequently, a better combustion phasing and a higher thermodynamic efficiency are attained. As a consequence of the combustion advancing, a lower temperature at the turbine inlet is reached and, thus, a less rich air-to-fuel ratio is required. The above effects determine a significant improvement in the fuel economy, that, in the specific case, is of about 9%.

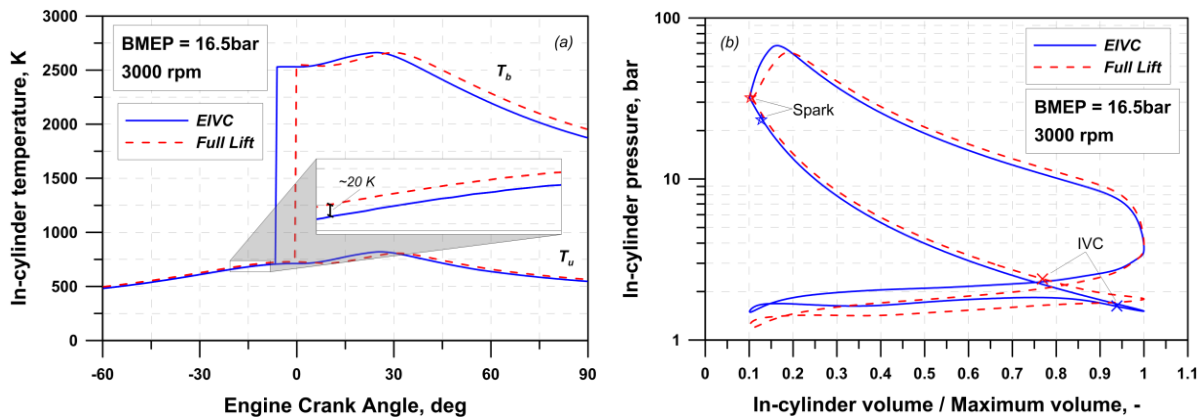


Figure 8.14 – In-cylinder unburned and burned temperatures (a) and pressure (b) comparison between optimal calibrations for Full Lift (a) and EIVC (b) strategies.

Summarizing, the proposed approach, based on the integration of 1D simulation and optimization tool, showed the capability to properly capture the complex interaction among the various calibration parameters that affect the engine performance. In this way, the potential to set up a “virtual” calibration of an engine on purely theoretical basis has been demonstrated, contributing to reduce the time and costs of an engine calibration at the test bench.

8.5 Optimization Procedure Description at Part Load

1D engine model represents the core of the optimization process aiming to define the engine calibration strategy that contemporary minimize BSFC and BMEP. The parameters for the engine calibration are the throttle valve opening, the intake valve closure angle, MFB_{50} angle and the waste-gate valve opening. The air-to-fuel ratio is fixed at the stoichiometric value, as usually required at part load, in order to ensure proper operation for the catalytic converter.

The Figure 8.15 illustrates the logical scheme of the optimization procedure, developed in the modeFRONTIER graphical environment. The optimizer, which is based on the genetic algorithm MOGA-II, iteratively selects the values of the above listed control parameters that are written in the input file of the 1D model. Then, a single analysis is performed at the predefined engine speed of 3000 rpm. At the end of each simulation, the computed BSFC and BMEP are passed back to the optimizer for the next iteration, until optimal values are identified. Proper constraints are imposed for the boost pressure (0.9 bar), turbocharger speed (255000 rpm), in-cylinder maximum pressure (100 bar) and turbine inlet temperature (950 °C). As usual, in a multi-objective optimization, the above search corresponds to the evaluation of the “Pareto-frontier” in the BSFC-BMEP plane, expressing the trade-off between the two objectives and collecting the infinite solutions of the optimization problem.

In a second stage, a further optimization is set up, where the ϕ_2 angle is fixed at a value corresponding to the full valve lift profile. In this way, a classical throttle-based engine calibration is accomplished.

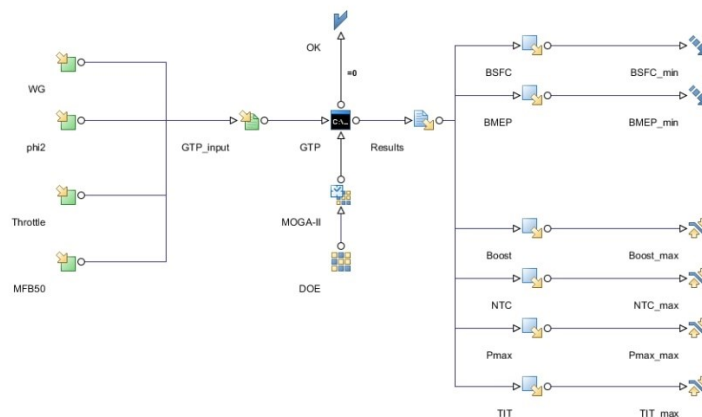


Figure 8.15 – Flowchart of the optimization process implemented in ModeFRONTIER environment.

8.6 – Results Discussion at Part Load

Figure 8.16a and Figure 8.16b collect all the engine calibrations investigated by the optimizer in the BSFC vs. BMEP plane both for the *EIVC* and *Throttled* strategies. In the Figures, green rhombuses corresponds to engine calibrations respecting the constraints on the maximum allowable boost level, turbocharger speed and turbine inlet temperature (labelled as “Feasible”), while the others, depicted as light blue crosses, represents unfeasible solutions (labelled as “Unfeasible”). The optimal solutions are represented by blue rhombuses; the latter are connected by a blue curve, denoting the Pareto frontier (labelled as “Pareto”). Figure 8.16a and Figure 8.16b also show the numerical results obtained by imposing the experimentally advised optimal calibration (labelled as “Exp Calibration”), already discussed in the “Model tuning” section.

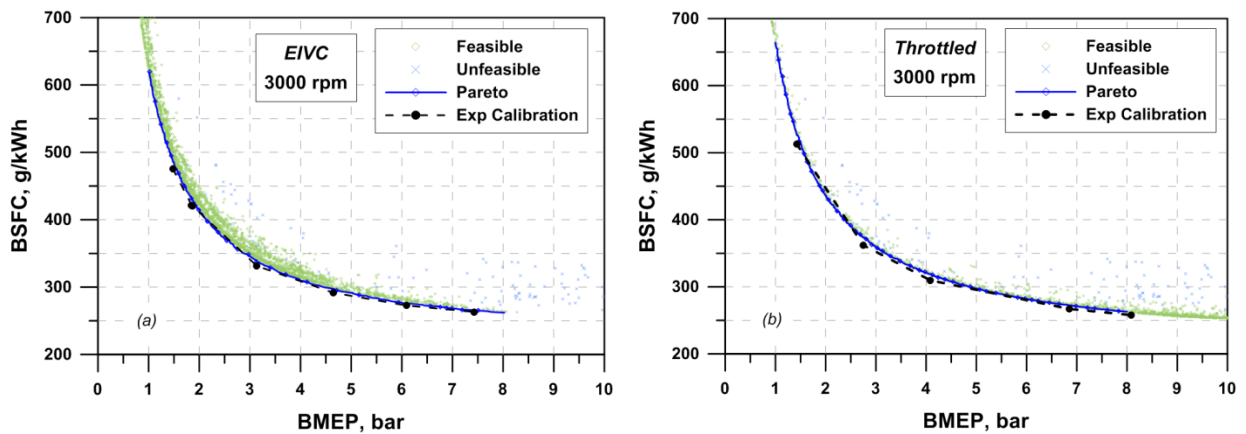


Figure 8.16 – Pareto frontiers in the BSFC vs. BMEP plane for *EIVC* (a) and *Throttled* (b) strategy.

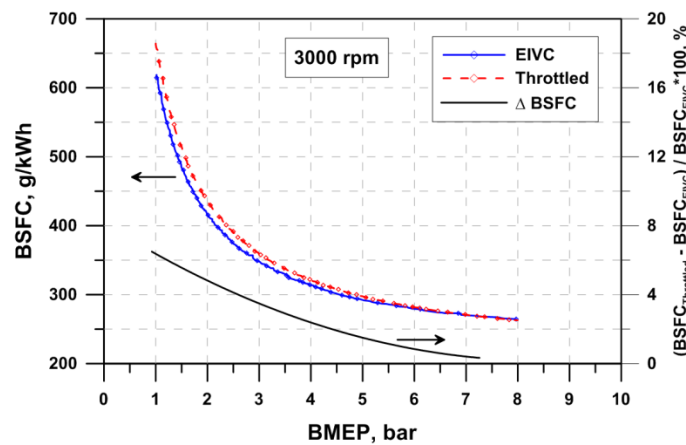


Figure 8.17 – Comparison of Pareto frontiers in the BSFC vs. BMEP for *EIVC* and *Throttled* strategies.

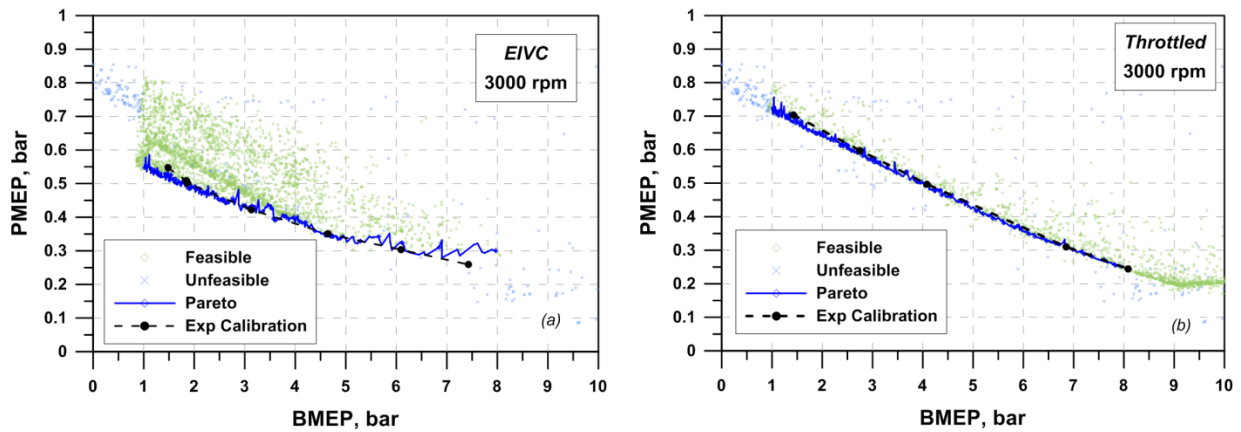


Figure 8.18 – PMEP vs. BMEP for EIVC (a) and Throttled (b) strategy.

It can be observed that the Pareto frontier is almost superimposed to the optimal calibrations identified at the test bench, denoting the reliability of the proposed optimization procedure. Figure 8.17 shows an absolute and percent comparison between the considered strategies, representing always a lower BSFC for *EIVC* calibrations. It can be observed that the advantages of the *EIVC* approach are minimum at the medium loads, while they increase as the load decreases, with a maximum advantage of about 6% at 1 bar of BMEP. The main driver for the BSFC improvements of *EIVC* strategy is, as expected, a lower pumping work, as shown in Figure 8.18a. The above occurrence is allowed by the possibility to adjust the amount of aspirated air by a modulation of the equivalent flow area through the intake valve, requiring a lower flow lamination by the throttle valve. This of course determines a higher in-cylinder pressure during the intake stroke, and consequently a lower pumping work.

Once discussed the capability of the proposed procedure in the identification of the optimal engine performance at part load operation, in the following the calibration parameters (input variables for the optimization) realizing the optimal performance will be compared with the experimentally actuated values.

Concerning the throttle valve, the angle imposed in the 1D simulation cannot be easily compared with any parameter set in the engine ECU. For this reason, the numerical/experimental throttle openings are indirectly compared by means of the pressure level in the intake manifold (labelled as “boost pressure” in Figure 8.19). It can be noted that the calibrations belonging to the Pareto frontier realize a boost pressure very close to the one derived by the experimental calibration. Figure 8.19a also underlines that an *EIVC* strategy allows to maintain an high boost level, even at very low engine loads, with significant advantages on PMEP and, consequently, BSFC. However, the above advantages are limited by the maximum allowable boost level that, as said, is set at 0.9 bar in order to limit the gas-dynamic noise emission at the intake mouth. The reliability of the optimization

process is further confirmed by Figure 8.20, showing a very good agreement between the numerically and experimentally-advised optimal values for the intake valve closure angles.

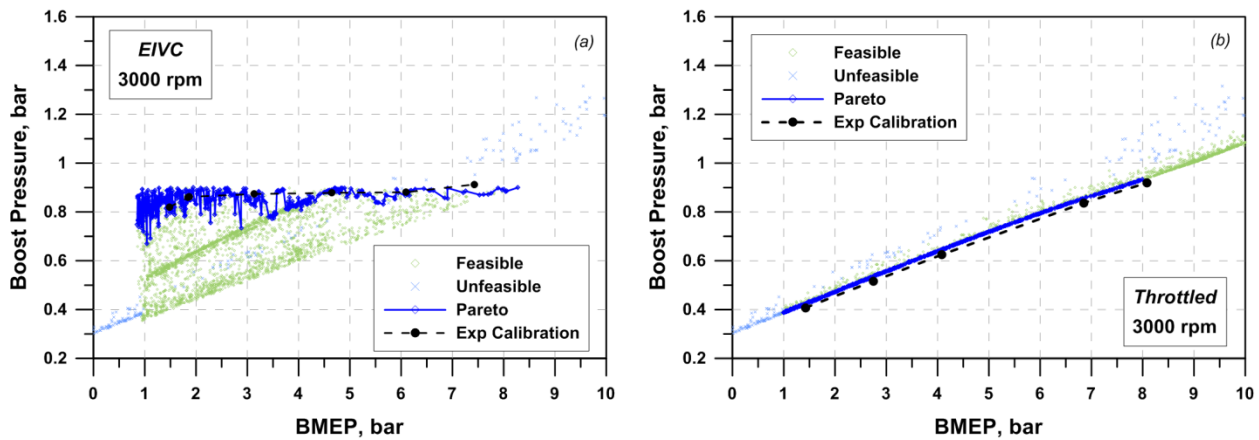


Figure 8.19 – Boost pressure vs. BMEP for EIVC (a) and Throttled (b) strategy.

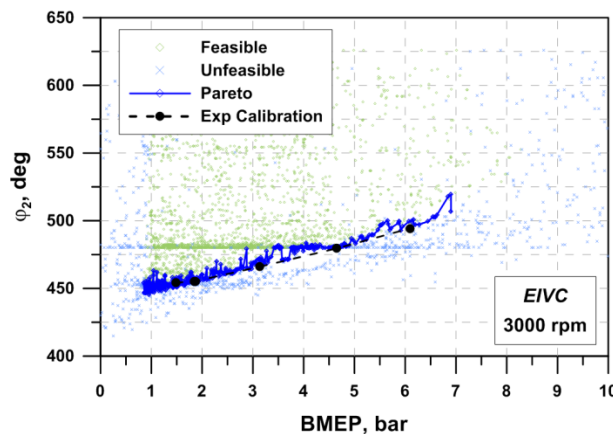


Figure 8.20 – Intake valve closure angle, φ_2 , vs. BMEP for EIVC strategy.

The automatic procedure also underlines that the optimal combustion phasing is attained for both the strategies with a MFB₅₀ angle between 6 and 8 degrees after the FTDC, denoting once again a very good agreement with the experimentally advised values (Figure 8.21). Finally, the optimization process reveals that the optimal calibrations are characterized by an almost fully opened waste-gate valve, in accordance with the experimental settings (Figure 8.22).

As said, the experimental WG setting is indirectly derived by the imposition of the turbocharger speed in the validation calculation. Summarizing, the proposed approach, based on the integration of 1D simulation and optimization tool, showed the potential to set up a calibration of the engine on purely theoretical basis, contributing to reduce the time and costs of an engine calibration at the test bench.

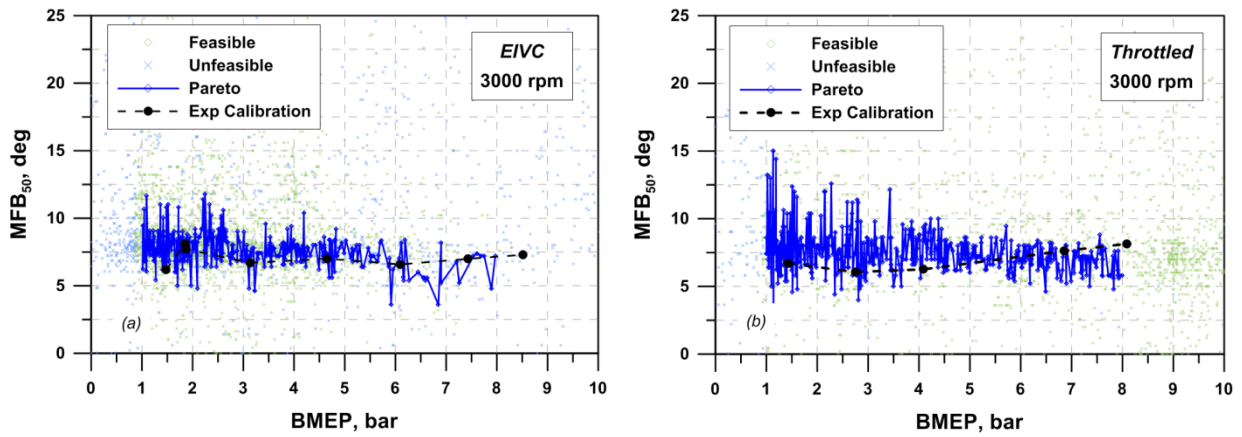


Figure 8.21 – MFB_{50} vs. BMEP for EIVC (a) and Throttled (b) strategy.

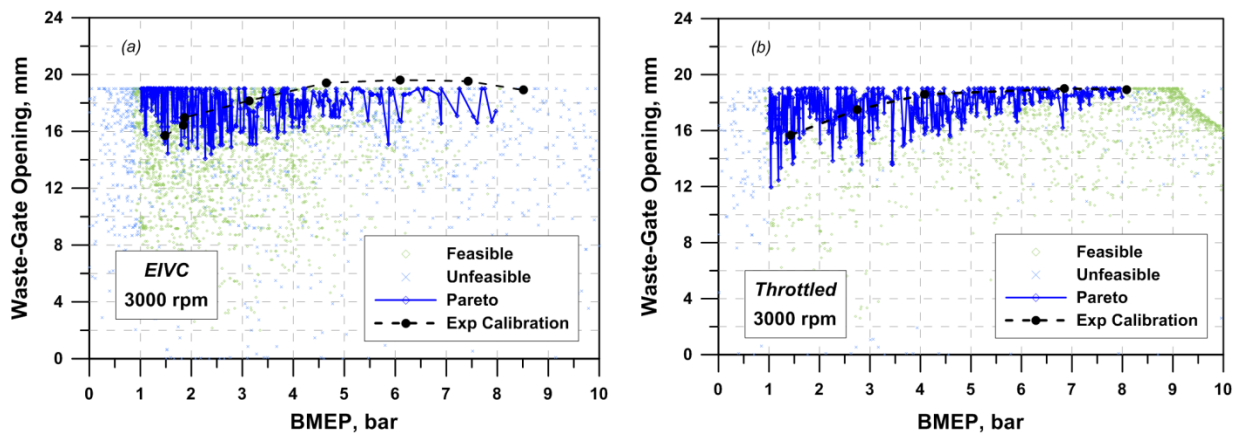


Figure 8.22 – Waste-gate opening vs. BMEP for EIVC (a) and Throttled (b) strategy.

Conclusions

In this work a twin-cylinder VVA downsized SI engine has been widely studied both from an experimental and numerical point of view. For this engine, particular attention has been devoted to the analysis of the in-cylinder processes, including turbulent combustion, knock and cyclic dispersion. Two main promising techniques for gasoline engines have been tested to improve the fuel consumption at high load operations. Issues related to the engine intake gas-dynamic noise and virtual calibration have been analyzed, too. First of all, the considered engine has been schematized by developing a detailed 1D model within GT-PowerTM environment. Proper in-house developed sub-models have been used to describe combustion process, turbulence phenomenon and knock occurrence. Cycle by cycle variation has been described by adopting a numerical procedure capable to reproduce both the *faster-than-average* and the *slower-than-average* in-cylinder pressure cycles strating from the average in-cylinder pressure cycle.

1D model has been widely validated against the experimental data both at part and full load operations. It showed the capability to reproduce with satisfactory accuracy the overall engine performance (power/torque, BSFC, air flow rate, boost pressure, turbocharger speed, SPL at the intake mouth, etc.). In-cylinder pressure cycles and burned rates predictions also showed a very high accuracy, mainly due to the refined user combustion model. An experimental knock detection analysis has been performed to identify knocking cycles with reference to the more critical operating conditions (high load and low speed). Knock model, takes into account the cycle by cycle variation, is validated at full load operation for various engine speed by the automatic identification of Knock Limited Spark Advance (KLSA). A good agreement between the 1D predicted KLSA and the experimental data has been reached. The effect of the employment of a Low pressure cooled EGR system on the engine performance at full load has been analyzed. Numerical results showed that the EGR increasing, a BSFC reduction is obtained for all the tested operating points. This is mainly ascribed to a higher knock resistance, allowing for an optimization of the combustion phasing and/or air-to-fuel ratio. Best BSFC improvements have been obtained at medium/low engine speeds with BSFC reduction above 20%.with respect to the base no-EGR configuration. The effects of port-water injection technique (WI) on the engine performance and on the knock resistance have been studied, too. 1D numerical results showed that the water injection technique involves substantial BSFC improvements for all the tested operating points. Once again, a higher knock resistance allows for an optimization of combustion phasing and/or reduction in the mixture over-fuelling. The heat subtracted by the water evaporation enhances the above effects, resulting in

Conclusions

most cases in increased BSFC benefits with respect to the EGR technique. WI technique allows for the maximum BSFC improvements at low/medium speed, with BSFC reductions up to 30 % with respect to the base configuration. Gas-dynamic noise at the intake mouth is reduced by a partial redesign of the intake system. In particular, two air-box configurations have been tested. The first solution includes an external Helmholtz resonator while the second one consists in an internal resonator. Both configurations have proved to allow for a reduction in the overall SPL at the engine intake mouth. The adoption of an external resonator has revealed a better improvement in the acoustic behavior at part and full load (up to a reduction of 5 dBA).

Finally, a numerical methodology aiming to calibrate the considered engine under high load knock limited and part load operations has been described. It showed the capability to identify with satisfactory accuracy the experimentally advised engine calibrations. This methodology, which considers the whole 1D engine model coupled to an external optimizer, has been employed to compare a common *Full Lift* strategy with an *EIVC* strategy. The results underlined that the latter involves BSFC benefits at medium loads and at very low loads, up to 8% with respect to the *Full Lift* strategy.

List of Papers during the Doctoral studies

- I. Bozza F., De Bellis V., Teodosio L., "Numerical analysis of the transient operation of a turbocharged diesel engine including the compressor surge", *Proceedings of the Institution of Mechanical Engineers Part D Journal of Automobile Engineering*, 12/2013; 227(11):1503-1517. doi:10.1177/0954407013501668;
- II. Siano D., Teodosio L., De Bellis V., and Bozza F., "Analysis and Design of an Intake Filter Box for a Downsized VVA Engine," *SAE Technical Paper 2014-01-1693*, 2014, doi:10.4271/2014-01-1693;
- III. Siano D., Bozza F., Teodosio L., and De Bellis V., "A Comparison Between External and Internal Resonators Employment to Reduce the Gas-Dynamic Noise of a SI Engine," *SAE Int. J. Engines* 8(1):42-52, 2015, doi:10.4271/2014-01-2864;
- IV. Bozza F., De Bellis V., Teodosio L., "EGR systems employment to reduce the fuel consumption of a downsized turbocharged engine at high load operations", *Energy Procedia* 81, pag. 886-873, 69° Congresso Nazionale ATI 2014 Milano, doi:10.1016/j.egypro.2015.12.134;
- V. Teodosio L., De Bellis V., and Bozza F., "Fuel Economy Improvement and Knock Tendency Reduction of a Downsized Turbocharged Engine at Full Load Operations through a Low-Pressure EGR System," *SAE Int. J. Engines* 8(4):1508-1519, 2015, doi:10.4271/2015-01-1244;
- VI. De Bellis V., Teodosio L., Siano D., Minarelli F. et al., "Knock and Cycle by Cycle Analysis of a High Performance V12 Spark Ignition Engine. Part 1: Experimental Data and Correlations Assessment," *SAE Int. J. Engines* 8(5):1993-2001, 2015, doi:10.4271/2015-24-2392;
- VII. Teodosio L., Attilio R., Nonatelli F., "1D/3D Methodology for the prediction and the calibration of a high performance SI engine", *Energy Procedia* 82, pag. 936-943, 70° Congresso Nazionale ATI 2015. doi:10.1016/j.egypro.2015.11.842;
- VIII. Bozza F., Teodosio L., " Performance Optimization of a Turbocharged Spark-Ignition VVA Engine at Part Load ", *Journal of Advances in Applied&Computational Mathematics*, 2(2): pag. 61-69, 2015, doi: <http://dx.doi.org/10.15377/2409-5761.2015.02.02.4>;
- IX. Bozza F., De Bellis V., Teodosio L., "Potentials of Cooled EGR and water injection for knock resistance and fuel consumption improvements of gasoline engines", *Applied Energy* 169: 112-125, 2016, doi: 10.1016/j.apenergy.2016.01.129.

References

1. H. Eichlseder and A. Wimmer, "Future perspectives of the IC engine ", 14th International Conference "Transport and Air Pollution", Graz, 2005.
2. Stacy C. David, Susan W. Diegel, Robert C. Boundy, "Transportation Energy data book: Edition 34", August 2015. Available on-line at cta.orln.gov/data.
3. Annual EU greenhouse gas inventory 1990-2009 and inventory report 2011. Available at <http://www.eea.europa.eu/publications/european-union-greenhouse-gas-inventory-2011/>.
4. Pilotto L.S., Douglas R.M., Attewel R.G. and Wilson S.R., "Respiratory effects associated with indoor nitrogen dioxide exposure in children", *Int. J. Epidemiol*, vol. 26, n.4, pag. 788-796, August 1997, doi: 10.1093/ije/26.4.788.
5. Regulation (EC) No 715/2007 of the European Parliament and of the Council of 20 June 2007 on type approval of motor vehicles with respect to emissions from light passenger and commercial vehicles (Euro 5 and Euro 6) and on access to vehicle repair and mai.
6. Fontana, G., Galloni, E., "Variable valve timing for fuel economy improvement in a small spark-ignition engine," *Applied Energy*, 86:96–105, 2009,doi : 10.1016/j.apenergy.2008.04.009.
7. Wirth, M., Schulte, H., "Downsizing and Stratified Operation – An Attractive Combination Based on a Spray-guided Combustion System," Intl. Conference on Automotive Technologies, Istanbul 2006.
8. Amman, H., Alger, T., Mehta, D., "The Effect of EGR on Low-Speed Pre-Ignition in Boosted SI Engines," SAE Technical Paper 2011-01-0339, 2011, doi: 10.4271/2011-01-0339.
9. Zhen, X., Wang, Y., Xu, S., Zhu, Y., et al., "The engine Knock analysis- An Overview," *Applied Energy* 92 : 628-636, 2012, doi : 10.1016/j.apenergy.2011.11.079.
10. Kuzstelan, Y. F. Yao, D. Marchant and Y. Wang, "Increasing Low Speed Engine Response of a Downsized CI Engine Equipped with a Twin-Entry Turbocharger", Ricardo European User Conference 2011, Ludwigsburg, Germany.
11. EPA and CARB Emission Standards To Control Nonroad Exhaust Emissions of Fire Pumps and Chain Saws, <http://www.fs.fed.us/t-d/pubs/html/02511204/02511204.htm>.
12. EC2002, Variable Compression Ratio Technology for CO₂ Reduction of Gasoline Engines in Passenger Cars, European Commission Community Research. http://ec.europa.eu/research/conferences/2002/pdf/presspacks/1-1-vcr_en.pdf.
13. Advanced Combustion Systems and Alternative powerplants, Module 7, Lecture 32. Available at <http://nptel.ac.in/downloads/112104033/>
14. EPA 2008, A Study of Potential Effectiveness of Carbon Dioxide Reducing Vehicle Technologies, Revised Final Report, EPA420- R-08-004a, United States Environment Protection Agency, June 2008.
15. TNO 2006, Review and analysis of the reduction potential and costs of technological and other measures to reduce CO₂-emissions from passenger cars, Contract nr. S12.408212, TNO/ IEEP/ LAT, October 2006.
16. IEA 2005, Making cars more efficient: Technology for Real Improvements on the Road, International Energy Agency and European Conference of Ministers of Transport Joint Report, 2005.
17. Drake and Haworth, Advanced gasoline engine development using optical diagnostics and

References

- numerical modelling, Proceedings of the Combustion Institute 31 (2007) 99-124.
18. Mittal V., Revier B., Heywood J.B., 2007, "Phenomena that Determine Knock Onset in Spark-Ignition Engines", SAE Technical Paper 2007-01-0007.
 19. Eckert P., Song-Charng Kong S., Reitz R., 2003, "Modeling Autoignition and Engine Knock", SAE Technical Paper 2003-01-0011.
 20. Carbon Trust 2003, Low Cost Solution for Gasoline Engine Controlled Auto Ignition, Project reference number 2003-5-22.
 21. D'Adamo A., Berni F., Breda S., Lugli M. et al., "A Numerical Investigation on the Potentials of Water Injection as a Fuel Efficiency Enhancer in Highly Downsized GDI Engines," SAE Technical Paper 2015-01-0393, 2015, doi:10.4271/2015-01-0393.
 22. EPA 2008, EPA Staff Technical Report: Cost and Effectiveness Estimates of Technologies Used to Reduce Light-duty Vehicle Carbon Dioxide Emissions, EPA420-R-08-008, United States Environment Protection Agency, March 2008.
 23. John B. Heywood "Internal Combustion Engine Fundamentals", Mc-Graw Hill 1988.
 24. C. R. Ferguson and A. T. Kirkpatrick, "Internal Combustion Engines: Applied Thermosciences", 2000.
 25. Bozza F., Gimelli A., Federico N., Merola S. S., and Vaglieco B. M., "Validation of a fractal combustion model through flame imaging", SAE Technical paper N. 2005-01-1120, April 2005, doi: 10.4271/2005-01-1120.
 26. Bozza F., Fontana G., Galloni E., Torella E., "3D-1D Analyses of the Turbulent Flow Field, Burning Speed and Knock Occurrence in a Turbocharged SI Engine", in 8th International Conference on Engines for Automobiles, 2007, N. 2007-24-0029, 10.4271/2007-24-0029.
 27. Bozza F., Gimelli A., Strazzullo L., Torella E., Cascone C., "Steady-State and Transient Operation Simulation of a Downsized Turbocharged SI Engine," in SAE Technical paper, 2007, N.2007-01-0381, 10.4271/2007-01-0381.
 28. Borghi R., "On the structure and morphology of turbulent premixed flames," Recent Adv. Aerosp. Sci., 1985.
 29. Demesoukas Sokratis, "0D/1D combustion modeling for the combustion systems optimization of spark ignition engines", Doctoral Thesis, Université D'Orléans, 2015.
 30. Shen H., Hinze C., Heywood J.B., "A study of cycle-to-cycle variations in SI Engines Using a Modified Quasi-Dimensional Model", SAE Technical paper, N. 961187, 1996, doi: 10.4271/961187.
 31. Keck J.C., "Turbulent flame structure and speed in spark ignition engines," Symposium Combustion, vol. 19, N. 1, pp. 1451-1466, January 1982, doi: 10.1016/S0082-0784(82)80322-6.
 32. Beretta G.P., Rashidi M., Keck J.C., "Turbulent flame propagation and combustion in spark ignition engines," Combustion and Flame, vol.52, pp. 217-245, January 1983, doi: 10.1016/0010-2180(83)90135-9.
 33. Galloni E., "Analyses about parameters that affect cyclic variation in a spark ignition engine", *Applied Thermal Engineering* 29 (5):1131-1137, 2009, doi:10.1016/j.applthermaleng.2008.06.001.
 34. Rashidi M., "The nature of cycle-by-cycle variation in the S.I. Engine from high speed photographs", *Combustion and Flame* 42: 111-122, 1981, doi: 10.1016/0010-2180(81)90150-4.
 35. Hamai K., Kawajiri H., Ishizuka T. and Nakai M., "Combustion Fluctuation Mechanism Involving Cycle-to-Cycle Spark Ignition Variation Due to Gas Flow Motion in S.I Engines",

References

- Proceedings of Combustion Institute* 21(1): 505-512, 1986, doi: 10.1016/S0082-0784(88)80279-0.
36. Hill P.G., "Cyclic variations and turbulence structure in spark-ignition engines", *Combustion and Flame*, 72(1):, 73-89, 1988, doi: 10.1016/0010-2180(88)90098-3.
37. Bates S., "Flame Imaging Studies of Cycle-by-Cycle Combustion Variation in a SI Four-Stroke Engine", SAE Technical Paper 892086, 1989, doi:10.4271/892086.
38. Fontanesi, S., Paltrinieri, S., and Cantore, G., "LES Analysis of Cyclic Variability in a GDI Engine," SAE Technical Paper 2014-01-1148, 2014, doi:10.4271/2014-01-1148.
39. Fontanesi, S., D'Adamo, A., Paltrinieri, S., Cantore, G. et al., "Assessment of the Potential of Proper Orthogonal Decomposition for the Analysis of Combustion CCV and Knock Tendency in a High Performance Engine," SAE Technical Paper 2013-24-0031, 2013, doi:10.4271/2013-24-0031.
40. Young, M., "Cyclic dispersion in the homogenous-charge spark ignition engine- A literature survey", SAE Technical paper 810020, 1981, doi: 10.4271/810020.
41. De Bellis V., Teodosio L., Siano D., Minarelli F. et al., "Knock and Cycle by Cycle Analysis of a High Performance V12 Spark Ignition Engine. Part 1: Experimental Data and Correlations Assessment," *SAE Int. J. Engines* 8(5):1993-2001, 2015, doi:10.4271/2015-24-2392.
42. Pundir, B., Zvonow, V., and Gupta, C., "Effect of charge non-homogeneity on cycle by cycle variation in combustion in SI engines", SAE Technical paper 810774; 1981, doi: 10.4271/810774.
43. Hassaneen, A., Varde, K., Bawady, A., and Morgan, A., "A study of the flame development and rapid burn duration in a lean-burn fuel injected natural gas S.I. engine", SAE Technical paper 981384; 1998, doi: 10.4271/981384.
44. Ozdor, N., Dulger, M., and Sher, E., "An experimental study of the cyclic variability in spark ignition engine", SAE Technical paper 960611; 1996, doi: 10.4271/960611.
45. Maurya, R.K, and Agarwal, A.K., "Experimental investigation of cyclic variations in HCCI combustion parameters for gasoline like fuels using statistical methods", *Applied Energy* 111:310-323, 2013, doi:10.1016/j.apenergy.2013.05.004.
46. E. Antonelli; G. Colasurdo, Contributo al miglioramento della caratteristica di regolazione dei motori ad accensione comandata, in ATA, vol. 26, pp. 540-554. - ISSN 0001-2661, 1974
47. Moriya Y, Watanabe A, Uda H, Kawamura H et al. A Newly Developed Intelligent Variable Valve Timing System – Continuously Controlled Cam Phasing as Applied to a New 3 Liter Inline 6 Engine. SAE Technical Paper 960579, 1996, doi:10.4271/960579
48. Sellnau M, Kunz T, Sinnamon J, Burkhard J. 2-step Variable Valve Actuation: System Optimization and Integration on an SI Engine. SAE Technical Paper 2006-01-0040, 2006, doi:10.4271/2006-01-0040.
49. Kreuter P, Heuser P, Schebitz M. Strategies to Improve SI-Engine Performance by Means of Variable Intake Lift, Timing and Duration. SAE Technical Paper 920449, 1992, doi:10.4271/920449.
50. Kutlar OA, Arslan H, Calik AT, Methods to improve efficiency of four stroke, spark ignition engines at part load, *Energy Conversion and Management*, Volume 46, Issue 20, December 2005, Pages 3202-3220, ISSN 0196-8904, <http://dx.doi.org/10.1016/j.enconman.2005.03.008>.
51. Tuttle J.H., *Controlling Engine Load by Means of Late Intake-Valve Closing*, SAE 800794, 1980.

References

52. Urata Y., Umiyama H., Shimizu K., Fujiyoshi Y., Sono H., Fukuo K., *A Study of Vehicle Equipped with Non-Throttling S. I. Engine with Early Intake Valve Closing Mechanism*, SAE paper 930820.
53. Leone T.G., Christenson E.J. Stein, R.A., Comparison of Variable Camshaft Timing Strategies at Part Load, SAE 960584, 1996.
54. Haugen D. J., Blackshear P. L., Piphro M. J., Esler W. J., Modifications of a Quad 4 Engine to Permit Late Intake Valve Closure, SAE paper 921663, 1992.
55. Lancefield T. M., Gayler R. J., Chattopadhyay A., The Practical Application and Effects of a Variable Event Valve Timing System, SAE paper 930825, SAE Int. Congr. & Exp., Detroit, MI, USA, 1993.
56. Vogel O., Roussopoulos K., Guzzella L., Czekaj J., Variable Valve Timing Implemented with a Secondary Valve on a Four Cylinder SI Engine, SAE paper 970335, SAE Int. Cong. & Exp., Detroit, MI, USA., February 24-27, 1997.
57. Bozza F., Gimelli A., Piazzesi R., Fortunato F., Pianese V., Siano D. (2007) The prediction of the performance and gasdynamic noise emitted by a medium-size spark-ignition engine by means of 1D and 3D analyses. In SAE Vol. SP-2079 "Modeling of SI and Diesel Engines, 2007", pp. 1-10 (ISBN 978-0-7680-1869-1).
58. Siano D., Corcione F.E., Bozza F., Gimelli A., Manelli S., Characterization of the Noise Emitted by a Single Cylinder Diesel Engine: Experimental Activities and 1D Simulation, SAE 2005 NOISE and Vibration, Traverse City (MI), Paper 133.
59. De Bellis V, Bozza F, Siano D, Gimelli A, Fuel Consumption Optimization and Noise Reduction in a Spark-Ignition Turbocharged VVA. SAE Int. J. Engines 6(2):2013, doi:10.4271/2013-01-1625.
60. D'Errico G, Cerri T, Pertusi G, Multi-objective optimization of internal combustion engine by means of 1D fluid-dynamic models. Applied Energy 2011, 88(3):767-777.
61. Millo F, Perazzo A, Pautasso E, Optimizing the calibration of a turbocharged GDI engine through numerical simulation and direct optimization. SAE Int. J. Engines 2010, 3(1): 556-570, doi: 10.4271/2010-01-0780.
62. Bianchi G., Fontanesi S., On the Applications of Low-Reynolds Cubic $k\text{-}\bar{\epsilon}$ Turbulence Models in 3D Simulations of ICE Intake Flows. SAE Paper 2003-01-0003, 2003, doi:10.4271/2003-01-0003.
63. Kolin O., Benkenida A., The 3-Zones Extended Coherent Flame Model (ECFM3Z) for Computing Premixed/Diffusion Combustion, Oil & Gas Science and Technology – Rev. IFP, Vol. 59 (2004), No. 6, pp. 593-609.
64. Shayler P., May S. and Ma T., "Heat Transfer to the Combustion Chamber Walls in Spark Ignition Engines", SAE Technical Paper 950686, 1995, doi: 10.4271/950686.
65. Sharief A., Chandrashekar T., Antony A. and Samaga B., "Study on Heat Transfer Correlation in IC Engines", SAE Technical Paper 2008-01-1816, 2008, doi: 10.4271/2008-01-1816.
66. Shojaeefard M. H., et al., Cooled EGR for a Turbo Charged SI Engine to Reduce Knocking and Fuel Consumption, International Journal of Automotive Engineering, Vol. 3, Num. 3, September 2013.
67. Grandin B., Ångström H., Replacing Fuel Enrichment in a Turbo Charged SI engine: Lean Burn or Cooled EGR, SAE Technical Paper 1999-01-3505, 1999, doi: 10.4271/1999-01-3505.

References

68. Tuccillo R., “Modellistica dei processi non stazionari in motori a combustione interna”, Notes from the course of “Termofluidodinamica delle Macchine”, University of Naples, 2012.
69. Hanjalic Kemal, ICE Physics & Chemistry AVL FIRE v. 2008, Users Guide.
70. Ferrari G., “Motori a Combustione Interna”, Edizione Il Capitello, Torino, 1996.
71. Matthews RD, Chin YW. A Fractal- Based SI Engine Model: Comparisons of Predictions with Experimental Data. SAE paper 910075, 1991.
72. Poulos SG, Heywood JB. The Effect of Chamber Geometry on Spark-Ignition Engine Combustion. SAE paper 830334, 1983.
73. North GL, Santavicca DA. The Fractal Nature of Premixed Turbulent Flames. Combustion Science and Technology, 1990.
74. Bradley D, Lau AKC, Lawes M. Flame Stretch Rate as a Determinant of Turbulent Burning Velocity. Phil. Trans. R. Soc. Lond. A 1992 338, 359-387, doi: 10.1098/rsta.1992.0012.
75. Lee TK, Filipi ZS. Improving the Predictiveness of a Quasi-D Combustion Model for Spark Ignition Engines with Flexible Intake Systems. International Journal of Automotive Technology, Vol. 12, No. 1, pp. 1-9 (2011).
76. Richard S, Bougrine S, Font G, Lafossas FA, Le Berr F. On the Reduction of a 3D CFD Combustion Model to Build a Physical 0D Model for Simulating Heat Release, Knock and Pollutants in SI Engines. Oil & Gas Science and Technology – Rev. IFP, Vol. 64 (2009), No. 3, pp. 223-242. doi: 10.2516/ogst/2008055.
77. Rivas M, Higelin P, Caillol C, Sename O, Witrant E, Talon V. Validation and Application of a New 0D Flame/Wall Interaction Sub Model for SI Engines. SAE paper 2011-01-1893.
78. Sjeric M, Kozarac D, Bogensperger M. Implementation of a Single Zone k-ε Turbulence Model in a Multi Zone Combustion Model. SAE paper 2012-01-0130, doi:10.4271/2012-01-0130.
79. Morel T, Keribar R. A Model for Predicting Spatially and Time Resolved Convective Heat Transfer in Bowl-in-Piston Combustion Chambers. SEA Paper 850204. International Congress & Exposition, Detroit, Michigan February 25 - March 1, 1985.
80. Achuth M, Mehta PS. Predictions of tumble and turbulence in four-valve pentroof spark ignition engines. International Journal of Engine Research 2001 2: 209, doi: 10.1243/1468087011545442.
81. Borgnakke C, Arpaci VS, Tabaczynski RT. A Model for the Instantaneous Heat Transfer and Turbulence in Spark Ignition Engine. SAE Paper 800287, 1980, doi:10.4271/800287.
82. Wong V, Hault D. Rapid Distortion Theory Applied to Turbulent Combustion. SAE Paper 790357, 1979, doi:10.4271/790357.
83. De Bellis V., Severi E., Fontanesi S., Bozza F., “Hierarchical 1D/3D approach for the development of a Turbulent Combustion Model Applied to a VVA Turbocharged Engine. Part I: Turbulence Model”, ATI 2013, 68th Conference of the Italian Thermal Machines Engineering Association, Vol. 45, 2014, Pag. 829-838.
84. Lipatnikiv AN, Chomiak J. Turbulent Flame Speed and Thickness: Phenomenology, Evaluation and Application in Multidimensional Simulations. Progress in *Energy and Combustion Science*, 28, pp. 1-74, 2002.
85. Hudson, C., Gao, X., Stone, R., “Knock measurement for fuel evaluation in spark ignition engines”, Fuel Journal 80 (2001) 395-407.
86. Chun K.M., Heywood J.B. “Characterization of knock in a spark-ignition engine”, SAE Paper, 1989, p. 890156.

References

87. Etefagh M.M., Sadeghi M.H., Prrouzpanah V., Arjmandi Tash H., "Knock detection in spark ignition engines by vibrational analysis of cylinder block: A parametric modeling approach", *Mechanical Systems and Signal Processing Journal*, 22, pp. 1495–1514, 2008.
88. Kearney-Delphi M.J., Knock signal conditioning using the discrete fourier transform and variable detection window length, SAE Technical Paper, 2007-01-1509, 2007.
89. Antoni J., Daniere J., Guillet F., Effective vibration analysis of IC engines using cyclostationarity. Part I. A methodology for condition monitoring, *Journal of Sound and Vibration* 257 (5) (2002) 815–837.
90. Wu G., A real time statistical method for engine knock detection, SAE Technical Paper, 2007-01-1507, 2007.
91. Bozza F., Siano D., Torella E., Cycle-by-Cycle Analysis, Knock Modeling and Spark-Advance Setting of a 'Downsized' Spark-Ignition Turbocharged Engine, *SAE International Journal of Engines*, 2, pp. 381-389, ISSN: 1946-3936, 2010.
92. Cavina N. et al., Combustion Monitoring Based on Engine Acoustic Emission Signal Processing, SAE Paper 2009-01-1024, 2009.
93. Millo F., Ferraro C., Knock in S.I. Engines: A Comparison between Different Techniques for Detection and Control," SAE Paper 982477, 1998, doi:10.4271/982477.
94. Elmqvist C., Lindström F. Angström H.E., Börje G., Kalghatgi G.,"Optimizing Engine Concepts By Using a Simple Model for Knock Prediction", SAE Paper 2003-01-3123, 2003.
95. Leppard, W., "Individual-Cylinder Knock Occurrence and Intensity in Multicylinder Engines," SAE Technical Paper 820074, 1982, doi:10.4271/820074.
96. Puzinauskas, P., "Examination of Methods Used to Characterize Engine Knock," SAE Technical Paper 920808, 1992, doi:10.4271/920808.
97. Brecq G., Bellettre J., Tazerout M., "A New Indicator for Knock Detection in Gas SI Engines", *International Journal of Thermal Sciences*, 42, pp.523-532.
98. Corti, E. and Moro, D., "Knock Indexes Thresholds Setting Methodology," SAE Technical Paper 2007-01-1508, 2007, doi:10.4271/2007-01-1508.
99. Forte C., Corti E., Bianchi G.M., "Combined Experimental and Numerical Analyses of Knock in Spark Ignition Engine", *Proceedings of the ASME Internal Combustion Engine Division, 2009 Fall Technical Conference ICEF09*, ICEF2009-14102, 2009.
100. Thomas J.R.; Clarke D.P., Collins J.M., Sakonji T., Ikeda K., Shoji F., Furushima K., A test to evaluate the influences of natural gas composition and knock intensity, *Trans. ASME J. ICE* 22, 1994.
101. Abu-Qudais M., Exhaust Gas Temperature for Knock Detection and Control in Spark Ignition Engine, *Energy Convers. Mgmt*, Vol. 37, No. 9, pp. 1383-1392, 1996.
102. Kawahara N, Tomita E, Sakata Y. Auto-ignited kernels during knocking combustion in a spark-ignition engine. *P Combust Inst* 2007;31:2999–3006.
103. Bozza et al., A Knock Model for 1D Simulations Accounting for Cyclic Dispersion Phenomena, SAE paper 2014-01-2554.
104. Chatfield C. *The Analysis of Time Series: An Introduction*. 6th ed. Boca Raton, FL: Chapman & Hall/CRC, 2004.
105. Rolf S. et al., Model identification and parameter estimation of ARMA models by means of evolutionary algorithms, *Comput. Intell. Financial Eng.* 23 (1997), pp. 237–243.
106. Liang G. et al., ARMA model order estimation based on the eigenvalues of the covariance

References

- matrix, IEEE Trans. Signal Process. 41 (1993), pp. 3003–3009.
107. Akaike H., Statistical predictor identification, Ann. Znst. Stat. Math. 22 (1970), pp. 203–217.
108. Spelina J. M. et al., Characterization of knock intensity distributions: Part 1: statistical independence and scalar measures, *Proceedings of the Institution of Mechanical Engineers, Part D: Journal of Automobile Engineering*, doi: 10.1177/0954407013496233, August 2013.
109. Millo, F., Rolando, L., Pautasso, E., and Servetto, E., "A Methodology to Mimic Cycle to Cycle Variations and to Predict Knock Occurrence through Numerical Simulation," SAE Technical Paper 2014-01-1070, 2014, doi:10.4271/2014-01-1070.
110. Pera C., Richard S., and Angelberger C., "Exploitation of Multi-Cycle Engine LES to Introduce Physical Perturbations in 1D Engine Models for Reproducing CCV," SAE Technical Paper 2012-01-0127, 2012, doi: 10.4271/2012-01-0127.
111. Fontana G., Bozza F., Galloni E., Siano D., "Experimental and Numerical Analyses for the Characterization of the Cyclic Dispersion and Knock Occurrence in a Small-Size SI Engine", SAE Paper 2010-32-0069 Small Engine Technology Conference (SETC), Linz, September 2010.
112. Andrae J, Headb R. HCCI experiments with gasoline surrogate fuels modeled by a semidetalled chemical kinetic model. *Combustion and Flame* 2009; 156:842–851.
113. Andrae J. Comprehensive chemical kinetic modeling of toluene reference fuels oxidation. *Fuel* 2013; 107:740–748.
114. Liu Y, Jia M, Xie M, Pang B, Development of a New Skeletal Chemical Kinetic Model of Toluene Reference Fuel with Application to Gasoline Surrogate Fuels for Computational Fluid Dynamics Engine Simulation. *Energy Fuels* 2013; 27(8):4899–4909.
115. Lafossas FA, Castagne M, Dumas JP, Henriot S. Development and validation of a knock model in spark ignition engines using a CFD code. SAE Technical Paper 2002-01-2701; 2002.
116. Douaud A, Eyzat P. Four-Octane-Number Method for Predicting the Anti-Knock Behavior of Fuels and Engines. SAE Technical Paper 780080; 1978.
117. Holly W., Lauer T., Schuemie H., Murakami S., "Modelling the Knocking Combustion of a Large Gas Engine Considering Cyclic Variations and Detailed Reaction Kinetics". SAE Technical Paper 2014-01-2690; 2014.
118. Teodosio L, De Bellis V, Bozza F. Fuel Economy Improvement and Knock Tendency Reduction of a Downsized Turbocharged Engine at Full Load Operations through a Low-Pressure EGR System. *SAE Int J Engines* 2015; 8(4):1508-1519.
119. Bozza F, De Bellis V, Minarelli F, Cacciatore D. Knock and Cycle-by-Cycle Analysis of a High Performance V12 Spark Ignition Engine. Part 2: 1D Combustion and Knock Modeling. *SAE Int. J. Engines* 2015; 8(5):2002-2011.
120. Cipolla G., Heat transfer correlations applicable to the analysis of internal combustion engine head cooling. *Heat and Mass Transfer in Gasoline and Diesel Engines. Proceedings of the International Center for Heat and Mass Transfer, Afgan and Spalding, 1988, pp. 373–396.*
121. Shiga, S., Yagi, S., Morita, M., Matsumoto, T., Nakamura, H. and Karasawa, T. "Effects of Early-Closing of Intake valve on the Engine Performance in a Spark-Ignition Engine" SAE paper 960585, 1985.
122. Ichimaru, K. Sakai, H. Kanesaka, H. and Winterbone, D. "A Rotary Valve Controlled High Expansion Ratio Gasoline Engine" SAE paper 940815, 1994.
123. Hitomi, M., Sasaki, J., Hatamura, K. and Yano, Y., "Mechanism of Improving Fuel

References

- Efficiency by Miller Cycle and its Future Prospect" SAE paper 950974, 1995.
124. Li Zhaowen, Shu Gequn, Wei Haiqiao, Liang Xingyu. "Experimental investigation on effect of EGR on combustion noise in transient conditions of DI – diesel engine". *Chinese Int Combust Engine Eng* 2010; 31:17–22.
 125. Wei Haiqiao, Liang Xingyu, Shu Gequn. "Influence of the accelerating operation mechanism on the combustion noise in DI – diesel engines". *Int J Automotive Technol* 2012; 13:373–88.
 126. Alger T., Mangold B., Roberts C., and Gingrich J., "The Interaction of Fuel Anti-Knock Index and Cooled EGR on Engine Performance and Efficiency," *SAE Int. J. Engines* 5(3):1229-1241, 2012, doi:10.4271/2012-01-1149.
 127. Hedge M., Weber P., Gingrich J., Alger T. et al., "Effect of EGR on Particle Emissions from a GDI Engine," *SAE Int. J. Engines* 4(1):650-666, 2011, doi:10.4271/2011-01-0636.
 128. Cairns, A., Blaxill, H., and Irlam, G., "Exhaust Gas Recirculation for Improved Part and Full Load Fuel Economy in a Turbocharged Gasoline Engine," *SAE Technical Paper* 2006-01-0047, 2006, doi:10.4271/2006-01-0047.
 129. Bourhis G., Chauvin J., Gautrot X., de Francqueville, L., "LP EGR and IGR Compromise on a GDI Engine at Middle Load," *SAE Int. J. Engines* 6(1):67-77, 2013, doi:10.4271/2013-01-0256.
 130. Francqueville L., Michel J., "On the Effects of EGR on Spark-Ignited Gasoline Combustion at High Load," *SAE Int. J. Engines* 7(4):2014, doi:10.4271/2014-01-2628.
 131. Potteau S., Lutz P., Leroux S., Moroz S. et al., "Cooled EGR for a Turbo SI Engine to Reduce Knocking and Fuel Consumption," *SAE Technical Paper* 2007-01-3978, 2007, doi:10.4271/2007-01-3978.
 132. Alger T., Chauvet T., Dimitrova Z., "Synergies between High EGR Operation and GDI Systems," *SAE Int. J. Engines* 1(1):101- 114, 2008, doi:10.4271/2008-01-0134.
 133. Pirault J., Ryan T., Alger T., Roberts C., "Performance Predictions for High Efficiency Stoichiometric Spark Ignited Engines," *SAE Technical Paper* 2005-01-0995, 2005, doi:10.4271/2005-01-0995.
 134. Galloni E., Fontana G., Palmaccio R., "Numerical analysis of EGR techniques in a turbocharged spark-ignition engine," *Applied Thermal Engineering* 39:95-104, 2012, doi: 10.1016/j.applthermaleng.2012.01.040.
 135. Kumano K., Yamaoka S., "Analysis of Knocking Suppression Effect of Cooled EGR in Turbo-Charged Gasoline Engine," *SAE Technical Paper* 2014-01-1217, 2014, doi:10.4271/2014-01-1217.
 136. Bozza F., Tuccillo R., De Falco D., "A Two-Stroke Engine Model Based on Advanced Simulation of Fundamental Processes", *SAE Technical Paper* 952139, 1995, doi:10.4271/952139.
 137. Bozza, F., De Bellis, V., Gimelli, A., Muccillo, M., "Strategies for Improving Fuel Consumption at Part-Load in a Downsized Turbocharged SI Engine: a Comparative Study," *SAE Int. Journal of Engines* 7(1): 60-71, 2014; doi:10.4271/2014-01-1064.
 138. De Bellis, V., Bozza, F., Siano, D., and Gimelli, A., "Fuel Consumption Optimization and Noise Reduction in a Spark-Ignition Turbocharged VVA Engine," *SAE Int. J. Engines* 6(2):1262-1274, 2013, doi:10.4271/2013-01-1625.
 139. Fontana, G., Galloni, E., "Experimental analysis of a spark-ignition engine using exhaust gas recycle at WOT operation," *Applied Energy* 87(7):2187-2193, 2010, doi: 10.1016/j.apenergy.2009.11.022.

References

140. Rhodes D, Keck J. “Laminar Burning Speed Measurements of Indolene-Air-Diluent Mixtures at High Pressures and Temperatures”. SAE Technical Paper 850047; 1985.
141. Hoppe F, Thewes M, Baumgarten H and Dohmen J. Water injection for gasoline engines: Potentials, challenges, and solutions. *International J of Engine Research* 1–11.
142. Soyelmez MS, Ozcan H. Water Injection Effects on the Performance of Four-Cylinder, LPG Fuelled SI Engine. *Open Access Scientific Reports* 2013; 2:591.
143. Busuttill D, Farrugia M. Experimental Investigation on the Effect of Injecting Water to the Air to Fuel Mixture in a Spark Ignition Engine, *MM (Modern Machinery) Science Journal* 2015, 1:585-590.
144. Boretti A. Water injection in directly injected turbocharged spark ignition engines. *Applied Thermal Engineering* 2013; 52(1):62-68.
145. Sjeric M, Kozarac D, Taritas I. Experimentally Supported Modeling of Cycle-to-Cycle Variations of SI Engine Using Cycle-Simulation Model. SAE Technical Paper 2014-01-1069; 2014.
146. Thewes M, Baumgarten H, Dohmen J, Uhlmann T, Seibel J, Balazs A, et al. “Gasoline combustion systems beyond 2020”. In: *Proceedings of the 23rd Aachen colloquium automobile and engine technology*, Aachen, Germany, 6–8 October 2014.
147. Vaja I, Gambarotta A. “Internal Combustion Engine (ICE) bottoming with Organic Rankine Cycles (ORCs)”. *Energy* 2010; 35(2):1084–1093.
148. Siano D., Costa M., Bozza F., “Prediction and enhancement of the acoustic performance of a spark ignition engine intake air filter box”, *Proceedings of the Institution of Mechanical Engineers, Part D: Journal of Automobile Engineering* published online 9 November 2012, doi: 10.1177/0954407012461746.
149. Ansys Fluent V14, User's Manual, Ansys Inc. 2011.
150. GT-Power V.7.3, User's Manual, Gamma Technology Inc., 2013.
151. Siano D., Bozza F., Auriemma F., “Acoustic and fluid-dynamic optimization of an automotive muffler”, *Proc. of Inst. Mech. Eng., Part D: Journal of Automobile Engineering*, published online December 10th 2012, doi: 10.1177/0954407012465689.
152. Torregrosa, A. J., Broatch, A., Climent, H., & Fernández, T.. “Time-domain modelling of turbo-compressors in direct injection diesel engines”, *Proceedings of the Institution of Mechanical Engineers, Part D: Journal of Automobile Engineering*, 220(4), 445-457, 2006.
153. Rämmal, H. Galindo, J., “The passive acoustic effect of turbo-compressors”, 9th *International Conference on Turbochargers and Turbocharging*. (Toim.) Institution of Mechanical Engineers. London, UK, 2010.
154. Veloso R., Elnemr Y., Reich F. M., Allam S., "Simulation of Sound Transmission through Automotive Turbochargers." SAE Paper 2012-01-1560, 2012.
155. Torregrosa A., Arnau F., Piqueras P., Reyes-Belmonte, M. et al., "Acoustic One-Dimensional Compressor Model for Integration in a Gas-Dynamic Code," SAE Technical Paper 2012-01-0834, 2012, doi:10.4271/2012-01-0834.
156. Bozza F., De Bellis V., “Steady modeling of a turbocharger turbine for automotive engines”, *Journal of Engineering for Gas Turbines and Power* 136 (1), art. no. 011701, 2014, DOI: 10.1115/1.4025263, ISSN: 07424795.
157. Rämmal H., Tiikoja H., Åbom M., Bodén, “Experimental Facility for the Complete Determination of Sound Transmission in Turbochargers”, SAE paper 2010-01-1424, 2010.

References

158. Holland JH. *Adaptation in natural and artificial systems*. Ann Arbor University of Michigan Press; 1975.
159. Goldberg DE. *Genetic algorithms in search, optimization, and machine learning*. Reading, MA: Addison-Wesley; 1989.
160. Jones DF, Mirrazavi SK, Tamiz M. Multiobjective meta-heuristics: an overview of the current state-of-the-art. *Eur J Oper Res* 2002;137(1):1–9.
161. Schaffer JD. Multiple objective optimization with vector evaluated genetic algorithms. In: *Proceedings of the international conference on genetic algorithm and their applications*, 1985.
162. Fonseca CM, Fleming PJ. “Multiobjective genetic algorithms”. In: *IEE colloquium on ‘Genetic Algorithms for Control Systems Engineering’* (Digest No. 1993/130), 28 May 1993. London, UK: IEE; 1993.
163. Horn J, Nafpliotis N, Goldberg DE. “A niched Pareto genetic algorithm for multiobjective optimization”. In: *Proceedings of the first IEEE conference on evolutionary computation. IEEE world congress on computational intelligence, 27–29 June, 1994*. Orlando, FL, USA: IEEE; 1994.
164. Hajela P, Lin C-y. Genetic search strategies in multicriterion optimal design. *Struct Optimization* 1992;4(2):99–107.
165. Murata T, Ishibuchi H. MOGA: multi-objective genetic algorithms. In: *Proceedings of the 1995 IEEE international conference on evolutionary computation, 29 November–1 December, 1995*. Perth, WA, Australia: IEEE; 1995.
166. Srinivas N, Deb K. Multiobjective optimization using nondominated sorting in genetic algorithms. *J Evol Comput* 1994;2(3):221–48.
167. Zitzler E, Thiele L. Multiobjective evolutionary algorithms: a comparative case study and the strength Pareto approach. *IEEE Trans Evol Comput* 1999;3(4):257–71.
168. Zitzler E, Laumanns M, Thiele L. *SPEA2: improving the strength Pareto evolutionary algorithm*. Swiss Federal Institute Technology: Zurich, Switzerland; 2001.
169. Knowles JD, Corne DW. Approximating the nondominated front using the Pareto archived evolution strategy. *Evol Comput* 2000;8(2):149–72.
170. Corne DW, Knowles JD, Oates MJ. The Pareto envelope-based selection algorithm for multiobjective optimization. In: *Proceedings of sixth international conference on parallel problem solving from Nature, 18–20 September, 2000*. Paris, France: Springer; 2000.
171. Corne D, Jerram NR, Knowles J, Oates J. PESA-II: region-based selection in evolutionary multiobjective optimization. In: *Proceedings of the genetic and evolutionary computation conference (GECCO- 2001)*, San Francisco, CA, 2001.
172. Deb K, Pratap A, Agarwal S, Meyarivan T. A fast and elitist multiobjective genetic algorithm: NSGA-II. *IEEE Trans Evol Comput* 2002;6(2):182–97.
173. Sarker R, Liang K-H, Newton C. A new multiobjective evolutionary algorithm. *Eur J Oper Res* 2002;140(1):12–23.
174. Coello CAC, Pulido GT. “A micro-genetic algorithm for multiobjective optimization”. In: *Evolutionary multi-criterion optimization. First international conference, EMO 2001, 7–9 March, 2001*. Zurich, Switzerland: Springer; 2001.
175. Lu H, Yen GG. Rank-density-based multiobjective genetic algorithm and benchmark test function study. *IEEE Trans Evol Comput* 2003;7(4): 325–43.
176. Yen GG, Lu H. Dynamic multiobjective evolutionary algorithm: adaptive cell-based rank and density estimation. *IEEE Trans Evol Comput* 2003;7(3): 253–74.

References

177. Poloni C. and Pediroda V. "GA coupled with computationally expensive simulations: tools to improve efficiency". In *Genetic Algorithms and Evolution Strategies in Engineering and Computer Science*, pages 267-288, John Wiley and Sons, England, 1997.
178. Yamamoto K. and Inoue O. New evolutionary direction operator for genetic algorithms. *AIAA Journal*, volume 33, number 10, pages 1990-1993, 1995.
179. Bozza F., De Bellis V., Teodosio L., "Potentials of Cooled EGR and water injection for knock resistance and fuel consumption improvements of gasoline engines", *Applied Energy* 169: 112-125, 2016, doi: 10.1016/j.apenergy.2016.01.129.